FACULTY OF SCIENCES

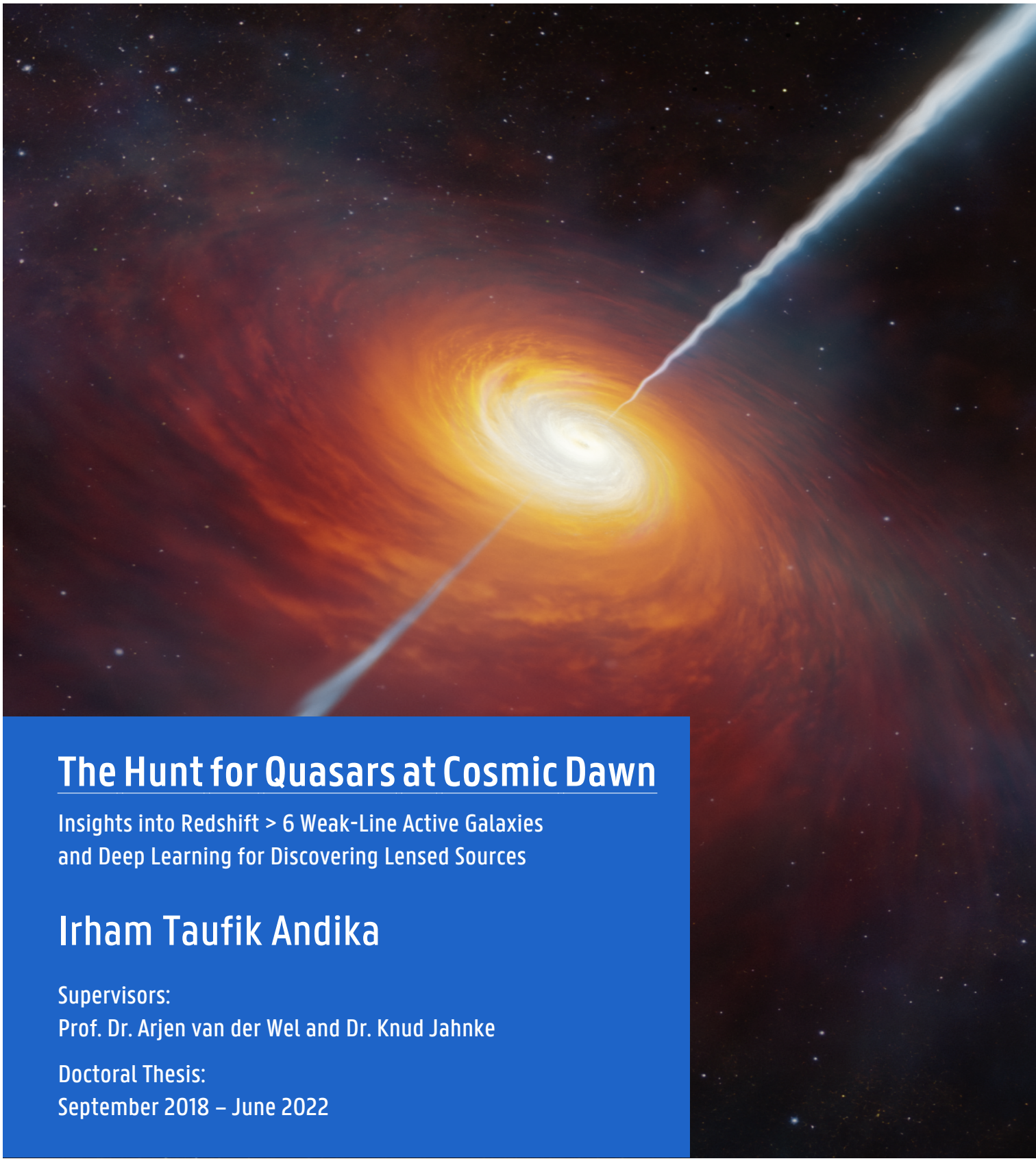

The Hunt for Quasars at Cosmic Dawn

Insights into Redshift > 6 Weak-Line Active Galaxies and Deep Learning for Discovering Lensed Sources

Irham Taufik Andika

Supervisors:
Prof. Dr. Arjen van der Wel and Dr. Knud Jahnke

Doctoral Thesis:
September 2018 – June 2022

GHENT UNIVERSITY

Max-Planck-Institut für Astronomie Heidelberg
Max Planck Institute for Astronomy Heidelberg

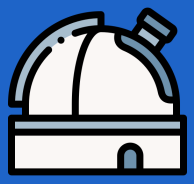

Quasars are one of the brightest sources in our universe, powered by matter accretion onto supermassive black holes (SMBHs). In the highest-redshift frontier, these SMBHs could already reach billion of solar masses when the cosmos was only less than a gigayear old. Hence, redshift > 6 quasars are excellent laboratories for unraveling the nature of the first SMBHs/galaxies formation and growth.

To date, more than three hundred quasars have been discovered. Interestingly, about ten percent of them belong to a class called "young quasars" showing lifetimes of only a few thousand years. These young quasars pose problematic issues since their ages are many times shorter than the typical timescale required for growing SMBHs (i.e., a few million to billion years). Additionally, a notable subset of high-redshift quasars exhibits weak emission lines, in contrast with the general quasar population. Therefore, expanding the sample size at this early era is crucial for investigating the connection between the rare weak-line sources and the cases of very young quasars, which might provide insights into the early growth modes.

Another prominent issue in the field of high-redshift quasar searches is the rarity of the gravitationally lensed sources. Because of the large lensing optical depths attained at this distance, it has been anticipated for decades that up to one-third of the high-redshift quasars will be strongly lensed. However, only one has been discovered so far. A re-examination of the search strategies employed in the past quasar surveys reveals a significant selection bias against lensed quasars. Accordingly, constructing a more robust selection method to uncover such hidden populations of lenses will be a crucial experiment to conduct.

In this work, we present an endeavor to increase the sample of known quasars and lensed sources in the early universe. By utilizing spectral energy distribution modeling and deep learning approaches applied to multi-band photometric data, we validate our search techniques and present new candidates to be followed up. We also report the discovery of PSO J083+11, a new redshift = 6.34 young weak-line quasar. Comprehensive multiwavelength campaigns using state-of-the-art instruments are carried out to examine the physical properties of this source and its host galaxy. Finally, we also characterize the proximate sub-damped Lyman-alpha system and the low-redshift metal absorber toward this quasar.

UNIVERSITEIT GENT

Ghent University
Department of Physics and Astronomy
Sterrenkundig Observatorium
Krijgslaan 281 S9
B-9000 Ghent, Belgium

FACULTY OF SCIENCES

The Hunt for Quasars at Cosmic Dawn

Insights into Redshift > 6 Weak-Line Active Galaxies and Deep Learning for Discovering Lensed Sources

Irham Taufik Andika
Student number: 02115018

Supervisors: Prof. Dr. Arjen van der Wel and Dr. Knud Jahnke

Dissertation submitted to Ghent University for the degree of
Doctor of Science in Astronomy

Academic year: 2018–2022

GHENT UNIVERSITY

Max-Planck-Institut für Astronomie Heidelberg
Max Planck Institute for Astronomy Heidelberg

Examination Committees

Promoter

Prof. Dr. Arjen van der Wel
Astronomical Observatory, Ghent University, Belgium

Dr. Knud Jahnke
Max Planck Institute for Astronomy, Germany

Jury

Prof. Dr. Ir. Toon Verstraelen (Chair)
Center for Molecular Modeling, Ghent University, Belgium

Prof. Dr. Ilse De Looze
Astronomical Observatory, Ghent University, Belgium

Prof. Dr. Archisman Ghosh
Experimental Particle Physics and Gravity Group, Ghent University, Belgium

Prof. Dr. Maarten Baes
Astronomical Observatory, Ghent University, Belgium

Prof. Dr. Jochen Heidt
Center for Astronomy of Heidelberg University, Germany

Contents

List of Figures

List of Tables

Preface

This dissertation is the culmination of four years of my doctoral research. Throughout this period, I have had the opportunity to work on several projects which revolve around the characterization of active galaxies and supermassive black holes at cosmic dawn. Specifically, this work presents an endeavor to discover the quasars at high redshifts and the hidden population of galaxy-quasar lenses, expanding the selection space missed by previous quasar surveys. *How many lensed quasars did everyone miss, and how to find them? What can we learn from the quasar spectra about the nature of high-redshift active galaxies showing weak emission lines?* These are the key questions that I hope to answer.

It is safe to say that this dissertation would not exist without the support of many people. First of all, I want to express my gratitude to **Knud Jahnke** and **Arjen van der Wel** for their invaluable guidance and encouragement. You have provided tremendous help, and I find myself very lucky to have both of you as my supervisors.

I want to thank the high-z team, in particular: **Masafusa Onoue**, for patiently addressing all of my questions on data analysis and observing strategies; **Eduardo Bañados**, for sharing your enthusiasm for quasar hunting and physics; **Fabian Walter**, for all of your assistance, from papers to suggestions to future choices.

I acknowledge the support from the International Max Planck Research School for Astronomy and Cosmic Physics at the University of Heidelberg (IMPRS-HD), which funded this doctoral project. I am grateful to **Christian Fendt**, who assisted me in navigating the German systems at the start of my study. Special thanks should also go to **Jochen Heidt** for agreeing to review my dissertation. I also want to thank my fellow 14th IMPRS-HD generation for a good time on the yearly trips and for helpful input throughout our scientific activities.

I should be eternally grateful to all of my Heidelberg and Indonesian friends, who have given me the most precious gift of making my campus life so meaningful and vibrant. Especially **Adri**, **Fenyka**, **Nimas**, and **Whytia**, I cannot even think where I would be now if I had never met you. Also, **Ali**, **Alifa**, **Ardhi**, and **Chandra**, thanks for battling beside me!

Last but not least, there is my family. **Elsa**, my wife, thank you for your unwavering love and never-ending encouragement, especially through the most challenging moments. **Mama** and **Faisal**, who always inspire me to chase my dreams, thank you for everything!

Abstract

Quasars in the early universe are excellent laboratories for analyzing the assembly of the first supermassive black holes and galaxies. In this work, we present an endeavor to discover $z \gtrsim 6$ quasars and lenses, expanding the selection space missed by many previous quasar surveys. Our strategy consists of three main steps: (i) candidates pre-selection based on their colors using catalog-level photometry, (ii) modeling the observed spectral energy distributions and calculating their probabilities to be a quasar plus lens galaxy or some contaminant, and (iii) image classification based on convolutional neural network analysis to detect potential lens configurations. Utilizing the combined optical multi-band images and infrared data, we validate our selection pipeline and compile new high-probability (lensed) quasar candidates.

We then present the discovery of a remarkable weak-line quasar at $z = 6.3401$, i.e., PSO J083+11. Using the spectrum taken with Gemini/GNIRS, we fit the continuum and Mg II line emissions, resulting in a black hole mass of $\log(M_{\rm BH}) = 9.30^{+0.16}_{-0.10}\ M_\odot$ and an Eddington ratio of $L_{\rm bol}/L_{\rm Edd} = 0.51^{+0.13}_{-0.17}$. The broad-line emissions of this source are inherently weak, where rest-frame equivalent widths Lyα + N V $= 5.65^{+0.72}_{-0.66}$ Å and C IV ≤ 5.83 Å. The spectrum reveals a small proximity zone size, suggesting a present quasar age of only $\approx 10^3 - 10^{4.5}$ yr. HST/WFC3–ACS imaging shows no strong lensing affecting the apparent flux. ALMA observations uncover a quasar host similar to hyper-luminous infrared galaxies having a star formation rate of $\approx$ 900–4900 $M_\odot$ yr^{-1}. Given its accretion lifetime and the timescale of the broad-line region formation, we propose that the PSO J083+11's weak-line nature originates from a still-emerging broad-line region event.

In addition, Magellan/FIRE and VLT/MUSE spectroscopy reveal the presence of a $z = 6.314$ metal-poor sub-damped Lyα absorber toward PSO J083+11, having a neutral hydrogen column density of $\log N_{\rm HI} = 20.03 \pm 0.30$ cm^{-2} along with an abundance ratio of $[{\rm C/O}] = -0.04 \pm 0.33$ and a metallicity of $[{\rm O/H}] = -2.19 \pm 0.44$. This absorber truncates PSO J083+11's proximity zone and complicates its quasar age estimation. However, at the same time, this quasar exhibits no trace of an extended Lyα halo, with a 1σ surface brightness limit of 2.76×10^{-18} erg s^{-1} cm^{-2} arcsec^{-2} at $1''$ aperture, or corresponds to a Lyα luminosity of ≤ 43.46 erg s^{-1}. This non-detection provides alternative support for the notion of a young quasar with a short accretion lifetime. Further statistical analyses with more samples at the highest redshifts are critical for establishing the relations between typical quasars, young sources, and weak-line active galaxies. This study will help us apprehend the rapid growth physics of the earliest black holes.

Nederlandse Samenvatting

Quasi-stellaire objecten (QSOs) in het vroege heelal zijn uitmuntende laboratoria om de vorming van de eerste super-massieve zwarte gaten en sterrenstelsels te analyseren. In dit werk presenteren we de ontdekking van QSOs en gravitationele lenzen op roodverschuiving $z \gtrsim 6$ die door voorgaande waarneemprogramma's gemist werden als gevolg van selectie effecten. Onze strategie bestaat uit drie stappen: (i) pre-selectie van kandidaten op basis van hun fotometrische kleuren; (ii) het modelleren van hun spectrale energieverdelingen, waarmee we de waarschijnlijkheden van de mogelijke classificaties (QSO, lens, contaminant) bepalen; (iii) beeldclassificatie op basis van een neuraal-netwerk analyse om potentiële lens configuraties te detecteren. Onze methodologie, op basis van de combinatie van optische en infrarode fotometrische gegevens, levert een nieuwe lijst van statistisch robuuste kandidaten van gelensde QSOs op.

Vervolgense presenteren we de ontdekking van een zeer opvallande QSO op $z = 6.3401$: PSO J083+11. We modelleren het optisch spectrum (van Gemini/GNIRS) als een continuum plus Mg II lijnemissie, hetgeen resulteert in de schatting van de massa van het zwarte gat ($\log(M_{\rm BH}) = 9.30^{+0.16}_{-0.10}\ M_\odot$) en de Eddington ratio ($L_{\rm bol}/L_{\rm Edd} = 0.51^{+0.13}_{-0.17}$). De brede-lijn emissie van deze bron is intrinsiek zwak, met een equivalente breedte van slechts Lyα + N V $= 5.65^{+0.72}_{-0.66}$ Å and C IV $\leq$ 5.83 Å. Het spectrum vertoont een kleine 'proximity zone', hetgeen een zeer jonge QSO leeftijd impliceert van slechts $\approx 10^3 - 10^{4.5}$ yr. HST/WFC3–ACS beelden vertonen geen bewijs voor een sterke toename in de fluxen via lenswerking. ALMA waarnemingen tonen een hyper-lumineus infrarood stelsel met een stervormings rato van $\approx$ 900–4900 $M_\odot$ yr^{-1}. De korte accretietijdschaal zouden kunnen impliceren dat de brede-lijnstralingszone van PSO J083+11 zich nog in de vormingsfase bevindt.

Magellan/FIRE and VLT/MUSE spectroscopie tonen een metaalarm 'sub-damped' Lyα absorptie systeem op $z = 6.314$ in de voorgrond van PSO J083+11, met een neutrale waterstofkolom van $\log N_{\rm HI} = 20.03 \pm 0.30$ cm^{-2}, abundanties [C/O] $= -0.04 \pm 0.33$, en [O/H] $= -2.19 \pm 0.44$. Dit systeem overlapt met de 'proximity zone' hetgeen de leeftijdschatting van de QSO compiceert. Tegelijkertijd is er geen indicatie van een Lyα halo, met een 1σ limiet op de oppervlaktehelderheid van 2.76×10^{-18} erg s^{-1} cm^{-2} arcsec^{-2} voor een $1''$ apertuur, hetgeen correspondeert met een Lyα lichtkracht van ≤ 43.46 erg s^{-1}. Deze limiet dient als ondersteunend bewijs voor een jonge QSO met een korte accretietijd. Verdere analyse van grotere aantallen QSOs zullen de verbanden tonen tussen jonge objecten en de volledige populatie. Deze studie zal tot een beter begrip leiden van de snelle groei van de vroegste zwarte gaten.

Part I

Context and Theoretical Framework

Chapter 1

The Standard Cosmological Model

Understanding how the earliest luminous sources in the universe arose and developed over the cosmic time is a central issue in observational cosmology. In this context, quasi-stellar radio sources (quasars) are one the brightest non-transient objects, powered by the matter accretion onto the supermassive black holes (SMBHS; Netzer 2013). In the high-redshift frontier, these sources are prime laboratories for exploring the assembly, growth, and structure of the first SMBHs and galaxies (Pacucci & Loeb 2022).

More than three hundred quasars have been discovered to date (Inayoshi et al. 2020). Interestingly, around ten percent of them show accretion lifetimes of only a few thousand years (Eilers et al. 2021). These young quasars pose problematic issues since their ages are many times shorter than the typical timescale required for growing SMBHs (i.e., a few million to billion years, Khrykin et al. 2021; Worseck et al. 2021). Additionally, a notable subset of high-redshift quasars exhibits weak emission lines, in contrast with the general quasar population (Andika et al. 2020). Therefore, extending the sample size at this very early epoch is paramount for exploring the association between the rare weak-line sources and the cases of very young quasars, which might provide insights into the early SMBH growth modes.

As the title implies, the focus of this work is on the detection and characterization of these exotic sources at cosmic dawn. To understand what is meant by cosmic dawn, we will start by providing a brief overview of the standard cosmological principles used throughout this work. We then present a brief review of our universe's history, highlighting the epoch of reionization, which becomes our primary interest. Following that, more specific subjects such as quasar physics and gravitational lens modeling that are critical to comprehend this work in a broader context will be introduced. The topics discussed in the following sections are compiled from Liddle (2015), Schneider (2015), Ryden (2016), and Dodelson & Schmidt (2020).

1.1 Redshift and Age of the Universe

Due to the expanding universe, nearly all galaxies seem to be receding away from us. At a given time t, the recession velocity $v(t)$ is related to the source's distance $r(t)$, namely:

$$v(t) = H_0 r(t). \tag{1.1}$$

This equation is recognized as the Hubble-Lemaître law, in which H denotes the Hubble constant and the "0" index reflects its value in the present-day universe. It is worth noting that this law accurately characterizes the typical behavior of distant galaxies but does not apply to the local sources due to their peculiar movement. Subsequently, the light emitted by a distant source would be redshifted due to the universe's expansion, meaning that their corresponding wavelengths are stretched into the lower energy regime. This phenomenon informs us how far the universe has enlarged since light started to propagate. The cosmic redshift z is then specified as:

$$1 + z = \frac{\lambda_{\rm obs}}{\lambda_{\rm em}} = \frac{a(t_{\rm obs})}{a(t_{\rm em})}, \tag{1.2}$$

where $\lambda_{\rm obs}$ and $\lambda_{\rm em}$ are respectively the observed and emitted wavelengths. The variable $a(t)$ is defined as the universe's scale factor that controls the pace of the cosmic expansion. It is a function that illustrates how physical separations increase over time. The scale factor is usually set to unity, that is $a(t_{\rm obs}) = 1$, at the current epoch, which is normally the time of the observations ($t_{\rm obs} = t_0$).

The Friedman equations, which are the solutions to Einstein field equations for an isotropic and homogeneous universe, regulate the nature of the scale factor and, hence, the dynamics of the cosmos:

$$H^2 = \left(\frac{\dot{a}}{a}\right)^2 = \frac{8\pi G}{3}\rho - \frac{\kappa c^2}{a^2} + \frac{\Lambda}{3}, \tag{1.3}$$

$$\frac{\ddot{a}}{a} = -\frac{4\pi G}{3}\left(\rho\frac{3p}{c^2}\right) + \frac{\Lambda}{3}, \tag{1.4}$$

where the gravitational constant is G, the universe's curvature is κ, the speed of light is c, and the cosmological constant is Λ. The Λ represents the dark energy contribution that causes the accelerated expansion of the cosmos (Riess et al. 1998; Perlmutter et al. 1998). These equations also relate the universe's density ρ and pressure p to the scale factor.

Presuming that the universe has a flat curvature ($\kappa = 0$; see e.g., Planck Collaboration et al. 2020), and by choosing $\Lambda = 0$, we may calculate the present-day critical density, that is:

$$\rho_{\rm crit}(t) = \frac{3H^2}{8\pi G} = 2.78h^{-1} \times 10^{11} M_\odot/(h^{-1}\ {\rm Mpc})^3, \tag{1.5}$$

where we adopt the normalized Hubble parameter as:

$$h = \frac{H_0}{100\ {\rm km\ s^{-1}\ Mpc^{-1}}}. \tag{1.6}$$

Our universe seems to be near the critical density because, on average, the galaxies have masses of 10^{11}–$10^{12}\ M_\odot$ while their typical separations are around one Mpc.

We then express the dimensionless density parameters for the matter (Ω_m), radiation (Ω_r), and cosmological constant (Ω_Λ) as:

$$\Omega_\mathrm{m} = \frac{\rho_{\mathrm{m},0}}{\rho_{\mathrm{crit},0}}; \qquad \Omega_\mathrm{r} = \frac{\rho_{\mathrm{r},0}}{\rho_{\mathrm{crit},0}}; \qquad \Omega_\Lambda = \frac{\rho_\Lambda}{\rho_{\mathrm{crit},0}} = \frac{\Lambda}{3H_0^2}, \tag{1.7}$$

and

$$\Omega_0 = \Omega_\mathrm{m} + \Omega_\mathrm{r} + \Omega_\Lambda, \tag{1.8}$$

where the $\Omega_0 = 1$, $\Omega_0 > 1$, and $\Omega_0 < 1$ imply a universe with the flat, open, and closed geometry, respectively. Subsequently, the Friedmann equations can be rewritten as:

$$H^2 = \left(\frac{\dot{a}}{a}\right)^2 = H_0^2 \left[\Omega_\mathrm{r} a^{-4} + \Omega_\mathrm{m} a^{-3} + \Omega_\Lambda \left(1 - \Omega_0\right) a^{-2}\right]. \tag{1.9}$$

This formalism allows us to separate the cosmic history into three main phases: a radiation-dominated period at very early times ($t < 47,000$ yr), succeeded by a matter-dominated era ($47,000$ yr $< t <$ 9.8 Gyr), and the present day dominated by the cosmological constant.

Integrating Equation 1.9 yields an estimate of the universe's age as a function of the scale factor, that is:

$$t(a) = \frac{1}{H_0} \int_0^{a'} \left(\Omega_\mathrm{r} a^{-2} + \Omega_\mathrm{m} a^{-1} + (1 - \Omega_0) + \Omega_\Lambda a^2\right)^{1/2} da. \tag{1.10}$$

Incorporating this formalism with Equation 1.2, we can calculate the corresponding age at the time when the source's light was emitted from the redshift of z. Using recent estimates from Planck Collaboration et al. (2020, i.e., $\Omega_\Lambda = 0.685$, $\Omega_\mathrm{m} = 0.315$, and $H_0 = 67.4$ km s^{-1} Mpc^{-1}) we obtain the ages of $t = 1.2$ Gyr, 927 Myr, and 759 Myr at the redshifts of $z = 5$, 6, and 7, respectively. In addition, our universe is around 13.8 Gyr old at the present day ($z = 0$).

1.2 Cosmological Distances

There are several options to express the distance between two sources in cosmology. The distances of faraway galaxies are frequently specified based on their redshifts, which are directly observable. In this dissertation, we employ multiple metrics, which we explain as follows.

The *proper distance* is the distance calculated between two sources across a geodesic at a specified, fixed point in time. However, owing to the expansion of the cosmos, this distance will vary over time.

The *comoving distance* between two sources shifting with the Hubble flow, in contrast, does not vary over time since it compensates for the universe's expansion, that is:

$$d_\mathrm{comoving}(z) = \int_0^z \frac{dz'}{H(z')}, \tag{1.11}$$

where $H(z')$ is provided by Equation 1.2 and 1.9. The scale factor connects the proper and comoving distances, so they are the same in the present-day universe:

$$d_{\text{proper}} = a(t)\, d_{\text{comoving}}. \tag{1.12}$$

The *angular diameter distance* is quantified as the source's angular size θ and its physical extent l as perceived by the observer from Earth, that is:

$$d_{\text{angular}}(z) = \frac{l}{\theta}. \tag{1.13}$$

In a flat universe, this relation could be rewritten in the comoving distance term:

$$d_{\text{angular}}(z) = \frac{d_{\text{comoving}}(z)}{1+z}. \tag{1.14}$$

The *luminosity distance* of a source is defined by the product of its luminosity (L) and measured flux (F), namely:

$$d_{\text{luminosity}} = \sqrt{\frac{L}{4\pi F}} \tag{1.15}$$

This value is essential for calculating distances to astronomical standard candles, for example, Type Ia Supernovae, from which we may compute their intrinsic absolute luminosity (e.g., Schmidt et al. 1998; Riess et al. 1998; Perlmutter et al. 1998). After establishing the relevant cosmological framework, we will briefly portray the key transition phases of the cosmos in the following sections.

1.3 History of the Universe and Reionization Era

The Big Bang occurred around 13.8 billion years ago, beginning the creation of our universe (see Figure 1.1). Within this moment, the cosmos was extraordinarily hot, dense, and energetic, and then it began to expand. During the first 10^{-37} s, our universe had an extremely fast expansion phase called the *cosmic inflation* (Guth 1981). There, the density fluctuations produced by the uncertainty principle were intensified, providing the foundation for the universe's large-scale structure to emerge. After this inflationary phase, the universe expansion continued, although noticeably slower than before.

After 400 thousand years since the Big Bang, or equivalent to $z \approx 1100$, the universe's temperature dropped to 3000 K, enabling the electrons and protons to recombine and produce light elements such as neutral hydrogen and helium. This period is named the *Epoch of Recombination*. In the energetic plasma, photons decoupled from baryons, resulting in the primordial radiation known as the *Cosmic Microwave Background*. Subsequently, the *Dark Ages* started when the diffused matter in the cosmos was mainly neutral.

The birth of the first generation stars, galaxies, and quasars indicated the emergence of a new cosmic era called the *Epoch of Reionization*. The cosmic dark ages ended at this stage,

and the cosmic gas transformed from a neutral state to the predominantly ionized medium that we see today. One of the primary aims of observational cosmology and extragalactic astrophysics today is to determine when and how this major phase transition occurred. The cosmic reionization process might hold clues into the nature of the primordial sources and the emergence of the large-scale structure.

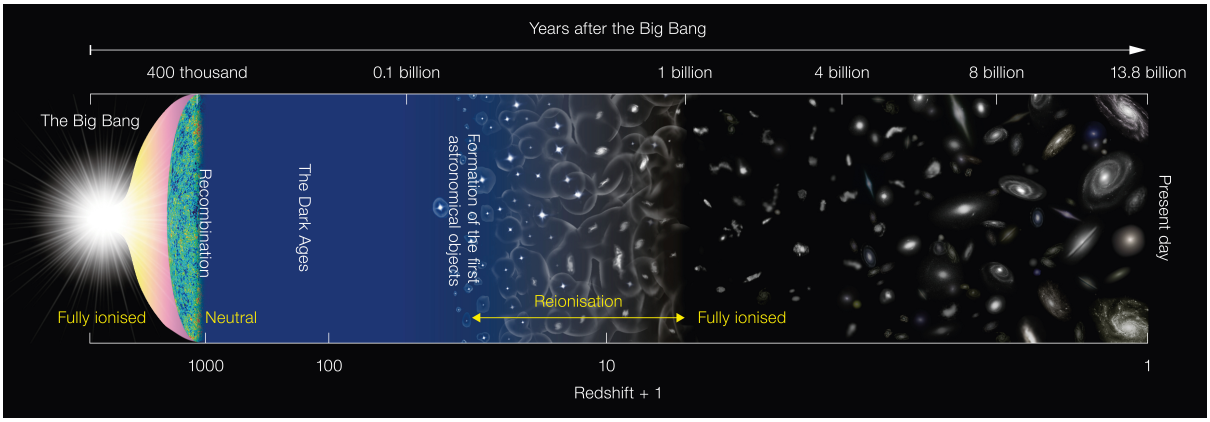

Figure 1.1. This figure illustrates some crucial eras in the cosmic evolution since the Big Bang 13.8 billion years ago. After 400 thousand years since the Big Bang, the universe was in a neutral state, and it stayed so until the light from the first stars began to ionize the hydrogen. The hydrogen gas in the universe was fully ionized after a few hundred million years. Image credit: NAOJ.

It is exceedingly challenging to map the reionization using a theoretical method because every simulation must account for several physical scales. It is essential to simulate the galaxy formation and gas accretion physics on sub-kpc regimes to describe the attributes of the earliest sources responsible for generating the ionizing radiation, such as star formation, radiative feedback, and metal enrichment. These primordial sources must also be positioned within a cosmic context – i.e., inside the large-scale dark matter distribution – where the typical inhomogeneities stretch up to $\approx$ 100 Mpc. Mixtures of the hydrodynamical and N-body simulations are often utilized in the first scenario, whereas the radiative transfer calculations are frequently used in the second (for an overview of these techniques, see Mesinger 2018).

Despite significant advances in the previous decade, the exact timing, length, and morphology of the reionization era remain unanswered. For example, the commencement of the reionization process is still very unknown, but there are definite observable considerations (for a review, see Fan et al. 2006). According to the latest the Thomson optical depth measurement, $\tau = 0.054 \pm 0.007$ (Planck Collaboration et al. 2020), the mid-point of reionization is at $z = 7.7 \pm 0.7$. In addition, the reionization should end by $z \sim 5.5$, inferred based on the observed intergalactic medium opacity evolution (e.g., Eilers et al. 2018a; Bosman et al. 2021b). The universe's structure continued to expand following the end of reionization. Then, quasar activity and star formation were at their climax at around $z \sim 2$, and the most intense growth might have occurred during this period (e.g., Madau & Dickinson 2014). At $z = 0$, the present-day universe exhibits a wide range of cosmic structures. Generally, they are arranged in filaments and sheets to create the cosmic web.

Observations of the ultraviolet-bright galaxy samples at $z \gtrsim 6$ argued that the primary contributors for the reionization were less-luminous star-forming galaxies (e.g., Bouwens et al. 2015 and references therein; but see also, e.g., Giallongo et al. 2015, for an alternative view). On the other side, luminous high-redshift quasars as beacons from the distant past are additional crucial reionization era probes. A single $z \gtrsim 6$ quasar discovered supplies tighter limits on the neutral fraction of hydrogen at a particular redshift and a sightline than cosmic microwave background data. In the next section, we will describe the latest knowledge of the sources observed near the frontier of cosmic reionization.

1.4 The Emergence of First Galaxies

Several deep-sky surveys have been performed in recent years to look for the earliest galaxies. Photometric observations, which measure the rest-frame optical or ultraviolet emission from the ionized nebular gas and newborn stars, are one method of discovering such galaxies. The search is usually carried out using, for example, the "dropout" technique to find Lyman-break galaxies (LBGs). In principle, the intergalactic neutral hydrogen absorption generates a drop in the observed galaxy spectrum, which is seen as an abrupt shift in broadband colors (e.g., Harikane et al. 2021). LBGs found from the ground-based surveys utilizing this approach tend to be massive and have intense ultraviolet stellar emission (e.g., Pacucci et al. 2022). Observations of the Lyα emission line, in contrast, enable sets of narrowband filters to easily detect the Lyα emitter (LAE) population. LAEs are thought to be high-z counterparts of the local universe's dwarf galaxies. They represent a compact metal-poor star-forming galaxy with stellar (halo) mass of around 10^8–10^9 $M_\odot$ (10^{10}–10^{11} $M_\odot$) and star formation rate (SFR) of approximately 1–10 $M_\odot$ yr^{-1} (Ouchi et al. 2020). Theoretical and empirical investigations imply that LBGs and LAEs are part of the same underlying galaxy population, with the primary distinction being the different selection methods (Garel et al. 2015).

To date, sensitive Hubble Space Telescope imaging complemented with Spitzer Space Telescope photometry has discovered early-forming galaxy candidates with possible redshifts as high as $z \sim 11$ (Oesch et al. 2016). The most distant galaxies with spectroscopically confirmed redshifts are at $z = 9$–10, where their spectra were obtained with various instruments such as Atacama Large Millimeter/submillimeter Array, Subaru, Keck, and Very Large Telescope. At lower redshifts ($z = 7$–9), photometric observations have yielded ~ 1000 galaxy candidates. Direct spectroscopic evidence exists for hundreds of $z \sim 7$ galaxies and a few at $z \gtrsim 8$ (see, for example, Bouwens et al. 2015; Ishigaki et al. 2018; Herenz et al. 2019; Kusakabe et al. 2020; Kakuma et al. 2021; Finkelstein et al. 2021). It is worth noting that performing spectroscopy to characterize high-z ultraviolet-selected galaxies is challenging because the Lyα is hard to detect due to neutral hydrogen absorption (Jiang et al. 2021). This phenomenon is partly because the Lyα photons escape fraction is heavily driven by the morphology, ionization state, and composition of surrounding galactic gas.

Quasars have been detected up to $z \approx 7.6$ owing to their extraordinary brightness, providing alternative probes for studying the intergalactic medium in the reionization era (Bañados et al. 2018; Yang et al. 2020a; Wang et al. 2021a). Their spectra also contain a lot of data, such as the chemical abundance, central black hole mass, and accretion mode (see, e.g., Inayoshi et al. 2020, for review). Furthermore, their host galaxies belong to the most gas-rich, massive, and star-forming sources at cosmic dawn (Decarli et al. 2018; Neeleman et al. 2021; Meyer et al. 2022). Therefore, quasars are prime laboratories for understanding the co-evolution of the first black holes and galaxies. In the next section, we will review the history of quasar discovery and the fundamental components of this exceptional source.

Chapter 2

Quasars as Relics from the Ancient Times

The word "quasar" was initially invented as an abbreviation for "quasi-stellar radio source" because of its initial radio-based discovery[1] (e.g., Hazard et al. 1963; Schmidt 1963). When a growing amount of quasars with no radio emission were identified in the subsequent years, the term "QSO", which stands for "quasi-stellar object", was introduced (e.g., Sandage 1965; Schmidt 1966). Today, these two terms are often used interchangeably by astronomers.

Quasars (and active galaxies in general) are fueled by the matter accretion onto SMBHs in galactic nuclei and produce strong radiations. They emit powerfully over the whole electromagnetic spectrum, from radio frequencies to X-rays and sometimes up to γ-ray. Moreover, due to their intrinsically high luminosities, quasars greatly expand our horizon of the observable universe up to the earliest cosmic epochs. According to the quasar-galaxy co-evolution theories, each high-mass galaxy passes through a bright quasar phase, resulting in the SMBHs seen in the cores of all local universe's bulge-dominated galaxies (e.g., Soltan 1982; Kormendy & Richstone 1995; Hopkins et al. 2008). Solid knowledge of the structure of quasars has been established after a few decades of both observational and theoretical efforts (Kormendy & Ho 2013; Heckman & Best 2014).

2.1 Main Components of Quasars

As proposed by the unification model of active galactic nuclei (see Figure 2.1; Antonucci 1993; Urry & Padovani 1995; Urry 2004; Netzer 2015; Spinoglio & Fernández-Ontiveros 2021), the quasars are mostly made of the following primary physical elements:

- A **supermassive black hole** having the mass of $\log 10^6 \lesssim M_{\rm BH}/M_\odot \lesssim 10^{10}$ hosted in the central region.

[1] For a comprehensive narrative of the circumstances that led to the finding of the very first quasar, i.e., 3C273, we refer to Hazard et al. (2018).

- A subparsec **accretion disk** consists of materials with non-zero angular momentum, accreted by the black hole and emits a considerable quantity of radiation in the ultraviolet/optical rest-frame wavelength.
- A **broad-line region** (BLR) producing the rest-frame ultraviolet/optical broad emission lines, formed by high-density ($n_e \geq 10^9$ cm^{-3}) and high-velocity ($\gtrsim 1000$ km s^{-1}) gas clouds, located at a luminosity-dependent distance of around 0.01–1 pc from the central black hole.
- A high-energy region called **X-ray corona**, which is the hot gas ($\gtrsim 10^7$ K) located around the accretion disk, emits heavily in the X-ray spectrum.
- An obscuring structure, referred to **dusty torus**, having luminosity-dependent dimensions of approximately 0.1–10 pc, absorbing accretion disk's energy and re-radiating it in the infrared region ($\lambda \sim 3$ μm).
- A **narrow-line region** (NLR), which is gas clouds with low-density ($n_e \sim 10^3$–10^6 cm^{-3}) traveling at speeds of around 300–500 km s^{-1}, extending across the ionization cones from outside the torus to very far distances ($\gtrsim 0.1$ kpc) and generating narrow-line emissions in the quasar spectrum.
- A pair of highly-collimated **jets** moving with relativistic speed and able to transport materials outwards for up to a few Mpc.

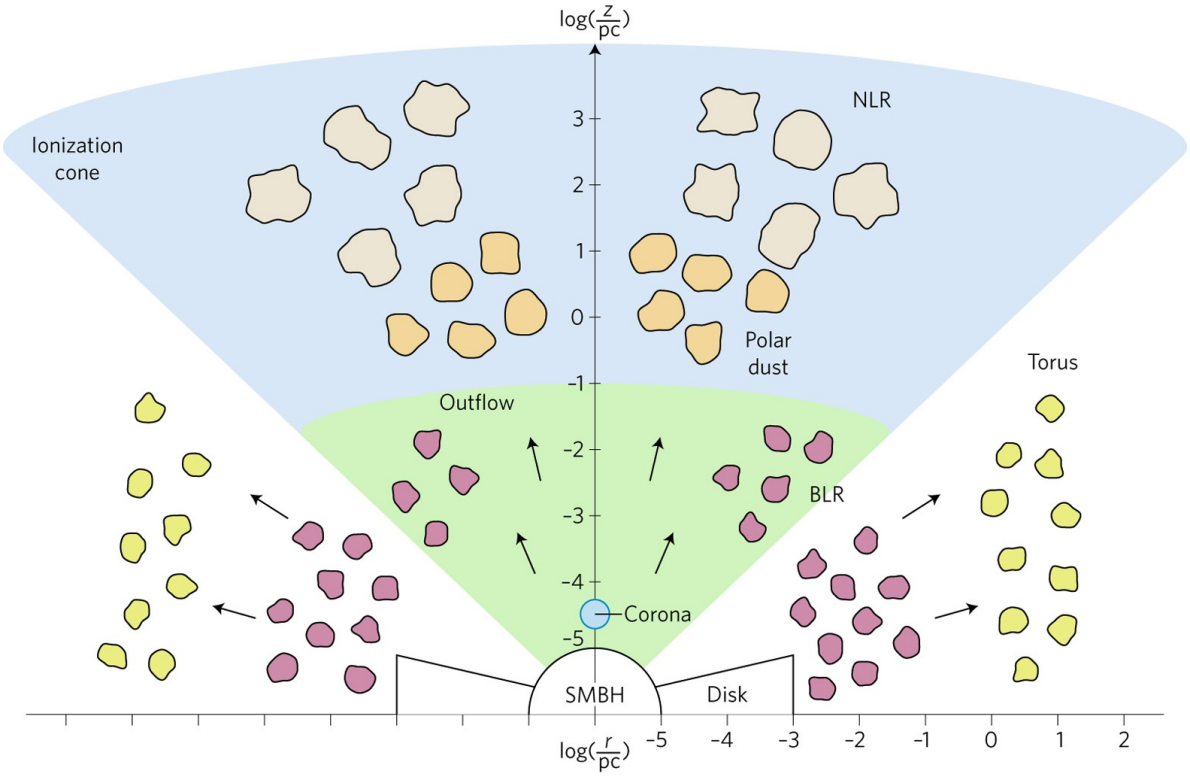

Figure 2.1. According to the active galactic nuclei unification model, the observed variations in quasar spectral energy distributions originates from a varying observer viewing angles and different covering factors of the obscuring material. Image credit: Ramos Almeida & Ricci (2017).

Depending on the power of the radio jets, we see two types of quasars: radio-quiet and radio-loud. Radio-loud sources constitute approximately 10% to 20% of the quasar population and frequently show luminous radio lobes (Bañados et al. 2015b). Their synchrotron emission is highly polarized, which is thought to be caused by the accelerated electrons inside the magnetic field trapped within the jets.

The unification model also suggests that for Type 1 quasars with broad emission lines, the observers have a clear view of the central region (Netzer 2013). On the other hand, for Type 2 quasars, the broad-line regions and the central accretion disk are obscured by considerable dust and gas inside the torus (Hickox & Alexander 2018). Hence, the observer only witnesses the narrow-line emissions from the clouds in the narrow-line region. The accretion disk radiation could not be directly observed in these obscured quasars. Note that the difference between obscured and unobscured quasars could also be caused by the evolutionary process, not only geometric phenomena (see Figure 2.2; Hopkins et al. 2008). In addition, it is crucial to highlight that the spectral energy distributions of quasars seem identical in the local and distant universe since similar physical mechanisms regulate the emission (Shang et al. 2011).

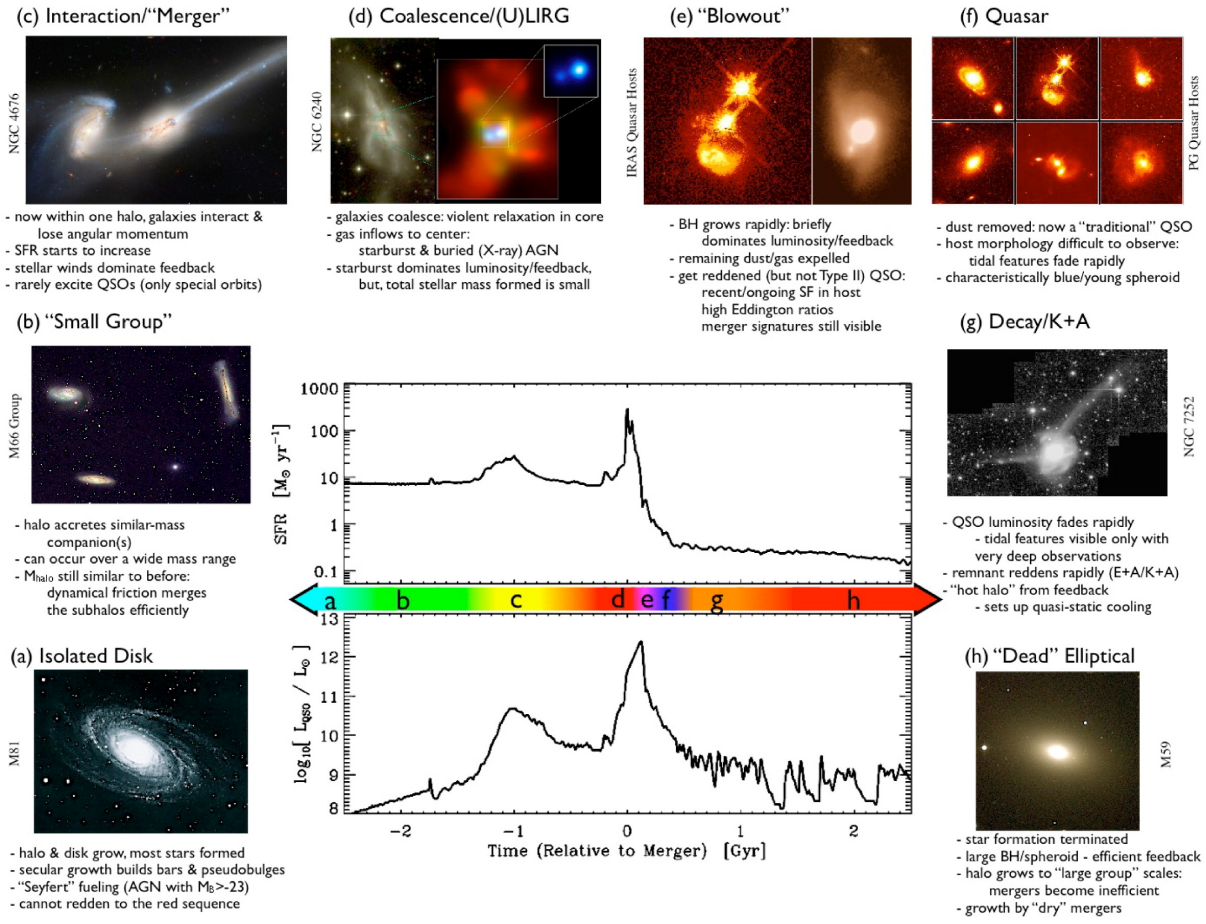

Figure 2.2. Schematic picture of the quasars, supermassive black holes, and elliptical galaxies co-evolution. In this framework, the unobscured and obscured quasars are evolutionary rather than geometric phenomena. Image credit: Hopkins et al. (2008).

2.2 Central Black Hole Properties

The spectra of high-z quasars offer an excellent probe for characterizing the central black hole properties. The search technique that we adopt for finding high-z quasars will be discussed later in Part II. In this section, we will give more insights into the topics of black hole characterization, using Vanden Berk et al. (2001) and Ghisellini (2013) as the primary reference. The accretion disk is made up of materials falling onto the black hole, which is losing angular momentum and emits radiation in the form of:

$$L = \epsilon \dot{M}_{\rm BH} c^2, \tag{2.1}$$

where ϵ is the radiative efficiency and $\dot{M}_{\rm BH}$ is the mass accretion rate.

The Eddington luminosity ($L_{\rm Edd}$), or theoretical maximum brightness allowed for the quasar, is another crucial quantity. This value is derived under the assumption that: (i) the gravitational pull and outward radiation pressure are in equilibrium, (ii) the gravitational force acts on protons, while the radiation pressure acts on electrons via Thomson scattering, and (iii) the accretion of black hole is spherically symmetric (i.e., Bondi accretion; Bondi 1952). Therefore, we can define a relation:

$$\frac{L_{\rm Edd}\sigma_{\rm T}}{4\pi r^2 c} = \frac{G M_{\rm BH} m_{\rm p}}{r^2}, \tag{2.2}$$

with r is the distance, and $\sigma_{\rm T}$ is the electron cross-section for Thompson scattering, and $m_{\rm p}$ is the proton mass. Subsequently, we can derive the equation:

$$L_{\rm Edd} = \frac{4\pi G m_{\rm p}}{\sigma_{\rm T}} M_{\rm BH} = 1.3 \times 10^{38} \frac{M_{\rm BH}}{M_\odot}. \tag{2.3}$$

Even under the strictest of assumptions, the Eddington limit paradigm appears to be widely followed among the known quasars (Trakhtenbrot et al. 2017). Note that this limit, however, can be surpassed by assuming a non-spherical geometry, resulting in super-Eddington accretion rates seen in a few quasars (Kubota & Done 2019; Tang et al. 2019).

The most reliable way of determining a black hole's mass is to examine the gas or stellar dynamics within the black hole's gravitational influence (Ghez et al. 2008; Genzel et al. 2010). However, because of the very high resolution necessary to probe the black hole's sphere of influence, this is unsuitable for cosmologically distant quasars. Alternatively, the central black hole mass can be calculated utilizing the reverberation mapping approach (e.g., Peterson & Bentz 2006; Kaspi 2007; Feng et al. 2021; Li et al. 2021). Assuming that the broad-line region gas clouds are in Keplerian orbits surrounding the black hole and are virialized, the black hole mass may be calculated using:

$$M_{\rm BH} = f(R_{\rm BLR}) \frac{R_{\rm BLR} v^2}{G}, \tag{2.4}$$

where $R_{\rm BLR}$ is the radial distance of the broad-line region and v is the velocity of the emitting gas. Typically, the velocity is estimated by a metric indicating the width of the utilized emission line, most often full width at half maximum (FWHM). The factor $f(R_{\rm BLR})$ is of the order of unity and influenced by the geometry, inclination, and kinematics of the clouds. However, it is also one of the primary causes of uncertainty in this computation (up to a factor of ≈ 0.55 dex;

Shen 2013) because a constant term is commonly presumed for all types of quasar for a given line emission, independent of brightness, radius, or inclination.

The temporal delay between the flux change recorded in the broad-line and continuum emissions can be used to constrain the shape and radius of the broad-line region (Bentz 2016). Equation 2.4, may thus be substituted by an empirical relationship as:

$$\log\left(\frac{M_{\rm BH}}{M_\odot}\right) = a + b\log\left(\frac{\lambda L_\lambda}{10^{44}\ {\rm erg\ s^{-1}}}\right) + 2\log\left(\frac{\rm FWHM}{\rm km\ s^{-1}}\right) \tag{2.5}$$

where the a and b constants are derived from observations of different line emissions (e.g., Vestergaard & Osmer 2009; Shen et al. 2011). Since black hole masses can be calculated using only a single measurement of luminosity L and an emission-line width, this approach is also known as a single epoch measurement. An application of the black hole mass estimate will be discussed further in Part III.

The hunt for high-z quasars has resulted in a sequence of discoveries that have consistently pushed the redshift frontier to the furthest one (e.g., Mortlock et al. 2011; Bañados et al. 2018; Yang et al. 2020a; Wang et al. 2021a). Intriguingly, these most distant quasars already contain black holes with masses of $\gtrsim 10^9 M_\odot$, accreting at rates near the Eddington limit[2]. To date, J0313−1806, a luminous quasar at $z = 7.642$ powered by a black hole of $(1.6 \pm 0.4) \times 10^9 M_\odot$, holds the record for the most distant quasar (Wang et al. 2021a) ever discovered. This finding places considerable pressure on the standard model of black hole growth, as it becomes harder to build up the SMBHs in time to match the observational data (for recent reviews, see Woods et al. 2019; Inayoshi et al. 2020). A black hole can evolve quickly from its original seed with initial mass $M_{\rm seed}$ to the final mass $M_{\rm BH}$, which can be written as:

$$M_{\rm BH} = M_{\rm seed}\ \exp\left(\frac{t}{t_{\rm S}} \times \frac{1-\epsilon}{\epsilon} \times \frac{L}{L_{\rm Edd}}.\right) \tag{2.6}$$

Assuming a Salpeter time of $t_{\rm S} = 0.45$ Gyr, an Eddington limited accretion ($L = L_{\rm Edd}$), and 10% radiative efficiency, we can derive:

$$M_{\rm BH} = M_{\rm seed}\ \exp\left(9 \times \frac{t/{\rm Gyr}}{0.45}\right). \tag{2.7}$$

As an illustration, a black hole could be developed by six times larger in a relatively small redshift range $z = 6.0$–6.5, which corresponds to ≈ 90 Myr.

The black hole seeds was most likely produced approximately at the same period when the first stars (Population III) were born – i.e., around $z = 20$–30, or 200 Myr since the Big Bang (Barkana & Loeb 2001). This timeline would allow ~ 500 Myr of cosmic time between the generation of the initial seeds and the currently furthest, fully-developed SMBHs (Loeb & Furlanetto 2013) observed. Seeds are generally classified as light and heavy, depending on their initial mass, with typical sizes of $\sim 10^2 M_\odot$ and $10^5 M_\odot$, respectively (see, e.g., Pacucci & Loeb 2022 and references therein). As shown in Figure 2.3, growing the light seeds into SMBHs

[2]Eddington limit is the rate at which the outward radiation force balances the inward gravitational pull.

is extremely difficult unless the developing black hole can withstand the super-Eddington or hyper-Eddington[3] accretions (Ohsuga et al. 2005; Tanaka & Haiman 2009).

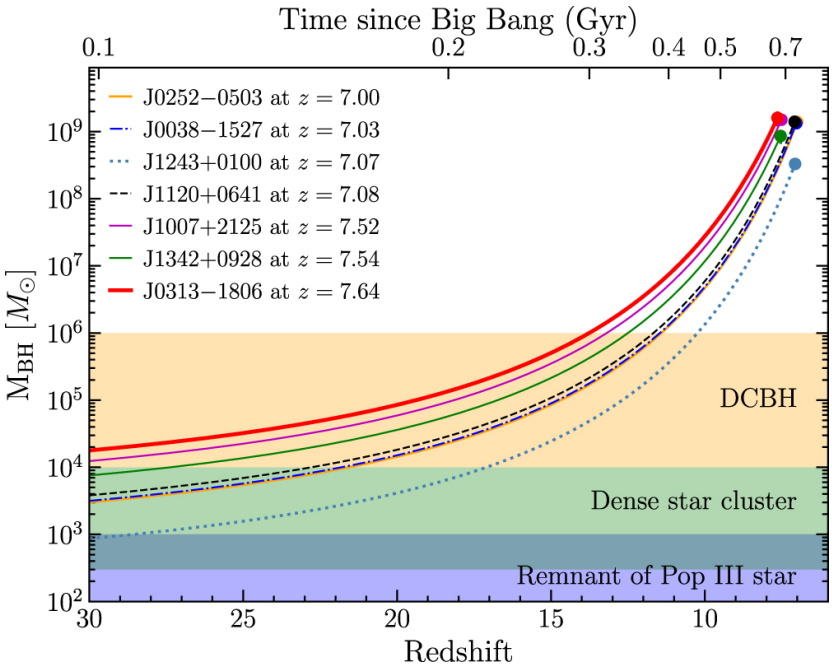

Figure 2.3. Growth track of the black holes in the $z \gtrsim 7$ quasars, assuming an accretion at the Eddington limit and a 10% radiative efficiency. The graph shows how much seed black hole mass is needed to develop each SMBH in these quasars (see also Equation 2.7). The shaded zones denote the approximate mass ranges of the seeds formed by the direct-collapse black holes (DCBHs), dense star clusters, and Population III stars. Image credit: Wang et al. (2021a).

From a different perspective, the theory of heavy seeds began to be developed to jump-start the growth of the SMBH and simplify the obstacles of assembling quasars by $z \sim 6$ (see Figure 2.3; e.g., Ferrara et al. 2014; Dayal et al. 2019). In this paradigm, there are two possible scenarios: (i) a monolithic collapse of a pristine cloud in atomic cooling halos, where the cooling activity of hydrogen molecules is halted by irradiation mechanisms, perhaps through a short-lived period of the supermassive star (Hosokawa et al. 2013; Piana et al. 2021), producing seeds with masses of around 10^5–$10^6 M_\odot$ (Begelman et al. 2006; Habouzit et al. 2016; Schauer et al. 2017; Lupi et al. 2021), and (ii) runaway collisions and mergers of Population III stars or black holes in a dense gaseous environment produce seeds with masses of 10^3–$10^4 M_\odot$ (Katz et al. 2015; Reinoso et al. 2018). From an observational standpoint, finding more quasars at the highest accessible redshifts can provide tighter constraints on the properties of black hole seeds and help select the most likely seed mass regime (Pacucci & Loeb 2022).

[3]While super-Eddington rates are within the similar magnitudes as Eddington rates, hyper-Eddington events could achieve hundreds or more times higher values owing to the photon trapping circumstances diminishing the influence of radiation's outward pressure on the infalling gas (see, e.g., Inayoshi et al. 2016; Begelman & Volonteri 2017, for reference).

2.3 Probing the Distant Universe with Quasars

Hydrogen absorption imprinted in the spectra of high-z quasars shows a significantly neutral environment with neutral fraction of $\overline{x}_{\rm HI} \gtrsim 0.4$ at $z \gtrsim 7$ (e.g., Bañados et al. 2018; Yang et al. 2020a; Wang et al. 2021a) and an end of cosmic reionization by $z \sim 5.3$ (Bosman et al. 2021b). These findings were inferred based on three commonly utilized techniques to probe the state of intergalactic gas described as follows. The first approach is by measuring the *Lyα forest transmission spikes* – i.e., the absorption structure bluewards of Lyα shaped by the intervening intergalactic medium. This method allows for the estimation of the Gunn-Peterson optical depth evolution with redshift, although limited by the Lyα emission rapid saturation in the case of $\overline{x}_{\rm HI} \geq 10^{-4}$ (Fan et al. 2006; Becker et al. 2015; Eilers et al. 2018a). Analysis of the Lyβ and Lyγ forests is thus required to investigate regions with higher neutral states. The second approach is by investigating the *Lyα damping wing*. If the quasar is surrounded by predominantly neutral gas with $\overline{x}_{\rm HI} > 0.1$, Gunn-Peterson absorption (Gunn & Peterson 1965) is identified, which might extend redward of the Lyα due to its inherent line width (Miralda-Escudé 1998). This damping wing signal has been found in the spectra of the $z \gtrsim 6.5$ quasars and utilized to constraint the neutral fraction of the surrounding gas (Davies et al. 2018a; Wang et al. 2020a; Greig et al. 2021). The third approach is by analyzing the *proximity zone sizes* – i.e., the region of increased Lyα forest transmission close to the quasar caused by its photoionization. Changes in proximity zone sizes have been studied to probe the evolution of hydrogen neutral fractions as a function of cosmic time (Mazzucchelli et al. 2017; Eilers et al. 2020; Andika et al. 2020).

It is widely suggested that the earliest bright quasars might be evolved in highly dense parts of the cosmic web, indicated by their high accretion power, enormous black hole masses, and low comoving space density (Lapi et al. 2006; Porciani & Norberg 2006). Consequently, these sources might be located in the overdensities of galaxy, gas, and dark matter that we should be able to observe (Meyer et al. 2022). This expectation has been tested in many distinct and complementary ways, but it has been difficult to reach a consensus (see Figure 2.4; e.g., Decarli et al. 2017; Mazzucchelli et al. 2017; Mignoli et al. 2020, and references therein). These findings are much more perplexing in context of many major large-scale overdensities discovered at similar redshifts not known to host bright quasars (e.g., Toshikawa et al. 2016; Ota et al. 2018; Calvi et al. 2019). Although duty cycle, variability, or obscuration may easily explain the absence of bright quasars in the large-scale structures, there are no plausible processes that might temporarily obscure these structures (Overzier 2022). Another possible explanation for the non-appearance of galaxies clustering around quasars is that powerful radiative feedback has elevated the circumgalactic medium temperature, preventing gas condensation and galaxy formation (e.g., Utsumi et al. 2010; Bañados et al. 2013; Mazzucchelli et al. 2017). In this situation, the quasars would still be surrounded by the overdensity of matters, but they would be devoid of galaxies within their ionization cone. However, it is challenging to conceal any structure on the Mpc-scales, as galaxies have been discovered inside the ionization cones of several quasars (Bosman et al. 2020; Mignoli et al. 2020). Therefore, in the immediate future, it will be important to perform more investigations on the typical environments that host the first quasars.

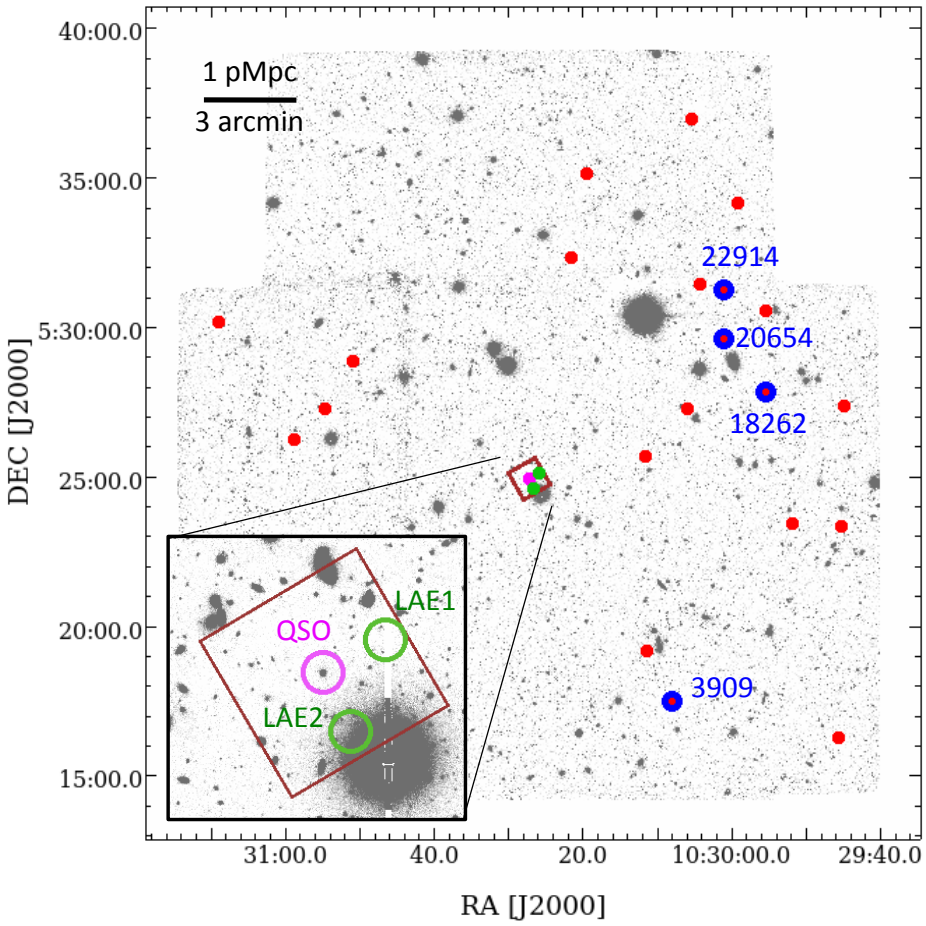

Figure 2.4. Presence of six galaxies – i.e., two Lyα emitters and four Lyman-break galaxies – around a luminous $z = 6.31$ quasar, SDSS J1030+0524. This discovery provides more insights into how supermassive black holes might have emerged within large web-like structures with lots of gas to fuel them. Image credit: Mignoli et al. (2020).

As additional information, many high-z quasars are hosted by the gas-rich and massive galaxies. However, in the rest-frame ultraviolet/optical energy, the quasar emission usually outshines the host galaxy's stellar radiation. Fortunately, the cold gas and dust in the quasar hosts can be traced through the (sub)millimeter observations of the [C II] 158 μm and the underlying continuum (Carilli & Walter 2013). In general, quasar hosts are similar to local universe's infrared-luminous galaxies ($L_{\rm IR} = 10^{11}$–$10^{12} L_{\odot}$) having star formation rates of 100–5000 $M_{\odot}$ yr^{-1}, dust masses of around 10^{8}–$10^{9} M_{\odot}$, and dynamical masses of approximately 10^{10}–$10^{11} M_{\odot}$ (Decarli et al. 2018). They have various morphologies/kinematics, ranging from rotating disks to disturbed/merger-like structures and compact, unresolved emissions (Novak et al. 2019; Neeleman et al. 2021; Meyer et al. 2022).

In this work, we will present an analysis of the proximity zone and its use case in the quasar lifetime estimation, along with a detailed characterization of a $z \sim 6$ quasar host galaxy utilizing submillimeter observations in Part III. Additionally, a detailed discussion on the quasar damping wing investigation and measurement will be presented in Part IV.

Chapter 3

Gravitational Lensing

Previous high-z quasar surveys are mainly focused on the most luminous, massive, and active SMBHs, while those fainter ones with modest to low accretion and lower mass are challenging to find (Inayoshi et al. 2020). Low-luminosity quasars might both make up the bulk of SMBHs, and their properties might differ. For example, in contrast to the most luminous quasars, dynamical masses of low-luminosity quasar hosts are comparable with those estimated from the local mass correlation between the host bulges and central black holes (Izumi et al. 2021). Therefore, we need to sample deeper into the luminosity and mass function to obtain a complete picture of early SMBHs and their host galaxies (Matsuoka et al. 2021). Unfortunately, spectroscopy for measuring intrinsically fainter quasar ($M_{1450} > -25$) SMBH masses with high accuracy is extremely challenging and time-consuming, even with 8 m telescopes (Onoue et al. 2019). In this work, we propose to take another approach. While being rare, lensed quasars are one of the best alternatives to probe both intrinsically lower-mass and -luminosity quasars as well as their host galaxies in unprecedented detail, thanks to the flux magnification and increased effective spatial resolution (Yue et al. 2021b).

The deflection of light owing to the presence of a massive object was first studied by Newton in 1704. Following that, by using classical mechanics, Soldner published the mathematical calculations of the light bending near the surface of the Sun in 1801 (Jaki 1978). Einstein (1911) then inferred the same result for this angle of deflection using his equivalence principle. When Einstein developed General Relativity and fully accounted for the curvature of the spacetime, he discovered that the deflection angle was double the classical value. Einstein's prediction was famously tested and proved by Eddington (1919), who calculated the movement of stars around the Sun during the solar eclipse. Since then, Einstein's theory of gravity is still one of our best descriptions of gravity (e.g., Treu 2010; Mandelbaum 2018; Abbott et al. 2018).

Decades ago, Chwolson (1924) and Einstein (1936) considered the likelihood of several pathways taken by the rays of light from the source to the observer and the possible detection of multiple images. They then concluded that the effect was unobservable with a star functioning

as a lens. However, Zwicky (1937) quickly proposed that a single or group of galaxies may also serve as gravitational lenses. The first gravitational lens was then discovered more than four decades later. Walsh et al. (1979) identified a quasar pair separated by $\approx 6''$ having similar spectra at $z = 1.41$ while looking for optical counterparts to radio sources. This source, Q 0957+561, also named Twin Quasar, was proposed to be lensed, and the $z = 0.36$ deflector galaxy was discovered shortly after, validating this theory (Stockton 1980; Young et al. 1980). The first quadruply-imaged lensed quasar, PG 1115+080, was found the following year (Weymann et al. 1980), and numerous other lenses were detected by chance during the next decade. By the 1990s, targeted surveys had been established, and today, more than three hundred lensed quasars are discovered. To discuss the details of galaxy-quasar lenses, we will first discuss the theory of gravitational lensing.

3.1 Lensing Basics and Formalism

Addressing the concept and processes of lensing is essential for undertaking scientific study with such systems. We will go through the fundamental gravitational lensing theory and how it may be used to calculate some physical quantities. Figures 3.1 depicts the typical geometry of a lens system (e.g., Bartelmann & Schneider 2001; Schneider 2015). The following arguments are used to derive the physical description of this lens for an arbitrary deflector mass distribution.

First, consider light rays from a source at a distance of D_s toward the observer pass through a mass distribution at D_d with a separation of $\boldsymbol{\xi}$. Note that we use boldfaced symbols to represent vector notations. Here, the true two-dimensional position of the source in the source plane is $\boldsymbol{\eta}$ while the true angular position of that source is $\boldsymbol{\beta}$. In the absence of light deflection, they are connected as:

$$\boldsymbol{\beta} = \frac{\boldsymbol{\eta}}{D_s}. \tag{3.1}$$

Then, we define the impact parameter $\boldsymbol{\xi}$, which describes the light ray position in the lens plane and its associated angular position $\boldsymbol{\theta}$, as:

$$\boldsymbol{\xi} = D_d \boldsymbol{\theta}. \tag{3.2}$$

Note that $\boldsymbol{\theta}$ denotes the observed source's location on the sphere relative to the lens central position, which we have selected as the coordinate system's origin, i.e., $\boldsymbol{\xi} = 0$. Similar to $\boldsymbol{\xi}$ and $\boldsymbol{\eta}$, which are position vectors, $\boldsymbol{\theta}$ and $\boldsymbol{\beta}$ are two-dimensional angular vectors, associated with the two directions on the sky.

We then define D_{ds} as the distance between the lens plane and the source plane. According to Figure 3.1, the source's light rays will reach the observer from the direction $\boldsymbol{\theta}$ (or $\boldsymbol{\xi}$) through:

$$\boldsymbol{\eta} = \frac{D_s}{D_d}\boldsymbol{\xi} - D_{ds}\hat{\boldsymbol{\alpha}}(\boldsymbol{\xi}), \tag{3.3}$$

or after dividing it with D_s, and utilizing Equation 3.1 and 3.2, we can obtain a relation in the form of:

$$\boldsymbol{\beta} = \boldsymbol{\theta} - \frac{D_{ds}}{D_s}\hat{\boldsymbol{\alpha}}\left(D_d\boldsymbol{\theta}\right). \tag{3.4}$$

After that, it is often easier to define the reduced deflection angle for practical purposes, that is:

$$\boldsymbol{\alpha}(\boldsymbol{\theta}) = \frac{D_{ds}}{D_s}\hat{\boldsymbol{\alpha}}\left(D_d\boldsymbol{\theta}\right), \tag{3.5}$$

so that Equation 3.4 can be simplified further into:

$$\boldsymbol{\beta} = \boldsymbol{\theta} - \boldsymbol{\alpha}(\boldsymbol{\theta}). \tag{3.6}$$

Note that the deflection angle $\boldsymbol{\alpha}(\boldsymbol{\theta})$ is specified by the distribution of lens mass. Accordingly, in the case of Equation 3.6 has several $\boldsymbol{\theta}$ solutions for a given source position at $\boldsymbol{\beta}$, that source will be multiply imaged and visible at several locations of $\boldsymbol{\theta}$ on the sphere.

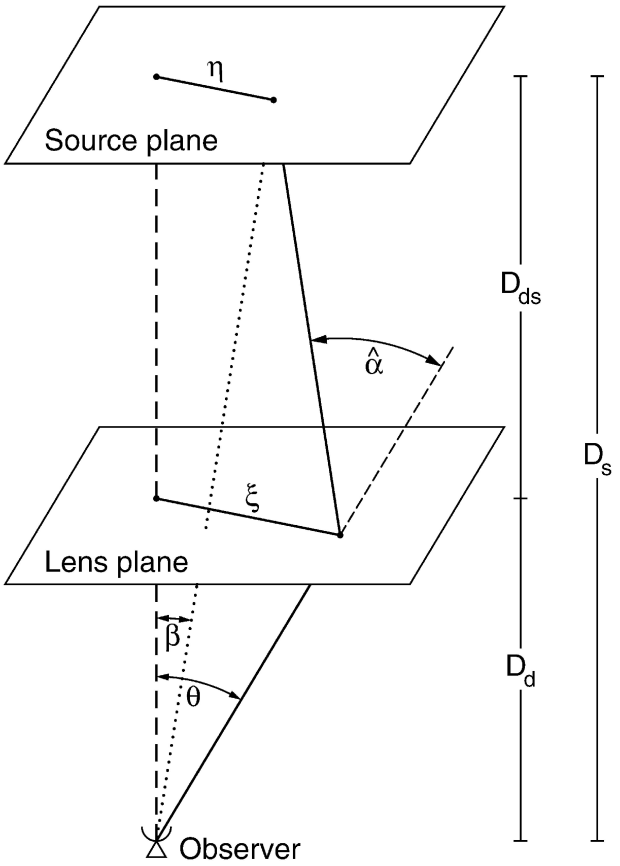

Figure 3.1. A sketch illustrating the lens geometry. The definition of each parameter is written in the main text. Image credit: Bartelmann & Schneider (2001).

A more extensive examination of the lens equation characteristics provides the following conclusion. The lensing effect is vital for extragalactic astronomy because the light deflection by gravity is independent of the deflecting matter state. Specifically, it is equally sensitive to both baryonic and dark matters and is not affected by whether or not the mass concentration is in equilibrium. Therefore, lensing is notably well suited to probe the distribution of matter without needing additional conjectures about the equilibrium state or the relationship between luminous and dark matter (Schneider 2015).

3.1.1 Point-mass Lens Equation

In a gravitational field, light, like heavy particles, is deflected. This consequence is predicted by Einstein's gravitational theory. Considering that the mass distribution affects the produced deflection angle $\boldsymbol{\alpha}(\boldsymbol{\theta})$ and assuming a beam of light passing through a point mass M, we obtain:

$$\boldsymbol{\alpha}(\boldsymbol{\theta}) = \frac{4GM}{c^2}\frac{D_{\mathrm{ds}}}{D_{\mathrm{s}}D_{\mathrm{d}}}\frac{\boldsymbol{\theta}}{|\boldsymbol{\theta}|^2}. \tag{3.7}$$

The equation above can be solved analytically by determining the respective image position $\boldsymbol{\theta}$ for each true source position $\boldsymbol{\beta}$. The left part of Equation 3.7 is an angle, while $\boldsymbol{\theta}/|\boldsymbol{\theta}|^2$ in the right part is an inverse of an angle. Therefore, the prefactor of this term should be the square of an angle, i.e., the Einstein angle of the lens:

$$\theta_{\mathrm{E}} = \sqrt{\frac{4GM}{c^2}\frac{D_{\mathrm{ds}}}{D_{\mathrm{s}}D_{\mathrm{d}}}}. \tag{3.8}$$

Following the equation above, the lens equation for the point-mass lens system can be rewritten in the form of:

$$\boldsymbol{\beta} = \boldsymbol{\theta} - \theta_{\mathrm{E}}\frac{\boldsymbol{\theta}}{|\boldsymbol{\theta}|^2}. \tag{3.9}$$

Because θ_{E} is a characteristic angle, we can normalize the associated variables and simplify the equation further to:

$$\boldsymbol{y} = \frac{\boldsymbol{\beta}}{\theta_{\mathrm{E}}}; \quad \boldsymbol{x} = \frac{\boldsymbol{\theta}}{\theta_{\mathrm{E}}}, \tag{3.10}$$

$$\boldsymbol{y} = \boldsymbol{x} - \frac{\boldsymbol{x}}{|\boldsymbol{x}|^2}. \tag{3.11}$$

For further details on the derivation of the point-mass lens equation solution, we refer to Bartelmann & Schneider (2001) and Schneider (2015).

Light is deflected not just as a whole but also in differential ways. For example, light rays closer to the lens are bended stronger than rays on the opposite beam's side. Because gravitational light deflection is not associated with the emission or absorption of radiation, the surface brightness (or intensity) is conserved. Note that a source's flux is defined as the product of its surface brightness and solid angle. Because the surface brightness is not affected by the light deflection, but the solid angle differs, the apparent emission of the source changes (Schneider 2015). The resulting magnifications for a point-mass deflector producing two lensed images can be calculated with:

$$\mu_{\pm} = \frac{1}{4}\left(\frac{y}{\sqrt{y^2+4}}\frac{\sqrt{y^2+4}}{y} \pm 2\right), \tag{3.12}$$

where the total magnification can be obtained from the sum of the two magnifications above, that is:

$$\mu = \mu_{+} + \mu_{-} = \frac{y^2+2}{y\sqrt{y^2+4}}. \tag{3.13}$$

3.1.2 Singular Isothermal Sphere Profile

The simplest approximations for the lens profiles are assuming that they are axially symmetric, i.e., $\Sigma(\boldsymbol{\xi}) = \Sigma(\xi)$, where $\xi = |\boldsymbol{\xi}|$ represents the distance of a source from the lens's center in the lens plane. Because $\boldsymbol{\alpha}$ and $\boldsymbol{\theta}$ are collinear, the lens equation is reduced to one dimension since only the radial coordinate must be taken into consideration, namely:

$$\beta = \theta - \alpha(\theta). \tag{3.14}$$

The singular isothermal sphere (SIS) is a simple analytical formula to approximate the mass profile of massive galaxies that produce strong lensing effects (e.g., Treu 2010, and references therein). Since the rotation curves of some galaxies are flat, this shows that the galaxy's mass increases with radius r so that the corresponding mass density is:

$$\rho(r) = \frac{\sigma_v^2}{2\pi G r^2}. \tag{3.15}$$

If the stellar orbit distribution is isotropic, then σ_v represents the one-dimensional velocity dispersion of stars in the potential mass distribution, which is measurable via spectroscopy. Accordingly, by projecting the relation above along the observer's sightline, we can derive the surface mass density:

$$\Sigma(\xi) = \frac{\sigma_v^2}{2G\xi}. \tag{3.16}$$

Then, the associated projected mass $M(\xi)$ within radius ξ is:

$$M(\xi) = 2\pi \int_0^{\xi} d\xi' \, \xi' \, \Sigma(\xi') = \frac{\pi \sigma_v^2 \xi}{G}. \tag{3.17}$$

After that, the deflection angle is defined as:

$$\hat{\alpha} = \frac{4\pi G M(\xi)}{c^2 \xi}, \tag{3.18}$$

or equivalent to:

$$\alpha(\theta) = 4\pi \left(\frac{\sigma_v}{c}\right)^2 \left(\frac{D_{\rm ds}}{D_{\rm s}}\right) \equiv \theta_{\rm E}. \tag{3.19}$$

Consequently, for the SIS model, the deflection angle is constant and equals to Einstein angle $\theta_{\rm E}$ as well as depends quadratically on σ_v. Therefore, the SIS lens equation is:

$$\beta = \theta - \theta_{\rm E} \frac{\theta}{|\theta|}. \tag{3.20}$$

If $|\beta| < \theta_{\rm E}$, the lens equation has two solutions, implying that it will create two images at angular locations of:

$$\theta_1 = \beta + \theta_{\rm E}; \quad \theta_2 = \beta - \theta_{\rm E}. \tag{3.21}$$

The separation of those two lensed images is independent of the source's position and can be computed using:

$$\Delta\theta = \theta_1 - \theta_2 = 2\theta_{\rm E}. \tag{3.22}$$

For $|\beta| > \theta_{\mathrm{E}}$, on the other hand, there will be just one image of the source, which is positioned at θ_1. The magnification produced by the SIS lens can be calculated as:

$$\mu = \frac{|\theta|}{|\theta| - \theta_{\mathrm{E}}}. \tag{3.23}$$

Finally, the total magnification can be computed from the sum of each magnified image.

3.2 Astrophysics with Strongly Lensed Quasars

We will briefly describe how lensed quasars have been utilized to investigate cosmology and astrophysics. See, for example, Jackson (2013) and Treu & Ellis (2015) for additional in-depth studies of these themes. The study reported in this work is motivated by the need to establish a larger sample of known lensed quasars at $z \gtrsim 6$ since only one high-z lens is known to date, limiting the strength of the subsequent scientific cases.

Figure 3.2. Examples of quasars strongly lensed by foreground galaxies. Image credit: NASA, ESA, A. Nierenberg (JPL) and T. Treu (UCLA).

Magnification of faraway galaxies. We want to observe the earliest cosmic epochs to comprehend galaxy evolution and cosmological physics, but this necessitates a high-resolution detector with vast photon collecting areas and long integration times. While, in principle, radio interferometry or 10 m telescopes with adaptive optics could do this, gravitational lensing allows for much better signal and resolution (see Figure 3.2, for example). There are at least three examples of how gravitational lensing has helped astronomers. First, at the X-ray regimes, Reis

et al. (2014) exploited the magnification factor of $\mu \approx 50$ experienced by a $z = 0.66$ quadruply-imaged lensed quasar in RX J1131−1231 to measure its black hole spin. Then, Hartley et al. (2019) utilized sub-micro-Jansky very-long baseline interferometry to probe HS 0810+2554 with ≈ 0.27 pc resolution and identify radio jets in that $z = 1.51$ radio-quiet quasar. In addition, the lensing effect allows us to examine the quasar-host galaxy interactions in unprecedented detail, leading to the results that black hole growth likely precedes host galaxy evolution. (e.g., Stacey et al. 2018; Yang et al. 2019a; Yue et al. 2021b; Stacey et al. 2021).

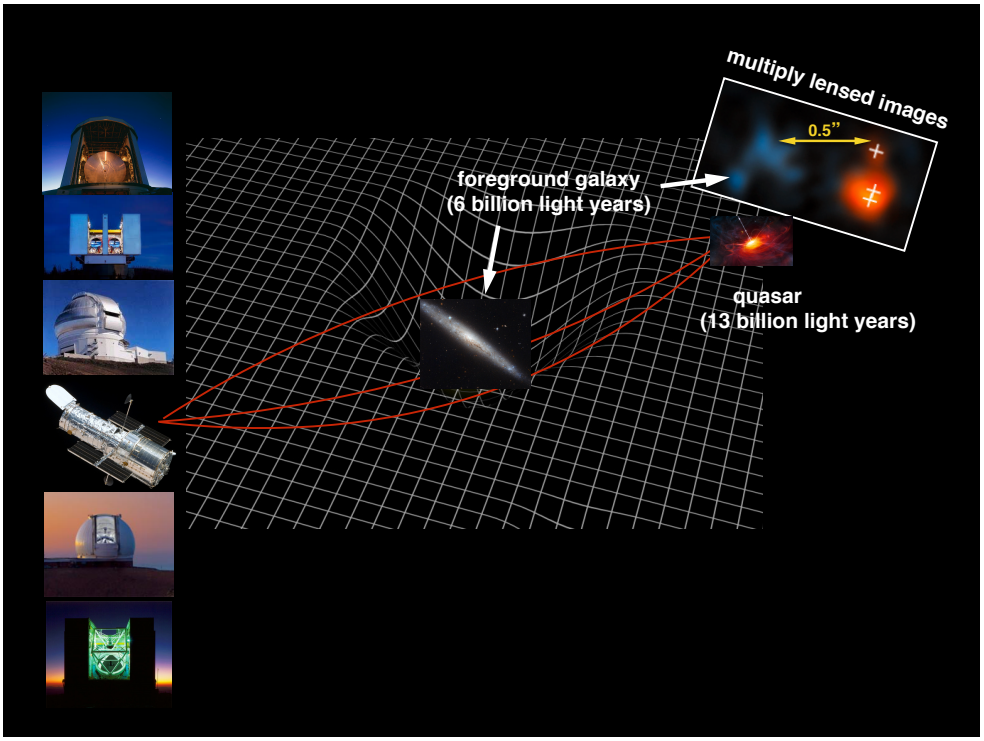

Figure 3.3. The *right panel* shows the Hubble Space Telescope image of a $z = 6.51$ quasar (red), magnified and split into three components by the gravitational lensing effect of a $z = 0.67$ deflector galaxy (blue). The quasar, J0439+1634, is the most distant lensed quasar known to date, making it a unique object for follow-up studies. Multiple ground-based facilities shown in the *left panel* are also being utilized to study this quasar's distance, black hole, and host galaxy. Image credit: NASA, ESA, and X. Fan (UArizona).

Time delay cosmography. It was the first suggested by Refsdal (1964) that the time delay could be calculated for a source with a varying emission and gives a method for calculating the Hubble constant. Supernovae were chosen as the targets first, but subsequent decades proved that lensed quasars are more abundant and relevant to this time delay analysis. Early observations were challenging due to the seasonal gaps, lengthy time delays, and microlensing. Furthermore, lens model and mass-sheet degeneracies created huge systematic errors in calculating the Hubble constant (see, e.g., Treu & Marshall 2016, and reference therein). Recent strategies have added knowledge from the host galaxy of lensed quasar (Suyu et al. 2017) and characterization of galaxies along the sightline compared to simulations (Sluse et al. 2017) to overcome these issues. Detailed modeling of several lensed quasars gave a measurement of the Hubble constant to within 2.5% precision (Bonvin et al. 2018; Birrer et al. 2019; Wong et al. 2020), which agrees with local distance ladder calculations based on Type Ia Supernovae.

Microlensing. The images of lensed quasar could be magnified by stars in the lens galaxy (Schneider 2015). These apparent flux changes could prevail from weeks to years depending on the relative movement of the observer, lens, and source, which adds complications when performing time delay analysis. Since the flux fluctuations are affected by the stellar density, dark matter fractions, and quasar accretion disk size-temperature profiles, it could be employed as a probe to study these physical parameters. Note that the typical image separations are on a scale of microarcseconds, which means that only the total flux change may be noticed (Schmidt & Wambsganss 2010). Note that because the quasar accretion disk has an extent close to the Einstein radius of the star, the microlensing signal might have a color dependency (Chan et al. 2021). A result emerging from various multiwavelength studies is that the accretion disks are larger than expected by classical thin-disk approximations and have flatter profiles of temperature-radius (e.g., Morgan et al. 2018; Hutsemékers et al. 2020; Cornachione et al. 2020; Shalyapin et al. 2021).

Dark matter substructure. In the absence of stellar dynamic data, gravitational lensing is the most potent tool for exploring distant galaxy mass contents. Although lens modeling has notable degeneracies (Schneider & Sluse 2013), robust estimations of total masses inside the Einstein ring have been done, with a widespread consensus that the mass profiles are well-described by near-isothermal approximation (e.g., Auger et al. 2010). While such models closely suit the image locations of lensed quasars and their hosts (e.g., Suyu et al. 2009), the flux ratios of the lensed images sometimes deviate from the theoretical forecasts. These disparities could be clarified partly by microlensing, while the remaining flux-ratio discrepancies might indicate the presence of hidden substructures along the sightline. This analysis is a good way of testing the cosmological models at the galaxy scale, and such flux-ratio peculiarities have been detected in several systems (Gilman et al. 2019; Hsueh et al. 2020).

The lack of statistically significant samples of lens systems to test these science cases at the high-z universe motivates our hunt for gravitationally lensed quasars. Furthermore, it is often challenging to find systems with specific characteristics to probe particular phenomena, for example, asymmetric quads for time delays and microlensed quasars for constraining the accretion disk. Therefore, it is paramount to continue discovering lensed quasars at the highest accessible redshift frontier to advance such investigations.

Chapter 4

Dissertation Outline

In this work, we present an effort to raise the number of discovered quasars and lensed sources at cosmic dawn, primarily for unraveling the nature of the earliest supermassive black holes–galaxies formation and growth. Utilizing the combined optical and infrared photometric data, we first validate our search techniques and present a list of high-confidence (lensed) quasar candidates to be followed up in **Part II**. We then discuss the characterization of a newly-discovered young weak-line quasar at $z = 6.3401$ in **Part III**. A comprehensive multiwavelength campaign using state-of-the-art instruments will serve as a foundation for examining the physical characteristics of this rare source, its host galaxy, and its environment. Afterward, based on the integral-field data and near-infrared spectroscopy, we report on the detection of a $z = 6.314$ absorption system, infer its metal contents, and constrain its effect on the quasar lifetime estimate in **Part IV**. Finally, we summarize our main findings, conclusions, and ideas for future work, including the challenges and open questions in the field of high-z universe exploration in **Part V**. A more detailed outline of this work is summarized below.

Part II – Chapter 5 introduces the dataset and search strategy that we adopt for selecting the $z \gtrsim 6$ quasar candidates. The first step is the preselection of the candidates based on their colors using the catalog-level multi-band photometric data. Then, the second step is modeling the observed spectral energy distributions and calculating their probabilities to be quasar or other contaminants.

Chapter 6 presents our third selection step, which is based on the deep learning classification to detect the potential lenses. This includes the strong lensing simulation, the dataset construction for training and testing our convolutional neural network model, as well as the final selection of the high-probability (lensed) quasar candidates to be followed up.

Part III – Chapter 7 provides the details on our spectroscopic follow ups, which led us to the discovery of a rare high-z weak-line quasar, namely PSO J083+11. Then, we analyze this source to constrain its black hole properties, proximity zone size, and accretion lifetime.

Chapter 8 reports on the high-resolution near-infrared imaging with Hubble Space Telescope to see if the gravitational lensing influences the PSO J083+11's apparent emission and search for any potential lens galaxy.

Chapter 9 discusses the constraints on the PSO J083+11's host galaxy properties, including the [C II] and dust continuum emissions along with the associated star formation rate, using data from Atacama Large Millimeter/submillimeter Array observations.

Chapter 10 presents extensive discussions regarding the probable explanations that might contribute to the weak-line signature of PSO J083+11. This finding also concludes our multi-wavelength analysis of PSO J083+11 as a young weak-line quasar.

Part IV – Chapter 11 explores the possibility of an intervening galaxy in the sightline of PSO J083+11, which led us to find an absorption cloud at $z = 6.314$. Subsequently, we start by presenting the integral-field spectroscopic data acquisition and reduction used for this work. After that, we provide the measurements of the metal contents and the Lyα damping wing profile observed in the spectra.

Chapter 12 provides an attempt to find and characterize the Lyα halo around PSO J083+11. We also explain the adopted point-spread function model construction and strategy for subtracting the quasar continuum emission to constrain the Lyα halo size. This experiment also offers an independent diagnostic for confirming the young quasar nature of PSO J083+11.

Chapter 13 discusses the elemental abundances measurement of the intervening absorption system and whether or not the proximate absorber influences the interpretation of the PSO J083+11's apparent proximity zone and complicates its accretion lifetime calculation.

Part V – Chapter 14 finally consolidates the main results of this work while **Chapter 15** presents potential future projects, including the outlook on the future challenges and unsolved mysteries in the field of high-z quasar surveys.

Part II

Searching for the Highest-Redshift (Lensed) Quasars

Chapter 5

Candidates Search using Multi-band Data

The content of this chapter is based on the work originally published as ***Andika, I. T.****, Jahnke, K., Onoue, M., et al. (2020; ApJ 903: 34) and is adapted from the manuscript* ***Andika, I. T.****, Jahnke, K., van der Wel, A., et al. (2022; in preparation).*

Powered by matter accretion onto SMBHs, quasars are one of the most luminous sources in the universe. In the highest-redshift frontier, these SMBHs can reach billion of solar masses as early as $\lesssim 1$ Gyr from the beginning of the cosmos (Bañados et al. 2018; Yang et al. 2020a; Wang et al. 2021a). Hence, $z \gtrsim 6$ quasars are excellent laboratories for unraveling the nature of the first SMBHs–galaxies assembly (Pacucci & Loeb 2022).

More than three hundred quasars have been found by various wide- and deep-field surveys (e.g., Fan et al. 2006; Willott et al. 2010; Mortlock et al. 2011; Venemans et al. 2015; Bañados et al. 2016; Mazzucchelli et al. 2017; Matsuoka et al. 2018a; Reed et al. 2019; Yang et al. 2019b; Wang et al. 2019; Pons et al. 2019; Matsuoka et al. 2021). Interestingly, about ten percent of them belong to a class called "young quasars" with the calculated lifetimes of just $t_{\rm Q} \approx 10^4$–10^5 yr (Eilers et al. 2021). These young quasars pose problematic issues since their ages are several times shorter than the typical timescale required for growing SMBHs (i.e., $t_{\rm Q} \approx 10^6$–10^9 yr; e.g., Khrykin et al. 2021; Worseck et al. 2021). The formation of these sources would need either: (i) direct collapse of seed black holes with huge masses ($\gtrsim 10^4\ M_\odot$; e.g., Begelman et al. 2006; Ferrara et al. 2014; Habouzit et al. 2016; Schauer et al. 2017; Dayal et al. 2019), (ii) continuous accretion near or beyond Eddington limit onto seeds with lower masses ($\lesssim 10^2$–$10^3\ M_\odot$; e.g., Ohsuga et al. 2005; Tanaka & Haiman 2009; Inayoshi et al. 2016), or (iii) the presence of radiatively inefficient accretion mode (e.g., Trakhtenbrot et al. 2017; Davies et al. 2019). Consequently, increasing the number of discovered quasars at cosmic dawn, especially looking for young quasars, and performing extensive analysis of their characteristics are critical for gaining a better understanding of early growth modes and the physics involved.

Another significant concern in the field of high-z quasar searches is the rarity of gravitationally lensed sources. Because of the large lensing optical depths attained at $z \gtrsim 6$, it has been anticipated for decades that up to one-third of the high-z quasars will be strongly lensed (Wyithe & Loeb 2002a; Pacucci & Loeb 2019; Yue et al. 2021a). However, only one discovered so far, namely J0439+1634, a lensed quasar at $z = 6.51$ (Fan et al. 2019a). A re-examination of the search strategies employed in the past quasar surveys reveals a significant selection bias against lensed quasars. Despite their scarcity, lensed quasars are one of the best options for probing sources both with intrinsically high and low luminosities, as well as the associated host galaxies in remarkable details, thanks to their magnified fluxes and spatial resolution increases due to the lensing effect (e.g., Stacey et al. 2018; Yang et al. 2019a; Yue et al. 2021b) Furthermore, lensed quasars are prime targets for investigating the foreground deflector dark matter profiles (e.g., Gilman et al. 2020; Hsueh et al. 2020), calculating the Hubble constant based on time delay analyses (e.g., Suyu et al. 2017; Millon et al. 2020), and and constraining the sizes of quasar accretion disk (e.g., Chan et al. 2021). Hence, constructing a more robust selection method to uncover such hidden populations of lenses will be a crucial experiment to conduct.

In this chapter, we present an effort to increase the number of quasars and lenses in the $z \gtrsim 6$ universe. Utilizing combined optical and infrared photometric data, we validate our search techniques and present new high-confidence (lensed) quasar candidates to be followed up. As an outline, our search consists of three main steps: (i) candidates preselection based on their colors using catalog-level multi-band photometric data, (ii) modeling the observed spectral energy distributions (SEDs) and calculating their probabilities to be quasar or other contaminants, and (iii) classification based on the convolutional neural network analysis to detect potential lenses. As a start, we will discuss step one and two in the following sections.

Throughout this work, we utilize the ΛCDM cosmological model where $\Omega_\Lambda = 0.685$, $\Omega_m = 0.315$, and $H_0 = 67.4$ km s^{-1} Mpc^{-1} (Planck Collaboration et al. 2020) for all of physical measurements. Consequently, at $z = 6.3401$ the age of universe is 0.863 Gyr and an angular scale of $\theta = 1''$ corresponds to a proper transverse separation of 5.7 kpc. In addition, all reported magnitudes are based on AB zero points.

5.1 Observational Datasets

5.1.1 Primary Optical Catalogs

For practical purposes, we first divide our primary data into two parts based on their sky locations: northern and southern hemispheres. The northern dataset will be used for finding quasars but not lens candidates. Subsequently, we use the second data release[1] of Panoramic Survey Telescope and Rapid Response System Survey 1 (Pan-STARRS1, hereafter PS1; Chambers et al. 2016) for candidates selection on the northern side. The PS1 imaged three-quarters of the sky from Haleakala Observatory in five broadband filters using a 1.8 meter telescope and its 1.4 Gigapixel Camera. The corresponding catalog depths based on PS1 co-added images

[1]Available via the PS1 data archive homepage at https://panstarrs.stsci.edu/.

are $g_{\rm PS1} = 23.3$, $r_{\rm PS1} = 23.2$, $i_{\rm PS1} = 23.1$, $z_{\rm PS1} = 22.3$, and $y_{\rm PS1} = 21.3$ while the associated median seeing is $grizy = 1\farcs31,\ 1\farcs19,\ 1\farcs11,\ 1\farcs07,\ 1\farcs02$. By default, we choose the flux and magnitude measurements based on point-spread function (PSF) photometry reported in the PS1 table.

PS1 also has overlapped coverage with the Dark Energy Spectroscopic Instrument Legacy Imaging Surveys Data Release 9 (DELS; Dey et al. 2019). DELS has the advantage of reaching approximately one magnitude level fainter than PS1. DELS is a survey[2] that uses imaging data from three separate telescopes to cover $\approx 14,000$ square degrees of extragalactic sky visible from the northern hemisphere ($-18\,{\rm deg} < {\rm Dec} < +84\,{\rm deg}$) in three optical bands. These data have 5σ depths of $g_{\rm DELS} = 24.0$, $r_{\rm DELS} = 23.4$, and $z_{\rm DELS} = 22.5$ mag. Subsequently, the DELS catalog is cross-matched to our primary PS1 table with a $2''$ radius, and its photometric data will be used when available.

For selecting quasar and lens candidates in the southern hemisphere, we exploit the Dark Energy Survey Data Release 2 (DES; Abbott et al. 2021) as the main catalog. DES is based on imaging using the Dark Energy Camera (DECam; Honscheid & DePoy 2008; Flaugher et al. 2015) equipped at the Blanco 4 m telescope at Cerro Tololo Inter-American Observatory in Chile. This survey observes $\approx 5000\,{\rm deg}^2$ of the Galactic cap in the southern direction with five bands, where the images have a median PSF FWHM of $g, r, i, z, Y = 1\farcs11,\ 0\farcs95,\ 0\farcs88,\ 0\farcs83,\ 0\farcs90$. In addition to that, for $1\farcs95$ diameter aperture and signal-to-noise ratio (S/N) of 10, the estimated median co-added catalog depth is $g_{\rm DES} = 24.7$, $r_{\rm DES} = 24.4$, $i_{\rm DES} = 23.8$, $z_{\rm DES} = 23.1$, and $Y_{\rm DES} = 21.7$ mag. Unless otherwise stated, we utilize the aperture-based magnitude MAG_AUTO by default – where the aperture size varies depending on the shape of each source – published in the DES main table. As additional information, DES tile images have a pixel scale of $0\farcs263$ and a fixed zero point of 30 mag.

The selection of $z \gtrsim 6$ quasar candidates by color criteria becomes problematic because of the contamination from other populations, i.e., early-type galaxies at $z \sim 1$–2 along with late M stars, L and T dwarfs (hereafter MLT dwarfs). These contaminants are more numerous than the quasars, yet their near-infrared colors are identical. Consequently, we have to exclude the sky area toward Andromeda Galaxy ($7\,{\rm deg} < {\rm RA} < 14\,{\rm deg}$; $37\,{\rm deg} < {\rm Dec} < 43\,{\rm deg}$) and Galactic plane ($|b| < 20\,{\rm deg}$) to reduce the number of contaminating MLT dwarfs. However, using dust maps[3] from Schlegel et al. (1998) and Green et al. (2019), we include some candidates located toward Galactic plane if their reddenings are $E(B-V) < 1$. Our method is contrast to the previous studies that rigorously excluded all regions with $E(B-V) > 0.3$ (e.g., Bañados et al. 2016; Mazzucchelli et al. 2017). Finally, using the same dust maps, we correct the Galactic reddening for all photometric measurements following Fitzpatrick (1999) extinction relation. As a side note, we also keep track of the known objects by using the list of previously discovered MLT dwarfs (Best et al. 2018; Carnero Rosell et al. 2019) and quasars (Flesch 2021).

[2]See the data release description at http://legacysurvey.org/.
[3]For the implementation, we refer the reader to check https://dustmaps.readthedocs.io/en/latest/.

5.1.2 Public Infrared Data

To make a more precise and robust selection, we have to utilize infrared photometric data, which provides a new dimension to separate quasars from MLT dwarfs and early-type galaxies. Subsequently, we look for the public infrared data whose footprints overlap with our primary optical catalogs. For our northern dataset, we retrieve the near-infrared catalogs from the United Kingdom Infrared Telescope Infrared Deep Sky Survey Data Release 10 (UKIDSS; Lawrence et al. 2007) and the United Kingdom Infrared Telescope Hemisphere Survey Data Release 1 (UHS; Dye et al. 2018). On the southern side, we utilize the data from Vista Hemisphere Survey Data Release 5 (VHS; McMahon et al. 2013, 2021).

Additionally, we make use of the mid-infrared measurements from the unWISE catalog (Schlafly et al. 2019), which comprises approximately two billion objects detected by the Wide-field Infrared Survey Explorer (WISE; Wright et al. 2010) across the entire sky. The unWISE data has a considerable advantage over the original WISE catalog (AllWISE) in terms of deeper imaging data and improved source extraction in the crowded sky locations (Schlafly et al. 2019). Hence, we employ a matching radius of $2''$ between the optical and infrared catalogs for all cross-matching purposes. We define the sources as infrared detected if the catalog entry of the relevant flux measurements is not empty – i.e., there is a match within the cross-matching radius. The measurements in near-infrared JHK as well as mid-infrared W1 (3.4 μm) and W2 (4.6 μm) bands are extremely useful for distinguishing whether the sources are quasars or MLT dwarfs (Mazzucchelli et al. 2017; Yang et al. 2019b; Wang et al. 2019). This cross-match method is also an effective way to discard spurious objects such as cosmic rays or moving sources which usually exist in one survey but not in others.

5.2 Simulating the Quasar Spectral Colors

At this point, we plan to create the mock spectra of our desired targets – i.e., (lensed) quasars – following Yang et al. (2016) prescription aided with SIMQSO[4] simulation code (McGreer et al. 2013). The SIMQSO is built for producing the spectra of quasars that mimic $\approx 60,000$ Sloan Digital Sky Survey (SDSS; Abdurro'uf et al. 2021) quasars at $2.2 < z < 3.5$. The code also presumes that quasar SEDs do not change significantly with redshift (Shen et al. 2019). However, we note that quasars at $z \gtrsim 6$ frequently exhibit high ionization broad emission lines with more dramatic velocity shifts than other lower-z quasars at the same luminosity (e.g., Mazzucchelli et al. 2017; Meyer et al. 2019; Schindler et al. 2020). Nonetheless, a substantial number of lower-z SDSS quasars give a solid starting point for generating the high-z quasar composite spectra.

One fundamental component of our quasar spectral model is the continuum emission, represented by a power-law function with four breaks. The associated continuum slopes follow a Gaussian distribution with a mean of $\mu(\alpha_\nu) = -1.5$ at the rest-wavelength range of 1100–5700 Å. On the other hand, we modify the slopes to $\mu(\alpha_\nu) = -0.48$, -1.74, and -1.17,

[4]The documentation for the code can be found at https://github.com/imcgreer/simqso.

for wavelengths of 5700–10,850 Å, 10,850–22,300 Å, and > 22,300 Å, respectively. Note that for each of the aforementioned slopes, we use a dispersion value of $\sigma(\alpha_\nu) = 0.3$. Following that, we add a sequence of iron emissions from ultraviolet to optical wavelengths to the spectral model (e.g., Boroson & Green 1992; Vestergaard & Wilkes 2001; Tsuzuki et al. 2006). Then, the broad and narrow line emissions from the circumnuclear gases are appended to the model following the FWHM and equivalent width distributions of SDSS quasars. Moreover, the intergalactic absorption by Lyα forest is included in the simulated spectra (e.g., Songaila & Cowie 2010; Worseck & Prochaska 2011). On top of that, we implement the Lyα damping wing absorption based on Miralda-Escudé (1998) formalism. This is due to the fact that $z \gtrsim 5.5$ quasar spectra frequently display the damping wing, which is shaped by the intergalactic medium with a neutral hydrogen fraction of $\overline{x}_{\rm HI} > 10\%$ (e.g., Bañados et al. 2019). Finally, the dust reddening is implemented using Calzetti et al. (2000) model with $E(B-V) = -0.02$ to 0.14. It should be noted that the negative values of reddening are used to accommodate the quasars that have bluer continua than the ones covered by the original templates.

Following the above procedure, we produce 300 mock quasars and arrange them in the redshifts of $5.6 \leq z \leq 7.2$ and the rest-frame 1450 Å absolute magnitudes of $-29.5 \leq M_{1450} \leq -25.5$. These absolute magnitudes assure that the target quasars are bright enough to be detected by our survey data. In this scenario, we use the quasar luminosity function from Matsuoka et al. (2018b) in the form of:

$$\Phi(M_{1450}, z) = \frac{10^{k(z-6)}\Phi_*}{10^{0.4(\alpha_{\rm qso}+1)(M_{1450}-M^*)} + 10^{0.4(\beta_{\rm qso}+1)(M_{1450}-M^*)}}. \tag{5.1}$$

Note that the slopes that we adopt are $\alpha_{\rm qso} = -1.23^{+0.44}_{-0.34}$ and $\beta_{\rm qso} = -2.73^{+0.23}_{-0.31}$, for the faint- and bright-end slopes, respectively. Moreover, we also use the break magnitude of $M^* = -24.90^{+0.75}_{-0.90}$, redshift evolution term of $k = -0.7$, and normalization of $\Phi^* = 10.9^{+10.0}_{-6.8}$. Subsequently, we derive the photometry based on the generated mock spectra, where its associated uncertainties are estimated following magnitude-error relations of each survey (e.g., Yang et al. 2016).

5.3 Modeling the Spectra of Deflector Galaxies

To get the deflectors for the lens modeling, we first look for a sample of spectroscopically confirmed galaxies in the SDSS Data Release 17 (Abdurro'uf et al. 2021) catalog via CasJobs[5] webpage. Then, we collect all sources designated as "GALAXY" by the SDSS pipeline and narrow our search to those with credible measured velocity dispersions σ_v – i.e., error of $\lesssim 30\%$ – which is one key metric to compute the lensing effect later. Furthermore, because most of the lensing optical depth for $z \gtrsim 6$ sources originates from early-type lens galaxies at $z \lesssim 1.5$, we only choose galaxies with the redshifts of $0.3 < z < 2.0$ (Wyithe et al. 2011; Mason et al. 2015; Pacucci & Loeb 2019; Yue et al. 2021a). Following that, we cross-match these sources to our main catalog to determine their corresponding optical-infrared magnitudes when they are present. Finally, we retrieve a sample of 109,808 galaxies through the DESaccess[6] webpage.

[5]Accessible through http://skyserver.sdss.org/CasJobs/default.aspx.
[6]To access the data, please check https://des.ncsa.illinois.edu/desaccess/.

The next step in our search strategy is to get the spectra of deflectors, which will eventually be used to build the mock SEDS of galaxy-quasar lenses. Therefore, we proceed to simulate those spectra using `Bagpipes`[7] code (Carnall et al. 2018) based on the multi-band photometric information of the previously mentioned galaxies. `Bagpipes` requires several priors on the physical parameters as inputs for the fitting. In such a situation, we first use a double power-law function to parameterize the star formation history (SFH) of galaxies:

$$\mathrm{SFR(t)} \propto \left[\left(\frac{\mathrm{t}}{\tau} \right)^{\alpha_{\mathrm{gal}}} + \left(\frac{\mathrm{t}}{\tau} \right)^{-\beta_{\mathrm{gal}}} \right]^{-1}, \tag{5.2}$$

where the slopes of falling α_{gal} and rising β_{gal} in the logarithmic range of 0.01–1000 (Carnall et al. 2019). Additionally, we set the peak star formation times τ from 0 Gyr to the age of the universe at each of the galaxy's redshift. After that, the SFH normalization prior is adjusted in the interval of $M_{\mathrm{formed}} = 10\text{–}10^{15}\ M_*/M_\odot$, where M_* denotes the stellar mass. Also, we vary the metallicity of each galaxy from $Z/Z_\odot = 0.0$ to 2.5, where $Z_\odot = 0.02$ represents solar metallicity.

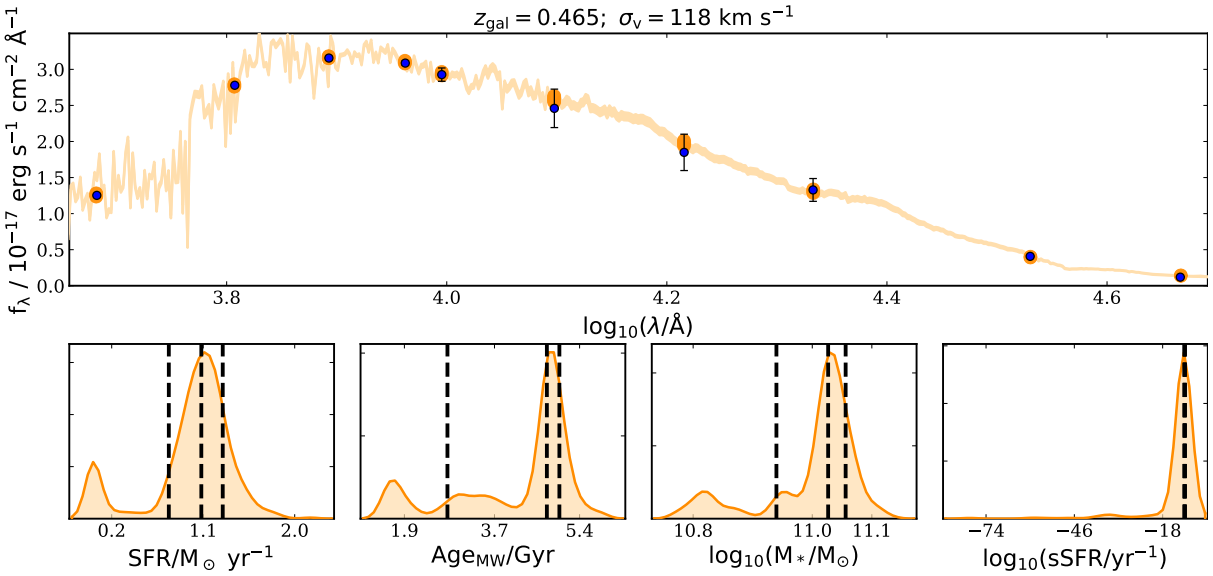

Figure 5.1. Example of the galaxy SED modeled with the `Bagpipes` code. *Upper panel*: The photometric data from DES, VHS, and unWISE (blue circles), the best-fit SED posteriors (orange line), and the synthesized photometry from the best-fit spectrum (orange circles) are presented. *Lower panel*: The star formation rate, mass-weighted age, stellar mass, and specific star formation rate posteriors derived from the SED fitting are shown. We mark the 16th, 50th, and 84th percentiles with vertical dashed lines. For details on how to estimate these parameters, we refer the reader to read Carnall et al. (2018).

Using Carnall et al. (2019) prescription, we incorporate Charlot & Fall (2000) dust reddening model of $A_\lambda \propto \lambda^{-n}$. In this case, we apply a Gaussian-prior to the attenuation curve's slope n with a mean and standard deviation of 0.3 and 1.5, respectively. By design, the V-band attenuation A_V ranges between 0 and 8 mag. Furthermore, we fix the maximum lifespan of stellar birth clouds to $t_{\mathrm{BC}} = 0.01$ Gyr and the ratio of attenuation between stellar birth clouds and

[7] See the documentation at https://bagpipes.readthedocs.io/en/latest/.

the surrounding interstellar medium to $\epsilon = 2$. It should be noted that the galaxy photometric redshifts priors are adjusted to match those obtained from SDSS-based spectroscopy with a minor fluctuation (i.e., $\Delta z = \pm 0.015$). Finally, we convolve the spectral model in velocity space with a Gaussian kernel utilizing σ_v information from the SDSS catalog. Figure 5.1 shows an example of lens galaxy fitted with `Bagpipes`. The end products of the above procedure are a sample of galaxy SEDs spanning from ultraviolet to infrared wavelengths and their corresponding photometric data points.

5.4 Constructing the Synthetic Spectra of Lensed Quasars

In this section, we focus on constructing spectral templates for lensed quasars. These templates can be created by adding the emissions of foreground galaxy and background quasars and subsequently producing the SEDs of lenses. We use a singular isothermal sphere profile to describe the mass of the lenses (Schneider 2015). Complemented with the measured σ_v, the Einstein radius can be calculated using the formula of:

$$\theta_{\rm E} = 4\pi \frac{\sigma_v^2}{c^2} \frac{D_{\rm ds}}{D_{\rm s}}, \tag{5.3}$$

where speed of light is c while $D_{\rm ds}$ and $D_{\rm s}$ are the angular diameter distances between the deflector and source and the observer and source, respectively

It is crucial to remember that real galaxy mass distributions are often not symmetric. The ellipticity of the mass profile or external shear forces, such as the tidal gravitational field of adjacent galaxies, are frequently responsible for symmetry violation. As a result, the SIS lens properties will be altered, and more than two images may be produced in the lensing process. However, we avoid employing a more complicated lens model, such as singular isothermal ellipsoid (SIE; Barkana 1998), which often demands precise measurements of deflector axis ratios and position angles. Nonetheless, SIS appears to reconstruct lens systems pretty well, with typical image separation remaining in the same order of magnitude as suggested by the SIE model (Schneider 2015). We suggest the reader recheck Section 3.1.2 for further information on the SIS lens computation.

The mock spectra of lenses are then generated by pairing each simulated galaxy with a randomly chosen quasar model. Assuming that β is the true angular position of the source, the quasar is then randomly positioned behind the lens within a range of $0\farcs01 \leq \beta \leq 1\farcs5$. The source image is then projected onto the lens plane, where the deflection angle and magnification are inferred depending on the lens geometry. We will accept the mock lens if it comprises a strong lensing effect and a magnification factor of $\mu \geq 2$ within $\theta_{\rm E} \leq 1''$. In principle, our selection of β and $\theta_{\rm E}$ is inspired by the Pacucci & Loeb (2019) research, which predicts that a substantial fraction of $z \gtrsim 6$ quasars are strongly lensed with modest to small image separations, that is, $\Delta\theta = 2\theta_{\rm E} \leq 1''$.

The distributions of lens galaxy redshifts, velocity dispersions, Einstein radii, and magnitudes in i-band implemented in our simulation are shown in Figure 5.2. The quantity of

galaxies is peaked at $z \approx 0.5$ in terms of redshift. Then, for the i-band magnitudes, we notice an increase in deflector numbers up to $i_{\rm DES} \approx 19.5$ before a sharp decline at the faint end. This phenomenon is predominantly produced by the bias of SDSS target selection. The faint limits for galaxies selected for spectroscopic observations are $i = 19.9$ for SDSS-III and $i = 21.8$ for SDSS-IV (Dawson et al. 2013; Prakash et al. 2016). Finally, we obtain 28,458 survived lens configurations that fulfill our criteria from the original 109,808 foreground galaxies and 300 mock background quasars. The lensed quasar spectra are then generated by combining the fluxes of the foreground galaxy with the magnified background quasar, as shown in Figure 5.3.

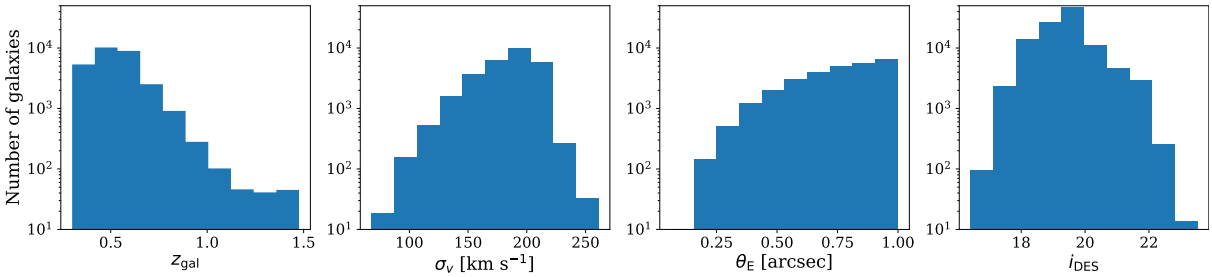

Figure 5.2. Distributions of the deflector galaxy redshifts $z_{\rm gal}$, velocity dispersions σ_v, Einstein radii $\theta_{\rm E}$, and magnitudes in i-band. These properties are utilized for producing the simulated lenses.

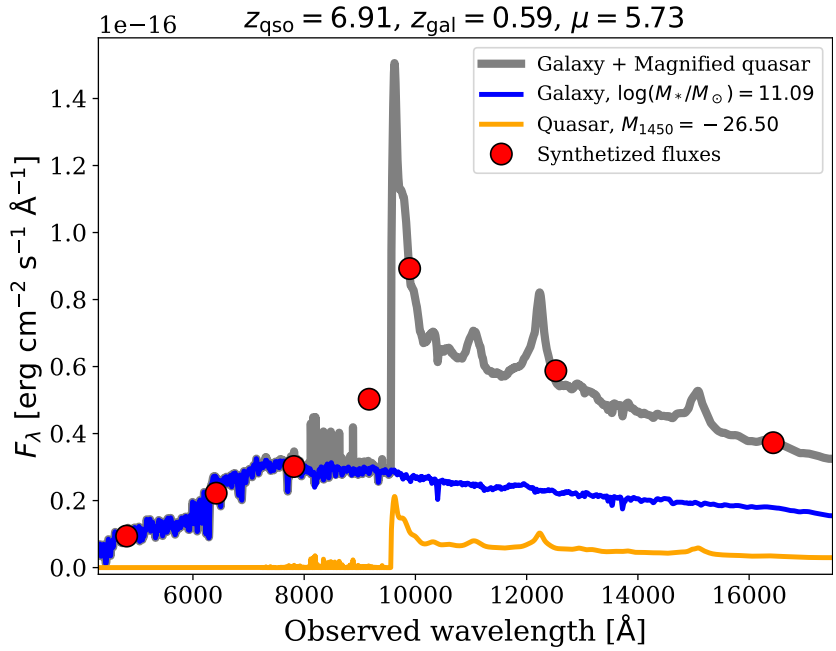

Figure 5.3. Simulated galaxy-quasar lens spectrum (gray line) and the corresponding synthetic photometry are shown (red circles). We show the emissions from an unlensed quasar in the orange line and a foreground galaxy in the blue line. After being magnified by a factor of μ, the quasar's emission is combined with the galaxy's light to produce the lensed quasar spectrum.

5.5 Additional Empirical Spectral Templates

As mentioned before, we want to use the SED fitting approach, as described in Andika et al. (2020), to extract the candidates from the contaminants. Therefore, we need to construct a set

of templates that can describe the observed SEDs of the candidates.

We first retrieve all spectra of the MLT dwarfs from the SpeX Prism Library[8] (Burgasser 2014). There are 360 templates in total, which reflect stars with M5–M9, L0–L9, and T0–T8 spectral classes observed in the wavelengths of 0.625–2.55 μm. We extend these templates further into the mid-infrared regime (e.g., Mazzucchelli et al. 2017; Andika et al. 2020). In short, we compute the corresponding W1 and W2 magnitudes using color scaling (K_W1 and W1_W2), which depends on the spectral type of each source, from Skrzypek et al. (2015) and the equation of:

$$\mathrm{W1} = K - K\_\mathrm{W1} - 0.783 \tag{5.4}$$

$$\mathrm{W2} = \mathrm{W1} - \mathrm{W1\_W2} - 0.63 \tag{5.5}$$

After that, we include the empirical quasar spectra from three different sources. The first comes from Selsing et al. (2016), who created a composite based on VLT/XSHOOTER observations of bright $1 < z < 2$ SDSS quasars. The second is from Jensen et al. (2016), constructed from 58,656 spectra of $2.1 < z < 3.5$ Baryon Oscillation Spectroscopic Survey (BOSS) quasars binned by brightness, spectral index, and redshift. Finally, the third composite is retrieved from Harris et al. (2016) and is created by averaging 102,150 BOSS quasars at $2.1 < z < 3.5$. It is worth noting that the composites from Jensen et al. (2016) and Harris et al. (2016) only contain a rest-frame wavelength of $\lesssim 3000$ Å. To extend them further, we stitch Selsing et al. (2016) spectrum at the redder part of those composites starting from 2650 Å. On top of that, we incorporate dust reddening using values of $E(B-V) = -0.02$ to 0.14 and Calzetti et al. (2000) extinction relation. We then generate a grid of spectra with redshifts of $4.0 \leq z \leq 8.0$ and interval of $\Delta z = 0.003$.

Additionally, we use the Brown et al. (2014) spectral atlas of galaxies to ensure that our candidates do not portray low-z galaxies. The atlas comprises 129 templates extracted from different types of $z \lesssim 0.05$ galaxies (e.g., elliptical, spiral, starbursts, etc.) We then use the Calzetti et al. (2000) model with $A(V) = 0$ to 1 to incorporate the reddening by dust. The SED grids are then built by spreading the templates throughout redshifts of $0.0 \leq z \leq 3.0$ with $\Delta z = 0.005$. Note that we incorporate the absorption induced by H I in the intergalactic medium to our quasar and galaxy SEDs using the formula from Inoue et al. (2014).

5.6 Classification via Spectral Energy Distribution Fitting

The second step of our search strategy is an implementation of modeling over the whole available SEDs to templates of (lensed) quasars and contaminants. The final result of this process is the likelihood calculation of the source being a quasar or contaminant and the associated photometric redshift. As a start, we will preselect the candidates in our northern and southern datasets with two different treatments.

[8]Accessible via http://pono.ucsd.edu/ adam/browndwarfs/spexprism/library.html.

As previously mentioned, we will only use the northern dataset for finding quasar candidates at $6.3 \leq z \leq 7.1$ rather than lenses. Subsequently, we first require the candidates to have red colors (e.g., Mazzucchelli et al. 2017), which are significantly detected in the y-band of PS1 and have counterparts in either the near-infrared J-band or unWISE W1-band. The $z \gtrsim 6.2$ quasar emissions on the blue side of Lyα should be substantially absorbed by the intervening H I. This absorption will also leave the flux almost undetectable in all bands bluer than the y-band. Consequently, in this case of non-detections, we replace these magnitudes with the associated 3σ upper limits. The criteria used for the quasar selection are:

$$\mathrm{S/N}(g_{\mathrm{PS1}},\ r_{\mathrm{PS1}},\ i_{\mathrm{PS1}}) < 8 \tag{5.6}$$

or

$$(g_{\mathrm{PS1}},\ r_{\mathrm{PS1}},\ i_{\mathrm{PS1}}) - y_{\mathrm{PS1}} > 3.0$$

$$\mathrm{S/N}(y_{\mathrm{PS1}}) > 7 \tag{5.7}$$

$$\mathrm{S/N}(z_{\mathrm{PS1}}) \geq 3 \text{ and } z_{\mathrm{PS1}} - y_{\mathrm{PS1}} > 1.2 \tag{5.8}$$

or

$$\mathrm{S/N}(z_{\mathrm{PS1}}) < 3 \text{ and } z_{\mathrm{PS1,lim}} - y_{\mathrm{PS1}} > 1.2$$

$$y_{\mathrm{PS1}} > 15. \tag{5.9}$$

Extremely luminous quasars, probably due to their inherently high luminosities (e.g., Wu et al. 2015) or strong lensing effects (e.g., Fan et al. 2019a; Fujimoto et al. 2020), on the other hand, might still be detected in PS1 dropout bands. Furthermore, the deflector galaxy at lower-z could contribute significant emissions in those dropout bands. To locate this unusual population, an extra condition in Equation 5.6 is used. Also, the magnitude limit criterion in Equation 5.9 is used to rule out too bright or spurious sources.

The PS1 catalog has three valuable entries that are useful for eliminating a significant fraction of contaminants. First, we can reduce the number of sources with an extended morphology and choose only the ones with point-like or compact shapes using:

$$|y_{\mathrm{PS1,aper}} - y_{\mathrm{PS1}}| < 0.5, \tag{5.10}$$

where $y_{\mathrm{PS1,aper}}$ and y_{PS1} are respectively the PS1 catalog aperture and PSF magnitudes of stacked images. This cutoff value is selected based on the examinations of spectroscopically confirmed galaxies and stars, as in Bañados et al. (2016). Then, for the consistency of measurements, the PSF magnitudes should satisfy:

$$|y_{\mathrm{PS1,stk}} - y_{\mathrm{PS1,wrp}}| < 0.5, \tag{5.11}$$

where "wrp" and "stk" are respectively the mean photometry of single-epoch images and stacked images. Lastly, the weighted PSF flux must be situated in good pixels to a percentage of 85% or greater – i.e., entries with the PSF coverage factor of $\mathrm{PSF_{QF}} > 0.85$.

In contrast with the northern dataset, we will use the southern catalog for finding quasars and lens candidates. Hence, we start by selecting sources with significant detections in the

DES Y-band, VHS J-band, and unWISE W1-band. In certain situations, if there is no detection in the bluer DES bands – namely, g, r, i, or z, we replace their magnitudes with the associated 3σ upper limits. Then we apply the flag and color cuts listed below:

$$\text{DES IMAFLAGS\_ISO } (g, r, i, z, Y) = 0 \tag{5.12}$$

$$\text{DES FLAGS } (g, r, i, z, Y) < 4 \tag{5.13}$$

$$\text{S/N}(Y_{\text{DES}}) \geq 5 \tag{5.14}$$

$$0.5 < z_{\text{DES}} - Y_{\text{DES}} < 2.5 \tag{5.15}$$

$$-0.6 < Y_{\text{DES}} - J_{\text{VHS}} < 1.0 \tag{5.16}$$

$$-0.5 < Y_{\text{DES}} - \text{W1} < 2.5. \tag{5.17}$$

Equation 5.12 and 5.13 are the basic flags to choose well-behaved objects from DES catalog (i.e., no problems with the source extraction or missing pixels; Abbott et al. 2021). The requirements in Equation 5.14–5.17, on the other hand, are inferred based on the photometric properties of the mock lenses created in Section 5.4.

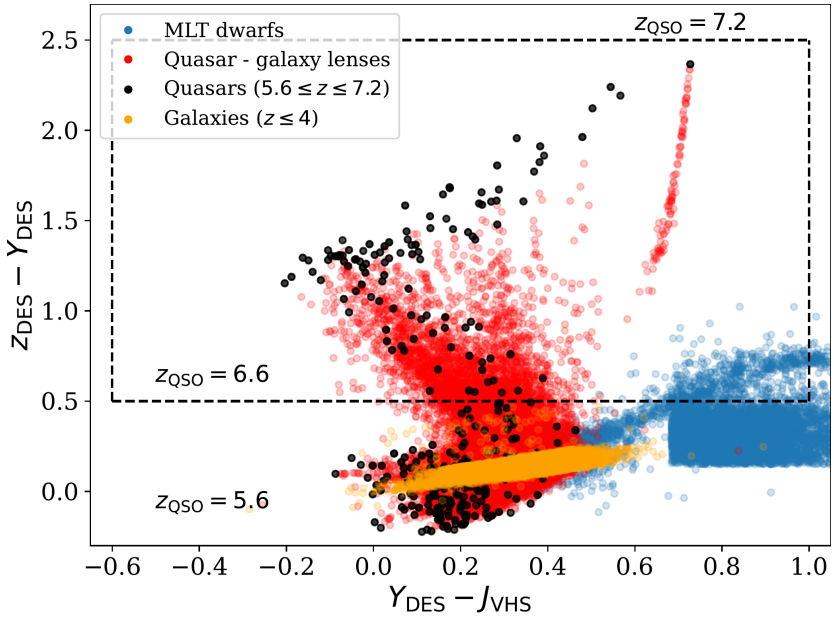

Figure 5.4. Color diagram of the $Y_{\text{DES}} - J_{\text{VHS}}$ versus $z_{\text{DES}} - Y_{\text{DES}}$. Colors of the simulated lenses (red circles), mock quasars (black circles), low-z early-type galaxies (orange circles), a sample of MLT dwarfs (blue circles; Best et al. 2018; Carnero Rosell et al. 2019) are presented in the figure. The dashed black box denotes our color cuts preselection, which concentrates on identifying lensed quasars at z = 6.6–7.2

As seen in Figure 5.4, there is a significant overlap between quasars, lenses, and other contaminants in the color space where $z_{\text{DES}} - Y_{\text{DES}} \leq 0.5$. Consequently, we opt to limit our cut to $z_{\text{DES}} - Y_{\text{DES}} > 0.5$, which narrows our search to the lenses with the background quasars located at z = 6.6–7.2. To assess the completeness of our selection, we apply a $z_{\text{DES}} - Y_{\text{DES}} > 0.5$ color cut to the remaining 28,458 simulated lenses created in the previous section. As a consequence, only 2793 of them meet this requirement. These remaining mock lenses are then used to estimate our selection completeness in recovering lens systems with quasars at z = 6.6–7.2.

Further selections are accomplished by applying criteria in Equation 5.14–5.17, resulting in 2791 surviving mock lenses, or around 99% completeness. This approach also eliminates around 70% of the contaminants – i.e., low-z galaxies and MLT dwarfs. Hence, these are sources that will be used in SED modeling for further consideration.

At this stage, we proceed to perform the SED fitting using four kinds of templates constructed in the previous sections: (i) mock lensed quasars, (ii) early-type galaxies at $z \leq 3$, (iii) MLT dwarfs, and (iv) unlensed quasars at $z \geq 4$. The primary purpose of this SED fitting is to determine the likelihood that each source is a lens, quasar, or contaminant along with its corresponding photometric redshift. We perform the fitting with EAZY code (Brammer et al. 2008). EAZY will walk through a grid of spectral templates, fit them to the photometric data of candidates, and select the best templates. The solutions with the smallest reduced chi-square ($\chi^2_{\rm red}$) are selected as the best models, which can be computed for each template i as:

$$\chi^2_{{\rm red},i} = \sum_{n=1}^{N} \left(\frac{{\rm data}_n - f_n({\rm model}_i)}{\sigma({\rm data}_n)} \right)^2 \Bigg/ (N-1), \tag{5.18}$$

where the number of photometric data and degree of freedom are indicated with N and $(N-1)$, respectively.

The sources with a high chance of becoming lensed quasars are selected based on the computed $\chi^2_{\rm red}$ of the lens ($\chi^2_{\rm red,L}$), galaxy ($\chi^2_{\rm red,G}$), MLT dwarf ($\chi^2_{\rm red,D}$), and quasar ($\chi^2_{\rm red,Q}$), as well as their associated ratios. In addition, we narrow the selection to the candidates with specific quasar photometric redshift values ($z_{\rm qso}$). As a result, the following criteria are used to identify high-z lensed and unlensed quasar candidates:

$$\frac{\chi^2_{\rm red,L}}{\chi^2_{\rm red,D}} < 0.2 \text{ and } \frac{\chi^2_{\rm red,L}}{\chi^2_{\rm red,G}} < 0.2, \tag{5.19}$$

or

$$z_{\rm qso} > 6.0 \text{ and } \frac{\chi^2_{\rm red,Q}}{\chi^2_{\rm red,D}} < 0.3. \tag{5.20}$$

The values in Equation 5.19 sed are obtained by fitting the synthetic photometry of the mock lenses generated in Section 5.4. The conditions in Equation 5.20, on the other hand, are empirically determined by modeling the SEDs of known MLT dwarfs and $z \gtrsim 6$ quasars (Carnero Rosell et al. 2019; Flesch 2021). Finally, applying the SED fitting to the previously survived mock lenses produces 2784 remaining objects, corresponding to completeness of roughly 99 percent.

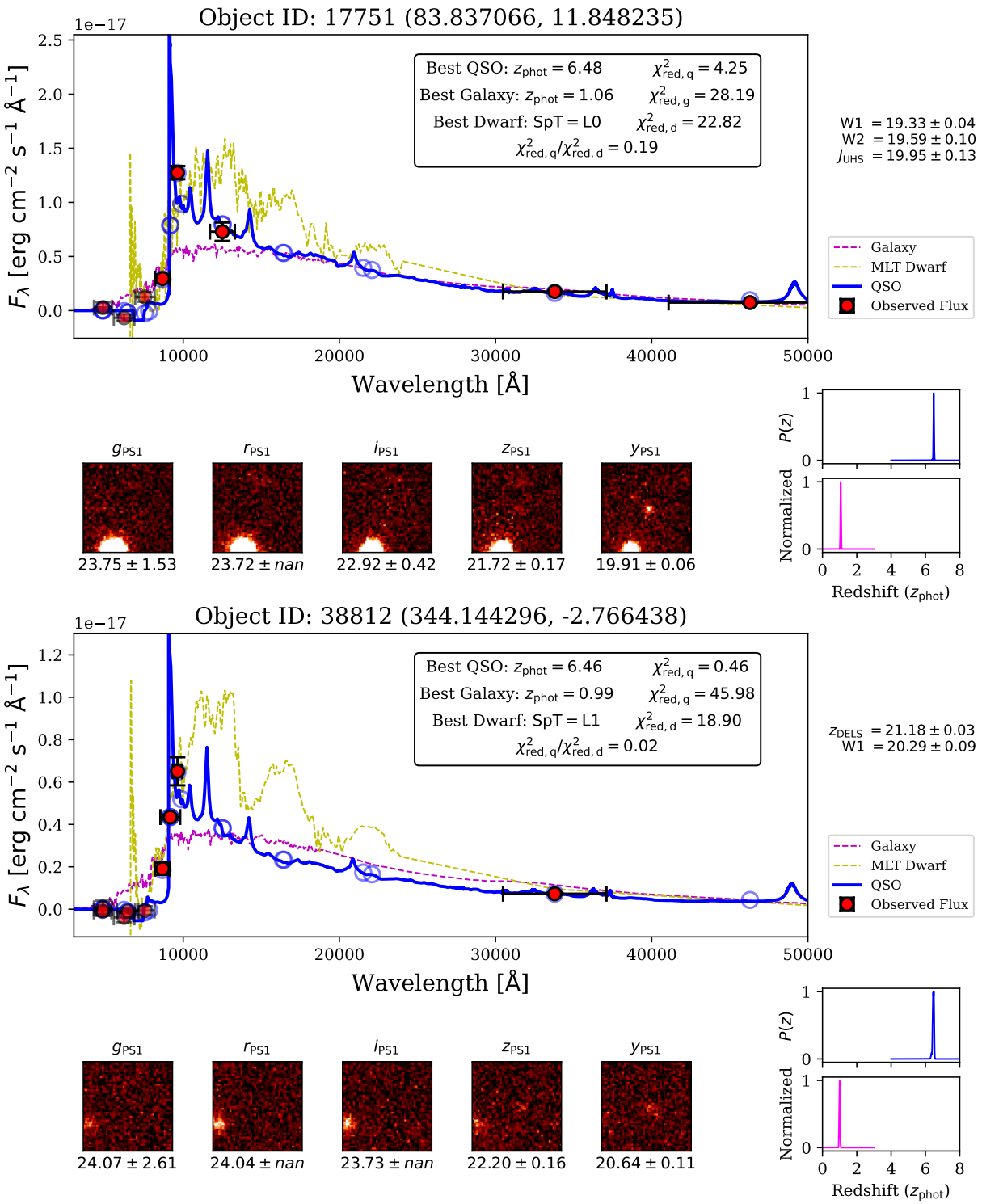

Figure 5.5. Example of the fitted SEDs for two quasar candidates: PSO J083.8371+11.8482 (*top*) and PSO J344.1442−02.7664 (*bottom*). The observed photometry of each source (red circles with error bars) modeled with quasar (blue), MLT dwarf (yellow), and early-type galaxy (magenta) templates. We present the photometric redshift probability density functions on the lower right of each figure. The $12'' \times 12''$ PS1 cutouts are also displayed. These two candidates later are confirmed as real quasars based on our follow-ups (see discussion in the next chapter).

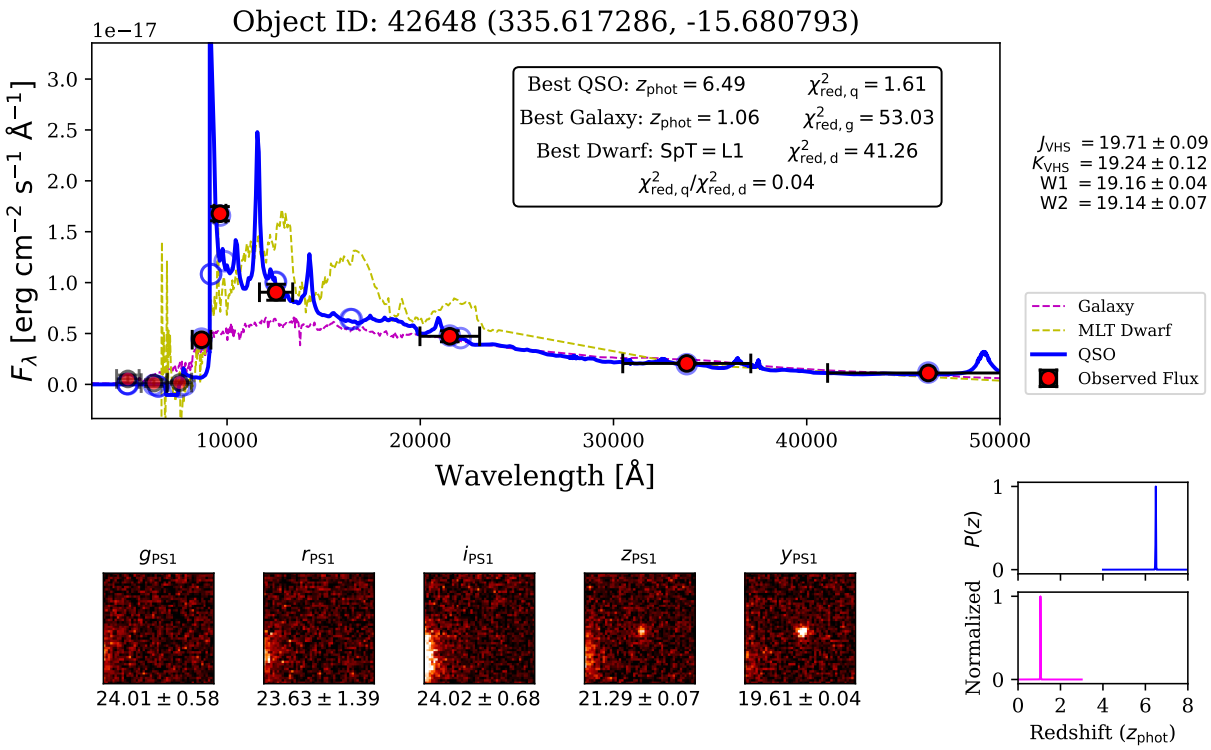

Figure 5.6. Similar to Figure 5.5, but for PSO J335.6173−15.6808.

To this end, we then employ the selection procedures explained above to the northern dataset (Pan-STARRS + DELS + UKIDSS + UHS + unWISE). We start the selection for this dataset from approximately 17 millions candidates, initially, then reduce their number to 74,374 sources after applying the Equation 5.6–5.9 dropout criteria. Next, applying SED-based selection to the previously color-selected candidates yields 7808 remaining sources. Examples of our SED fitting results are presented in Figure 5.5 and 5.6. Additionally, we conduct forced photometry on the candidates to verify the catalog measurements and eliminate spurious detections (for further information, see Bañados et al. 2014, 2016). In principle, we compute the photometry within 2″ radius aperture centered on each candidate using 1′ × 1′ the PS1 stacked images[9] in five bands. The aperture photometry is likely to be noisier than the PSF photometry. As a result, we require that our magnitude calculations from the stacked images be consistent within 2σ compared to the original PS1 catalog measurements. In addition to that, the measured photometry again must satisfy Equation 5.6–5.9, leaving us with 1263 remaining sources. Finally, the images are inspected visually to eliminate spurious sources like moving objects, hot pixels, or charge-coupled device (CCD) artifacts. This approach yields 155 quasar candidates and concludes our search in the northern dataset.

On the other side, from approximately 8 million sources that initially existed in the southern dataset (DES + VHS + unWISE), 662,322 of them passed our flag, S/N, and color criteria. Finally, applying the SED classification yields 21,879 remaining candidates. An example of lens finding using our SED modeling is displayed in Figure 5.7. We note that although forced photometry is good for finding point sources like quasars, it is not suitable for finding lenses, which are

[9]The PS1 stacked images can be retrieved via https://panstamps.readthedocs.io/en/latest/index.html.

extended sources and have a wide range of morphology. On the other hand, performing a visual inspection on more than twenty thousand images of candidates is not an efficient approach for finding lenses. Therefore, we will use a deep learning method for discovering lenses and discuss the details in the next chapter.

A curious reader would ask why we decided to only use the northern dataset for finding quasars but not lens candidates. Historically, at the beginning of this project, we only focused on discovering new quasars using the northern dataset through SED fitting. The idea for exploring deep learning algorithms to find lenses in large databases came much later, near the end phase of this project. The DES, as a primary optical catalog for the southern dataset, has the advantage of reaching around one magnitude fainter compared to PS1, which led us to exploit it first over the northern dataset. Unfortunately, in the end, we do not have enough time to apply our lens finding strategy to the northern dataset.

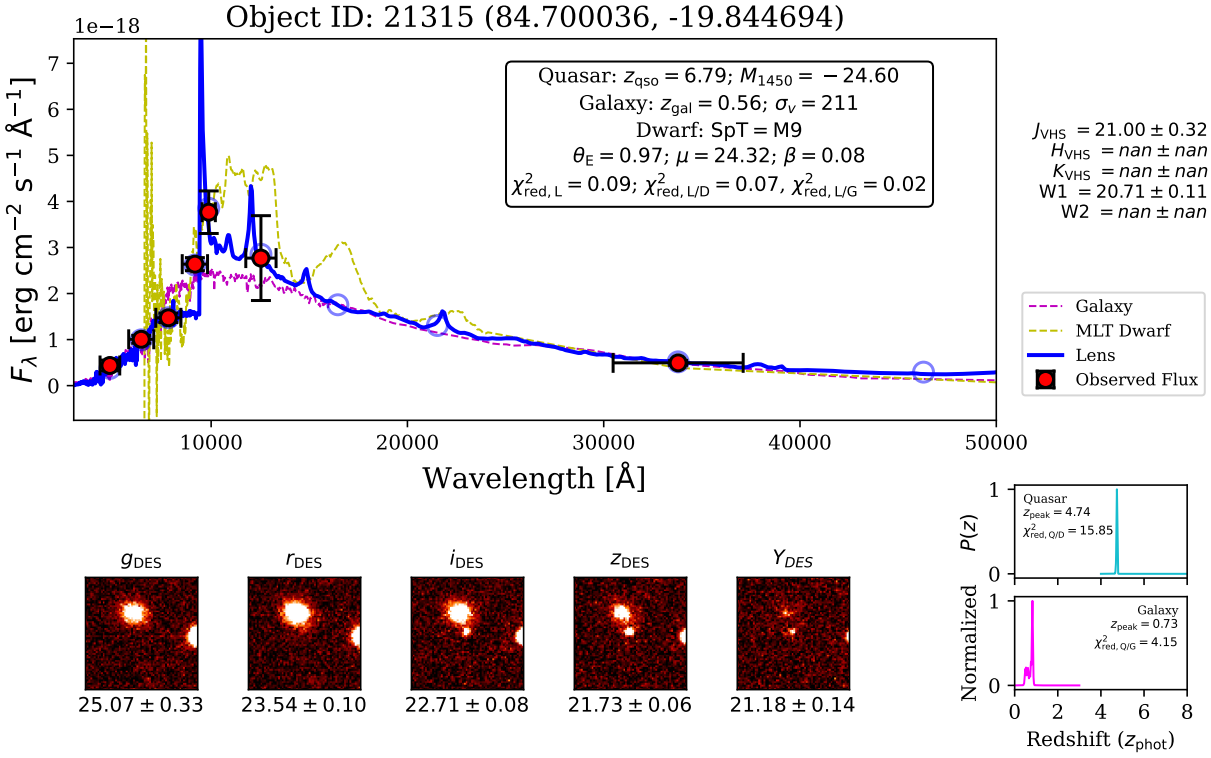

Figure 5.7. Example of the SED modeling outcome for a lensed quasar candidate. The *upper panel* depicts the observed photometry of the source (red circles with error bars) matched with three distinct templates. A blue line represents the best-fit lens spectral template, while blue circles represent the synthetic photometry. Best-fit models employing MLT dwarf and unlensed low-z galaxy templates, on the other hand, are shown in yellow and magenta. In the *lower right panel*, we present the photometric redshift probability density functions, which are generated by fitting the data to unlensed high-z quasar (cyan line) and low-z galaxy (magenta line) templates. Starting with the *lower left panel*, the DES cutouts with a size of $16\farcs8 \times 16\farcs8$ are shown.

Chapter 6

Deep Learning for Lens Finding

The content of this chapter is based on the work originally published as ***Andika, I. T.****, Jahnke, K., Onoue, M., et al. (2020; ApJ 903: 34) and is adapted from the manuscript* ***Andika, I. T.****, Jahnke, K., van der Wel, A., et al. (2022; in preparation) and the ESO VLT/FORS2 proposal: 110.243U.*

The third step of our lensed quasar search strategy is based on supervised deep learning, which requires a realistic input dataset for the training. Specifically, we will construct a classifier following the convolutional neural network (CNN) algorithm, which is widely known to be highly successful in pattern recognition tasks such as discovering gravitational lenses in big datasets (e.g., Metcalf et al. 2019). The architecture of CNN may vary depending on the task at hand. In general, images are used as input, and they will be processed by a sequence of convolutional, pooling, fully connected, and output layers. In the following sections, we will discuss the details of our simulation for constructing the input dataset, classifier training, performance evaluation, and final (lensed) quasar candidates selection.

6.1 Mock Lens Images Creation

Since there is only one galaxy-quasar lens system known at $z \gtrsim 6$ (Fan et al. 2019a), we need to mock up additional lenses for the training dataset. For that case, we adopt a data-driven approach, outlined as follows. First, we reuse the deflector galaxies, simulated quasars, and lens configurations discussed in Section 5.4. The quasar's light is then modeled as a point source convolved with a Gaussian PSF. Next, through the lens equation whose parameters are defined, we implement the light deflection effects and project the quasar's emission onto the lens plane using `PyAutoLens`[1] software (Nightingale et al. 2021). After producing the simulated lensed arcs, we overlay them to the original DES galaxy cutouts to construct realistic galaxy-quasar lens images. At this point, we disregard any additional Poisson noise for the

[1]For the documentation and implementation, see https://pyautolens.readthedocs.io/en/latest/.

modeled lensed arcs. We accept a mock image if it comprises a strong lensing effect with a configuration of $0.''01 \leq \beta \leq 1.''5$ and $\mu \geq 2$ within $\theta_{\rm E} \leq 1''$. As an illustration, we display our simulation workflow in Figure 6.1 and examples of mock lenses made by mixing izY-bands data in Figure 6.2.

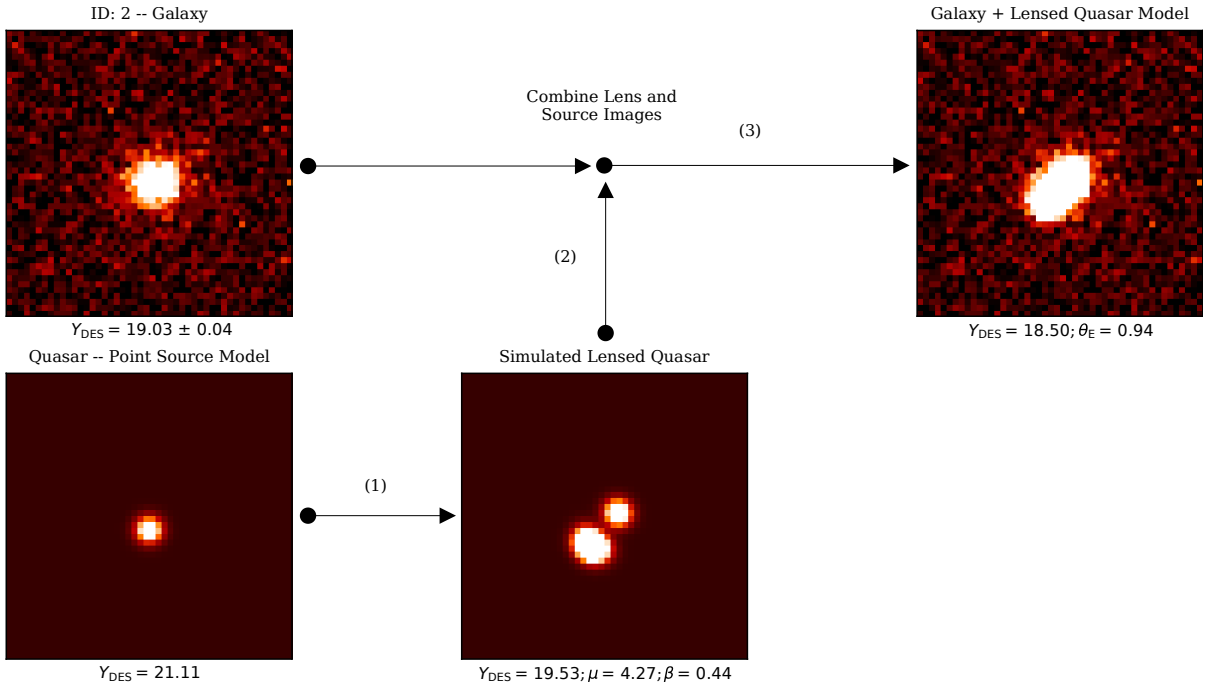

Figure 6.1. Simulation workflow that we adopt for constructing the lensed quasar images. In this case, we use $12.''6 \times 12.''6$ DES cutouts as the input dataset. The *upper left panel* presents a spectroscopically confirmed galaxy that acts as a lens. The *lower left panel* shows a simulated point-source light convolved with a Gaussian PSF, which represents a quasar as a background source. The *lower middle panel* present the deflected quasar's flux, which is computed based on the corresponding lens configuration. Lastly, we overlay the simulated arcs over an actual galaxy image and display it in the *upper right panel*. The lens parameters (i.e., β and $\theta_{\rm E}$ in arcseconds) and catalog photometry are denoted in the figure. In this work, we construct the mock images for all DES bands.

6.2 Training the Convolutional Neural Networks

Here, we will divide the inputs for CNN classifier training into four categories: (i) the mock galaxy-quasar lenses constructed in the previous section, (ii) the galaxies that are not chosen in the lens simulation, (iii) a sample of MLT dwarfs retrieved from Carnero Rosell et al. (2019), and (iv) a subset of known quasars listed by Flesch (2021). Class (i) and (ii) each consists of 12,750 sources, while class (iii) and (iv) contain of 8500 objects each. In total, we make use of 42,500 sources for the CNN input.

The dataset for training the CNN is constructed from DES $grizY$-images, trimmed to 48×48 pixels or equivalent to angular sizes of $12.''6 \times 12.''6$. Their fluxes are then min-max adjusted, resulting in values between 0 and 1. Moreover, we augment each image during the training by applying random $\pm\pi/2$ rotations, 4-pixels translations, and horizontal or vertical flips. This

strategy, therefore, increases the amount of training data while also improving the probability that the network will properly categorize numerous orientations of the same image.

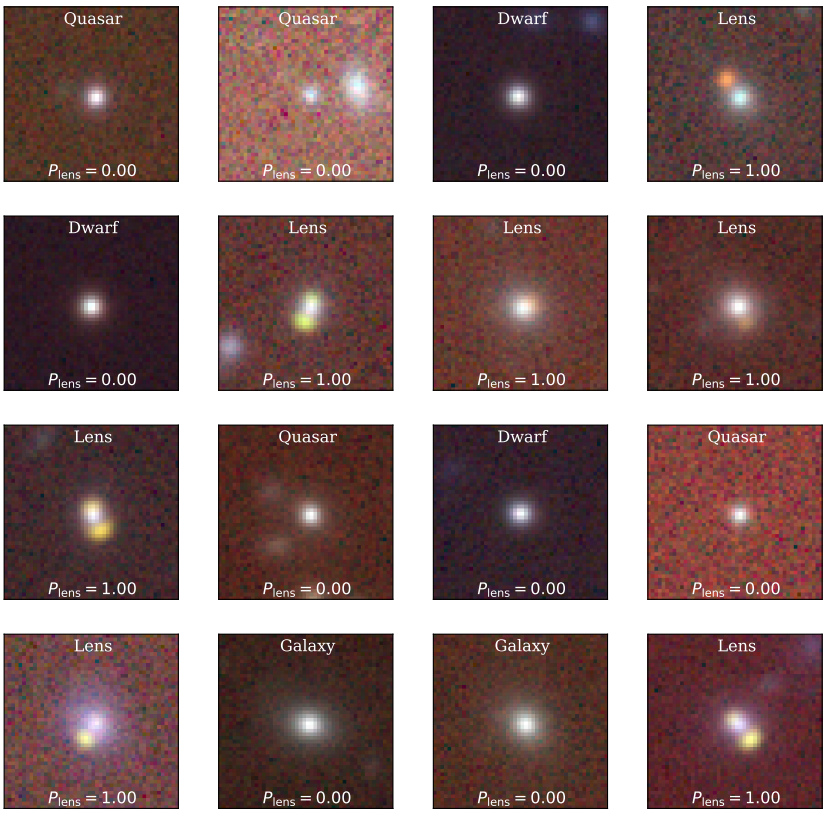

Figure 6.2. Examples of the training dataset that consists of mock lenses, galaxies, MLT dwarfs, and quasars. The images are generated based on $12\farcs6 \times 12\farcs6$ DES *izY* cutouts, and square-root stretching is applied to improve contrast and enhance the visual appearance. The computed probabilities and the true label of each source are displayed in the image.

Inspired by the classical CNN models (fore review, see e.g., LeCun et al. 1989; Sultana et al. 2019), we begin designing the networks with a sequence of three convolutional layers appended by one fully connected layer of 128 neurons (see Figure 6.3), implemented with `TensorFlow`[2] deep learning framework (Abadi et al. 2016). Then, we use a stride of 1×1 with a "same" padding for each convolutional layer, where the sizes of the kernel are $3 \times 3 \times C$, with $C = 32,\ 64,\ 64$ for the first, second, and third layers, respectively. Next, we stitch max pooling layers with a "same" padding, a size of 2×2, and a stride of 2×2 to each convolutional layer. After that, dropout regularizations are employed on convolutional (drop rate = 0.2) and fully connected (drop rate = 0.5) layers. Note that we also include the L2-norm regularization with a weight decay of 10^{-4}. The learning rate is set at 10^{-3} while the weight and bias of each neuron are generated at random values initially, then optimized during training. We implement the Rectified Linear Unit (ReLu) activations everywhere except for the output layer that uses a softmax function. During the training, the input datacube will pass through the networks and be processed by the final layer that generates four outputs: the probabilities of a candidate being a lensed quasar, galaxy, MLT dwarf, or unlensed quasar.

[2]Accessible via https://www.tensorflow.org/.

To evaluate the performance of the networks, we have to split the images into three parts: training (60% of the total data), validation (20%), and test (20%). We then subdivide them into random batches, each with a size of 256. The sparse categorical cross-entropy[3] is chosen for our loss function because it is widely known to be effective for data classifications with multi-label classes. The networks first compute the outputs of one batch using forward propagation for each iteration, then loop over the training batches to complete one epoch. The current batch loss information is then relayed back for optimizing the weights and biases of the neurons, computed following a stochastic gradient descent method to minimize the loss (e.g., Adam optimization; Kingma & Ba 2014). For each epoch, this optimization is performed first on the training batches. Then, we calculate the average loss for the whole training dataset. After that, the processes are repeated for the validation dataset but with no adjustments to the neuron parameters. By comparing training and validation losses, we can determine if model optimization has improved or whether overfitting has occurred. Overfitting usually arises when the networks fail to generalize and perform poorly on the unseen data. To mitigate this, we randomly re-arrange the training dataset after each epoch to boost generalization and develop networks with optimum accuracy. Finally, we stop the training after the losses have converged over numerous epochs.

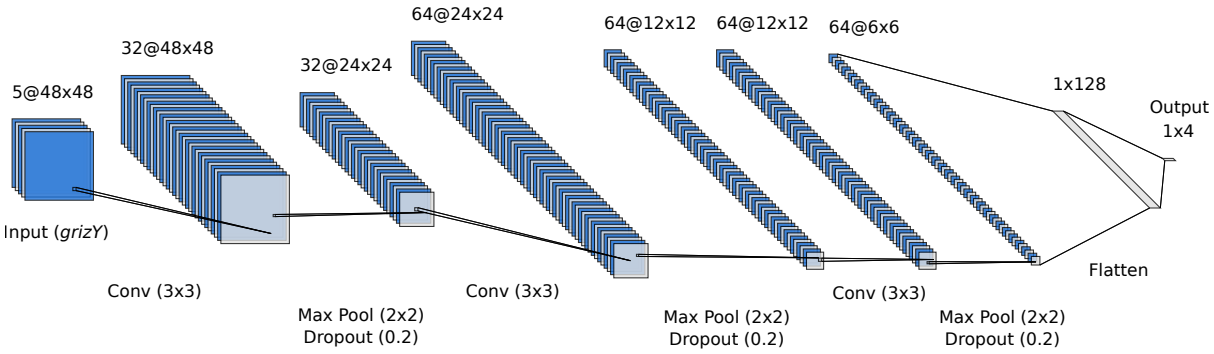

Figure 6.3. Design of the CNN architecture that we use for discovering (lensed) quasars. The first layer takes DES *grizY* images, each with a size of 48×48 pixels, as input datacube. Followed by that, there are three series of convolutional, max pooling, and dropout layers. We indicate the sizes of each kernel and dropout rates in the schematic diagram. The datacube is then flattened and passed through fully connected and dropout layers before reaching the output layer. The softmax activation in the final layer will generate four classification probabilities – i.e., $P_{\rm lens}$, $P_{\rm galaxy}$, $P_{\rm dwarf}$, and $P_{\rm quasar}$.

6.3 Evaluation of the Classifier Performance

As mentioned in the previous section, our CNN classifier will compute four probability scores, i.e., the probabilities of a candidate being a lensed quasar ($P_{\rm lens}$), galaxy ($P_{\rm galaxy}$), MLT dwarf $P_{\rm dwarf}$, and normal quasar ($P_{\rm quasar}$). The score of $P_{\rm lens} = 1$ indicates that the categorized image is likely to include a lensed quasar. The value of $P_{\rm lens} = 0$, on the other hand, indicates that the image is not a lensed quasar and is more like other contaminants. It is worth noting that

[3]More details are available at https://www.tensorflow.org/api_docs/python/tf/keras/losses/.

$P_{\text{lens}} + P_{\text{galaxy}} + P_{\text{dwarf}} + P_{\text{quasar}} = 1$ by definition. After 92 epochs, our CNN training converges and achieves 98.0 (98.4) percent accuracy and a loss value of 0.090. (0.077) for the assessment utilizing the training (validation) dataset. According to the general view, the high accuracy achieved in the training dataset might be influenced by overfitting. Hence, we compare the accuracy–loss learning curves created by assessing the CNN prediction to the training and validation datasets (see Figure 6.4). The training and validation loss values converge and follow the same pattern after decreasing for multiple consecutive epochs. The absence of any overfitting signals – i.e., the training loss continues to reduce while the validation loss increases – gives us confidence that our CNN classifier can learn and generalize.

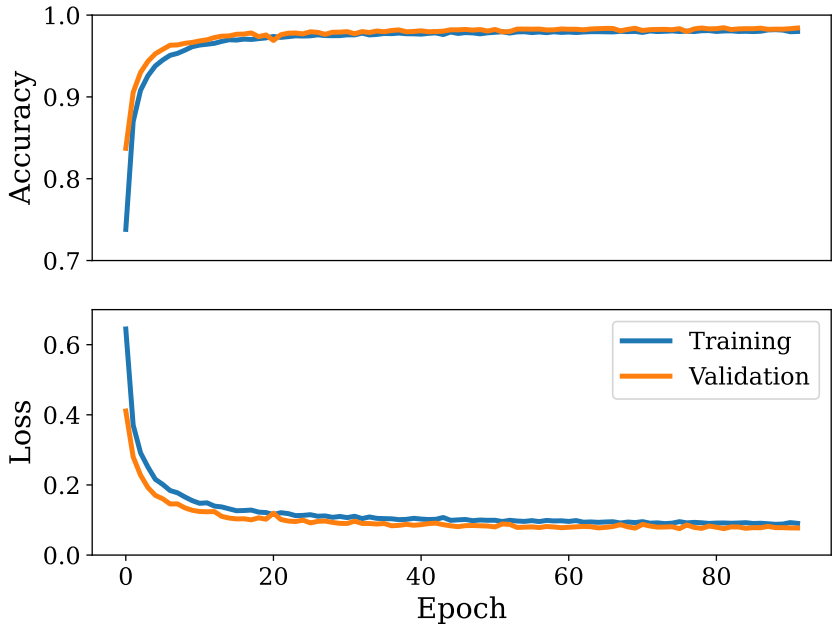

Figure 6.4. Accuracy (upper panel) and loss (lower panel) curves as the function of the training epoch. These metrics are computed by comparing the CNN classifier to the training and validation datasets, shown by blue and orange lines, respectively.

The receiver operating characteristic (ROC) curve is another metric for evaluating the overall performance of the trained model. In theory, it demonstrates how successfully a binary classifier distinguishes between two classes when the decision threshold is adjusted. We first define positives (P) as lenses and negatives (N) as non-lenses or contaminants. True positives (TP) are events in which the model correctly classifies the lenses, whereas true negatives (TN) are where the non-lenses are accurately recognized. On the other hand, false positives (FP) occur when the classifier wrongly identifies contaminants as lenses. In addition, we define false negatives (FN), which occur when the model mistakenly rejects lenses. The ROC curve displays false positive rate (FPR) versus true positive rate (TPR) for the validation dataset, where:

$$\text{TPR} = \frac{\text{TP}}{\text{P}} = \frac{\text{TP}}{\text{TP} + \text{FN}} \tag{6.1}$$

and

$$\text{FPR} = \frac{\text{FP}}{\text{N}} = \frac{\text{FP}}{\text{FP} + \text{TN}}. \tag{6.2}$$

The ROC curve is subsequently built by gradually increasing the probability threshold from 0 to 1. A perfect classifier has an AUC of one, while a classifier that only makes random guesses has an AUC of 0.5. Because we have four classes for classifying the candidates, i.e., multi-label classification, we have to binarize our CNN output using the "one versus all" paradigm. Thus, we generate four ROC curves: (i) lensed quasars versus galaxies and other point-source contaminants, displayed with a solid blue line, (ii) galaxies against lens systems plus other contaminants, presented with a dashed magenta line, (iii) MLT dwarfs versus other sources, denoted with a dashed yellow line, and (iv) quasars against lenses, galaxies, and others, marked with a dashed cyan line. We generate these ROC curves based on the CNN classifier assessment to the test dataset that is previously unseen, which yields high area under the curve (AUC) values, as shown in Figure 6.5, indicating high performance.

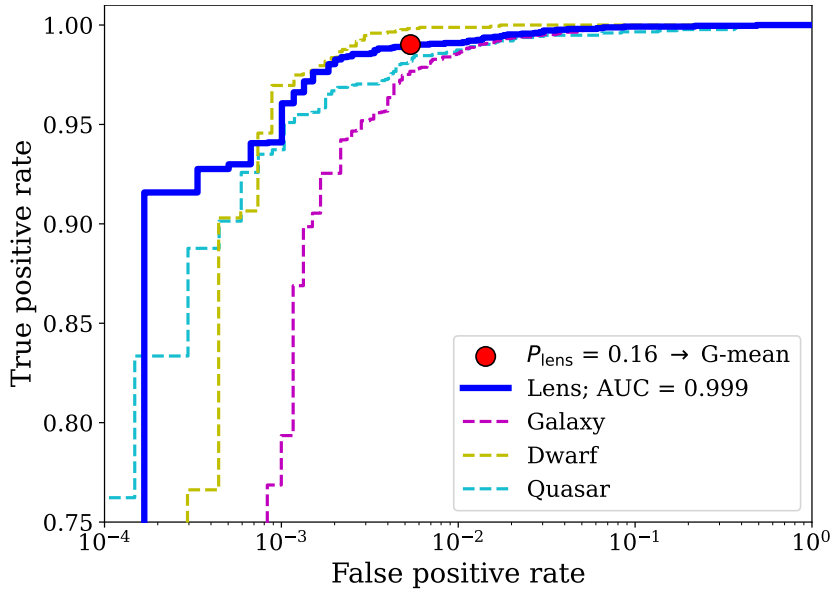

Figure 6.5. Receiver operating characteristic curves and their corresponding area under the curve. A solid blue line is a curve for categorizing lensed quasars. The curves for forecasting galaxies, MLT dwarfs, and quasars, on the other hand, are shown by magenta, yellow, and cyan dashed lines, respectively. A red circle represents the FPR and TPR values for the adopted $P_{\rm lens}$ threshold.

Based on the ROC curves, we employ the geometric mean, or G-mean[4], metric to find a balance between TPR and FPR. The highest G-mean score suggests the optimum $P_{\rm lens}$ threshold that optimizes TPR while minimizing FPR. In this situation, we find a suggested threshold of $P_{\rm lens} > 0.16$, resulting in FPR = 0.01 and TPR = 0.99. Below this $P_{\rm lens}$ threshold, the number of candidates grows exponentially as their quality deteriorates, making visual evaluation more time-consuming and less effective. We note that it is difficult to find a perfect threshold without a reference sample of $z \gtrsim 6$ lensed quasars. In terms of purity and completeness trade-off, we must seek a balance in which the quantity of candidates is manageable for follow-up observations.

As a complement, we conduct a supplementary test with independent data. This test dataset

[4]The definition of geometric mean is G-mean = $\sqrt{\text{TPR} \times (1 - \text{FPR})}$.

is constructed from a sample of confirmed lensed quasars listed in Gravitationally Lensed Quasar Database[5] (Inada et al. 2012; Agnello et al. 2015, 2018; Spiniello et al. 2018; Lemon et al. 2018, 2019, 2020; Jaelani et al. 2021). About 34 of the 220 these systems have DES images. Followed by that, we use our CNN classifier to evaluate this dataset and successfully recover 28 lenses, resulting in 82% completeness. For further information on the resultant probability score distribution, please consult Appendix A. As evaluated against unseen real lens systems, our CNN model's performance falls compared to the evaluation on the mock lenses. This reduced performance might be due to the peculiarity of some strong lenses that are not captured by our simulation. Four false negatives in the test dataset, for example, might comprise lensed arcs that are too dim to be detected, compact lenses, numerous distortions induced by substructures, or other factors (see Figure A.2). Nevertheless, our CNN classifier is able to generalize and accurate enough for our objectives.

6.4 Final List of Candidates and Initial Follow-ups

6.4.1 Lens Candidates

The current reported lensed fraction among $z \sim 6$ quasars ($\approx 0.2\%$; Yue et al. 2021a, 2022) is significantly smaller than theoretical estimates ($\gtrsim 4\%$; Wyithe & Loeb 2002a; Pacucci & Loeb 2019). According to Yue et al. (2021a), this tension might be produced by unexamined systematic bias. Many previous studies incorporate older observations of quasar luminosity functions and deflector velocity distributions for predicting lens fraction. By using more recent measurements, Yue et al. proposed that the lensed fraction among $z \sim 6$ quasars is ≈ 0.4–0.8% for a survey depth of 22 mag. As a result, we estimate just a few handfuls of lensed quasars to be found in the existing DES data.

As a reminder, from the previous chapter, we obtained 21,879 lens candidates selected via their catalog photometry and SED modeling using the southern dataset. We then perform the CNN-based classification to those remaining candidates, which reduces their number to only 400 sources. After that, we visually inspect their images to remove spurious sources (e.g., moving objects, hot pixels, CCD artifacts, etc.), and a total of 30 candidates are selected. In addition to that, we also find six unlensed quasar candidates. A list of the candidates is presented in Table 6.1 while their image composites displayed in Figure 6.6. Also, the distributions of the lens candidate properties are presented in Figure 6.7.

As a side point, prior high-z quasar surveys frequently used extra magnitude cuts at the bluer wavelengths (e.g., Mazzucchelli et al. 2017; Wang et al. 2019; Reed et al. 2019; Andika et al. 2020). Their strategies are reasonable since the emission of $z \gtrsim 6$ quasars at wavelengths blueward of Lyα is severely absorbed by the intervening intergalactic medium, causing a break in the spectrum. In other words, we are not expecting any substantial fluxes observed in the DES g or r bands. This feature, however, is not the case for the lensed quasars, where the lens galaxies might provide considerable emissions at $\lambda_{\rm obs} \lesssim 8000$ Å. For example, if we use

[5]Accessible through https://research.ast.cam.ac.uk/lensedquasars/.

an extra S/N($g_{\rm DES}, r_{\rm DES}$) < 5 cuts, there is no mock lenses generated in Section 5.4 survive. To put it differently, we will lose all of the lens systems that host bright galaxies as deflectors. Conversely, if the deflectors are faint and less massive, these systems will produce compact lenses. As a result, the light from these sources is expected to be quasar-dominated with a slightly stretched morphology. Because of the blending between the deflector galaxy and the lensed quasar images, we expect that neither a PSF nor a standard Sérsic profile will provide a satisfactory description of their morphology (Fan et al. 2019a; Yue et al. 2022).

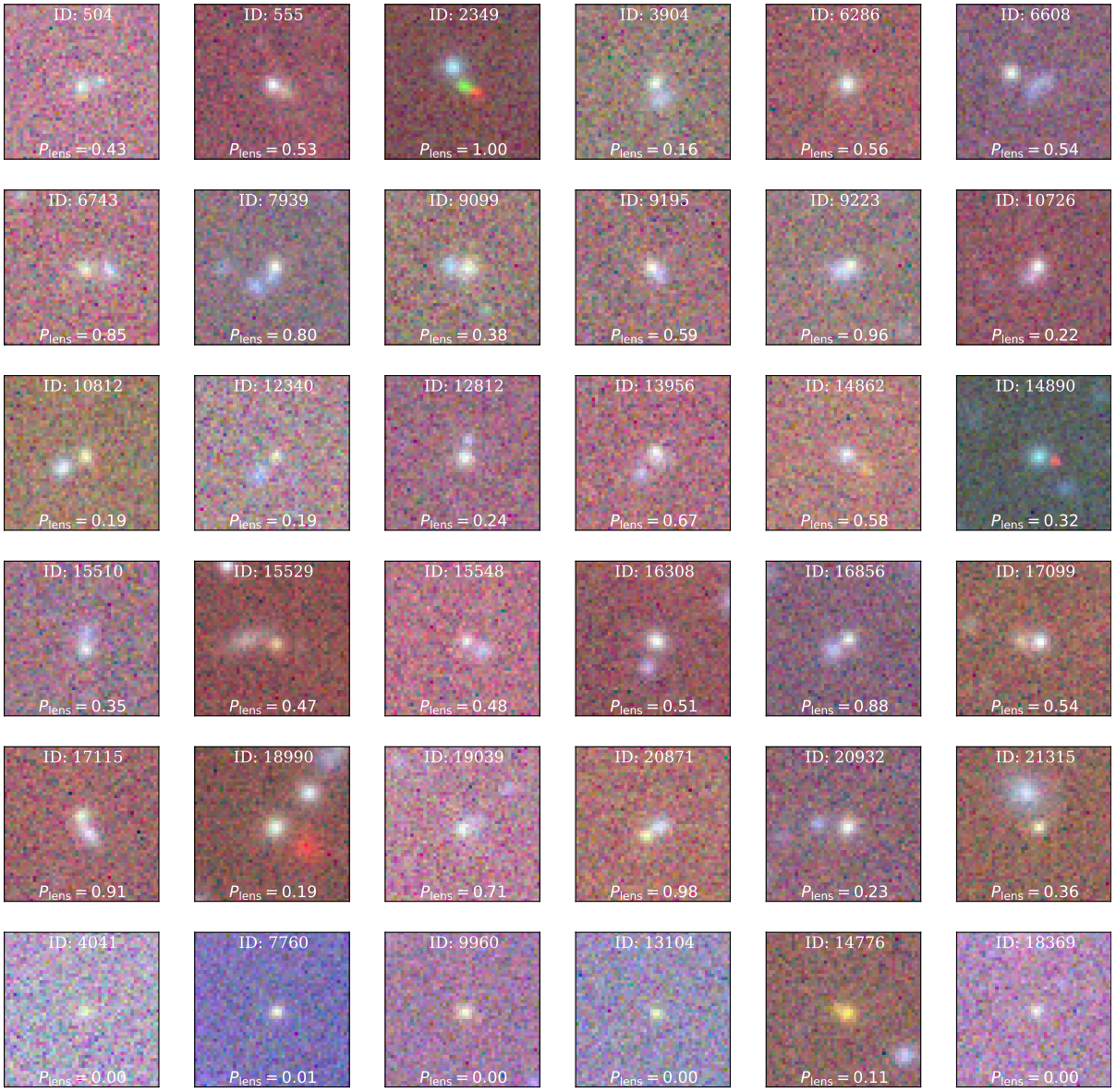

Figure 6.6. Color images of the (lensed) quasar candidates. The lenses are displayed in the first five rows from the top, while the unlensed quasar candidates are shown at the bottom. The images are made from 12.″6 × 12.″6 DES *izY* cutouts. Normalization using square-root stretch is used to increase contrast and clarity. The identifier of each object is presented at the top of each panel. At the bottom of each cutout, we provide the CNN score ($P_{\rm lens}$).

Note that sources with erratic morphologies that do not match either class in the training dataset will earn unexpected CNN scores. They can have a variety of morphologies, such as

irregular sources or spiral arms that resemble lensing arcs. There are also red point sources around bright blue stars with diffraction spikes, whose colors approximate lens system SEDs. Furthermore, in some circumstances, sources with low S/N in the DES Y-image do not provide enough information for discovering lensing signals. Therefore, future studies into more sophisticated CNN-based classifiers, as well as simulation improvements, will be valuable.

ID	Name	$z_{\rm DES}$	$Y_{\rm DES}$	$J_{\rm VHS}$	W1	$\chi^2_{\rm red,Q}$	$\chi^2_{\rm red,G}$	$\chi^2_{\rm red,L}$	$\chi^2_{\rm red,D}$	$z_{\rm qso}$	$z_{\rm gal}$	$P_{\rm lens}$	Grade
504	J036.96123−50.21938	21.69	21.06	20.60	20.03	11.32	2.82	0.35	4.17	6.84	0.71	0.43	A1
555	J040.71110−51.68291	20.57	20.06	19.86	19.10	63.09	4.69	0.73	33.55	6.95	0.65	0.53	A1
2349	J018.04700−00.87444	21.24	20.20	20.08	19.75	1.06	116.97	0.61	19.46	6.82	0.86	1.00	A1
3904	J025.08084−06.38508	21.22	20.72	20.60	20.09	41.18	3.08	0.38	6.12	6.73	0.87	0.16	A1
6286	J327.79776−51.87795	20.84	20.25	20.28	19.83	23.68	9.41	0.35	7.50	6.76	0.68	0.56	A1
6608	J082.83621−54.01355	21.11	20.35	20.23	19.54	37.66	3.40	0.58	13.62	6.95	0.82	0.54	A1
6743	J068.45382−33.48967	21.82	21.13	20.99	20.11	13.84	1.26	0.15	3.94	6.95	0.68	0.85	A1
7939	J085.89481−57.30598	21.49	20.97	20.37	20.85	40.17	2.25	0.42	2.96	6.88	0.34	0.80	A1
9099	J080.70670−38.89704	21.04	20.54	20.47	19.69	47.80	4.42	0.59	16.70	6.72	0.70	0.38	A1
9195	J046.81510−17.29557	21.24	20.70	20.48	20.20	35.80	6.78	1.16	7.42	6.71	0.79	0.59	A1
9223	J345.07684−58.84036	20.79	20.15	20.35	19.92	50.77	6.58	0.80	4.16	6.94	0.86	0.96	A1
10726	J322.05036−45.50413	20.96	20.42	20.43	19.83	37.81	6.00	0.64	7.75	6.94	0.87	0.22	A1
10812	J079.81120−25.37072	22.16	21.18	21.18	20.44	30.62	6.09	0.42	4.53	6.89	0.53	0.19	A1
12340	J030.94768−16.39863	22.75	21.73	21.59	21.12	9.45	2.35	0.11	1.38	7.08	0.59	0.19	A1
12812	J061.07527−33.99544	21.27	20.52	20.60	20.08	24.12	5.07	0.24	6.91	6.82	0.59	0.24	A1
13956	J026.51434−18.52573	21.81	21.29	21.03	20.75	18.11	2.52	0.34	1.80	6.64	0.79	0.67	A1
14862	J000.12710−47.46657	21.67	21.04	21.30	20.69	14.81	3.12	0.23	3.16	6.83	0.70	0.58	A1
14890	J003.79587−43.48657	21.00	20.28	20.20	19.34	42.46	8.95	1.05	16.23	6.92	0.75	0.32	A1
15510	J067.87033−20.39097	21.38	20.78	20.36	20.23	20.23	1.25	0.10	8.40	7.08	0.47	0.35	A1
15529	J068.16592−22.11713	21.61	21.01	20.89	20.40	63.70	5.18	0.81	9.59	7.04	0.59	0.47	A1
15548	J069.10890−22.95532	22.10	21.32	21.40	20.39	14.61	2.05	0.31	3.91	6.97	0.77	0.48	A1
16308	J089.11616−24.83778	20.61	20.07	19.85	19.24	37.01	3.57	0.18	18.86	6.93	0.58	0.51	A1
16856	J092.60966−35.90861	20.83	20.20	20.07	19.60	14.82	3.69	0.52	14.10	6.93	0.68	0.88	A1
17099	J051.90568−11.59229	20.42	19.81	19.47	18.90	58.33	7.96	1.57	26.39	6.87	0.70	0.54	A1
17115	J331.94605−62.27649	20.72	20.21	20.07	19.48	80.55	3.56	0.67	21.17	7.00	0.61	0.91	A1
18990	J012.54668−02.00288	20.40	19.64	19.49	18.72	80.17	12.04	1.83	29.71	7.09	0.85	0.19	A1
19039	J059.49147−51.51484	21.65	20.91	21.05	20.15	23.37	2.57	0.25	11.33	6.84	0.79	0.71	A1
20871	J041.09428−01.94383	21.14	20.50	20.71	20.31	39.75	4.41	0.81	5.00	6.94	0.66	0.98	A1
20932	J060.23733−21.39838	21.23	20.47	20.65	19.82	44.95	6.79	0.90	10.04	6.76	0.59	0.23	A1
21315	J084.70004−19.84469	21.73	21.18	21.00	20.71	20.06	4.84	0.09	1.27	6.79	0.56	0.36	A1
4041	J051.27758−18.82994	22.76	21.48	21.03	21.05	0.21	6.20	0.30	1.40	7.00	1.45	0.00	A2
7760	J358.77772−49.96887	21.22	20.23	20.21	20.41	1.24	33.94	2.56	12.07	6.71	0.76	0.01	A2
9960	J080.61260−42.70559	21.91	21.09	20.96	20.10	0.88	16.38	1.71	3.46	6.77	0.97	0.00	A2
13104	J002.72340−59.61451	22.76	22.15	21.61	21.07	0.10	7.98	1.18	0.64	6.77	0.97	0.00	A2
14776	J070.86138−20.09059	21.37	20.65	20.13	19.75	0.46	32.69	1.96	4.87	6.77	0.97	0.11	A2
18369	J080.68560−33.47577	22.16	21.21	21.43	20.39	0.87	4.96	0.25	3.24	6.77	0.97	0.00	A2

Table 6.1. List of the $z \gtrsim 6$ quasar candidates (lensed and non-lensed) selected in this work. Column values are candidate identifier, source name, z- and Y-magnitudes of DES, VHS J-magnitude, unWISE W1-magnitude, reduced chi-squares for quasar (Q), galaxy (G), lens (L), MLT dwarf (D) fitted templates, photometric redshifts of the background and foreground sources, classification score from CNN, and visual inspection grade. Lens candidates are denoted with "A1" grade while unlensed quasar candidates are denoted with "A2". We adopt the "JRRR.rrrrr+DD.ddddd" convention for naming the sources, where RRR.rrrrr and +DD.ddddd are respectively the R.A. and declination in decimal degrees (J2000).

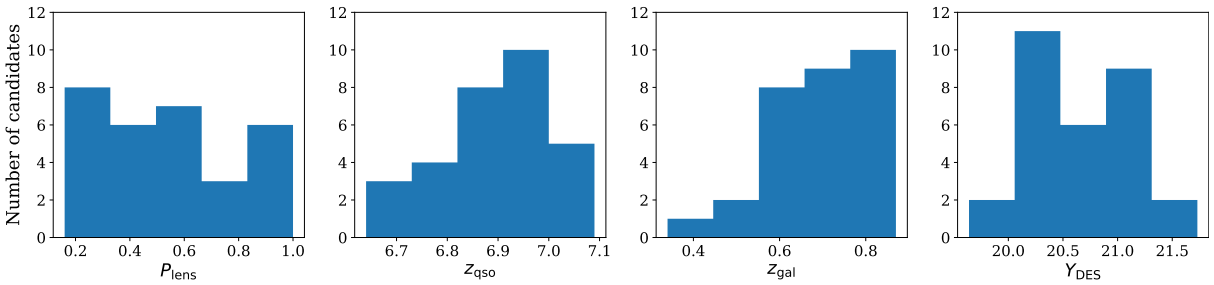

Figure 6.7. Distributions of the lens candidate probabilities ($P_{\rm lens}$), quasar redshifts ($z_{\rm qso}$), deflector redshifts ($z_{\rm gal}$), and Y-band magnitudes.

6.4.2 Confirmed Quasars

Several spectroscopic surveys were performed using 6.5 m–Magellan/FIRE (Folded-port Infrared Echellette; Simcoe et al. 2013) to confirm the quasar nature of our targets. Typically, each source is observed for ten to fifteen minutes in high-throughput prism mode utilizing a slit width of 0.″6. In theory, this provides us a $R = 500$ spectral resolution with a wavelength coverage of 0.82–2.51 μm. A total of ten candidates have been followed-up as of March 2022, where seven are confirmed to be MLT dwarfs while the other three, PSO J083.8371+11.8482, PSO J344.1442−02.7664, and PSO J335.6173−15.6808, are previously undiscovered $z \gtrsim 6$ quasars. The rejected candidates are reported in Table 6.2, but a precise spectral categorization of these sources is beyond the scope of our work.

Name	$z_{\rm PS1}$	$y_{\rm PS1}$	$J_{\rm VHS}$	Class
PSO J065.5314−13.3353	22.06 ± 0.18	20.54 ± 0.11	20.54 ± 0.16	MLT dwarfs
PSO J134.2027−07.1366	22.03 ± 0.26	20.30 ± 0.09	19.73 ± 0.10	MLT dwarfs
PSO J123.0135−01.9006	21.93 ± 0.19	20.44 ± 0.10	19.96 ± 0.19	MLT dwarfs
PSO J002.1774−02.9102	22.83 ± 0.30	21.06 ± 0.13	20.19 ± 0.15	MLT dwarfs
PSO J303.7815−00.4066	22.01 ± 0.15	20.49 ± 0.10	19.97 ± 0.13	MLT dwarfs

Table 6.2. List of the spectroscopically rejected candidates. Here, we provide their names, PS1 z and y magnitudes, VHS magnitudes in the J-band, and classifications.

We present the two-dimensional spectra of three newly-discovered quasars in Figure 6.8. Based on the presence of prominent Lyα breaks at around the observed-frame wavelength of 9100 Å, we presume that those sources are located at $z \approx 6.5$. Unfortunately, the existing low-resolution spectra of PSO J344.1442−02.7664 and PSO J335.6173−15.6808 are insufficient for determining their precise black hole masses and emission line properties. Hence, further analyses will be presented in our upcoming publication (Andika et al., in preparation). On the other hand, because PSO J083+11 is a rare weak emission line quasar, we performed extensive multiwavelength campaigns and will discuss it in detail in the next chapter.

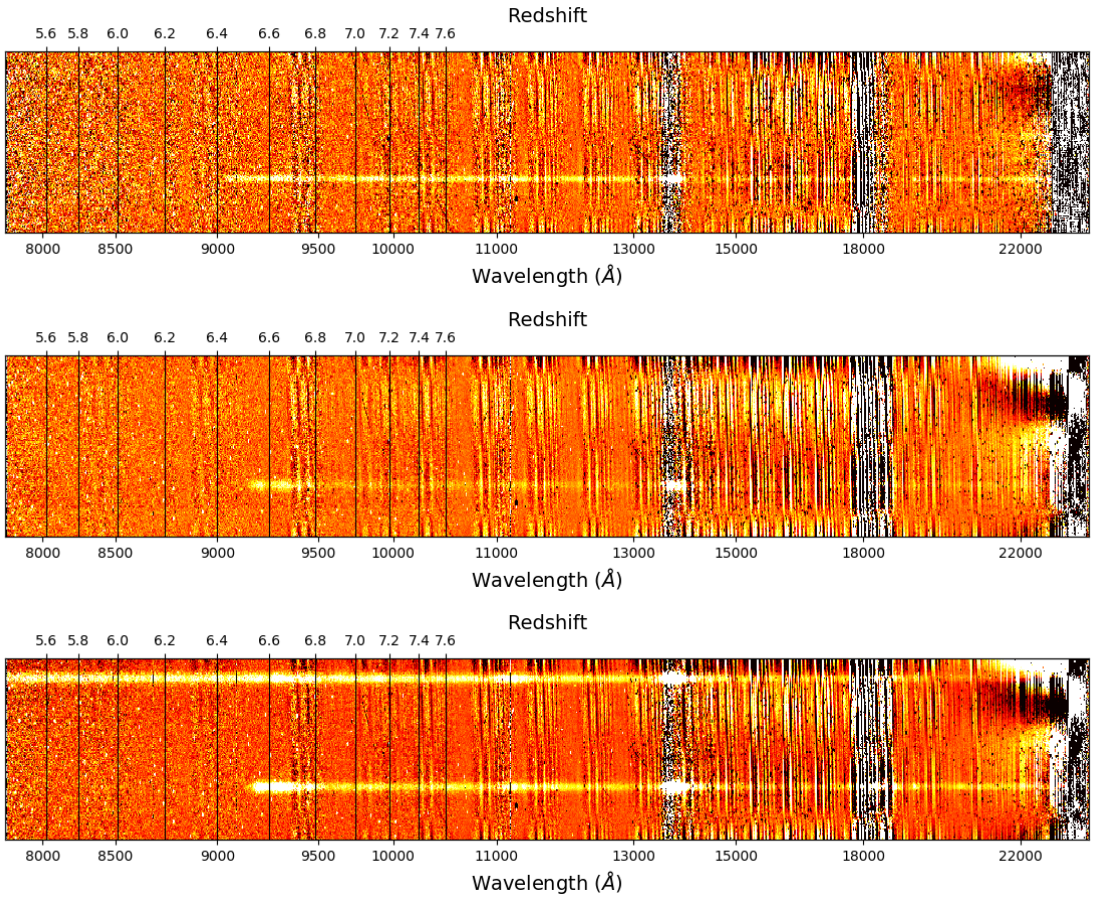

Figure 6.8. Magellan/FIRE two-dimensional spectra of PSO J083.8371+11.8482 (*upper panel*), PSO J344.1442−02.7664 (*middle panel*) and PSO J335.6173−15.6808 (*lower panel*). A prominent emission break can be found around the observed-frame wavelength of 9100 Å, indicating that the Lyα emission is redshifted to $z \approx 6.5$.

6.5 Discussion and Summary

In this work, we use combined survey catalogs in the northern and southern hemispheres to conduct a systematic search for $\gtrsim$ 6 (lensed) quasars. Our strategy is summarized as follows. First, we use the catalog information to preselect the candidates via photometric colors. This step gives us a few million sources, coming from the combined northern and southern datasets, as a starting point. Next, we calculate their probabilities of being (lensed) quasar or other contaminants and the associated photometric redshifts using SED fitting. This way, we significantly reduce the number of candidates to only around few thousand. We then focus on selecting quasars using the northern dataset and subsequently perform forced photometry and visual inspection on the sources present in this catalog, which gives us the surviving 155 quasar candidates. Although forced photometry is good for finding point sources, we need to use a better strategy for discovering lens candidates, which tend to have a wide range of morphology. For that reason, we apply a CNN-based analysis followed by visual inspections to the southern dataset, which leads us to find 30 lens and six quasar candidates.

Our findings indicate that automated SED modeling and CNN classification, supplemented with little human input, are promising for recognizing strong lenses in large databases. The technique proposed in this work is readily adaptable for finding lenses at different redshifts and is suited for forthcoming surveys such as the Euclid (Scaramella et al. 2021) and the Rubin Observatory Legacy Survey of Space and Time (Ivezić et al. 2019). In general, to acquire good results, modifications to the filter profiles, seeing distribution, and image resolution must be made to match the target surveys. Extending the diversity of SEDs and morphologies for the sources and lenses in the training set will also help future searches. Using more realistic galaxy mass profiles, such as SIE, may thus increase classifier performance. Furthermore, testing with other network models, such as EfficientNet and ResNet, which have been suggested, may provide better results than the standard CNNs (Cañameras et al. 2021; Rojas et al. 2021). Lastly, spectroscopic and high-resolution imaging campaigns for confirming the lensed quasar nature of all of our candidates will be performed and reported in our future work.

Part III

Exploring the Nature of a Young Weak-Line Quasar

Chapter 7

Spectroscopic Observations and Analysis

The content of this chapter is based on the published work ***Andika, I. T.****, Jahnke, K., Onoue, M., et al. (2020; ApJ 903: 34) and is adapted from the Gemini/GNIRS proposal: GN-2019A-FT-204.*

Quasars at the highest-z frontier are excellent probes for investigating the formation of the earliest SMBHs, as well as their host galaxies (for review, see e.g., Volonteri 2010; Inayoshi et al. 2020). Interestingly, a notable subset of $z \gtrsim 6$ quasars exhibits weak emission lines, in contrast with the general Type 1 quasar population at similar luminosity and SMBH mass. These so-called weak emission line or weak-line quasars (commonly abbreviated as WLQs) are characterized as showing rest-frame equivalent widths (REWs) of C IV λ1549 < 10 Å and/or Lyα + N V λ1240 < 15.4 Å (e.g., Bañados et al. 2016; Shen et al. 2019). A study at lower-redshifts ($z \sim 3$–5) found that the C IV REWs of Type 1 quasars typically follow a log-normal distribution with a mean of 42^{+25}_{-16} Å (Diamond-Stanic et al. 2009). WLQs, surprisingly, is the 3σ outliers at the low-end of this distribution.

Several ideas have been presented to explain the WLQ phenomena, in particular for those that are located at low-z, and according to Plotkin et al. (2015), they fall into two basic categories: (1) the soft ionizing continuum concept and (2) the anemic broad emission line region[1] paradigm. According to the soft ionizing continuum model, the broad-line region is simply less photoionized, so the produced broad emission lines are weak. This situation is most likely due to (i) inefficient photoionizing photons caused by an extremely high accretion rate (Leighly et al. 2007a,b), (ii) low accretion rate in the very massive black hole leading to a radiatively inefficient cold accretion disk (Laor & Davis 2011), or (iii) high-energy photons generated by the accretion disks are absorbed by shielding materials and preventing it reaching the broad-line region (Wu et al. 2011; Luo et al. 2015; Ni et al. 2018, 2022; Paul et al. 2022). The anemic broad-line region paradigm, on the other hand, argues that the gas in that region itself might be particularly

[1]We use the words "broad emission line region" and "broad-line region" interchangeably. These terms are also commonly abbreviated as "BLR" or "BELR".

deficient (Shemmer et al. 2010; Nikołajuk & Walter 2012), possibly because the quasar is in an early stage of accretion and the broad-line clouds have not yet completely formed (Hryniewicz et al. 2010; Meusinger & Balafkan 2014). So far, only ~ 20 of the detected $z \gtrsim 6$ quasars have been recognized as WLQs (Bañados et al. 2016; Shen et al. 2019). Therefore, an expansion in the quasar sample size at this early epoch is crucial for increasing sampling points and investigating the connection between WLQs and cases of very young age quasars, which allows us to understand early growth modes.

As part of our endeavor to increase the number of known quasars at $z \gtrsim 6$, we present the discovery of PSO J083.8371+11.8482 (hereafter PSO J083+11) at $z = 6.34$. A comprehensive multiwavelength campaign using state-of-the-art instruments is performed to examine the physical characteristics of this quasar, its host galaxy, and its surroundings. As an outline, we first provide the spectroscopic follow-up data that confirms PSO J083+11 is a quasar and subsequently investigate the associated central SMBH properties. Then, we present a high-resolution Hubble Space Telescope near-infrared imaging to see if gravitational lensing influences the quasar's apparent emission and search for any potential lens galaxy. Next, the proximity zone size and quasar lifetime estimations are discussed. After that, constraints on the host galaxy properties are presented using data from Atacama Large Millimeter/submillimeter Array observations. Finally, we discuss the probable explanations that might contribute to the weak-line nature of PSO J083+11.

Note that for this part we adopt the ΛCDM cosmological model where $\Omega_\Lambda = 0.7$, $\Omega_m = 0.3$, and $H_0 = 70$ km s^{-1} Mpc^{-1} for all of physical measurements. Accordingly, at $z = 6.3401$ the age of universe is 0.852 Gyr and an angular scale of $\theta = 1''$ corresponds to a proper transverse separation of 5.5 kpc.

7.1 Preliminary Characterization with Magellan/FIRE

We initially validated PSO J083+11 as a quasar at $z \approx 6.3$ by utilizing the 6.5 m–Magellan/FIRE (PI: R. Simcoe; Simcoe et al. 2013) on December 31, 2018, with a total integration time on target of approximately five minutes. The observation was carried out in high-throughput prism mode with a slit width of $0\farcs6$, yielding a spectral resolution of $R = 500$ at the observed wavelengths of 0.82–2.51 μm.

Later in January and February 2019, the same telescope was used to obtain a significantly deeper PSO J083+11's near-infrared spectra. Subsequently, the quasar was observed for 5 hours with a high-resolution echellette configuration using a slit of $0\farcs6$. In theory, this provides us a spectral resolution of $R = 6000$ or a velocity resolution of ≈ 50 km s^{-1} in the wavelength range of 0.82–2.51 μm. Unfortunately, the S/N of the data was degraded in this second run due to suboptimal weather conditions. Nonetheless, a brief examination of the spectra revealed that all of the important emission lines, such as Lyα λ1216, C IV λ1549, and Mg II λ2798, looked unusually weak. Despite the noisy spectrum, we fit the emission lines and continuum and discovered that the power-law slope of the continuum is compatible with a Type 1 quasar at

$z = 6.34$. The area around Mg II is significantly contaminated by telluric absorptions, making precise line measurements problematic. We then performed another spectroscopic observation to address this issue and minimize instrument-specific effects.

7.2 Near-infrared Spectroscopy with Gemini/GNIRS

On March 20–22, 2019, we performed near-infrared spectroscopy with the Gemini Near-Infrared Spectrograph (GNIRS) at the 8.1 m–Gemini North telescope (GN-2019A-FT-204, PI: M. Onoue) with a total integration time on target of 8060 s. The runs were carried out in cross-dispersed mode to cover the observed wavelength ranges of 0.9–2.5 μm, or corresponds to wavelengths of 1200–3400 Å in the rest-frame. We used the "short" camera with a pixel resolution of 0.″15 and a grating resolution of 31.7 l/mm. Then, we employed a slit with an aperture of 0.″675 to achieve a spectral resolution of $R \sim 750$. For minimizing skylines contamination, the exposure time for a single frame was adjusted to 155 s, and a typical ABBA offset pattern was used between the exposures. In addition, the observations were performed at an air mass of ≈ 1.1–1.7.

The `PypeIt`[2], an open source spectroscopic data reduction pipeline (Prochaska et al. 2020), was used to reduce the data. By incorporating standard techniques, each exposure was bias-subtracted and flat-fielded. The wavelength solution is achieved by comparing the sky spectrum to the conspicuous OH and water lines[3] (Rousselot et al. 2000). Following the removal of cosmic rays contamination, the pipeline effectively subtracts the background by modeling the sky emission using a b-spline function that follows the curvature of the spectrum on the detector. The one-dimensional spectrum of the quasar is then generated for each exposure using optimum weighting (Kelson 2003). Stars with the spectral type of A are observed before and after the target exposures to calibrate the relative flux. We subsequently utilized `Molecfit`[4] (Kausch et al. 2015; Smette et al. 2015) to correct the telluric absorption. For absolute flux calibration, all one-dimensional spectra were co-added and scaled to the measured UHS J-band photometry ($J_{\rm UHS} = 20.09 \pm 0.13$, uncorrected for Galactic extinction). The reddening caused by Galactic extinction is then corrected using the dust map from Green et al. (2019) and extinction relation from Gordon et al. (2016). The final spectrum is displayed in 7.1. Unless otherwise specified, we will now utilize the GNIRS over the FIRE as the primary spectrum for the remainder analysis.

7.3 Modeling the Continuum and Line Emissions

A multi-component fitting strategy is employed to model the PSO J083+11 spectrum. The entire continuum is modeled using a combination of power-law and ultraviolet Fe II templates (Vestergaard & Wilkes 2001; Tsuzuki et al. 2006; Salviander et al. 2007). The free parameters are the normalization factor for each Fe II group and the slope of the power-law continuum.

[2]For documentation, visit https://pypeit.readthedocs.io/en/latest/.
[3]The database is accessible through https://hitran.org.
[4]The software is stored at https://www.eso.org/sci/software/pipelines/skytools/molecfit.

We use a customized PyQSOFit[5] version, a software to model Type 1 quasar spectra (Guo et al. 2018). We enhance the performance of PyQSOFit in handling high-z quasar spectra better by improving the fit of the broad and narrow emission lines, replacing the continuum windows, and making other minor changes. We establish the continuous window for the fit by repeatedly identifying emission- and telluric-line-free areas. The following wavelengths are chosen as the continuum windows: $\lambda_{\rm rest}$ = 1285–1290 Å, 1315–1325 Å, 1350–1370 Å, 1445–1465 Å, 1580–1650 Å, 2140–2300 Å, 2340–2400 Å, 2420–2480 Å, 2630–2710 Å, 2745–2765 Å, and 2850–3000 Å.

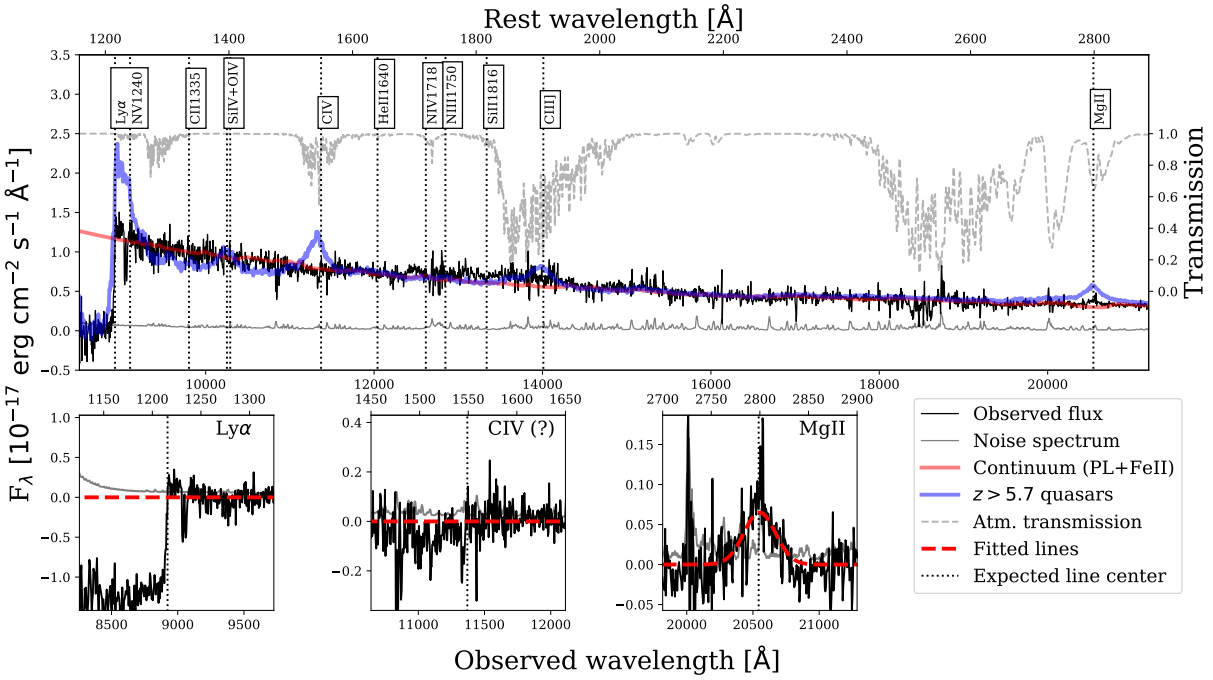

Figure 7.1. *Upper panel*: Gemini/GNIRS spectrum of PSO J083+11. The measured flux (black), noise (gray), normalized atmospheric transmission (dashed gray, unit in the right axis), and power-law continuum plus Fe II emissions (red) are displayed. The anticipated emission line centers are represented by black vertical dotted lines. In parallel, the median spectrum of $z \gtrsim 5.7$ quasars from Shen et al. (2019) is displayed in blue. The Shen et al. composite spectrum is adjusted by using the median of the PSO J083+11's continuum flux at $\lambda_{\rm rest}$ = 1300–2000 Å so that those two spectra have similar flux levels. *Lower panel*: Spectrum after subtracting the continuum surrounding the major emission lines (black) and the best-fit Gaussian models (dashed red). Produced by inadequate telluric correction, the sharp emission near Mg II is not genuine. We also find metal absorptions near the Lyα emission, at $\lambda_{\rm obs}$ = 9037 Å and 9066 Å.

The best-fit power-law continuum is used to determine the rest-frame 1450 Å absolute magnitude and the 3000 Å monochromatic luminosity – i.e., M_{1450} and L_λ(3000 Å). Subsequently, the bolometric luminosity $L_{\rm bol}$ is calculated using the empirical calibration derived by Richards et al. (2006), namely:

$$L_{\rm bol} = 5.15 \times \lambda L_{3000}. \tag{7.1}$$

Each emission from the broad lines is modeled using the Gaussian function after removing

[5]Available at https://github.com/legolason/PyQSOFit.

the fitted continuum and scaled iron templates. We compute the rest-frame equivalent width (REW), center wavelength, FWHM, and velocity dispersion for each line. To assess the errors in the calculated parameters, we employ a Monte Carlo approach and construct the mock spectra. In principle, the noise vector is utilized to create random flux errors with a normal distribution and subsequently is applied to the original spectrum 1000 times. In the end, we adopt the 16th and 84th percentiles of the measurement distributions as the lower and upper limit errors.

Parameter	Value	Unit
α_λ	$-1.66^{+0.01}_{-0.04}$	
M_{1450}	-26.67 ± 0.01	mag
$M_{\rm BH}$	$\left(2.00^{+0.74}_{-0.44}\right) \times 10^9$	$M_\odot$
$L_{\rm bol}$	$\left(1.33^{+0.01}_{-0.03}\right) \times 10^{47}$	erg s^{-1}
$L_{\rm bol}/L_{\rm Edd}$	$0.51^{+0.13}_{-0.17}$	
FWHM (Mg II)	4140^{+880}_{-430}	km s^{-1}
Δv (Mg II − C II)	237 ± 150	km s^{-1}
REW (Mg II)	$8.71^{+0.67}_{-0.64}$	Å
REW (Lyα + N V)	$5.65^{+0.72}_{-0.66}$	Å
REW (C IV)	≤ 5.83	Å
$R_{\rm p}$	1.17 ± 0.32	pMpc
$t_{\rm Q}$	$10^{3.4 \pm 0.7}$	yr
$z_{\rm [C\,II]}$	6.3401 ± 0.0004	
FWHM (C II)	229 ± 5	km s^{-1}
Flux (C II)	10.22 ± 0.35	Jy km s^{-1}
$S_{244\,\rm GHz}$	5.10 ± 0.15	mJy
$S_{258\,\rm GHz}$	5.54 ± 0.16	mJy
$L_{\rm [C\,II]}$	$(1.04 \pm 0.04) \times 10^{10}$	$L_\odot$
$L_{\rm FIR}$	$(1.22 \pm 0.07) \times 10^{13}$	$L_\odot$
$L_{\rm TIR}$	$(1.72 \pm 0.09) \times 10^{13}$	$L_\odot$
SFR$_{\rm [C\,II]}$	$800 - 4900$	$M_\odot$ yr^{-1}
SFR$_{\rm TIR}$	$900 - 7600$	$M_\odot$ yr^{-1}
$M_{\rm dust}$	$(4.88 \pm 0.14) \times 10^8$	$M_\odot$

Table 7.1. Calculated physical characteristics of PSO J083+11. The Δv (Mg II − C II) shows velocity shift of Mg II is computed with respect to C II. The derived REW (C IV) is the 3σ upper limit value.

However, as seen in Figure 7.1, the only significantly detected broad line is Mg II, for which we discover FWHM (Mg II) = 4140^{+880}_{-430} km s^{-1} and REW (Mg II) = $8.71^{+0.67}_{-0.64}$ Å. Furthermore, we estimate the redshift of $z_{\rm Mg\,II} = 6.346 \pm 0.001$ using the measured Mg II central wavelength. The Lyα signal is feeble, and we cannot identify the C IV line. Assuming that C IV has an FWHM similar to or larger than Mg II, we do not detect any possible broad absorption line signatures in the region where C IV is predicted to be present (see bottom panel of Figure 7.1). As a result, we infer that the lack of C IV is not just due to the broad absorption line phenomena, but rather

to the true nature of this quasar.

We employ Diamond-Stanic et al. (2009) prescription to compute the REWS of Lyα + N V, where the fluxes above the power-law continuum in 1160–1290 Å range is integrated. Consequently, we obtain REW (Lyα + N V) = $5.65^{+0.72}_{-0.66}$ Å. Note that, this region is dominated by Lyα λ1216 plus N V λ1240 emissions, with a little contribution from Si III λ1263 line. In addition, we use the same approach to estimate the 3σ upper limit of the C IV λ1549 REW, which we found to be REW (C IV) $\leq$ 5.83 Å for the wavelengths of 1500–1600 Å. According to Diamond-Stanic et al. empirical definition, we could categorize PSO J083+11 as a weak-line quasar. Figure 7.2 compares the C IV REWs of Type 1 quasars in general and WLQs as a function of continuum luminosity. Although WLQs were first described as quasars with REW (C IV) $\lesssim$ 10 Å and discovered at low redshifts, this definition is still applicable even for high-z quasars. Shen et al. (2019) shown that there is no substantial redshift evolution of C IV REWs for up to $z \sim 6$.

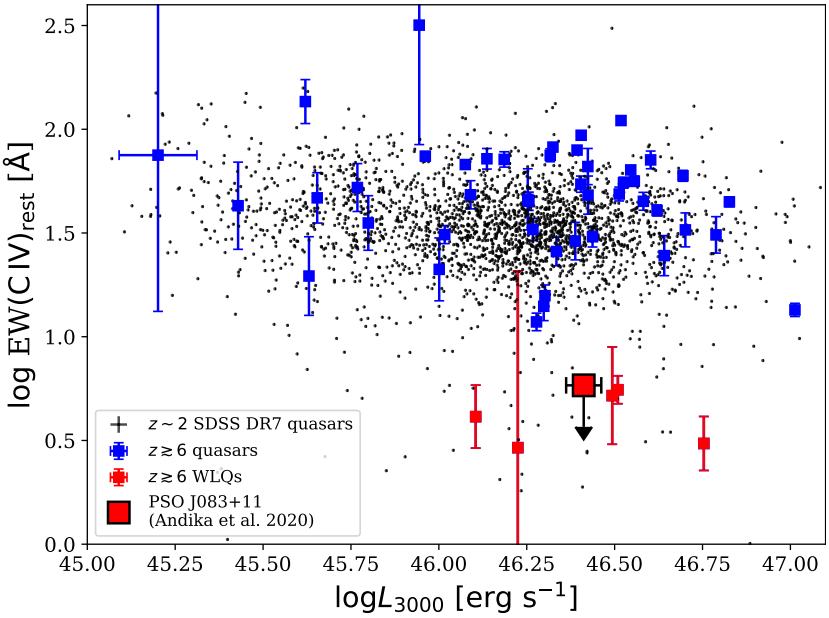

Figure 7.2. Rest-frame C IV equivalent width versus the continuum luminosity at 3000 Å. The black dots represent a sample of $z \sim 2$ quasars from Shen et al. (2011). A sample of $z \gtrsim 5.7$ Type 1 quasars (blue squares) and WLQs (red squares) from Shen et al. (2019) are also presented. PSO J083+11 belongs to the 3σ outliers at the lower end of this distribution.

7.4 Black Hole Mass and Eddington Ratio Estimates

Single-epoch near-infrared spectrum will be used for calculating PSO J083+11's black hole mass. Hence, we utilize the scaling relation for the Mg II line from Vestergaard & Osmer (2009) with the premise that the virial theorem is applicable for the broad-line region dynamics:

$$\frac{M_{\rm BH}}{M_\odot} = 10^{6.86} \left(\frac{\rm FWHM\ (Mg\,II)}{10^3\ \rm km\ s^{-1}} \right)^2 \left(\frac{\lambda L_\lambda (3000\ \text{Å})}{10^{44}\ \rm erg\ s^{-1}} \right)^{0.5}, \tag{7.2}$$

where FWHM (Mg II) is the full width at half maximum of Mg II and λL_λ(3000 Å) is the luminosity at 3000 Å rest-frame wavelength. Subsequently, we estimate the Eddington luminosity

using the formula of:

$$L_{\rm Edd} = 1.3 \times 10^{38} \left(\frac{M_{\rm BH}}{M_\odot} \right) \ {\rm erg\ s^{-1}}. \tag{7.3}$$

The Eddington ratio can thus be calculated as $L_{\rm bol}/L_{\rm Edd}$. For the GNIRS spectrum, we calculate a black hole mass of $\log(M_{\rm BH}/M_\odot) = 9.30^{+0.16}_{-0.10}$ and a normalized accretion rate of $L_{\rm bol}/L_{\rm Edd} = 0.51^{+0.13}_{-0.17}$. In parallel to that, we compute $\log(M_{\rm BH}/M_\odot) = 9.06^{+0.24}_{-0.16}$ and $L_{\rm bol}/L_{\rm Edd} = 0.77^{+0.33}_{-0.33}$ from the FIRE spectrum. We also provide the uncertainties propagated from the errors of monochromatic luminosity and Mg II line width. Please keep in mind that we do not explicitly include the associated systematic errors from the reverberation mapping, which are often larger ($\approx$ 0.5 dex) than the observed random errors (Vestergaard & Osmer 2009; Shen 2013).

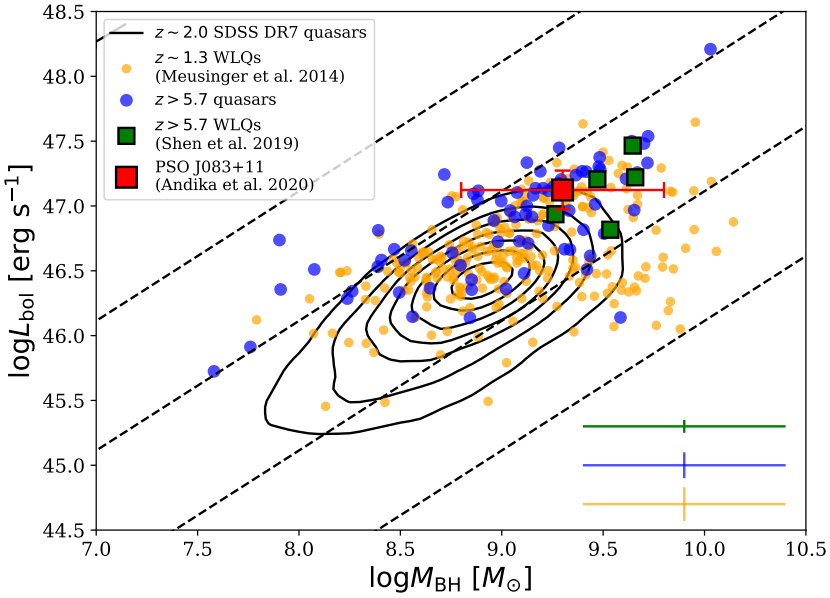

Figure 7.3. BH mass–bolometric luminosity relation of the quasars at various redshifts. These parameters are determined for a sample of $z \sim 1.3$ WLQs (magenta; Meusinger & Balafkan 2014), $z \gtrsim 5.7$ WLQs (green; Shen et al. 2019), and additional $z \gtrsim 5.7$ Type 1 quasars obtained from literature (blue; see text for details). The error bars account for the 0.5 dex systematic uncertainty associated with the Mg II-based BH mass estimate (Shen 2013) as well as measurement errors (red square with error bars). Contours display the location of $z \sim 2$ quasars (Shen et al. 2011). From top left to bottom right, the diagonal lines depict Eddington ratios of $L_{\rm bol}/L_{\rm Edd} = 10$, 1, 0.1, and 0.01. The corresponding typical uncertainties for each sample are presented as error bars in the bottom right.

We then compile Mg II line width and continuum luminosity values of $\sim$ 70 previously reported $z \gtrsim 5.7$ quasars for comparing PSO J083+11 characteristics to other similar sources at high redshifts (Jiang et al. 2007; Willott et al. 2010; De Rosa et al. 2011, 2014; Wu et al. 2015; Mazzucchelli et al. 2017; Eilers et al. 2018b; Tang et al. 2019; Fan et al. 2019a; Shen et al. 2019; Onoue et al. 2019). There, we find five high-z WLQs and subsequently add 261 more $z \sim 1.3$ WLQs taken from Meusinger & Balafkan (2014). We utilize their Mg II FWHMs and continuum luminosities to compute bolometric luminosities and virial masses. This is done by using the same cosmological assumption and scaling relation (see Equation 7.1 and 7.2) as those used for PSO J083+11. As a result, Figure 7.3 displays the distributions of the BH mass–bolometric

luminosity. PSO J083+11 occupies the same Eddington ratio and black hole mass parameter space as other quasars at $z \gtrsim 5.7$ and those seen at $z \sim 2$. Therefore, we conclude that our quasar is fueled by a common established and actively accreting SMBH, as observed in other quasars with comparable luminosities. Finally, we show the summary of the estimated physical parameters in Table 7.1.

7.5 Proximity Zone Size and Lifetime Measurements

According to Eilers et al. (2017), the lifespan of quasars can be deduced from the size of their proximity zones. The proximity zone is defined as the region of increased Lyα forest transmission near the quasar caused by its ionizing radiation. In this paradigm, the intergalactic medium will have a limited reaction time to achieve a new ionization equilibrium state as a result of the quasar's photoionization, with a timeframe of $t_{\rm eq} \approx \Gamma_{\rm HI}^{-1} \approx 3 \times 10^4$ yr. In this case, $\Gamma_{\rm HI}$ is the photoionization rate (Eilers et al. 2017).

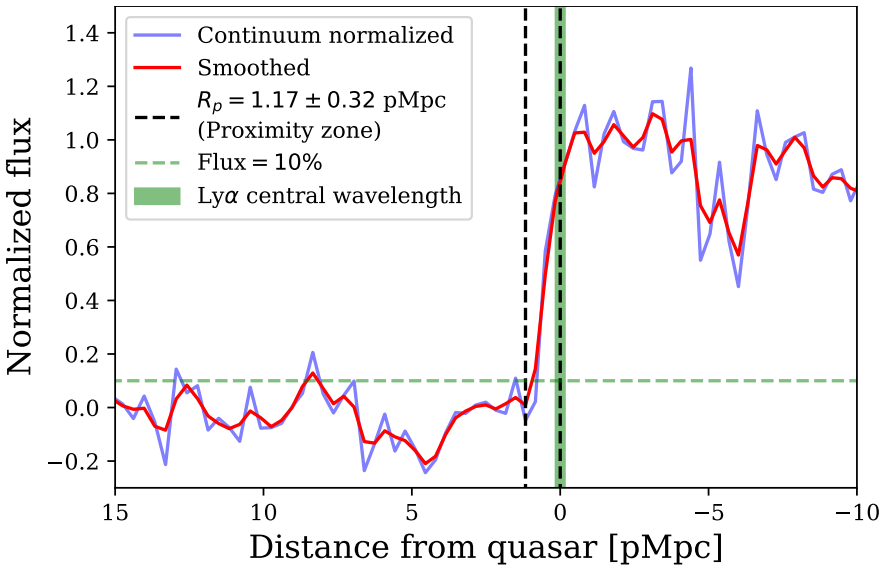

Figure 7.4. PSO J083+11's proximity zone measurement ($R_{\rm p}$). The size is indicated with the two black dashed lines. The Lyα expected location is marked with a green line. Smoothed and continuum normalized spectra are depicted as blue and red lines, respectively. Here, we see a relatively small proximity zone size of $R_{\rm p} = 1.17 \pm 0.32$ pMpc.

In practice, we first perform a continuum normalization to the quasar spectrum and convolve it using 20 Å resolution boxcar kernel. Subsequently, the proximity zone size is defined as the distance from the center of Lyα to blueward wavelengths, where the transmitted flux first decreases below 10% of the level at the line (Fan et al. 2006). We should note that this is done in the observed-frame wavelengths, and then Figure 7.4 zone depicts the outcome. The transformation of proximity zone size to quasar lifetime is thus derived using radiative transfer simulations (see e.g., Davies et al. 2016, for details), for a quasar with similar redshift and luminosity as PSO J083+11, as illustrated in Figure 7.5. We see a relatively small proximity zone ($R_{\rm p} = 1.17 \pm 0.32$ pMpc) in the spectrum, implying that PSO J083+11 has a quasar age of

just $t_{\rm Q} = 10^{3.4\pm0.7}$ yr. In comparison, the average sizes for sources with $-27.5 \lesssim M_{1450} \lesssim -26.5$ are $R_{\rm p} = 3 - 7$ pMpc, while their lifetimes are $t_{\rm Q} = 10^{5-6}$ yr (Eilers et al. 2017).

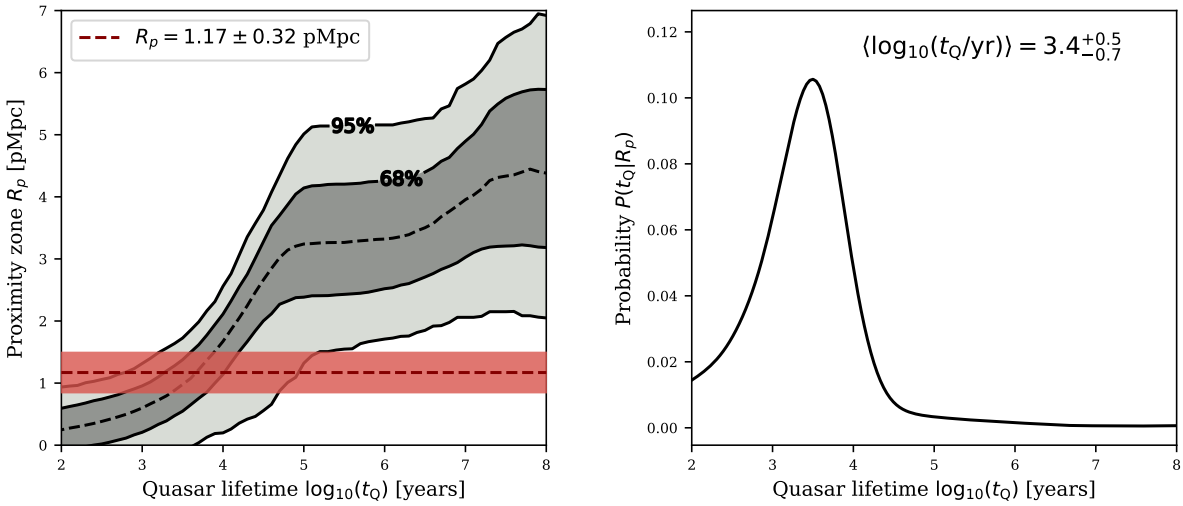

Figure 7.5. Quasar age ($t_{\rm Q}$) as a function of the proximity zone size ($R_{\rm p}$, see *left panel*). The calculation is performed for a source with a redshift ($z = 6.3401$) and an absolute magnitude ($M_{1450} = 26.67$) similar to PSO J083+11. The red lines mark the value of $R_p = 1.17 \pm 0.32$ pMpc. The $t_{\rm Q}$ probability distribution indicates that PSO J083+11 is a young quasar with a lifetime of only $t_{\rm Q} = 10^{3.4\pm0.7}$ yr (see right panel).

Chapter 8

Searching for a Lens Galaxy

The content of this chapter is based on the work originally published as ***Andika, I. T.****, Jahnke, K., Onoue, M., et al. (2020; ApJ 903: 34) and is adapted from the HST/WFC3–ACS proposal: 15707.*

It is widely known that gravitational lensing can significantly magnify quasar fluxes, leading to overestimation of the associated powering black hole masses. This process would affect our knowledge of the intrinsic characteristics of those high-z quasars. A substantial lensed fraction among bright high-z quasars has been anticipated for decades (e.g., Comerford et al. 2002; Wyithe & Loeb 2002b). Moreover, Pacucci & Loeb (2019) predicted that there would be several modestly magnified ($\mu \leq 10$) quasars at $z \gtrsim 6$ with small image separation ($\Delta\theta \lesssim 0\farcs2$). The first validation of this theory is the lensed quasar discovered by Fan et al. (2019a) – i.e., J043947.08+163415.7 at $z = 6.51$.

While our discovery images show no evident companion in the vicinity of PSO J083+11, the ground-based seeing prevents us from spotting possible lens configurations with small image separations. Accordingly, we then utilized the Hubble Space Telescope (HST) to put the lensing notion for this quasar to the test. We will discuss the results of our investigation in the following sections.

8.1 Near-infrared Imaging with HST

We obtained high-resolution images of PSO J083+11 using HST (GO 15707, PI: K. Jahnke). Our objective is to use two approaches to test the gravitational lensing hypothesis for PSO J083+11. The first one is conducted by looking for any potential multiple quasar images using the Wide Field Camera 3 (WFC3) equipped with the near-infrared F125W filter ($\lambda_{\rm eff} = 12,365$ Å). The second experiment is subsequently performed by searching for a foreground galaxy directly using the Advanced Camera for Surveys (ACS) equipped with the ramp-filter FR853N

($\lambda_{\rm eff}$ = 8528 Å) at the quasar Gunn-Peterson absorption trough region (Gunn & Peterson 1965) blueward of Lyα. At these short wavelengths, the quasar light will be heavily absorbed, maximizing the visibility of any nearby sources. Each camera was exposed for two orbits for a total integration time of ≈ 80 minutes per band. When performing imaging with WFC3/F125W, we rotated the field of view by ≈ 15 deg between exposures for conducting image differencing analysis and reducing the interference of instrumental point-source spikes inherent to the HST PSF. Note that the standard HST pipeline was used to process the data to generate clean images with a pixel scale of $0\farcs128$ pixel^{-1}. As a result, we obtain a 26 mag arcsec^{-2} in the final image for the 5σ surface brightness limit, calculated using a circular aperture with a radius of $1''$.

The next step is to examine the WFC3/F125W image and search for any possible extended emissions, which might be originating from an intervening lens galaxy, a companion source, or multiple components of PSO J083+11 itself. Here, we first use `Photutils`[1] code (Bradley et al. 2019) to eliminate the contaminating point-source emission from the central quasar. The PSF is then modeled by median-averaging eight stars in the field around PSO J083+11. They are specifically selected to be sufficiently distant from the CCD's edge, bad pixels, or other contaminants. Also, these stars must be 1.5–15 times brighter than PSO J083+11 to produce a precise PSF wings model. It should be noted that we do not account for the influence of the spectral types of the selected reference stars. Therefore, there may be color-dependent uncertainties owing to systematic SED discrepancies. Nonetheless, the model is then fitted to the central quasar emission in the image, allowing the PSF centroid to change by less than a pixel. As a result, Figure 8.1 presents the observed image and PSF subtraction residual.

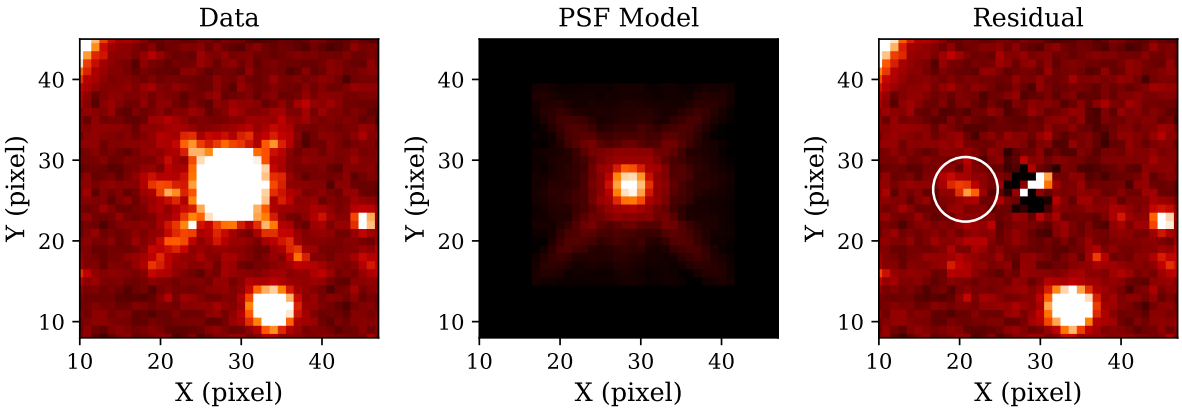

Figure 8.1. PSO J083+11 imaging with the HST WFC3/F125W. The measured quasar emission (*left*), PSF model (*middle*), and PSF-subtracted images (*right*) are displayed. The scale of each image is $0\farcs128$ pixel^{-1}. The white circle in the right panel represents the aperture utilized to compute the photometry of a (possible) foreground galaxy, situated at ≈ $1''$ from the quasar in the center. We employ a 4-pixel aperture radius (corresponds to ≈ $0\farcs5$) to obtain a magnitude of 25.42 ± 0.07 in the F125W band.

[1]Accessible through https://photutils.readthedocs.io/en/stable/.

8.2 Modeling a Possible Lensing Effect

We discover an extended emission in the WFC3/F125W residual images that might be attributable to a foreground galaxy with a putative gravitational lensing effect, positioned at 1″ to the southwest of PSO J083+11. However, we could not determine the redshift of this galaxy solely by using the HST data. The corresponding AB magnitude is then calculated using aperture photometry, employing a radius of 4 pixels (≈ 0.″5), which results in an F125W magnitude value of 25.42 ± 0.07. However, this emission is not visible in the ACS/FR853N image. Nonetheless, we perform photometry utilizing a similar aperture size and constrain a 5σ upper limit FR853N magnitude of ≤ 23.25.

By simulating the galaxy's spectrum from far-ultraviolet to microwave regimes utilizing `Bagpipes` (Carnall et al. 2018) software, we want to explore whether the intervening source may potentially magnify the apparent PSO J083+11's emission. As input data, we use the observed fluxes from WFC3/F125W image, together with upper limit measurements from the ACS/FR853N and PS1 bands. We then presume that the foreground emission detected in the F125W image originates from a star-forming main sequence galaxy. To calculate the associate stellar mass and SFR, we must fit the observed galaxy SED with `Bagpipes` model assuming a specific SFH parameter.

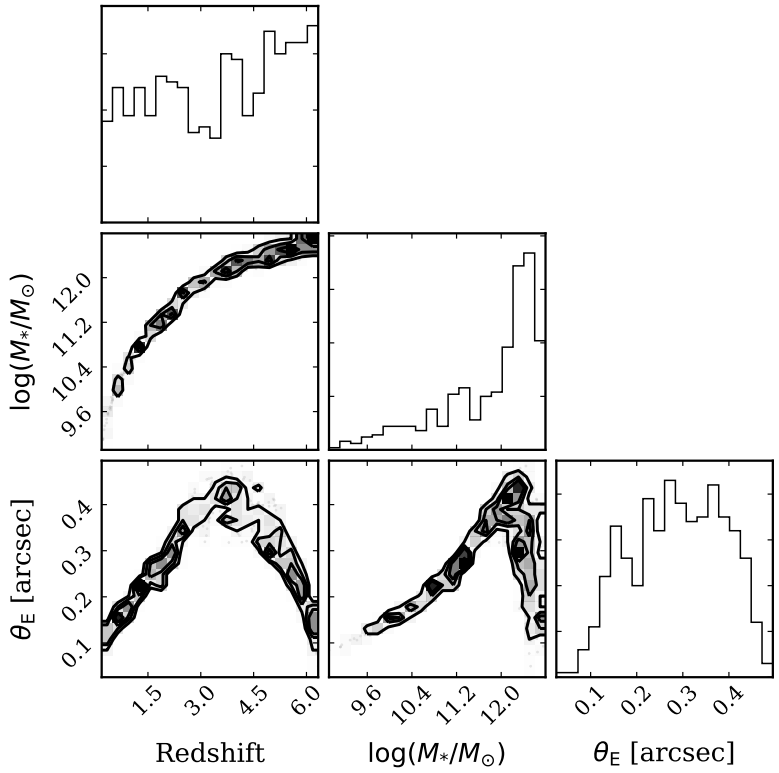

Figure 8.2. A corner plot displaying estimated Einstein radii as a function of the galaxy masses and redshifts.

The most basic and extensively utilized parametric SFH model is exponentially declining or τ-model. However, we choose the delayed exponentially declining SFH model instead for this study – i.e., the τ-model multiplied by the period since star formation began (T_0). This model eliminates both the SFR discontinuity at T_0 and the increasing SFH if the SFR timescale τ is large (see, e.g., Carnall et al. 2018). With uniform priors of $M_{\text{formed}} = 10^{1-15}\ M_\odot$ and $T_0 = 0.5$–0.8 Gyr, our model will fit the total stellar mass formed and period since star formation began, respectively. We use constant values for the SFR timescale ($\tau = 0.3$ Gyr), metallicity ($Z = 0.02$; equivalent to solar metallicity), and nebular ionization parameter ($\log(U) = -3$). Furthermore, following the Calzetti et al. (2000) extinction law, a value of $A_V = 1$ mag is also applied.

The core output computed by `Bagpipes` is the total stellar mass of the galaxy, which also depends on its redshift and subsequently will be used to estimate the putative lensing magnifications experienced by PSO J083+11. The dark matter contribution is then incorporated to compute the maximum total lens mass by assuming a typical mass-to-light ratio upper limit of 100 for elliptical and disk galaxies. Then, assuming a lensing event caused by a point mass (see Section 3.1.1), various combinations of Einstein radius θ_{E} and magnification μ can be inferred (for review, see e.g., Schneider 2015). Consequently, we discover the limits of $\theta_{\text{E}} \leq 0\farcs5$ and $\mu \leq 1.07$, and therefore, the strong lensing magnification of the PSO J083+11's emission by the foreground galaxy is ruled out. Finally, Figure 8.2 shows the predicted Einstein radii as a function of modeled galaxy redshifts and masses.

Chapter 9

Probing the Quasar Host Galaxy

The content of this chapter is based on the work originally published as ***Andika, I. T.****, Jahnke, K., Onoue, M., et al. (2020; ApJ 903: 34) and is adapted from the ALMA proposal: 2019.1.01436.S and the IRAM/NOEMA proposal: S21DI.*

9.1 Submillimeter Observation with ALMA

The ALMA band-6 observations (2019.1.01436.S, PI: I.T. Andika) were carried out on October 9, 2019, to estimate the precise redshift of PSO J083+11 and probe the [C II] 158 μm emission originating from its host galaxy. Subsequently, we utilized ALMA C43-4 array configuration and applied a total on-source time of 3145 s. Then, the receivers are programmed to accommodate $\sim$ 258 GHz, or equivalent the predicted [C II] frequency at the Mg II-based redshift of PSO J083+11, that is $z_{\rm Mg\,II} \approx 6.34$.

For data calibration purposes, we use standard procedure implemented in Common Astronomy Software Application[1] (CASA; McMullin et al. 2007). Following that, TCLEAN task is used with natural weighting to image the visibilities while optimizing the point-source sensitivity. Here, we limit the area of interest to the radius of 5″ in the vicinity of PSO J083+11 and clean it down to 2σ. Next, we masked away channels containing the emission line and fit the continuum with a simple median approximation. After that, we generate continuum-free data by removing the modeled continuum from the visibilities. The final imaged datacubes have 30 MHz channel width, $0\farcs42 \times 0\farcs37$ synthetized beam, and 0.24 mJy beam^{-1} root-mean-square (RMS) noise level.

[1] See the documentation at https://casa.nrao.edu/.

9.2 Spectral Profile of the [C II] Line

To maximize recoverable emission, the [C II] spectrum is extracted with 1.″5 (≈ 8.3 kpc) circular aperture radius. We select this particular size since there is no apparent [C II] beyond this radius. Note that the problem of ill-defined units makes flux calculation in the interferometric maps difficult (for further information, see Novak et al. 2019). To tackle this issue, we first define the aperture flux calculated inside the dirty image as D, the clean component as C, and the residual image as R. The correction scaling factor is thus $\epsilon = C/(D - R)$. The clean and dirty beam sizes are the most critical elements governing the scaling factor ϵ. In our situation, $\epsilon = 0.6$. The dirty image flux is then multiplied by ϵ to obtain the final flux density in an appropriate unit. It is worth noting that if we simply use the final image to calculate the flux, we would get ≈ 10% overestimation. This overestimation occurs because the final image is a superposition of the clean Gaussian components appended by residuals.

The extracted spectrum is given in Figure 9.1, and a Gaussian fit yields total [C II] line flux of 10.22 ± 0.35 Jy km s^{-1}, FWHM of 229 ± 5 km s^{-1}, and redshift of 6.3401 ± 0.0004. The Mg II line (quasar broad-line region tracer) is redshifted by 237 ± 150 km s^{-1} with respect to the [C II] line (host galaxy tracer). In comparison, Schindler et al. (2020) discovered that Mg II in high-z quasars can be strongly shifted relative to [C II], with a median velocity shift of -416^{+304}_{-398} km s^{-1}. The Mg II emission, which emerges from the broad-line region, may suffer severe internal movements or winds, potentially shifting the line centers from the systemic redshift (Mazzucchelli et al. 2017; Meyer et al. 2019).

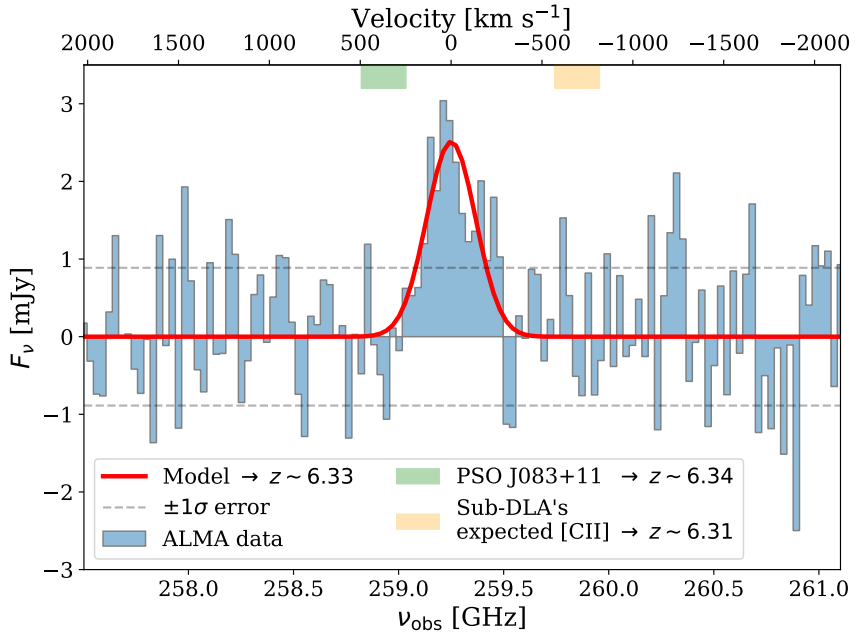

Figure 9.1. Continuum-subtracted [C II] spectrum of PSO J083+11 extracted using a circular aperture with a radius of 1.″5. Observed fluxes (black) are modeled with a Gaussian profile (red) to characterize the line emission. The velocities centered at $z = 6.3401$ are shown in the upper axis.

9.3 Momen Maps for the [C II] and Dust Continuum Emissions

We observe two spectral windows of dust emissions – i.e., 244 and 258 GHz. Pure continuum datacubes are then generated by choosing frequencies that are devoid of line emissions, with an effective bandwidth set to around 2500 km s^{-1}. Then, we collapse these line-free spectral channels to construct the zeroth-moment map of the dust continua. The resultant 244 and 258 GHz maps have RMS noise levels of 30.7 and 35.8 μJy beam^{-1}, respectively. As an illustration, the dust continuum centered at 258 GHz is shown in Figure 9.2. We obtain flux densities of $S_{244\,\mathrm{GHz}} = 5.10 \pm 0.15$ mJy and $S_{258\,\mathrm{GHz}} = 5.54 \pm 0.16$ mJy by applying the similar circular aperture photometry as for [C II] – i.e., a radius of 1.″5. The [C II] zeroth-moment map is then also generated by collapsing the 700 km s^{-1} cube width, as seen in Figure 9.2. Note that this width corresponds to three times the [C II] FWHM.

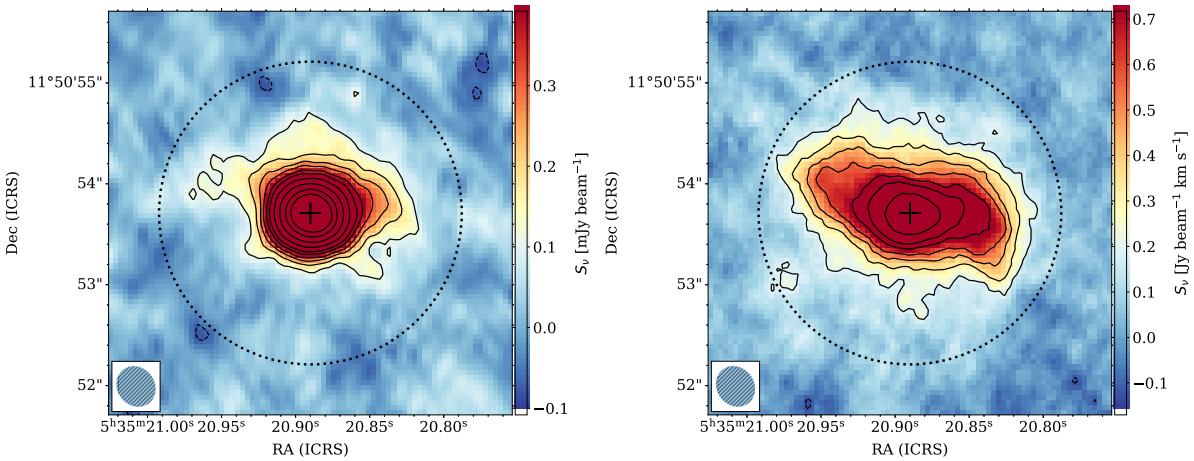

Figure 9.2. ALMA dust (*left panel*) and velocity-integrated [C II] observations (*right panel*) of PSO J083+11. The synthesized beam size is displayed at the bottom left. The solid lines in the left panel depict the $[3, 5, 7, 9, 12, 15, 21, 30, 42, 54] \times \sigma$ contours with $\sigma = 0.04$ mJy beam^{-1} of the continuum flux density, while the solid lines in the right panel represent the $\sigma = 0.06$ Jy beam^{-1} km s^{-1} of the [C II] velocity-integrated flux. Negative contours are presented with dashed lines. The dotted circles show the 1.″5 ($\approx$ 8.3 kpc) aperture size utilized to compute total flux density. A black cross marks the location of the central quasar.

Both continuum and [C II] emission are spatially resolved, as presented in Figure 9.2, with the estimated sizes of 2.3 kpc × 1.7 kpc and 8.2 kpc × 4.3 kpc, respectively. These dimensions are defined as the major and minor axis FWHMs of the two-dimensional Gaussian profile fitted to the emissions. Furthermore, the peak of continuum emission coincides with the center of the [C II]. The velocity field and dispersion maps[2] of the continuum subtracted [C II] emission are shown in Figure 9.3. There is a modest velocity gradient, where the northern region is redshifted, and the southern part is blueshifted. The associated morphology is depicted in Figure 9.2 as a single resolved blob, although the integrated spectrum (Figure 9.1) is nicely represented by a simple Gaussian profile.

[2]See the moment map equations, the sigma linewidth map definition, and the detailed implementation of the model at https://spectral-cube.readthedocs.io/en/latest/moments.html.

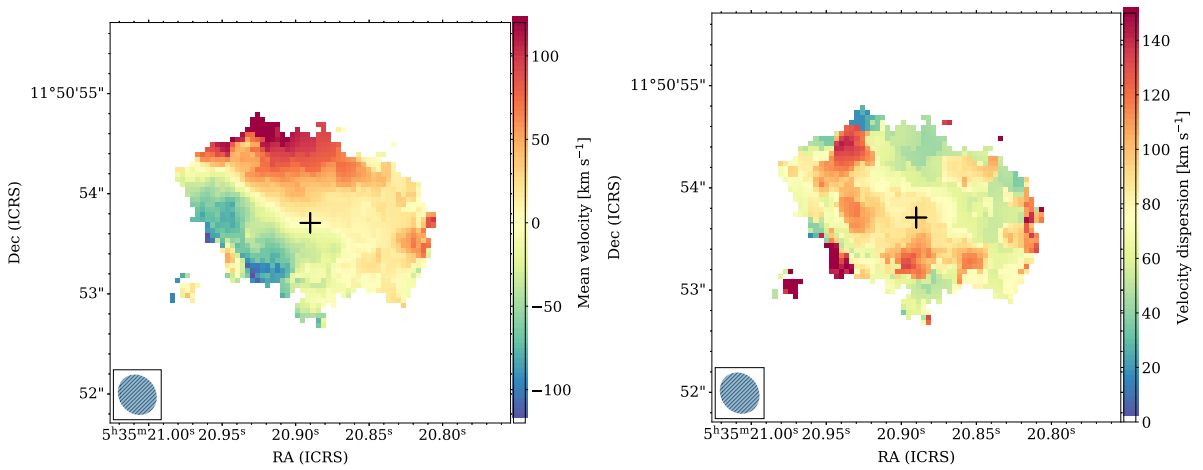

Figure 9.3. The PSO J083+11's [C II] intensity-weighted velocity (*left panel*) and velocity dispersion (*right panel*) maps. Pixels with flux values of $< 3\sigma$ above the background in the zeroth-moment map of [C II] are excluded. The central quasar's location is denoted with a black cross, while the synthesized beam is displayed in the bottom left.

Finally, as shown in Figure 9.4, we superimpose the ALMA data over the PSF-subtracted HST image. Previously, we discovered a probable lens galaxy or putative companion, as seen in Figure 8.1. However, there is no visible dust or [C II] emission at the location of this source of interest (see Figure 9.4), indicating that it is not physically connected with PSO J083+11.

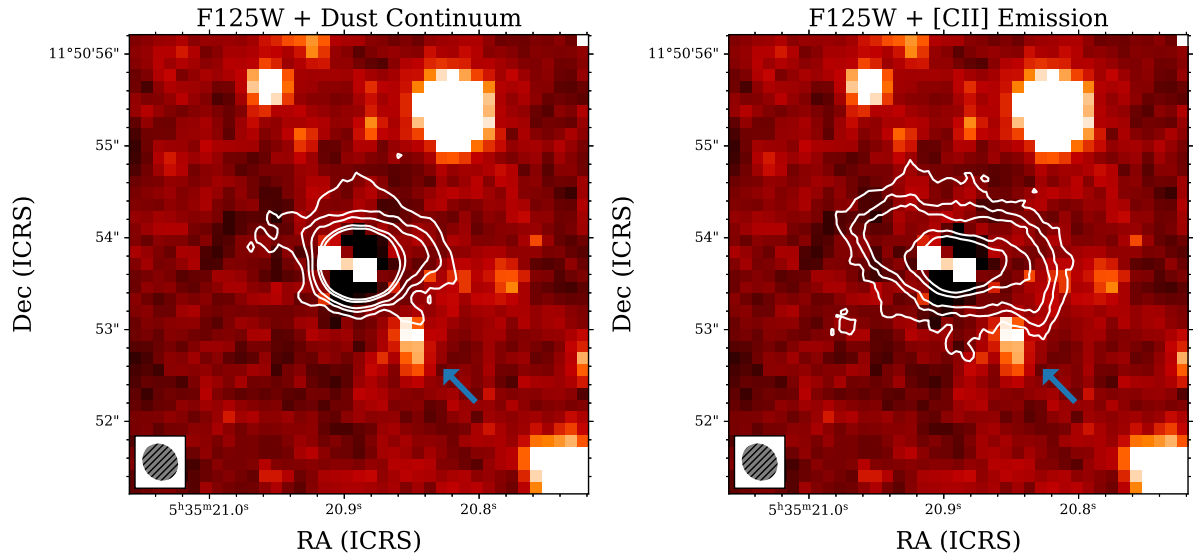

Figure 9.4. The PSO J083+11's PSF-subtracted HST image with a superimpose of ALMA dust and [C II] emissions as contours (from Figure 9.2). The solid lines colored in white in the *left panel* depict the $[3, 5, 7, 12, 15] \times \sigma$ contours with $\sigma = 0.04$ mJy beam^{-1} for continuum, while the *right panel* displays $\sigma = 0.06$ Jy beam^{-1} km s^{-1} for the [C II] emission maps. The PSF-subtracted HST image has been rotated so that the North is up and the East is left. The ALMA synthesized beam is given in the bottom left. The putative companion is located southwest of the quasar (blue arrow). However, there is no visible [C II] or dust emission at this location, indicating that it is not a physically connected companion.

9.4 Star Formation Rate Calculations

To determine the star formation rate of PSO J083+11's host galaxy, we first compute the [C II] 158 μm line luminosity from the associated integrated flux $S_{\text{line}}\,\Delta v$ and distance D_L using the relation from Carilli & Walter (2013), namely:

$$\frac{L_{\text{line}}}{L_\odot} = 1.04 \times 10^{-3} \frac{S_{\text{line}}\,\Delta v}{\text{Jy km s}^{-1}} \left(\frac{D_L}{\text{Mpc}}\right)^2 \frac{\nu_{\text{obs}}}{\text{GHz}}. \tag{9.1}$$

This results in a luminosity of $L_{[\text{C II}]} = (1.04 \pm 0.04) \times 10^{10}\ L_\odot$, which subsequently put PSO J083+11 as one of the brightest $z \gtrsim 6$ [C II] emitter known to date (Decarli et al. 2018; Venemans et al. 2018). After that, we calculate the corresponding SFR by employing the SFR-$L_{[\text{C II}]}$ scaling relation from De Looze et al. (2014) for galaxies at $z \gtrsim 5$, that is:

$$\frac{\text{SFR}_{[\text{C II}]}}{M_\odot\ \text{yr}^{-1}} = 3.0 \times 10^{-9} \left(\frac{L_{[\text{C II}]}}{L_\odot}\right)^{1.18}. \tag{9.2}$$

This practically results in the value of $\text{SFR}_{[\text{C II}]} \approx 1990\ M_\odot\ \text{yr}^{-1}$. However, one must account for a factor of ≈ 2.5 for systematic uncertainty from the scaling relation, which extends the feasible range of the estimation to $\text{SFR}_{[\text{C II}]} = 800\text{–}4900\ M_\odot\ \text{yr}^{-1}$.

Additional key measurements that can be inferred using ALMA data are total infrared luminosity (L_{TIR}, rest-frame 3–1100 μm), far-infrared luminosity (L_{FIR}, rest-frame 42.5–122.5 μm), and dust mass, from which we can compute an independent SFR (e.g., Helou et al. 1988; Kennicutt & Evans 2012; Carilli & Walter 2013). This estimate can be accomplished by presuming low dust optical depth in the Rayleigh–Jean wavelengths, in which case fitting the SED with a modified blackbody will suffice (e.g., Beelen et al. 2006; Novak et al. 2019). The expression is:

$$S_{\nu_{\text{obs}}} = f_{\text{CMB}}\,(1+z)\,(D_L)^{-2}\,\kappa_{\nu_{\text{rest}}}\,M_{\text{dust}}\,B_{\nu_{\text{rest}}}\,(T_{\text{dust},z}), \tag{9.3}$$

where D_L is the luminosity distance, M_{dust} is the dust mass, $B_{\nu_{\text{rest}}}$ is the blackbody radiation function, with the rest and observed frequencies are linked as $\nu_{\text{rest}} = (1+z)\nu_{\text{obs}}$, and all measurements are in SI units. Following Dunne et al. (2003) and Novak et al. (2019), the chosen opacity coefficient is:

$$\kappa_{\nu_{\text{rest}}} = \kappa_{\nu_0} \left(\frac{\nu_{\text{rest}}}{\nu_0}\right)^\beta = 2.64 \left(\frac{\nu_{\text{rest}}}{c/125\ \mu\text{m}}\right)^\beta\ \text{m}^2\ \text{kg}^{-1} \tag{9.4}$$

where speed of light and dust spectral emissivity index are respectively c and β. Because of the utilized opacity coefficient scaling relation, the computed dust mass will have a systematic uncertainty of at least a factor of two.

Dust heating by the cosmic microwave background (CMB) is incredibly relevant at $z \gtrsim 6$ and must be taken into account after (da Cunha et al. 2013), which is often expressed as:

$$f_{\text{CMB}} = 1 - \frac{B_{\nu_{\text{rest}}}(T_{\text{CMB},z})}{B_{\nu_{\text{rest}}}(T_{\text{dust},z})} \tag{9.5}$$

$$T_{\mathrm{dust},z} = \left(T_{\mathrm{dust}}^{\beta+4} + T_{\mathrm{CMB,z=0}}^{\beta+4}\left[(1+z)^{\beta+4} - 1\right]\right)^{\frac{1}{\beta+4}}, \tag{9.6}$$

where the source's intrinsic dust temperature at redshift zero is T_{dust} and the CMB temperature at a specified redshift is $T_{\mathrm{CMB}} = 2.73(1+z)$ K. In our situation, we adopt $T_{\mathrm{CMB}} = 20.04$ K.

It is worth noting that we only have two data points for the continuum observations – i.e., 244 and 258 GHz – both of which are placed on the Rayleigh-Jeans tail and do not cover the peak of the dust SED. Due to degraded fitting parameters, we then could not constrain the whole SED form and dust temperature. Consequently, we have to adopt the assumptions of $T_{\mathrm{dust}} = 47$ K and $\beta = 1.6$, which is often utilized for $z \gtrsim 6$ quasar hosts (Beelen et al. 2006; Venemans et al. 2018; Decarli et al. 2018). Normalizing the SED model (Equation 9.3) to the observed PSO J083+11's FIR photometric data at 244 and 258 GHz yields $M_{\mathrm{dust}} = (4.88 \pm 0.14) \times 10^8\ M_\odot$. Subsequently, integrating the fitted SED results in $L_{\mathrm{FIR}} = (1.22 \pm 0.07) \times 10^{13}\ L_\odot$ and $L_{\mathrm{TIR}} = (1.72 \pm 0.09) \times 10^{13}\ L_\odot$. Because of its extreme luminosity, PSO J083+11 is categorized as a hyper-luminous infrared galaxy (HyLIRG, $L_{\mathrm{TIR}} > 10^{13}\ L_\odot$).

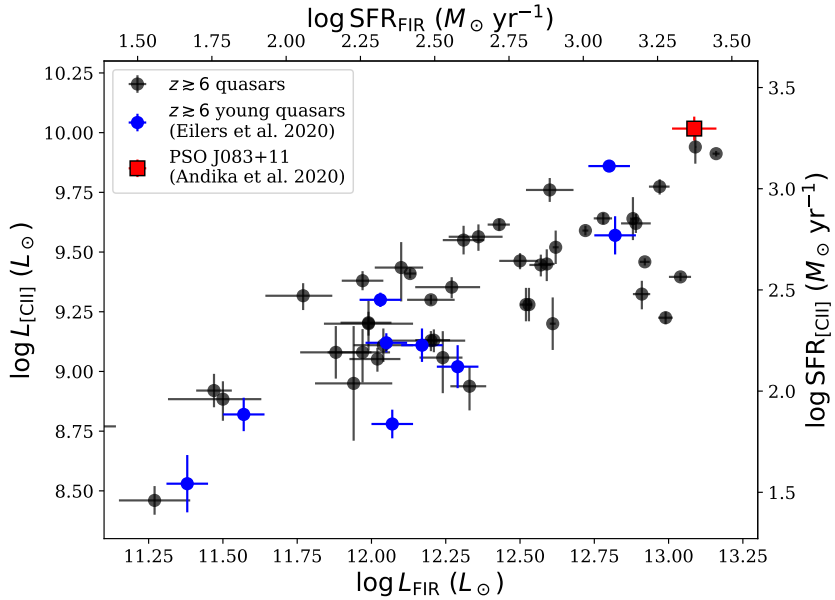

Figure 9.5. Comparison of the star formation rates calculated using the dust emission (following Murphy et al. 2011 and Kennicutt & Evans 2012) and the [C II] luminosity (following De Looze et al. 2014), assuming $T_{\mathrm{dust}} = 47$ K. A subset of $z \gtrsim 6$ quasars from literature (black dots, see text) and young quasars (blue dots, Eilers et al. 2020) are displayed. PSO J083+11 (red square) has [C II] and FIR luminosities equivalent to those seen in high-z quasars, with the highest SFR and FIR emission. For clarity, the PSO J083+11's error bars have been multiplied by a factor of three.

An independent SFR estimate can be inferred from the TIR luminosity, using the relation from Murphy et al. (2011) and Kennicutt & Evans (2012), that is:

$$\mathrm{SFR}_{\mathrm{TIR}}\ [M_\odot\ \mathrm{yr}^{-1}] = 1.49 \times 10^{-10} L_{\mathrm{TIR}}\ [L_\odot]. \tag{9.7}$$

This subsequently results in $\mathrm{SFR}_{\mathrm{TIR}} \approx 2560\ M_\odot\ \mathrm{yr}^{-1}$. Furthermore, we find a 1σ possible range of $\mathrm{SFR}_{\mathrm{TIR}} = 900\text{–}7600\ M_\odot\ \mathrm{yr}^{-1}$ after accounting for the systematic uncertainty with a factor

of three in the scaling relation. Note that this result agrees with our previous calculation of [C II]-based SFR. Finally, Table 7.1 contains a summary of the estimated parameters.

To compare the features of PSO J083+11 with those of other $z \gtrsim 6$ quasars, we exploit $L_{[\mathrm{C\,II}]}$ and L_{FIR} observations from the literature (Walter et al. 2009; Venemans et al. 2012; Wang et al. 2013; Willott et al. 2013; Bañados et al. 2015a; Willott et al. 2015; Wang et al. 2016; Venemans et al. 2016; Mazzucchelli et al. 2017; Willott et al. 2017; Decarli et al. 2018) which are then recomputed by Decarli et al. (2018). We also include ten young quasars observed by Eilers et al. (2020). As shown in Figure 9.5, PSO J083+11 has the $L_{[\mathrm{C\,II}]}$ and L_{FIR} values comparable to those high-z quasars with the highest SFR and FIR emission.

Chapter 10

Discussion on the Notion of Young Weak-Line Quasar

The content of this chapter is based on the work originally published as ***Andika, I. T.****, Jahnke, K., Onoue, M., et al. (2020; ApJ 903: 34).*

Type 1 quasars tend to have intense broad-line emissions in the optical to ultraviolet rest-frame wavelengths. However, this is not true for WLQs, which exhibit abnormally faint or non-existent broad lines. Note that WLQs are not Blazar or BL Lacertae objects, which typically show a featureless continuum dominated by non-thermal emission (Diamond-Stanic et al. 2009). This phenomenon is a consequence of their relativistic jet aligned to the observer's sightline (Netzer 2013). On the other hand, most of WLQs are radio-quiet and have nothing to do with the broad absorption line phenomena (e.g., Kumar et al. 2018).

Diamond-Stanic et al. (2009) and Shemmer et al. (2006) established that WLQs are a rare, distinct population whose nature cannot be described by gravitational lensing. Our HST investigations of PSO J083+11 identified a putative lens galaxy located at 1″ from the central quasar. The highest possible magnification of $\mu \leq 1.07$, on the other hand, does not offer a noticeable increase to the apparent emission of the quasar continuum. Furthermore, we demonstrated that PSO J083+11's ultraviolet-optical (Figure 5.7) and far-infrared SED (Section 9.4) are comparable to those of Type 1 quasars in general, rather than a galaxy experiencing strong lensing. Consequently, the weak-line aspect of PSO J083+11 cannot be explained by the strong lensing phenomenon based on these findings. It is worth noting that further investigation for discovering the reappearance of the PSO J083+11's broad lines via spectroscopic monitoring is required to rule out microlensing completely. The characteristic timeframe for microlensing event for a star lens in a foreground galaxy is ≈ 10 yr (Gould 1995). Nonetheless, the nearest foreground galaxy observed in the HST image is already sufficiently far from the central quasar ($\theta > \theta_{\rm E}$, see Chapter 8), making the microlensing interpretation improbable.

Several ideas have been presented to address the WLQ phenomena. In general, they may be divided into two main groups (e.g., Plotkin et al. 2015), namely: (i) the soft ionizing continuum concept and (ii) the anemic broad emission line region paradigm. In the following sections, we will present and discuss the most probable scenarios that can explain the weak-line signature of PSO J083+11.

10.1 Soft Continuum and Super-Eddington Accretion

As a result of the soft ionizing continuum, one would anticipate the broad-line region to be less photoionized, resulting in weak broad emission lines. What made this possible? The first hypothesized mechanism is an inherently soft continuum caused by a cold accretion disk surrounding a massive black hole with a low accretion rate (Laor & Davis 2011; Plotkin et al. 2015). However, this likelihood is quite low in the context of PSO J083+11. This is unlikely due to the fact that the minimum mass threshold required is $M_{\rm BH} > 1.4 \times 10^{10}\ M_{\odot}$ for a nearly maximally rotating ($a = 0.998$) or $M_{\rm BH} > 3.6 \times 10^{9}\ M_{\odot}$ for a non-rotating ($a = 0$) black hole. Note that the mass estimated for PSO J083+11 is already two times smaller compared to these limits (see Section 7.4). Furthermore, high-z SMBHs should be quickly spinning, which would enhance this discrepancy (Volonteri et al. 2013).

The second hypothesized process is that a high Eddington ratio quasar will have an optically and physically dense inner accretion disk, known as a slim disk (Luo et al. 2015). The scale height of this disk grows as the Eddington ratio rises, becoming a shielding component, which prevents energetic photons from the central area from reaching and ionizing the broad-line region, subsequently resulting in the observed weak high-ionization line emissions (Ni et al. 2018). This concept has been supported by observations of WLQs with weak X-ray emission, which usually have harder X-ray spectra than regular quasars, showing intrinsic X-ray absorption in these objects (Wu et al. 2011, 2012). Due to the lack of X-ray data for PSO J083+11, we cannot entirely rule out the shielding gas presence between the accretion disk and the broad-line region.

The third hypothesized explanation is that an extraordinarily high accretion rate might result in less efficient generation of X-ray photons, resulting in a SED that peaks in the ultraviolet (Leighly et al. 2007a,b). This event might be due to a quenched X-ray corona, which shrinks in size, or X-ray photons that cannot diffuse out because of the trapping and advection process into the black hole. In other words, there will not be enough energetic photons released by the central engine to form high-ionization potential lines like C IV. However, establishing lower-ionization lines – e.g., Hα, Hβ, and Mg II – would be not difficult.

According to the second and third stated processes, low-z WLQs have much higher Eddington ratios and luminosities on average than other Type 1 low-z quasars (Meusinger & Balafkan 2014). PSO J083+11, on the other hand, does not exhibit this pattern when compared to other high-z quasars. Its Eddington ratio, estimated based on the Mg II line and the corresponding continuum, is not unusually strong ($L_{\rm bol}/L_{\rm Edd} \approx 0.5$, see Figure 7.3). However, we

must emphasize that the virial mass estimate is based on the scaling relation established from the reverberation mapping, which may be insufficient for WLQs due to their weak emission lines (Luo et al. 2015). Because the computed black hole mass is probably overestimated, the true Eddington ratio may be lower than the currently measured (Marculewicz & Nikolajuk 2020). Furthermore, the systematic uncertainty of the single-epoch virial-mass technique is $\approx$ 0.4–0.5 dex (Shen 2013) and possibly higher if the Mg II broad-line region is complicated and has not yet been virialized in this type of unusual sources (Plotkin et al. 2015).

Another possible sign of exceptionally high accretion rate is the power-law continuum shape itself, as observed in J006+39, a super-Eddington quasar with $L_{\rm bol}/L_{\rm Edd} \geq 9$ at $z \approx 6.6$ (Tang et al. 2019). Even though J006+39 is accreting at a super-Eddington rate, it does not belong to the WLQ population – i.e., C IV REW $\approx$ 84 Å. On the other hand, PSO J083+11's power-law slope index is similar to a normal quasar ($\alpha_\lambda = -1.66 \pm 0.01$) and not steeper than the previously stated models, confirming the lack of super-Eddington accretion. Therefore, soft continuum theories seem insufficient to describe PSO J083+11's weak-line nature.

10.2 Are Weak-line Sources Young Quasars?

Another possible reason for the weak-line phenomenon is that the quasar is in the early stages of its accretion process, resulting in gas-deficient or anemic broad-line clouds, albeit with the caveats described in the previous section. In the first model of the anemic broad-line cloud, there may be just a tiny quantity of gas or covering factor in the WLQ broad-line region (Shemmer et al. 2010; Nikołajuk & Walter 2012). Consequently, all broad-line emissions should have comparable widths and small fluxes.

The second model, on the other hand, argued that at the start of a quasar phase, broad-line clouds are still unestablished because the gas and dust from the accretion disk have not yet had enough time to reach the region where the broad lines will later develop (Hryniewicz et al. 2010). Assuming that the accretion disk's wind has a velocity of $\approx$ 100 km s^{-1}, the time required to construct the broad-line region is $\approx 10^3$ yr (Hryniewicz et al. 2010). Hence, WLQs should be uncommon if they constitute an evolutionary quasar phase. Intriguingly, the percentage of WLQs among quasars appears to grow with redshift (e.g., Bañados et al. 2016; Shen et al. 2019). In the concept of a still-emerging broad-line region, the high-ionization ions such as C IV will be the weakest in the WLQs phase because they arise in an area higher above the disk that has not yet fully developed. The low-ionization ions (e.g., Hβ and Mg II) produced closer to the accretion disk, on the other hand, may seem normal (Plotkin et al. 2015).

We should highlight that the majority of low-z WLQ studies lack access to Lyα and the quasar age could not be estimated using the approach described in Section 7.5. The intergalactic medium at $z \gtrsim 6$ has a limited reaction time to the quasar's photoionization. This process thus makes the proximity zone is sensitive to quasar lifetime. The PSO J083+11's accretion lifetime, as determined by its proximity zone size, is within the range of $t_{\rm Q} = 10^{3.4\pm0.7}$ yr, which is consistent with the timescale of broad-line region formation at the lower-end. Therefore,

there is a chance that the broad-line region of this source is not yet fully established, resulting in the weak-line features observed in the spectrum (Hryniewicz et al. 2010). However, as Eilers et al. (2018b) points out, this source may have a long time of considerable accretion already than the one calculated based on its proximity zone size. In that scenario, this quasar might have been growing in a highly obscured phase, with its ultraviolet continuum radiation just breaking out of this obscuring medium $\approx 10^3$–10^4 yr ago (see also Hopkins et al. 2005; DiPompeo et al. 2017; Mitra et al. 2018). This event might be due to a massive supply of dust and gas in the early universe being driven into the host galaxy's center, fueling the black hole and the star formation while concealing the quasar. Following it, Sanders et al. (1988a) proposed that when heavy obscuration occurs, ultra-luminous infrared galaxies (ULIRGs) may represent the first phases of a quasar. Only after this emerging dust-enshrouded phase would the quasar be detected in the ultraviolet-optical wavelengths as an unobscured object (e.g., Sanders et al. 1988b; Sanders & Mirabel 1996; Hopkins et al. 2008). A theory provided by Liu & Zhang (2011) even forecasts that newly unobscured quasars will not have broad-line emissions because the broad-line region will arise later when the dusty torus feeds the fuel to the accretion disk. The bright far-infrared features discovered in Section 9.4 would imply that PSO J083+11 is still at the early stage of its unobscured phase, while the host galaxy is still undergoing very active star formation. This paradigm is consistent with the young accretion lifespan calculated from the associated proximity zone size.

10.3 A Caveat Regarding the Small Proximity Zone Size

We previously ascribed the small PSO J083+11's proximity zone size to a short unobscured accretion lifetime. An alternative possibility is the truncation of proximity zone given the presence of a proximate absorber within $\lesssim 10,000$ km s^{-1} (or $z \gtrsim 6.3$). Owing to its optically thick characteristic near the Lyman limit, such a system, like a damped Lyα absorber or Lyman limit system, would suppress the ionizing photons from the quasar (Eilers et al. 2017, 2018b; D'Odorico et al. 2018; Bañados et al. 2019; Farina et al. 2019). Figure 10.1 displays the potential absorption systems at $z = 6.295$ (or $z = 2.233$, see below) that might truncate the proximity zone. This redshift corresponds to a distance of $R \approx 2.43$ pMpc relative to the quasar, and as a comparison, the proximity zone size found in Section 7.5 is $R_p = 1.17 \pm 0.32$ pMpc. The redshift of that absorber is selected such that related N V $\lambda\lambda$1238, 1242 fit the location of the two strong absorption lines seen at 9037 Å and 9066 Å. However, the locations of additional lines that typically exist in DLAs (e.g. Si II λ1260, O I λ1302, Si IV λ1402, etc.) do not fit any probable absorption lines visible in the actual spectrum. The existence of those low-ionization lines is particularly significant since it generally indicates the optically thick self-shielding absorber (Eilers et al. 2020). Also, given that the predicted distance between quasar and absorber is not particularly near, such a hypothetical system might affect the proximity zone, but it is unlikely to be substantial.

In contrast, it is also possible that the two strong lines previously noted are connected with Mg II $\lambda\lambda$2796, 2803 originates from a z=2.233 metal absorber. However, due to the limited

resolution of our existing spectrum, looking for extremely faint metal lines is problematic. With VLT/MUSE data, we will conduct a more extensive study to place tight constraints on the possibly linked absorption systems, which we will report in the next chapter.

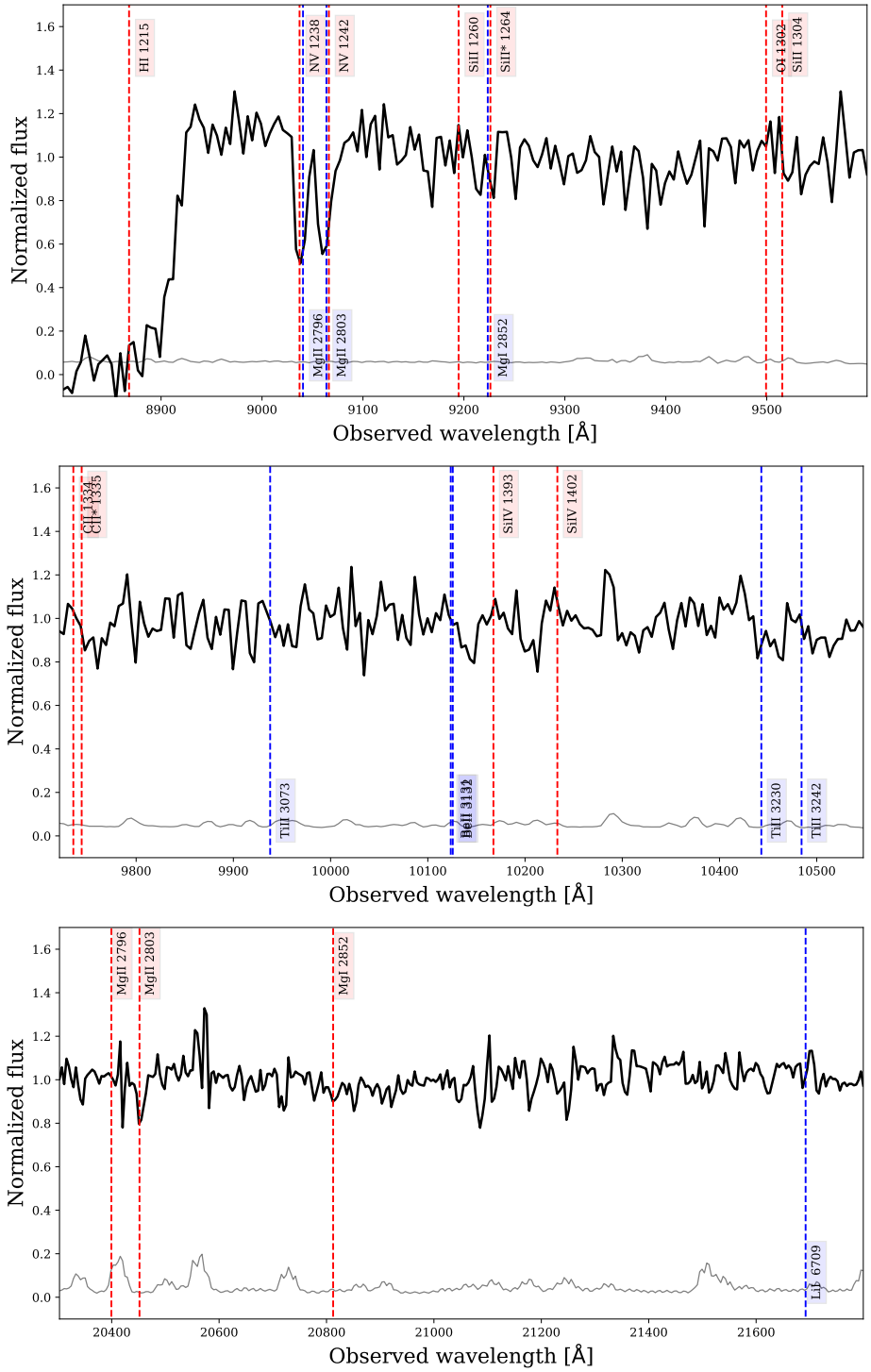

Figure 10.1. The PSO J083+11's continuum normalized GNIRS spectrum (black) for finding a hypothetical proximate absorber. The anticipated metal lines originate from a potential absorber located at $z = 6.295$ as well as $z = 2.233$ are displayed in red and blue, respectively. Moreover, the noise spectrum is shown with a gray line. There are no strong metal lines identified at the predicted wavelengths (despite the poor spectral resolution data), indicating the absence of a damped Lyα absorber or Lyman limit system extremely close to the quasar.

10.4 Summary and Conclusion

In this work, we described our efforts to expand the number of known quasars at $z \gtrsim 6$, which resulted in the finding and the characterization of PSO J083+11, a new weak emission line quasar at $z = 6.3401$. This source was first detected using our northern dataset – i.e., PS1, UHS, and unWISE. Our key findings on PSO J083+11 are as follows.

Using Gemini/GNIRS near-infrared spectrum, we fitted the Mg II emission and the corresponding continuum to estimate a black hole mass of $\log(M_{\rm BH}) = 9.30^{+0.16}_{-0.10}\ M_\odot$ and an Eddington ratio of $L_{\rm bol}/L_{\rm Edd} = 0.51^{+0.13}_{-0.17}$. These estimates show that PSO J083+11 is powered by an actively accreting black hole with an accretion rate comparable to other typical Type 1 quasars. The broad emission lines of this quasar are weak – e.g., REW (Lyα + N V) $= 5.65^{+0.72}_{-0.66}$ Å, indicating that it belongs to the population of weak-line quasars. The weakness of Lyα + N V is not due to the strong absorption by the intergalactic medium in the sightline. This suggestion is reinforced by the lack of C IV emission, with REW (C IV) ≤ 5.83 Å, which suggests that the strength of the broad-line region emission is intrinsically weak. The spectrum indicates a very narrow size of proximity zone, where $R_{\rm p} = 1.17 \pm 0.32$ pMpc, implying a current quasar age of only $10^3 - 10^{4.5}$ yr, which contradicts the reported instantaneous accretion rate for growing the central SMBH.

We discovered a putative intervening galaxy with a magnitude of 25.42 ± 0.07 situated at around $1''$ to the southwest of the central quasar using HST/WFC3 imaging in the F125W band. Utilizing a point-mass lens model and assuming it is a star-forming main sequence galaxy at low-z, we established an upper limit of the potential lensing magnification of $\mu \leq 1.07$, suggesting no substantial effect of boosting on the apparent quasar emission. The morphology of the quasar is also seen as a pure point source with no extended component.

ALMA band-6 investigations of PSO J083+11 revealed both dust continuum and spatially resolved [C II] emission from the host galaxy. We calculated a precise redshift of $z_{\rm [C\,II]} = 6.3401 \pm 0.0004$ based on the observed [C II] line center. The [C II] resolved extended morphology might be the result of a merger or, in any event, unrelaxed continuous formation. To date, this quasar is one of the brightest [C II] emitters known in the early universe. Using a modified blackbody function to model the Rayleigh-Jeans tail of the dust continuum produces a limit on dust mass of $M_{\rm dust} = (4.88 \pm 0.14) \times 10^8\ M_\odot$ and star formation rate of $\rm SFR_{TIR} = 900$–$7600\ M_\odot\ yr^{-1}$, which is equivalent to HyLIRGs. This estimate agrees with the [C II]-based SFR, i.e., $\rm SFR_{[C\,II]} = 800$–$4900\ M_\odot\ yr^{-1}$.

Given the accretion lifetime of PSO J083+11 and the timescale of broad-line region formation, we propose that the weak-line nature of this source is due to a still-emerging broad-line region. The alternative theories such as gravitational lens boosting to the continuum emission or soft continuum concept caused by a super-Eddington accretion seem unlikely. However, given the lack of X-ray spectroscopy, we cannot entirely dismiss the existence of shielding gas between the accretion disk and the broad-line region.

Overall, this quasar offers a perplexing image of the SMBH, despite the fact that it appears to have just recently begun to exhibit relatively mild accretion. In the next chapter, we will conduct a comprehensive search for a potentially proximate absorber that might alter the accuracy of our accretion lifetime estimate using the newly obtained VLT/MUSE data. In the future, the availability of the X-ray spectra from the facilities like XMM-Newton or Chandra X-ray Observatory would be highly advantageous to obtain better limits on the SED model along with the associated accretion rate. These data would also be beneficial for investigating the likelihood of shielding gas existing between the accretion disk and the broad-line region.

In the early stages of quasar (re)activation, the narrow-line region will take a longer time to emerge than the broad emission line region and is likely to be missing (Hryniewicz et al. 2010). We will be able to observe $z \gtrsim 6$ WLQs in the mid-infrared with future facilities such as the James Webb Space Telescope (JWST). Therefore, we can test the mentioned idea by probing the narrow-line region characteristics through [O III] λ5007 line spectroscopy. Further statistical analyses, supported by more samples of WLQs at the highest accessible redshift frontier, are necessary to demonstrate the associations between typical quasars, young sources, and those that are weak lines. This study will help us comprehend the quasar evolution, the rapid growth of the earliest SMBHs, and the structure evolution at cosmic dawn.

Part IV

A Deep Look into the Shadows of Ancient Galaxies

Chapter 11

Lyα Damping Wing Analysis

The content of this chapter is based on the published work ***Andika, I. T.****, Jahnke, K., Bañados, E., et al. (2022; AJ 163: 251) and is adapted from the ESO VLT/MUSE proposal: 0104.B-0665(A).*

In the previous chapter, we discovered a new weak-line quasar, PSO J083+11 (Andika et al. 2020), located at $z = 6.3401$. Based on its small proximity zone size, we suggested that this source belongs to the population of young quasars, with an accretion lifetime of only $t_{\rm Q} \lesssim 10^4$ yr from its recent activation phase. However, we obtained preliminary evidence suggesting the existence of a damped Lyα system (DLA; Wolfe et al. 2005). This absorber intrudes our sightline to PSO J083+11 and may spectrally truncate the quasar's proximity zone, complicating the use of the standard accretion lifetime estimation technique (Eilers et al. 2017). The primary goal of this work is to resolve the mentioned issue above and thoroughly assess the possible consequences along with offering independent evidence supporting the young accretion lifetime model of PSO J083+11 (Andika et al. 2022).

The high-z DLAs themselves, on the other hand, are intriguing sources. They are prime subjects for studying the H I reservoirs, which fuel the galaxy build-ups at cosmic dawn. These systems are also excellent tracers for investigating the reionization history in the universe and potentially holding clues to the metal enrichment chronicle contributed by the first generation stars (e.g., Kulkarni et al. 2014; Ma et al. 2017). Furthermore, the $z \gtrsim 6$ metal-poor DLAs are thought to be the present-day dwarf galaxy progenitors, which inhabit the galaxy mass function at the low end (Cooke et al. 2015). The rising opacity of the Lyα forest of the intergalactic medium (IGM) makes discovering and studying $z \gtrsim 6$ DLAs exceedingly challenging (Eilers et al. 2018a; Bosman et al. 2018). Although metal absorbers are commonly identified at $z \gtrsim 6$, their hydrogen column density $N_{\rm HI}$ is usually unknown, making the associated absolute metal abundances impossible to calculate (e.g., Cooper et al. 2019). The current best strategy is to examine the so-called "proximate" DLA absorbers located near the background quasar. In terms of spectral velocity space, their separation should be within $\approx$ 5000 km s^{-1} so that

their associated Lyα absorptions reach into the forest-free quasar continuum, enabling us to calculate their $N_{\rm HI}$. So far, only four proximate absorption systems have been discovered at $z \gtrsim 6$, namely: SDSS J2310+1855 ($z_{\rm DLA} = 5.939$; D'Odorico et al. 2018), PSO J056−16 ($z_{\rm DLA} = 5.967$; Davies 2020), PSO J183+05 ($z_{\rm DLA} = 6.404$; Bañados et al. 2019), and P007+04 (Farina et al., in preparation).

Here, we provide a study and characterization of the absorption system toward PSO J083+11. By utilizing a new integral-field spectroscopic data in conjunction with the near-infrared spectra presented in the previous chapters: (i) we report on a newly-found absorption cloud at $z = 6.314$ and constrain its effects on the PSO J083+11's lifetime estimate, and (ii) we search for and characterize the presence of a Lyα halo around the central quasar. The content of this chapter is outlined as follows. First, we start by presenting the integral-field spectroscopic data acquisition and reduction used for this study. Then, we provide the measurements of the metal contents and the Lyα damping wing profile observed in the spectra of PSO J083+11. After that, we explain our PSF model construction and strategy for subtracting the quasar continuum emission to put constraints on the Lyα halo size. Furthermore, we examine the results, consisting of the elemental abundances investigation and whether or not the absorber influences the interpretation of the quasar's apparent proximity zone. Finally, we conclude with discussions and a summary of our findings.

We employ here the ΛCDM cosmology for all observations, with $\Omega_\Lambda = 0.7$, $\Omega_{\rm m} = 0.3$, and $H_0 = 70$ km s^{-1} Mpc^{-1}. As a result, at $z = 6.3401$, the universe's age is 0.852 Gyr, and the angular scale of $\theta = 1''$ corresponds to the proper transverse separation of 5.5 kpc.

11.1 Integral-Field Spectroscopy and Data Processing

As previously indicated, we have two primary objectives. The first one is to constrain the Lyα damping wing profile and its possible influence on the PSO J083+11's proximity zone. For this purpose, we will reutilize the Gemini/GNIRS and Magellan/FIRE spectra described in Chapter 7, which are also beneficial for characterizing the physical features of the putative proximate absorber producing the observed strong metal absorption lines. It is worth noting that the details on PSO J083+11's discovery and characterization have been presented in the previous chapters (see also Andika et al. 2020). Our second objective is to test the prediction of the young quasar paradigm, which might be related to the limited presence of an extended Lyα emission around the central quasar. This particular aim motivated us to acquire a new integral-field data on PSO J083+11 using the Multi Unit Spectroscopic Explorer (MUSE; Bacon et al. 2010) mounted at the 8.2 m–ESO Very Large Telescope (0104.B-0665(A), PI: I.T. Andika).

The MUSE instrument is configured to wide-field mode assisted with adaptive optics. The generated datacube has a wavelength coverage of 0.47–0.93 μm and a spectral resolution of $R \approx 4000$. PSO J083+11 was observed with a total integration time of three hours, split into five exposures of 2116 s each. We also applied an image shift of $< 5''$ and 90 deg rotation between the exposures. The median PSF of the bright stars in the field of view is $0\farcs5$, around

the Lyα observed wavelength. For reducing the data, we utilize the standard MUSE pipeline[1] version 2.6 (Weilbacher et al. 2012, 2014, 2020), supplemented with a processing software built by Farina et al. (2019). For minimizing the photometric fluctuations caused by the varying weather conditions, each exposure is flux-rescaled before being co-added. Then, we also rescale the variance-datacube to fit the variance of the observed background. Next, the astrometric calibration is improved by aligning the sources using the PS1 catalog (Chambers et al. 2016) as a reference, while the Galactic reddening correction is subsequently applied. Furthermore, we minimalize the night skylines contaminations using the `Zurich Atmospheric Purge`[2] software (Soto et al. 2016). Finally, an aperture with a 0.″75 radius is employed to datacube for obtaining the final quasar's spectrum in the red optical wavelengths.

The MUSE, FIRE, and GNIRS spectral data enable us to explore the possibility of an absorber, such as (sub)-DLA or Lyman Limit System, near the quasar, which might affect the Lyα damping wing. It is worth noting that following Cooper et al. (2019), we use the H I-based definition to identify the absorber as a Lyman Limit System ($\log N_{\rm HI} \geq 17.2$ cm^{-2}), sub-DLA ($19.0 < \log N_{\rm HI} < 20.3$ cm^{-2}), or DLA ($\log N_{\rm HI} \geq 20.3$ cm^{-2}). Related to the search for an absorber, we then discovered absorption lines linked with the Mg II $\lambda\lambda$2796, 2803 doublet at $\lambda_{\rm obs} = 20\,449.9, 20\,501.1$ Å; C II λ1334 at $\lambda_{\rm obs} = 9756.9$ Å; and a marginal detection of O I λ1302 at $\lambda_{\rm obs} = 9522.8$ Å. These lines are a strong indicator of the existence of a nearby absorber at $z = 6.314$. On the other hand, we are unable to discover additional related metal line absorptions such as Si II, Al II, and Fe II that we would anticipate for a strong DLA system. This finding suggests that the mentioned system is not a particularly strong absorber. Subsequently, we will calculate the associated $N_{\rm HI}$ and investigate whether the proximate absorber is dominating the Lyα damping wing profile found in the PSO J083+11 spectrum.

As an aside, we discover additional line traces of a strong Mg II absorber at $z = 2.2305$ that we recognize from the absorptions of Mg II $\lambda\lambda$2796, 2803 doublet and Mg I λ2853 at $\lambda_{\rm obs} = 9032.5,\ 9055.1,$ and 9216.6 Å, respectively.

11.2 Analysis of the Metal Absorption Lines

The spectra used for metal lines characterization in this section are obtained using a combination of MUSE and FIRE data. As previously stated, the FIRE data were collected in less-than-ideal weather circumstances, which reduces its S/N. Therefore, we first need to bin and convolve this spectrum to achieve a similar spectral resolution as MUSE (i.e., $R \approx 4000$), which subsequently boosts the signal in the data. Then we join them by preserving the MUSE data at $\lambda_{\rm obs} \leq 9300$ Å wavelengths while utilizing the FIRE data at $\lambda_{\rm obs} > 9300$ Å.

To determine the metal column densities shown in Figure 11.1, we first have to continuum normalize the PSO J083+11 spectrum. We perform this under the premise that the majority of the high-frequency structures are either absorption lines or noise. Then, the continuum

[1]The software can be found at https://www.eso.org/sci/software/pipelines/muse/.
[2]The documentation is available at https://zap.readthedocs.io/en/latest/.

is reconstructed utilizing `QSmooth`[3] (Ďurovčíková et al. 2020). This code initially bins the spectrum using a running median consisting of 50 data points to provide a preliminary estimation of the main continuum and possible broad line emissions. The upper envelope of the spectrum is then built by executing a peak-finding strategy above the previously mentioned running median and subsequently interpolating the peaks. This envelope is nearly independent of the strong absorption signals. It is then subtracted from the spectrum to get an initial approximation of continuum-subtracted data while ignoring the influence of noise. `QSmooth` then searches for statistical outliers in this intermediate spectrum using the "Random Sample Consensus" regressor method (Fischler & Bolles 1981). This approach determines the intrinsic noise structures in the remaining peak-subtracted continuum while rejecting the majority of the absorption lines. This technique flags the inliers or data points that are not part of the emission or absorption signals, and subsequently, these are interpolated and smoothed again using a running median. The residual structure is then eliminated once again, yielding the final smooth flux fit of the spectrum. A visual check to the continuum-normalized spectrum is performed to look for probable additional metal lines associated with the highly prominent Mg II at $z = 6.314$. The column densities are then calculated directly from the spectral data using `Python` codes created by Simcoe et al. (2020). Here, to investigate the probability distributions of the column densities, the influence of saturation, and the degeneracies in the fitting parameters, the algorithm implements Markov Chain Monte Carlo (MCMC) samplers.

The user must first give a hierarchical absorption `Model` class before performing the fitting. This class can be made up of one or more `Component` variables that represent an absorber with single or multiple velocity clouds. After that, for each `Component`, the priors on turbulence parameter b, redshift z, and thermal parameter T, which corresponds to temperature, must be specified. Each `Component` has numerous `Ion` children, each of which has a name (e.g., Mg II or Fe II), a prior on column density N, and a related array of `Transitions`. The `Transitions` themselves, in principle, are absorption lines specified by their rest wavelengths and related atomic data (Morton 2003). Afterwards, the user generates a `Model` class by supplying `Component`, `Ion`, and `Transitions`, as well as relevant wavelength regions to be analyzed. Generally, we fit areas inside a velocity space of $\Delta v = \pm 125$ km s^{-1} around the absorption line centers, with minor adjustments for noisy locations. It is worth noting that the `Model` class includes a built-in method for generating Voigt profiles and convolving them with the instrumental resolution. This approach naturally models the line absorptions, which comprise many ions and column densities with a single value of z, b, or T. Additionally, a single N can be utilized for a group of transitions.

In our situation, we use a model with one velocity component and column densities determined for 11 independent ions, resulting in 14 fitting parameters. This model and its accompanying priors are then fed into the `emcee` program (Foreman-Mackey et al. 2013), which then carries out the MCMC sampling and evaluates the posterior distributions of the parameters. Note that we employ flat priors all input parameters, in which $11 \leq \log N \leq 17$, $3 \leq \log T \leq 5$, and $2 \leq b \leq 100$ km s^{-1} are utilized. Because the posterior runs from the prior

[3] See the implementation at https://github.com/DominikaDu/QSmooth/.

lower limit to the highest N permitted by the observed spectrum, the procedure could also estimate the upper limit of N. The z and b parameters of undiscovered ions or lines are then determined by the other ions in the same velocity component but having significant detections. The upper limits for non-detections are the maximum values where 95% of the posteriors are distributed.

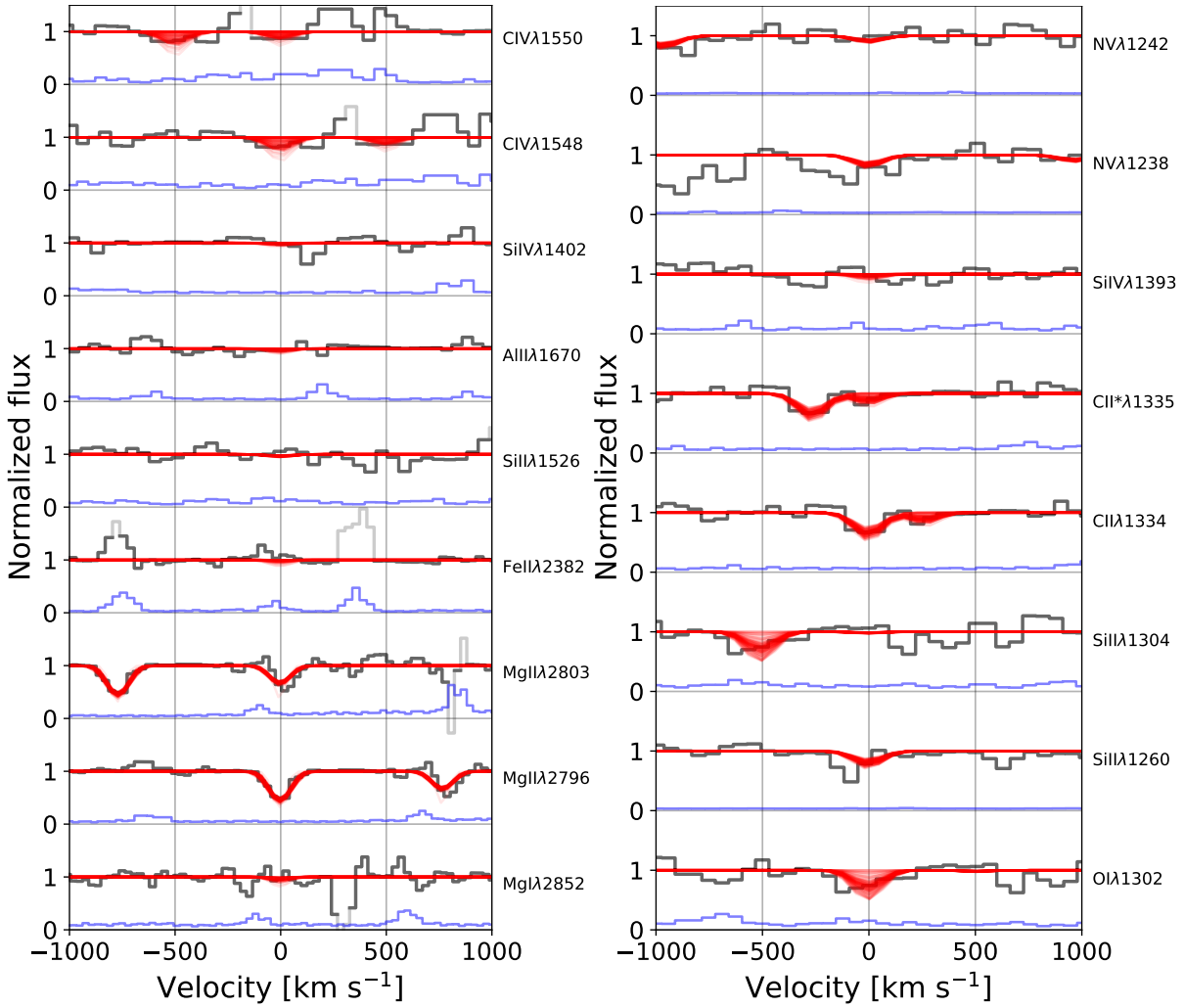

Figure 11.1. Metal absorptions from a sub-DLA at $z = 6.314$, discovered in the MUSE + FIRE spectrum of PSO J083+11. The data is displayed by black lines, with the fitted models superimposed in red. It is worth noting that the red line widths relate to the model uncertainty (see text). The blue lines depict a 1σ shot noise spectrum. The grey lines indicate noisy data in the highly contaminated areas due to skylines. The absorptions from Mg II $\lambda\lambda$2796, 2803 doublet and C II λ1334 are easily visible, whereas O I λ1302 is only marginally detected. Finally, the other related metals such as Si II, Al II, and Fe II that would be expected for a strong absorber are not seen in the spectrum.

The models fitted to the MUSE + FIRE spectra are displayed in Figure 11.1. The red lines represent a sample of 100 models picked at random from the posterior distribution. Correspondingly, the width of the red lines thus relates to the model uncertainty. Table 13.1, third column, displays the fitted parameters that are obtained. The adopted abundances of C, O, Mg, Al, Si, and Fe are based on the calculated column densities of C II, O I, Mg II, Al II, Si II, and C II, respectively. Here, we provide the median and the corresponding 5% and 95% confidence

intervals, along with the 95% upper limit for the undetected lines. Our preferred model includes a proximate absorber at $z = 6.314$ having a thermal parameter of $\log T = 4.13 \pm 0.80$ K and a turbulent parameter of $b = 59 \pm 20$ km s^{-1}. The majority of high-excitation lines, such as C IV, S IV, and N IV, are undetectable within our sensitivity limits. Hence, higher resolution and S/N spectra would be necessary to provide stringent constraints on those ions.

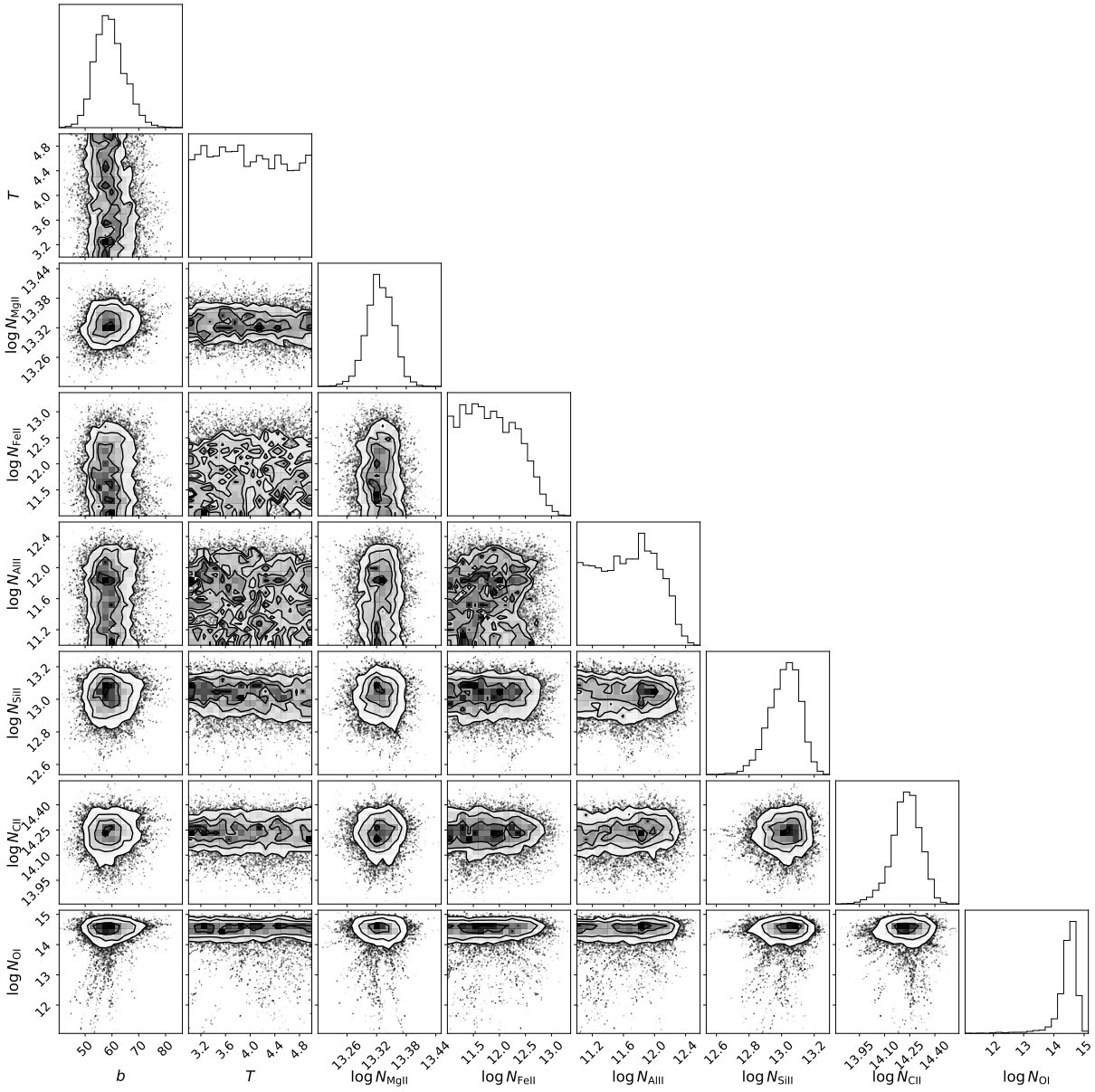

Figure 11.2. A corner plot displaying the posteriors of the thermal parameter (T), turbulent parameter (b), and metal column densities from Table 13.1. The inferred b appears to be skewed toward high values, whereas T is quite unclear (see text). The Mg II and C II column densities are highly constrained since they are significantly identified in the spectrum (see Figure 11.1). The marginal detection of O I, on the other hand, causes its imputed column density to be somewhat imprecise. The non-detections are clear for Al II and Fe II, whose posteriors stretch to the minimum value of the input prior. We also utilize the upper limit value for Si II because its existence in the spectrum is not robust.

Figure 11.2 illustrates the resulting posterior distributions of the fitted parameters. Because

we only evaluate the absorption model with one velocity component, the inferred b appears skewed toward large values, whereas T is weakly constrained. As a comparison, lower-z metal absorbers exhibit more quiescent kinematics with $b \lesssim 30$ km s^{-1} (e.g., Cooper et al. 2019). Thus, clouds having more than one velocity component are probably present in the sub-DLA toward PSO J083+11. Due to spectral resolution limitations, this is impossible to constrain with our existing data. Nonetheless, Simcoe et al. (2020) discovered that their algorithm is resilient enough to calculate the cumulative column density N in the presence of numerous unresolved narrow components, even if the N of each constituent is imprecise.

As additional information, the previously discovered Mg II absorber at low$z$ is best modeled with $z = 2.2305$, $\log T = 3.99 \pm 0.69$ K, and $b = 56 \pm 16$ km s^{-1}. Subseqently, the column densities for this absorber are $\log N_{\rm Mg\,I} = 12.86 \pm 0.07$ cm^{-2} and $\log N_{\rm Mg\,II} = 13.75 \pm 0.04$ cm^{-2}.

11.3 Modeling the Intrinsic Lyα Emission

What is the Lyα absorption strength from the intervening proximate absorber toward the PSO J083+11? We first need to reconstruct the intrinsic Lyα emission of PSO J083+11 to get an approximation. This modeling is accomplished through two independent strategies: (i) creating the stacked spectra of low-z quasars having similar emission-line properties as PSO J083+11 to generate a template (e.g., Bañados et al. 2019) and (ii) building a reference based on principal component analysis (PCA; e.g., Davies et al. 2018b; Bosman et al. 2021a). We will utilize the MUSE + GNIRS spectrum for this purpose because while having a lower resolution than FIRE, GNIRS provides better continuum S/N in the spectral data, which is beneficial for predicting the intrinsic quasar emission. The combined spectrum is subsequently constructed by combining $\lambda_{\rm obs} \leq 9300$ Å MUSE data to $\lambda_{\rm obs} > 9300$ Å GNIRS data.

The first strategy relies on the notion that there is no substantial change on the quasar spectra over redshifts so that we can produce an empirical composite using the low-z analogs (e.g., Shen et al. 2019). However, when compared to other $z \lesssim 5$ quasars of the same luminosity, $z \gtrsim 6$ quasars frequently display strong ionization broad lines with more dramatic velocity shifts (Mazzucchelli et al. 2017; Meyer et al. 2019; Schindler et al. 2020). Nonetheless, the significant fraction of SDSS (Abolfathi et al. 2018) quasars at lower-z offers an acceptable reference for generating a composite spectrum. Our approach is summed up as follows:

1. All quasars tagged as non-broad absorption lines (BI_CIV = 0 km s^{-1}) in the SDSS Data Release 14 Quasar Catalog (Pâris et al. 2018) are queried. We restrict the selection to the redshifts of $2.0 < z < 2.5$ to include the Lyα, C IV, and Mg II lines in the spectra. This selection resulted in 85,535 quasars.

2. The wavelengths surrounding C IV are fitted with a power-law function to represent the local continuum (for reference, see e.g., Shen et al. 2011). Then, using the excess flux above the continuum across the wavelengths where C IV is predicted, we calculate the associated C IV rest-frame equivalent width (REW). In this manner, we chose quasars with a C IV REWs comparable to PSO J083+11 (i.e., REW $\lesssim 5.8$ Å). These criteria resulted in the

identification of 23 quasar analogs having spectral features comparable to PSO J083+11.

3. These analog spectra are subsequently smoothed using `QSmooth` (Ďurovčíková et al. 2020) to eliminate particularly noisy regions and strong absorption lines. Each of the 23 spectra is then normalized at 1290 Å before being averaged to produce the final composite spectrum.

Figure 11.3 displays the median composite spectrum along with the associated 1σ uncertainty. The composite spectrum fits the majority of the features seen in the PSO J083+11 spectrum and forecasts an inherently weak Lyα line.

For the second technique, we utilize the PCA, constructed using low-z quasar spectra as a training dataset, to estimate the intensity and shape of the Lyα emission exploiting the strong correlations between Lyα emission and other rest-frame ultraviolet broad lines (Francis et al. 1992; Yip et al. 2004; Suzuki 2006). This approach subsequently makes PCA a viable method for predicting the blue side ($\lambda_{\rm rest} < 1290$ Å) of the quasar spectrum based only on its red side ($\lambda_{\rm rest} \geq 1290$ Å; e.g., Suzuki 2006; Pâris et al. 2011; Davies et al. 2018b,a). For further information on the PCA design we employed, see Bosman et al. (2021a). In summary, our training set comprises $\approx$ 4000 quasars obtained from the SDSS DR14 quasar catalog (Pâris et al. 2018). Then, for the red- and blue-side spectra, PCA decomposition is then used to capture $\approx$ 80% of the overall spectrum variance using a linear combination of just 10 and 6 principal components, respectively. Following that, we compute a projection matrix that relates the red-side coefficients to the blue-side coefficients of the spectrum. Therefore, the spectrum on the blue side may be forecasted based on the projected coefficients and the related spectral template. Figure 11.3 shows the PCA model for PSO J083+11. It forecasts a weaker Lyα compared to the composite spectrum of low-z analogs and subsequently gives a formally better fit to the observed data. Note that both models are nonetheless compatible with each other within the uncertainties. However, compared to the composite spectrum based on the low-z analogs, the PCA incorporates not just C IV but essentially all broad line features, making it superior thanks to the extra information it employs. Consequently, we will use the PCA model for the rest of this study to reap the benefits of its well-quantified uncertainties.

This result enables us to simulate the absorption profile around the Lyα line. Subsequently, a Voigt function centered at $z = 6.314$ is fitted to the damping wing signal in the spectrum of PSO J083+11, where this nearby absorber redshift is chosen based on the position of the metal line absorptions (see Section 11.2). The least-squares optimization produce a best-fit value of $\log N_{\rm HI} = 20.11 \pm 0.30$ cm^{-2}. Then, overplotting the Voigt profiles and changing the column density input to establish the allowable limit by the observed spectrum and the continuum model yields an uncertainty of range in $N_{\rm HI}$. Because it is difficult to quantify the complete set of errors from continuum mismatch, unaccounted-for absorption lines and shot noise, this approach to making a subjective visual estimate of the uncertainty in the absorption profile is currently the standard methodology in the field (e.g., Bañados et al. 2019). Note that stating the goodness of fit based only on χ^2 would yield an excessively tiny range of presumably consistent $N_{\rm HI}$ values. Even though a single Voigt profile already provides an acceptable overall

fit, we want to evaluate how much the PSO J083+11's proximity zone is constricted owing to the existence of the aforementioned proximate absorber.

Another process that is likely to be involved and affects the damping wing is the hydrogen absorption in the IGM, which has a neutral fraction of $\overline{x}_{\rm HI} > 10\%$ (Miralda-Escudé 1998; Bañados et al. 2019). Thus, we attempt to describe the IGM damping wing using the formalism of Miralda-Escudé (1998), assuming a constant neutral fraction from the quasar's proximity zone at $z = z_{\rm s}$ to $z = 5.5$ while being completely ionized at $z \lesssim 5.5$. The proximity zone is defined as the physical radius where the transmitted flux reduces to 10%, which for PSO J083+11 is similar is $R_{\rm p} = 1.17 \pm 0.32$ pMpc (Andika et al. 2020).

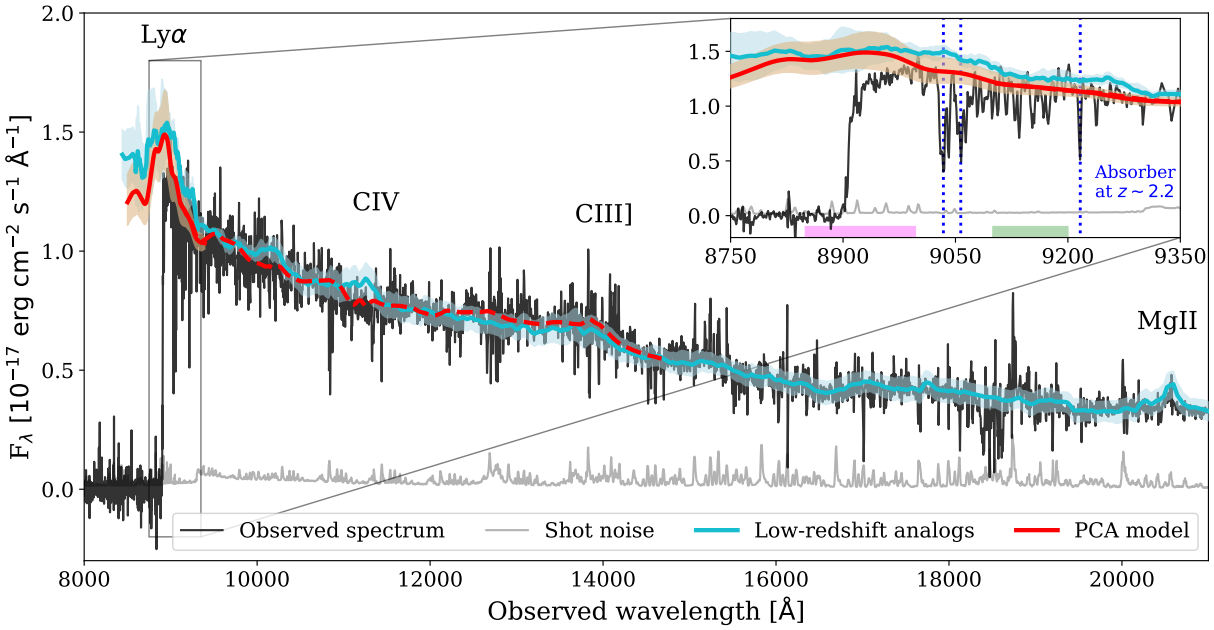

Figure 11.3. PSO J083+11's MUSE + GNIRS spectrum (black line) and shot noise (grey line) are presented. The cyan line denotes the median composite spectrum of the low-z analogs, whereas the light blue region represents the 1σ dispersion around the median. This composite fits the primary characteristics reported in the PSO J083+11 spectrum redward of the Lyα emission rather well. The red line and shaded region, on the other hand, display the PCA model used to forecast the blue side of the quasar spectrum, as well as its 1σ dispersion. The red dashed line indicates the wavelengths and spectra utilized in the PCA fit to forecast the Lyα emission. The inset image offers a zoomed-in view of the area surrounding Lyα. The blue dotted lines highlight the Mg II $\lambda\lambda$2796, 2803 doublet and Mg I λ2853 absorptions at $z = 2.2305$. The wavelengths marked with magenta ($\lambda_{\rm obs} = 8850$–8997 Å) and green ($\lambda_{\rm obs} = 9100$–9200 Å) colors represent the regions for constructing the Lyα pseudo-narrowband and continuum images, respectively.

The least-squares minimization of the IGM + DLA combined model with three free parameters – i.e., $\overline{x}_{\rm HI}$, $N_{\rm HI}$, and $R_{\rm p}$ – would result in a highly degenerated outcome, as indicated by Bañados et al. (2019). Hence, we use a grid of constant $\overline{x}_{\rm HI}$ and $R_{\rm p}$ to walk through some IGM damping wing appearances to reduce the dimensionality. The DLA Voigt profile is then matched to the previously attenuated continuum. As a consequence, a combination model of IGM and DLA always provides a slightly better, though not statistically significant, fit than using only a DLA, especially at $\lambda = 1216$–1225 Å (see Figure 11.4). We discover that the allowable PCA-based

DLA profiles that match the observed damping wing have $\log N_{\rm HI} = 20.03–19.73\,{\rm cm}^{-2}$ for an IGM that is 10–50% neutral. As a result, this exercise also provides the proximity zone size permitted by the measured spectrum, i.e., $R_{\rm p} \gtrsim 1.35$ pMpc. It is important to note that we can only compute the lowest limit of $R_{\rm p}$. In the case of the quasar's proximity zone goes further than the DLA location (i.e., $z_{\rm s} < z_{\rm DLA}$), it would be concealed from the observer and inadequately constrained, owing to the DLA cloud's blocking. In addition, the proximity zone size would no longer be responsive to quasar lifespan, necessitating an independent diagnostic to determine the age. Appendix B shows how different combinations of neutral fractions and $z_{\rm s}$ impact the damping wing model.

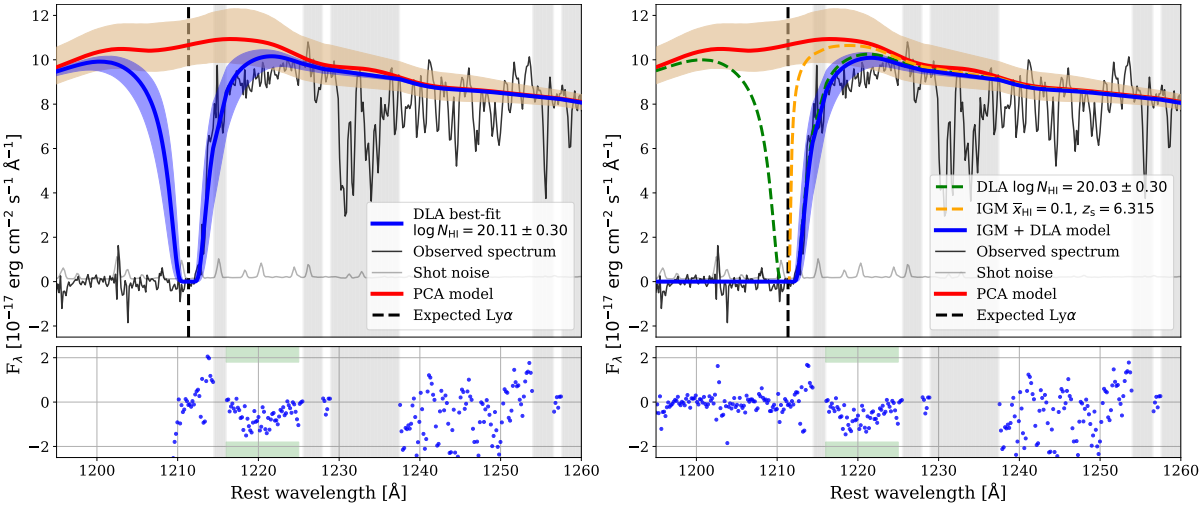

Figure 11.4. Constraints on the PSO J083+11's damping wing profile. The PSO J083+11 (black line), shot noise (grey line), and its corresponding PCA model (red line and shaded region) spectra around the wavelengths where the quasar's Lyα emission is predicted. The absorption from a $z = 6.314$ sub-DLA with a hydrogen column density of $\log N_{\rm HI} = 20.11 \pm 0.30\,{\rm cm}^{-2}$ is depicted in the *left panel* (blue line and shaded region). Although it already provides a decent match, we try to investigate an alternate model to determine how much of PSO J083+11's proximity zone is constricted owing to the existence of associated sub-DLA. The *right panel* shows a joint model in which we include attenuation owing to an IGM with $\bar{x}_{\rm HI} = 0.1$ (orange dashed line) and a sub-DLA with $\log N_{\rm HI} = 20.03 \pm 0.30\,{\rm cm}^{-2}$ (green dashed line). This combined IGM + DLA model (blue line and shaded region) matches the data a little better at λ =1216–1225 Å (see wavelengths indicated with green), even though not significant. The plot also shows the residual of the fits (blue circles) and masked wavelength regions to prevent strong absorption lines or highly contaminated areas due to imperfect skylines subtraction (grey shaded area). For the effect of different $\bar{x}_{\rm HI}$ values, see Appendix B.

For the rest of the study, we will use our fiducial model, a 10% neutral IGM with the best-fit DLA Voigt profile of $\log N_{\rm HI} = 20.03 \pm 0.30\,{\rm cm}^{-2}$. This value includes the best-fit $N_{\rm HI}$ for all situations when $\bar{x}_{\rm HI} \leq 50\%$. Furthermore, $\bar{x}_{\rm HI} > 50\%$ values appear improbable since the best-fit damping wings profiles continuously underestimate the measured fluxes at $\lambda = 1216–1225$ Å. The choice of this model is also influenced by the fact that IGM with $\bar{x}_{\rm HI} \gtrsim 0.4$ has only been discovered at higher redshifts (e.g., Davies et al. 2018a; Wang et al. 2020a). Furthermore, Yang et al. (2020b) inferred a lower bound for the neutral fraction at $z \sim 6$, which is $\bar{x}_{\rm HI} \gtrsim 10^{-4}$. They calculated this number using the Lyα effective optical depth measurements and hydrodynamical

simulations with a homogeneous ultraviolet background. However, Yang et al. also notes that their prediction does not dismiss the possibility of $\overline{x}_{\rm HI} \sim 0.1$–$0.2$, but not much higher.

We also attempt to simulate the Lyα damping wing using the MUSE and lower-quality FIRE spectra for completeness, as shown in Appendix C. In this instance, the telluric line residuals have a stronger influence on the PCA model. This phenomenon leads to inaccurate, considerably larger predictions of Lyα fluxes, which requires an unphysical neutral fraction of $\overline{x}_{\rm HI} \geq 80\%$. As a result, we do not believe the FIRE spectrum to be a reliable source of independent data for analyzing the damping wing absorption.

Chapter 12

Constraints on the Lyα Halo Properties

The content of this chapter is based on the published work ***Andika, I. T.****, Jahnke, K., Bañados, E., et al. (2022; AJ 163: 251) and is adapted from the ESO VLT/MUSE proposal: 0104.B-0665(A).*

We want to use the MUSE data to estimate the extent of the Lyα halo around PSO J083+11 and uncover the alternate evidence for the young quasar argument. The previously observed Lyα halos surrounding early quasars (Farina et al. 2019) inform our expectations on the probable extent ($\lesssim$ 30 pkpc) and luminosity ($\log L_{\mathrm{Ly}\alpha} \sim 42$–$44$ erg s^{-1}). These characteristics clearly indicate the necessity to remove the quasar point-source light, smeared out by the VLT/MUSE $\sim$0.″5 PSF, before searching for the halo.

12.1 Quasar Point Source Modeling and Subtraction

Using (Drake et al. 2019) as a guide, we will reconstruct the PSF using data in the following sequences. First, several spectral channels in the MUSE datacube containing the quasar's continuum are chosen and collapsed to generate a local PSF model. To enhance the corresponding S/N, we would ideally like to incorporate as wide a spectral range as feasible. However, there are contaminations from the night skylines across the wavelengths of interest, which affect the noise characteristics of the neighboring wavelength layers, resulting in the deterioration of the signals. On the other hand, the PSF is chromatic due to wavelength-dependent diffraction in the varying density air, necessitating the selection of wavelengths for the PSF construction near the regions for which the PSF is produced. Hence, we collapse the spectral channels of $\lambda_{\mathrm{obs}} = 9100$–$9200$ Å where the contaminations are relatively low and the quasar continuum has high enough signals while remaining within a few percent distances from the Lyα wavelength (see the inset of Figure 11.3).

With the PSF model in place, we remove the quasar point-source light by scaling the model to match each MUSE datacube channel inside the Lyα spectral wavelength, i.e., at $\lambda_{\rm obs}$ = 8850–8997 Å. We then normalize the fluxes measured within an aperture radius of two spatial pixels (0.″4, at an angular resolution of 0.″3–0.″4 for the MUSE data), assuming that this central area is substantially dominated by the unresolved quasar's emission (e.g., Farina et al. 2017, 2019). Finally, removing the matched PSF model from the Lyα cube channels generates an entire quasar point-source-subtracted datacube having an extended residual emission.

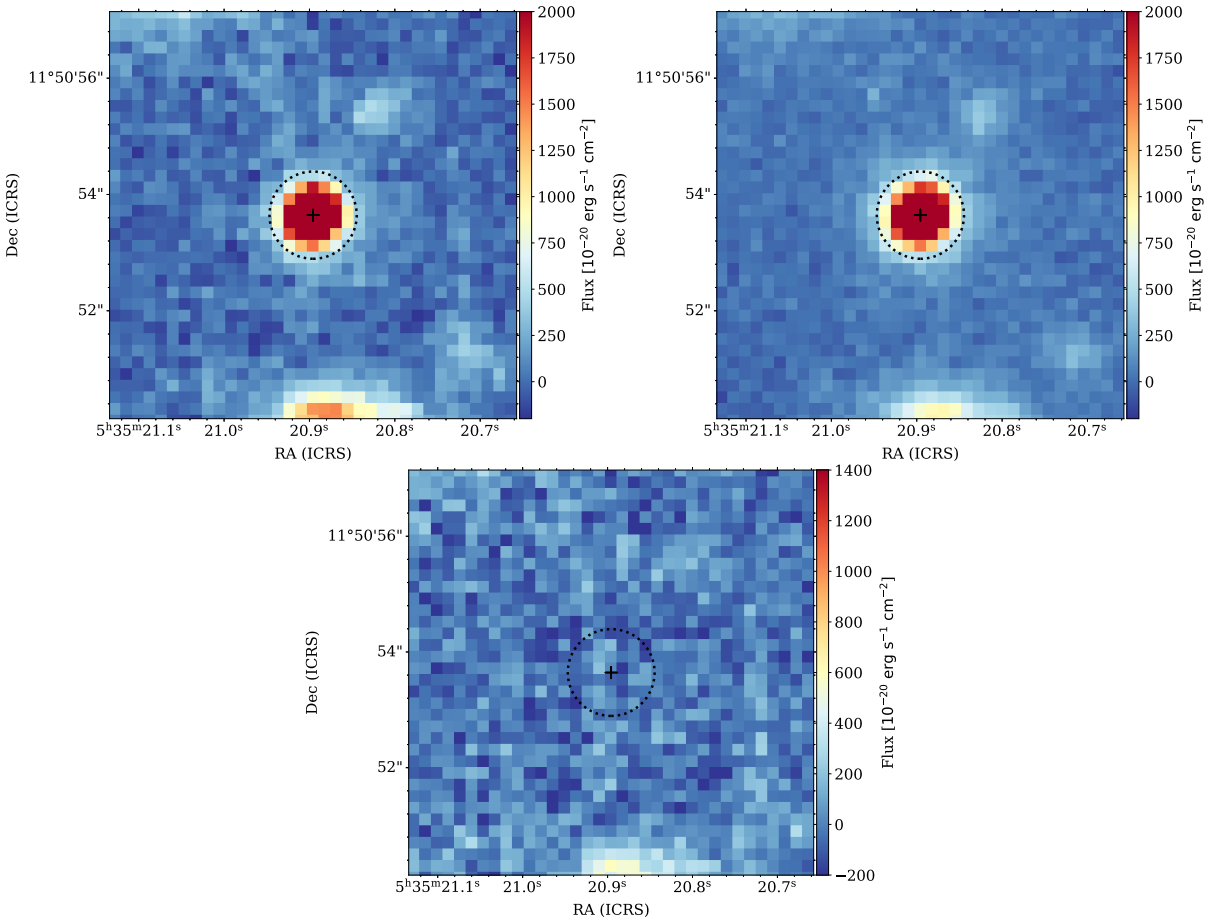

Figure 12.1. Pseudo-narrowband images of PSO J083+11 generated from the MUSE datacube. The dotted black circles denote a 0.″75 aperture utilized to derive the quasar spectra. The image focused on the predicted Lyα emission region ($\lambda_{\rm obs}$ = 8850–8997 Å) is shown in the *top left panel*, as underlined by the magenta part of the spectrum in the inset of Figure 11.3. The continuum, and thus point-source image, is displayed in the *top right panel*, created by collapsing the datacube channels surrounding the quasar continuum emission. In the inset of Figure 11.3, the wavelengths integrated into this image is marked in green ($\lambda_{\rm obs}$ = 9100–9200 Å). Finally, the *bottom panel* displays the pseudo-narrowband image centered on the Lyα line after the quasar point source has been removed using the PSF subtraction approach described in Section 12.1. As shown in the point-source-subtracted residual image, there is no evident detection of the Lyα halo. As an aside, the bright blob in the south direction originates from a foreground galaxy at $z \approx 0.29$.

12.2 The Non-detection of an Extended Lyα Emission

Figure 12.1 shows the MUSE-based images of PSO J083+11. The quasar's Lyα and continuum spectra are retrieved utilizing a radius of 0.″75, as seen by the dotted black circle in the images. The left panel shows the produced pseudo-narrowband image focused on the Lyα line, while the middle image shows a continuum image utilized as a quasar PSF model. The right panel shows the quasar point-source-subtracted image, equivalent to the continuum minus the Lyα image.

The image does not appear to have a noticeable halo with high surface brightness. We then follow Drake et al. (2019) and perform aperture photometry using various radii to produce an azimuthally-averaged radial light profile of the putative extended Lyα emission (see the result in Figure 12.2). The continuum-subtracted image 1σ surface brightness limit is 2.76×10^{-18} erg s^{-1} cm^{-2} arcsec^{-2}, corresponds to an upper limit of Lyα luminosity of $\log L_{\mathrm{Ly}\alpha} \lesssim 43.46$ erg s^{-1} at 1″ aperture radius. Furthermore, we discover a minor halo flux detection inside a 0.″6 aperture, but no visible extended Lyα emissions outside this region.

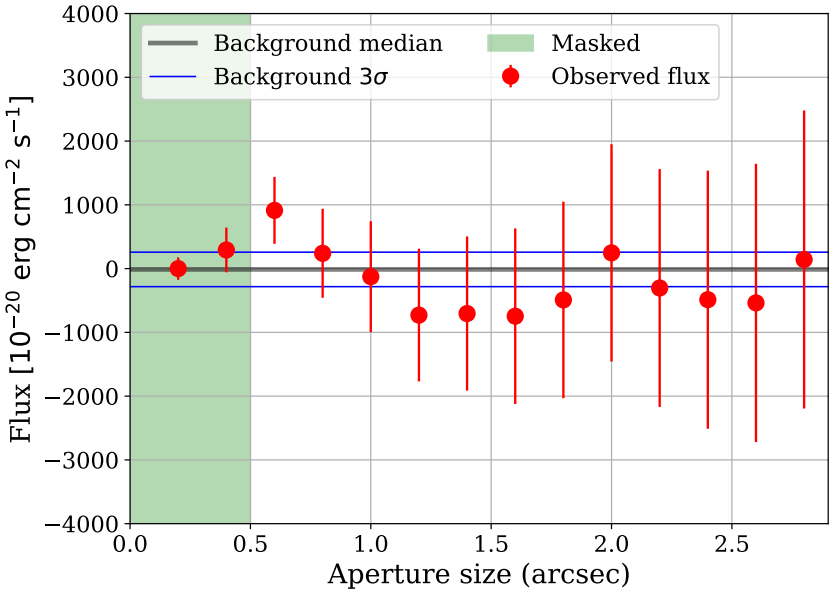

Figure 12.2. PSO J083+11's azimuthally averaged radial light profile, calculated from the point-source-subtracted image centered around the Lyα wavelengths. The halo flux is tentatively detected within a 0.″6 aperture radius, though there are no visible extended emissions on the larger radii.

Previous research found that the Lyα halo brightness is not directly related to the quasar's instantaneous ionizing flux, measurable using the rest-frame 1450 Å absolute magnitude (M_{1450}; e.g., Arrigoni Battaia et al. 2019; Drake et al. 2019). In other terms, the circumgalactic medium parameters like ionization state, temperature, and density have a more significant role in generating the Lyα halo emission (see e.g., Mackenzie et al. 2021). Farina et al. (2019) examined 31 quasars, 19 of which have absolute magnitudes equivalent to PSO J083+11, i.e., $-26 \lesssim M_{1450} \lesssim 27$. We then compute the limit of our MUSE data surface brightness based on Farina et al. prescription to perform a direct comparison. The estimation is done by collapsing five wavelength layers – or 6.25 Å – around the estimated position of the PSO J083+11's Lyα emission.

Following that, for a circular aperture with a radius of 1″, we find a 5σ surface brightness limit of 0.29×10^{-17} erg s^{-1} cm^{-2} arcsec^{-2}. This suggests that our data is equivalent to Farina et al. samples depth, i.e., surface brightness limits of $0.1–1.1 \times 10^{-17}$ erg s^{-1} cm^{-2} arcsec^{-2}.

Interestingly, ten of 19 quasars in the Farina et al. subsample have halos with luminosities of $\log \mathrm{Ly}\alpha = 42.9–44.3$ erg s^{-1}, whereas the other nine have no indications of extended Lyα emission. In other terms, at the present depth of our MUSE data, there is a $\sim 50\%$ chance that the PSO J083+11's Lya halo is inherently non-existent and a 50% chance that it presents but is beyond our detection limit. However, if we wish to reduce the present surface brightness limit by a factor of two, we would need additional ten hours of observation time – both for PSO J083+11 and each of the nine similar quasars from Farina et al. (2019). We also identify two noticeably fainter quasars, J2329−0301 ($M_{1450} = -25.19$) and J2228+0110 ($M_{1450} = -24.47$), which have halos with luminosities of $\log \mathrm{Ly}\alpha > 43.7$ erg s^{-1}. It is also worth noting that none of the three young quasars with the calculated lifetimes of $t_{\mathrm{Q}} \sim 10^3–10^4$ yr – namely, J2229+1457 ($M_{1450} = -24.72$), J0100+2802 ($M_{1450} = -29.09$), and J2100−1715 ($M_{1450} = -25.50$) – reveal the existence of an extended Lyα emission (Farina et al. 2019; Davies et al. 2020b; Eilers et al. 2021). In the context of PSO J083+11, this might mean that there is not enough Lyα gas in the vicinity of the central quasar to produce a halo or that ionizing radiation from the young quasar has not had the time to reach far enough. It is worth noting that the light travel time for a 0.″6 (or 3.32 pkpc) halo size is $\sim 10^4$ yr.

Chapter 13

Discussion on the Quasar Absorber and the Damping Wing Profile

The content of this chapter is based on the work originally published as ***Andika, I. T.****, Jahnke, K., Bañados, E., et al. (2022; AJ 163: 251).*

13.1 Elemental Abundance Ratios

The newly-discovered $z = 6.314$ proximate absorber discussed here is similar to the low-ionization systems characterized by previous studies (e.g., Cooper et al. 2019; Simcoe et al. 2020), in which large column densities of elements such as Mg II, C II, and O I are observed but no absorptions from the highly ionized elements such as C IV and Si IV are identified. In our situation, we discover $\log N_{\rm MgII} = 13.33 \pm 0.03$ cm^{-2}, $\log N_{\rm CII} = 14.23 \pm 0.09$ cm^{-2}, $\log N_{\rm OI} = 14.53 \pm 0.32$ cm^{-2}, $\log N_{\rm SiIV} < 12.91$ cm^{-2}, and $\log N_{\rm CIV} < 13.87$ cm^{-2}. This source also contrasts from the typical low-redshift DLAs ($2 \lesssim z \lesssim 4$), which are likely to contain the C IV absorptions, although this is not surprising for the given redshift because of the decreasing rate of the high-ionization absorbers at $z \gtrsim 5$ (Cooper et al. 2019). However, the lack discovery of Mg I with $\log N_{\rm MgI} < 11.98$ cm^{-2} suggests some ionization degree from the radiation field originates from the massive stars in the far-ultraviolet domain (Simcoe et al. 2020). Furthermore, we are unable to locate additional related metal line absorptions such as Si II, Al II, and Fe II, namely, $\log N_{\rm SiII} < 13.16$ cm^{-2}, $\log N_{\rm AlII} < 12.15$ cm^{-2}, and $\log N_{\rm FeII} < 12.67$ cm^{-2}, that we would anticipate for a particularly strong DLA absorber.

In Table 13.1, we give the elemental ratios scaled to the solar metallicities (Asplund et al. 2009). We obtain the solar abundances for O and C from the photospheric values, but for the other elements, we use the meteoritic data (see, for example, Bañados et al. 2019). It is worth noting that that the observed $\log N_{\rm HI} = 20.03 \pm 0.30$ cm $^{-2}$ denotes that this cloud is more

comparable to a sub-DLA system ($19.0 < \log N_{\rm HI} < 20.3$ cm^{-2}; Milutinovic et al. 2010; Cooper et al. 2019) and the real abundances may require dust depletion and ionization corrections totaling $\sim$ 0.0–0.7 dex. (e.g., Milutinovic et al. 2010; Quiret et al. 2016; Berg et al. 2021).

The [C/O] elemental ratio is generally expected to increase linearly with the metallicity in the $-0.5 <$ [C/O] < 0.5 and [O/H] > -1 regime. Akerman et al. (2004) explained that this phenomenon was caused by the rise in carbon production by massive rotating stars – which also increases with metallicity – as well as the delayed carbon production from the lower-mass stars. At [O/H] $\lesssim -1$, on the other hand, there is an opposite trend found in the metal-poor DLAs (Cooke et al. 2017; Bañados et al. 2019) and metal-poor stars (Akerman et al. 2004; Fabbian et al. 2009) – i.e., a rise in [C/O]. PSO J083+11 appears to follow this empirical pattern, with comparable [C/O] abundance and [O/H] metallicity to other metal-poor DLAs (see the red square in Figure 13.1). The computed abundance is [C/O] $= -0.04 \pm 0.33$, and the deduced metallicity is [O/H] $= -2.19 \pm 0.44$. Further references on the probable formation scenarios that might elucidate the chemical composition of the DLAs can be found in Cooke et al. (2011) and Ma et al. (2017).

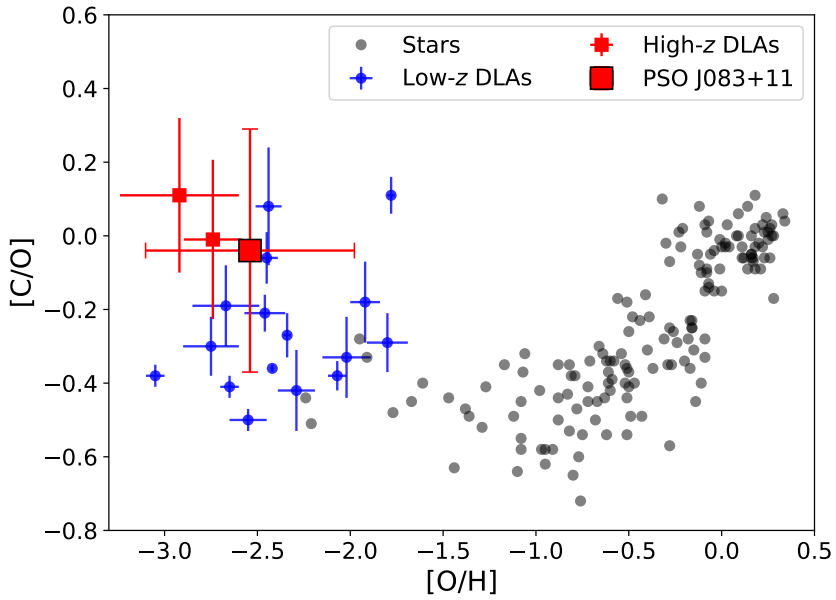

Figure 13.1. Relationship between [C/O] chemical evolution and [O/H] metallicity is presented. The Milky Way star measurements from Fabbian et al. (2009) and Nissen et al. (2014) are signified by grey circles, whereas low-redshift DLAs ($2 \lesssim z \lesssim 4$) from Cooke et al. (2017) are designated by blue circles. The red squares represent the $z \gtrsim 6$ metal-poor DLAs from Bañados et al. (2019) and D'Odorico et al. (2018). We provide a metallicity-corrected value for the sub-DLA toward PSO J083+11 using a correction factor of 0.35 ± 0.35 dex (see text) to account for ionization and depletion impacts. As a result, the computed [O/H] changes from -2.19 ± 0.44 to -2.54 ± 0.56.

X	$\log \epsilon(\mathrm{X})_\odot$	$\log N_\mathrm{X}$ (cm^{-2})	[X/H]
H	12.00	20.03 ± 0.30	–
C	8.43	14.23 ± 0.09	-2.23 ± 0.31
O	8.69	14.53 ± 0.32	-2.19 ± 0.44
Mg	7.53	13.33 ± 0.03	-2.23 ± 0.30
Al	6.43	< 12.15	< -2.31
Si	7.51	< 13.16	< -2.38
Fe	7.45	< 12.67	< -2.81

Table 13.1. Elemental abundances of the $z = 6.314$ sub-DLA in the sightline toward PSO J083+11. The computed abundances do not account for the dust depletion and ionization corrections. The reported ratios are scaled to the solar values, i.e., $[\mathrm{X/Y}] = \log(N_\mathrm{X}/N_\mathrm{Y}) - \log(N_\mathrm{X}/N_\mathrm{Y})_\odot$. Note that by definition, $\log \epsilon(\mathrm{X})_\odot = 12 + \log(N_\mathrm{X}/N_\mathrm{H})_\odot$.

13.2 Proximate Absorber and Proximity Zone Truncation

Around the edge of the reionization era ($z \sim 6$), there exist the IGM zones with largely remaining neutral hydrogen components, inhibiting all photon transmission blueward of the Lyα wavelength (e.g. Gunn & Peterson 1965). A bright quasar, on the other hand, can ionize the surrounding medium with its strong radiation, resulting in a bubble of boosted transmission in the neighboring Lyα forest known as the proximity zone (see, for example, Fan et al. 2006; Eilers et al. 2017).

We suggested in Andika et al. (2020) that PSO J083+11 has a tiny proximity zone in absolute terms ($R_\mathrm{p} = 1.17 \pm 0.32$ pMpc). This signature might be caused by the limited lifespan of an unobscured accretion phase – and hence unobscured emission – into its surroundings ($t_\mathrm{Q} = 10^{3.4 \pm 0.7}$ yr; i.e., a young quasar). This measured proximity zone is significantly smaller than that of typical $z \sim 6$ quasars with the same luminosities as PSO J083+11, i.e., $R_\mathrm{p,typical} \sim 4$ pMpc (Eilers et al. 2020). Accordingly, the accretion lifetime can be deduced from the proximity zone extent, where smaller sizes correspond to younger lifespans (Eilers et al. 2018b; Davies et al. 2020a; Eilers et al. 2020; Chen & Gnedin 2021). However, given the limitations of our earlier data, we were unable to determine if the proximate absorber may have a substantial role in limiting ionizing radiation from the central quasar to the IGM, perhaps causing the proximity zone calculation to be erroneous.

We have improved this by finding and constraining the $z = 6.314$ sub-DLA with a neutral hydrogen column density of $\log N_\mathrm{HI} = 20.03 \pm 0.30$ cm^{-2}. Subsequently, we use a grid of constant $\overline{x}_\mathrm{HI}$ and proximity zone sizes to walk through a variety of IGM damping wing forms in Section 11.3, then fit a Voigt function as the sub-DLA model to the already attenuated continuum. Consequently, we can get the lowest limit of the proximity zone size from this exercise, that is, $R_\mathrm{p} \gtrsim 1.35$ pMpc, or corresponds to a lifetime of $t_\mathrm{Q} \gtrsim 10^{3.5}$ yr. We emphasize that if the quasar's ionization bubble approaches the sub-DLA site and beyond but is concealed from the observer, the proximity zone will no longer be a good tracer for the accretion lifetime

estimate. Hence, another independent diagnostic for the young quasar lifetime would be necessary.

We obtain such evidence given the observed Lyα halo size of PSO J083+11 in this circumstance. As an estimation, we calculate the size as the distance traveled by light from the accretion disk in the center to the halo, i.e., $R_{\rm halo} = c \times t$. We define the speed of light as c along with the time it takes for light to travel as t. Figure 12.2 shows the identification of a halo inside a 0.″6 aperture radius, but then, the flux decreases and reaches the background level at roughly 1″. Therefore, the halo might have a minimum projected size of 3.32 pkpc and a maximum radial extension of 5.54 pkpc, with no detection of extended Lyα outside this radius. This halo size translates to a light travel time of $t \approx 10^4$ yr, giving further and additional evidence justifying the notion of young quasar for PSO J083+11. If the quasar has been active for a much longer time (i.e., $t_{\rm Q} \gtrsim 10^5$ yr), but its ionizing radiation is hidden due to the obscuration along the observer's sightline, the Lyα halo of this source is likely to extend along the other unobscured line of sights. (Farina et al. 2019; Eilers et al. 2021). This argument is unlikely to be valid for PSO J083+11 since there is no evidence of the existence of Lyα halo. In contrast, if the quasar's luminous accretion has only recently been active, the Lyα ionized nebula is expected to be small or non-existent (Eilers et al. 2018a; Andika et al. 2022).

13.3 Looking for the Sub-DLA Host Galaxy Emission

Finding the associated emission from the $z \gtrsim 2$ DLA host galaxies is a tricky undertaking due to their intrinsic faintness (e.g., Kulkarni et al. 2006; Fumagalli et al. 2015). So far, only a few tens of them have been discovered, either at the optical/near-infrared or far-infrared wavelengths (e.g., Krogager et al. 2017; Fynbo et al. 2018; Kanekar et al. 2018; Møller et al. 2018; Klitsch et al. 2019; Neeleman et al. 2019, 2020). Using Atacama Large Millimeter/submillimeter Array (ALMA; C43-4 array configuration) data collected by Andika et al. (2020), we attempt to look for the emission associated with the sub-DLA toward PSO J083+11. The [C II] 158 μm fine-structure line is redshifted within the wavelengths accessible by ALMA band-6 at $z \sim 6.3$, which helps locate the companion galaxy near PSO J083+11. For further information on the data reduction, we refer the reader to see Chapter 9 or Andika et al. (2020). In short, the resulting datacube has a spectral window of 257.5–261.1 GHz, a synthetic beam of 0.″42 × 0.″37, a channel width of 30 MHz, and an RMS noise level of $\sim$ 0.24 mJy beam^{-1}.

We find an emission associated with a companion galaxy, J083.8372+11.8474, toward the southwest from PSO J083+11, with a projected angular distance of 2.″88, or corresponds to a projected physical separation of $\approx$ 16 kpc. We then construct a zeroth-moment map of [C II] 158 μm with a velocity width of 800 km s^{-1} centered at $\nu_{\rm obs} = 259.25$ GHz and show it in the left panel of Figure 13.2. The companion galaxy is detected as a compact single blob with the size of 0.″89 × 0.″37. At its redshift, this size corresponds to a physical extent of 4.9 kpc × 2.1 kpc. The above size corresponds to the major and minor axis FWHMs, which are computed by matching a two-dimensional Gaussian profile to the velocity-integrated [C II] map. Then, we utilize a 1″ aperture to retrieve the spectrum surrounding the companion galaxy's position.

This aperture size is chosen since there are no visible emissions outside this area. The preceding analysis resulted in the finding of a [C II] emission at $z = 6.3309 \pm 0.0004$ with an observed frequency of $\nu_{\rm obs} = 259.25 \pm 0.02$ GHz.

The [C II] line luminosity is then calculated using the Carilli & Walter (2013) prescription, with the final value being $L_{\rm [CII]} = 6.22 \pm 0.14 \times 10^8 L_\odot$. Following that, the SFR can be approximated using the well-known SFR–$L_{\rm [C\,II]}$ conversion for high-z galaxies (De Looze et al. 2014), yielding SFR = 71 $M_\odot$ yr^{-1}. Note that the previously mentioned relation involves a systematic uncertainty of a factor of ≈ 2.5, resulting in a range of 29–179 $M_\odot$ yr^{-1} for the derived SFR.

Neeleman et al. (2019) previously reported the [C II] emission from a sample of four DLAs at $z \sim 4$. These DLA host galaxies have a rather wide projected separation from the central quasar (i.e., 16–45 kpc), SFRs of 7–110 $M_\odot$ yr^{-1}, and luminosities of $L_{\rm [CII]} = 0.36$–$30 \times 10^8 L_\odot$. The companion galaxy we discovered here has [C II] line characteristics identical to the Neeleman et al. DLAs. The [C II]-based redshift of the PSO J083+11's companion galaxy, on the other hand, differs considerably from our sub-DLA's redshift of $z_{\rm DLA} = 6.314$, computed using the centroids of the rest-frame ultraviolet metal-line absorptions. The estimated velocity offset between those two sources is $\Delta V = 692$ km s^{-1}, or roughly twice the FWHM of the [C II] line, indicating that they are most likely unrelated galaxies. Therefore, we find no evidence of the sub-DLA host galaxy emission.

We are likewise unable to determine the optical counterpart of J083.8372+11.8474 with certainty. We look for it by examining the MUSE image around PSO J083+11, superimposed with the [C II] emission from the ALMA data (see Figure 13.3). Then, we also retrieve the associated optical spectrum by employing an aperture with a radius of 0.″5. There are no notable emission lines identified at $\lambda_{\rm obs} = 8839$–8985 Å, where the companion galaxy's Lyα emission is predicted. The weak continuum emission observed in the spectrum is most likely originates from the nearby bright galaxy at $z \approx 0.29$.

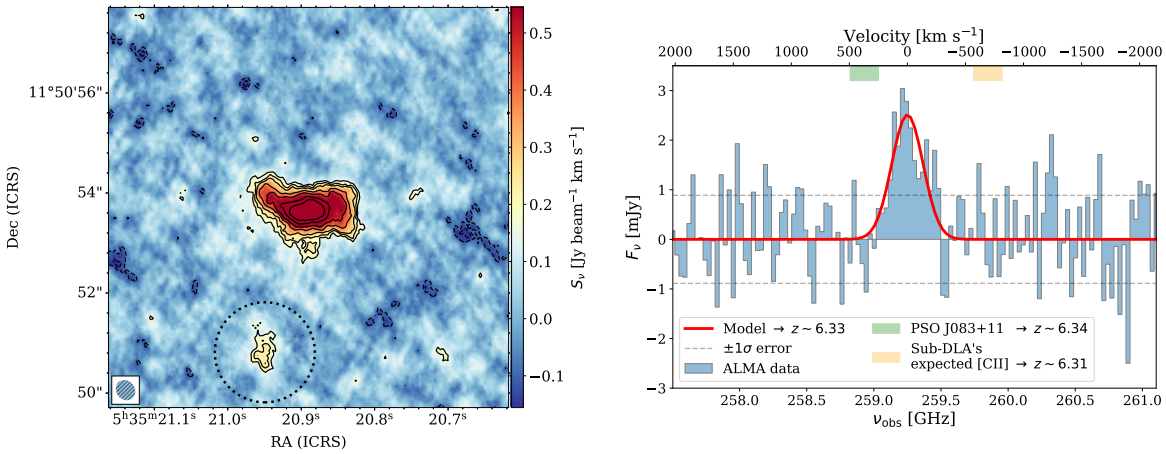

Figure 13.2. *Left panel*: [C II] velocity-integrated map of the sky area surrounding PSO J083+11. A companion galaxy with a projected angular separation of 2.″88, or ≈ 16 kpc at $z = 6.3309$, is discovered in the southwest direction from the central quasar. At the bottom left, the ALMA synthesized beam is displayed. The black solid lines represent the [C II] velocity-integrated flux contours with [3, 4, 5, 7, 9, 12, 15] $\times\sigma$, with $\sigma = 0.053$ Jy beam^{-1} km s^{-1}. The negative contours are presented with the dashed black lines. We utilize an aperture with a radius of 1″ (corresponding to 5.5 kpc, see the dotted circles) in this case to extract the spectrum and calculate the overall [C II] flux density of the companion galaxy. *Right panel*: companion galaxy's [C II] emission at the observed-frame frequency of $\nu_{obs} = 259.25$ GHz. The blue, dashed gray, and solid red lines depicted in the figure represent the measured flux density, its associated $\pm 1\sigma$ uncertainty, and the fitted Gaussian model, respectively. The velocity axis is shown at the top, centered at $z = 6.3309$. The orange and green areas represent the predicted [C II] center wavelength from a sub-DLA at $z = 6.314$ and PSO J083+11 at $z = 6.3401$ mentioned in the main text.

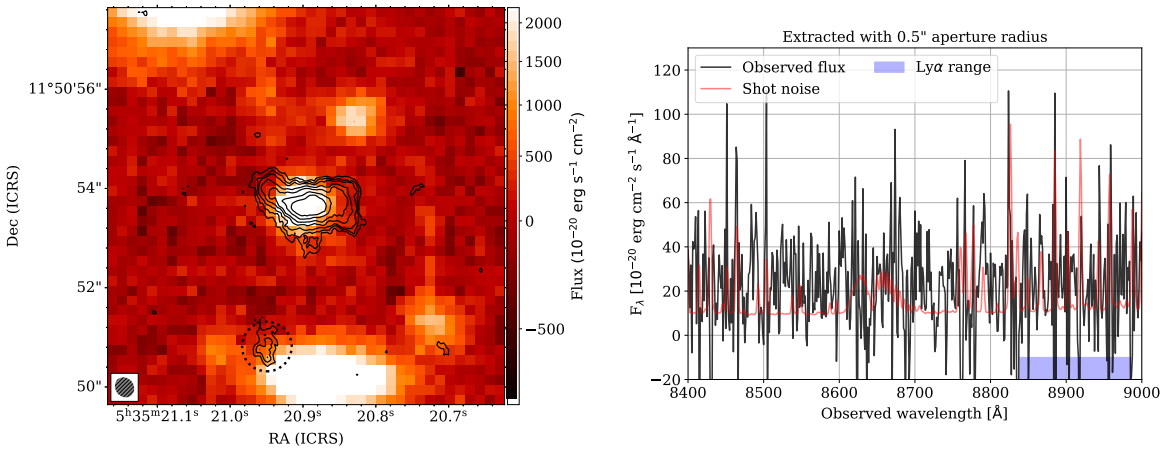

Figure 13.3. *Left panel*: Image of PSO J083+11 is presented, generated by collapsing the $\lambda_{obs} = 8000$–9000 Å MUSE datacube channels. The dark contour represents an overlay of the [C II] emission from the ALMA data. The spectrum is extracted at the area of interest utilizing a 0.″5 aperture radius (dotted circles). *Right panel*: MUSE spectrum of J083.8372+11.8474 (black line) – i.e., the $z = 6.3309$ companion galaxy neighboring PSO J083+11 – and the related shot noise (red line). We discover no conspicuous emission in the wavelengths where the companion galaxy's Lyα is predicted (blue area). A modest continuum emission is visible toward the southeast, which originates from a galaxy at $z \approx 0.29$.

13.4 Summary and Conclusion

We presented a study of the environment and metal absorbers toward PSO J083+11, a weak-line quasar at $z = 6.3401$. The Gemini/GNIRS, Magellan/FIRE, and VLT/MUSE spectra show the strong Lyα absorption as well as various metal lines (e.g., Mg II, O I, and C II). These findings imply the presence of a $z = 6.314$ sub-DLA system and a strong $z = 2.2305$ Mg II absorber. We discover that the observed Lyα damping wing signal is formed by a sub-DLA with a column density of the neutral hydrogen of $\log N_{\rm HI} = 20.03 \pm 0.30$ cm^{-2} and absorption from an IGM with a neutral fraction of approximately 10%. The abundance ratio of [C/O] $= -0.04 \pm 0.33$ and metallicity of [O/H] $= -2.19 \pm 0.44$ of the sub-DLA near PSO J083+11 are comparable to those of low-z metal-poor DLAs. The presence of this sub-DLA shortens the proximity zone of PSO J083+11 and complicates the quasar age calculation. At the same time, this quasar displays no trace of an extended Lyα nebula, with an estimated 1σ surface brightness limit of 2.76×10^{-18} erg s^{-1} cm^{-2} arcsec^{-2} at $1''$ aperture, or equivalent to a Lyα luminosity of ≤ 43.46 erg s^{-1}. This non-detection provides alternate and complementary evidence for the young quasar notion, in which the unobscured accretion lifetime results in a tiny or no Lyα halo due to the so-far limited light travel distance.

Observations of the PSO J083+11's narrow-line region may be required in the future to gain further evidence. If this source is still in the early quasar phase, the radial extent of the narrow-line region – which can be probed using [O III] λ5007 or Hα λ6563 – must be small. This study would necessitate JWST mid-infrared measurements with great sensitivity and angular resolution. Establishing a more coherent sample of the young quasars with high black hole masses at this epoch will be the next step in determining whether these are occasional accretion phases in the late stage of SMBH formation. On the other hand, we can also check whether we have reached the limit of observing the bulk of the black hole mass growth using the optical/near-infrared selection techniques. If most SMBH mass build-up occurs through obscured, possibly radiatively inefficient accretion modes, better strategies to find those hidden sources would be needed.

From a completely different perspective, analyzing the absorption systems toward the quasars in the highest-redshift frontier can help us learn more about the period of reionization and the birth of the earliest galaxies. These systems, which at $2 \lesssim z \lesssim 4$ resemble the modern-day dwarf galaxies (Cooke et al. 2015), are expected to play crucial roles in advancing the IGM reionization, as anticipated by numerical models. They have seen a significant enrichment of their gas while keeping a high neutral hydrogen fraction in just a few hundred million years after the Big Bang, which gives an essential indication regarding the associated contributing star populations. However, even with the next-generation telescope, direct identification of these dwarfs will be difficult. Hence, "quasar absorption spectroscopy" is possibly still the greatest means to investigate them in fine detail – and hunting for and discovering more higher-redshift DLAs will be beneficial, although challenging.

Part V

Discussion and Conclusion

Chapter 14

Review of this Dissertation

Quasars in the first billion years of the universe are prime laboratories for understanding the formation, growth, and structure of the first supermassive black holes and galaxies. As part of the endeavor to expand the number of known quasars in the highest-redshift frontier, we present a novel method to discover quasars and lens systems at $z \gtrsim 6$, expanding the selection space missed by many previous quasar surveys. The main results of this dissertation are summarized as follows.

In Chapter 5, we introduce the dataset and survey technique that we employ for discovering the $z \gtrsim 6$ (lensed) quasar candidates. Specifically, we first preselect the candidates based on their optical and infrared photometric colors. Then, spectral energy distribution modeling is applied to compute the probabilities of each candidate for being a quasar or other contaminants. At the end of this selection, we obtain 155 quasar candidates extracted from the northern dataset (Pan-STARRS + DELS + UKIDSS + UHS + unWISE), complemented with 21,879 quasar plus lens candidates from the southern dataset (DES + VHS + unWISE).

In Chapter 6, we focus further on selecting potential lenses using the convolutional neural networks algorithm. The datasets for training and validating our model are constructed semi-empirically via strong lensing simulation. In particular, we paint simulated lensed arcs over actual galaxy images to generate realistic galaxy-quasar lens models, optimized to find systems with small image separations – i.e., Einstein radii of $\theta_{\rm E} \leq 1''$. From about thousands of candidates that are initially existed in the southern dataset, this search technique leads us to find 30 lens and six quasar candidates. Hence, we suggest that automated spectral modeling and deep learning classification, when augmented with modest human input, are promising for identifying strong lenses in large databases.

In Chapter 7, we provide the details of our spectroscopic follow-ups, which result in the discovery of a unique $z = 6.3401$ weak-line quasar, i.e., PSO J083+11. Based on Gemini/GNIRS near-infrared spectroscopy, we model the Mg II line and the underlying continuum emissions,

resulting in a black hole mass of $\log(M_{\rm BH}) = 9.30^{+0.16}_{-0.10}\,M_\odot$ and an Eddington ratio of $L_{\rm bol}/L_{\rm Edd} = 0.51^{+0.13}_{-0.17}$. These calculations indicate that PSO J083+11 is powered by an energetic black hole with an accretion rate identical to other Type 1 quasar populations. The broad-line emissions of this source are weak, e.g., REW (Lyα + N V) = $5.65^{+0.72}_{-0.66}$ Å, implying that it belongs to the population of weak-line quasars. The weakness of Lyα + N V is not owed to the strong absorption by the intergalactic medium in the sightline. This proposition is strengthened by the absence of C IV emission, with REW (C IV) $\leq$ 5.83 Å, which indicates that the strength of the broad-line region emission is inherently weak. The spectrum reveals a small proximity zone size, where $R_{\rm p} = 1.17 \pm 0.32$ pMpc, suggesting a present quasar age of only $\approx 10^3 - 10^{4.5}$ yr, which creates a significant challenge for explaining how to grow a supermassive black hole in the center of PSO J083+11.

In Chapter 8, we report our high-resolution near-infrared observations with HST to test if strong gravitational lensing impacts the PSO J083+11's apparent flux. From the HST/WFC3 F125W image, we find a putative foreground galaxy with a magnitude of 25.42 ± 0.07 positioned at $\approx 1''$ to the southwest of the central quasar. Assuming a model consists of a star-forming galaxy at low-z and a point-mass lens, we put an upper limit of the possible lensing magnification, i.e., $\mu \leq 1.07$, implying no substantial boosting effect on the apparent quasar emission. The morphology of the quasar is also seen as a point source with no extended emission.

In Chapter 9, we discuss the PSO J083+11's host galaxy properties, including the dust continuum and [C II] emissions along with the corresponding star formation rate, utilizing ALMA data. We derive here a precise redshift of $z_{\rm [C\,II]} = 6.3401 \pm 0.0004$ from the observed [C II] line center. The [C II] extended morphology might be caused by a merger event or an unrelaxed continuous formation. Utilizing a modified blackbody model to fit the Rayleigh-Jeans tail of the dust emission put a limit on dust mass of $M_{\rm dust} = (4.88 \pm 0.14) \times 10^8\,M_\odot$ and star formation rate of ${\rm SFR_{TIR}} = 900{-}7600\,M_\odot\,{\rm yr}^{-1}$. This calculations agrees with the [C II]-based SFR, i.e., ${\rm SFR_{[C\,II]}} = 800{-}4900\,M_\odot\,{\rm yr}^{-1}$. At the time of this dissertation writing, PSO J083+11 is one of the brightest [C II] emitters known at cosmic dawn.

In Chapter 10 we present comprehensive discussions concerning the potential reasons that might contribute to the weak-line nature of PSO J083+11. Given the accretion lifetime of PSO J083+11 and the timescale of broad-line region formation, we propose that the weak-line nature of this source is due to a still-emerging broad-line region. Alternative ideas such as strong lensing affecting the continuum emission or soft continuum paradigm due to a super-Eddington accretion appear improbable. However, it is worth noting that given the absence of X-ray spectroscopy, we cannot entirely disregard the presence of shielding gas between the accretion disk and the broad-line region. Overall, this quasar shows a complex picture of an early supermassive black hole that recently commenced its relatively mild accretion.

In Chapter 11, we search for any putative absorbers in the line of sight of PSO J083+11. We start by introducing the spectroscopic data acquisition and reduction utilized for this analysis. The Gemini/GNIRS, Magellan/FIRE, and VLT/MUSE spectra reveal the strong Lyα absorption as well as various metal lines (e.g., Mg II, O I, and C II). These discoveries suggest the presence

of a $z = 6.314$ sub-DLA system and a strong $z = 2.2305$ Mg II absorber. We then find that the observed Lyα damping wing profile is shaped by a sub-DLA with a neutral hydrogen column density of $\log N_{\rm HI} = 20.03 \pm 0.30$ cm^{-2} and absorption from an intergalactic medium with a neutral fraction of approximately 10%.

In Chapter 12, we attempt to search and characterize the Lyα halo around PSO J083+11. We first describe our PSF modeling and method for subtracting the quasar continuum emission to constrain the Lyα halo size. Accordingly, we find that PSO J083+11 exhibits no sign of any extended Lyα nebula, with a 1σ surface brightness limit of 2.76×10^{-18} erg s^{-1} cm^{-2} arcsec^{-2} at $1''$ aperture, or corresponds to a Lyα luminosity of ≤ 43.46 erg s^{-1}.

In Chapter 13, we constrain the elemental abundances of the intervening absorption cloud toward PSO J083+11. The observed abundance ratio [C/O] $= -0.04 \pm 0.33$ and metallicity [O/H] $= -2.19 \pm 0.44$ of the sub-DLA near PSO J083+11 are analogous to those of metal-poor DLAs at low-z. The existence of this sub-DLA also truncates the proximity zone of PSO J083+11 and problematizes the quasar age estimation. However, at the same time, this quasar exhibits no trace of an extended Lyα halo. This non-detection gives alternate proof for the young quasar idea, where the short unobscured accretion lifetime results in a small or no Lyα halo caused by the limited light travel time.

Further statistical analyses, backed by more samples of weak-line quasars at the highest accessible redshift frontier, are critical for establishing the relationships between typical quasars, young sources, and those that are weak lines. This investigation will enable us to apprehend the quasar evolution, the rapid growth of the earliest supermassive black holes, and the structure evolution at cosmic dawn. If most supermassive black hole mass growth occurs via obscured, possibly radiatively inefficient accretion phase, better strategies to find those hidden sources would be required. In addition, despite being a rare situation, some high-z quasars will be gravitationally lensed. Such systems are one of the best alternatives to probe intrinsically lower-mass and -luminosity quasars. They also allow us to study the quasar host galaxies in unprecedented detail, thanks to flux magnification and, very importantly, an increased effective spatial resolution.

This dissertation advances our knowledge of the high-z quasar population in at least two aspects. First, we present a comprehensive study of a weak-line quasar's physical characteristics and its connection to the cases of young accretion lifetime. Second, we introduce a novel selection technique to discover hidden populations of lenses. In the next chapter, we will explore potential future research aimed to tackle some unsolved questions and challenges revealed by this work, taking advantage of future observational facilities and surveys.

Chapter 15

Future Directions

High-z quasars are essential tracers for understanding the primordial black hole evolution and the assembly of massive galaxies at cosmic dawn. Decades of multiwavelength high-z quasar surveys have advanced our knowledge of the early universe physics, opening up some new puzzles and questions that remain unsolved, which can be summarized as follows.

Supermassive black holes with masses up to 10^{10} $M_\odot$ already found within the $\lesssim$ 1 Gyr of cosmic history, putting the most stringent constraints on the black hole formation model. The first question is, how massives were the first black hole seeds, and how did they develop so quickly to become the high-z active galaxies we see today? Then, the number density of bright quasars decreases rapidly at $z \gtrsim 7$, making them the rarest sources detected in the most distant universe. Hence, are we finally approaching the earliest luminous quasars epoch that we can reach? In addition, the host galaxies of luminous $z \gtrsim 6$ quasars are rapidly forming stars with a diverse spectrum of masses, kinematics, and large-scale environments. Therefore, what is the correlation between the early black hole seeding and the galaxy formation? Several revolutionary instruments are planned to be operational in the near and long-term future, bringing a new foundation for the quasar survey and pushing the limit to the lower luminosities and higher redshifts regime.

15.1 The Next Generation of Extragalactic Surveys

The Rubin Observatory Legacy Survey of Space and Time (LSST; Ivezić et al. 2019) is a ground-based optical survey designed to monitor the 18,000 deg^2 sky seen from Cerro Pachón, northern Chile. The primary aims of this project are for investigating dark energy and dark matter, probing the Solar System, studying the transient sky, and charting the Milky Way. The telescope has a primary mirror of 8.4 m, complemented with a 3.2 Gigapixels camera with six bandpasses (*ugriz*) covering 320–1050 nm wavelengths, producing a 9.2 deg^2 field of view. The project is currently under development, and regular survey activities will commence in

late 2023. Interestingly, together with the produced color and variability data, LSST offers deep co-added images ($r \approx 27.5$) and proper motion measurements, which are beneficial for improving our quasar selection strategy.

Euclid is a space-based survey mission led by the European Space Agency that will exploit the weak gravitational lensing and galaxy clustering phenomena to characterize the dark energy and gravity in our universe (Laureijs et al. 2011). The instrument will be launched in 2023 and placed at the second Lagrange point, a location where the gravitational pull from the Earth and Sun balance the orbital motion of a satellite. By utilizing its 1.2 m telescope, Euclid will conduct wide-area imaging and spectroscopy for six years in visual (550–920 nm) and near-infrared (0.92–2.0 μm) wavelengths, covering $\approx 15,000$ deg^2 of the extragalactic sky. The expected 5σ image depths are 24.5 and 24.0 mag in the visual and YJH bands, respectively (Scaramella et al. 2021; Euclid Collaboration et al. 2022).

The Wide-Field Infrared Survey Telescope (Spergel et al. 2013, 2015) is a National Aeronautics and Space Administration project scheduled to launch in the mid-2020s. In the current plan, the spacecraft will be equipped with a 2.4 m telescope complemented with a wide-field near-infrared (0.76–2.0 μm) camera and a coronograph. These instruments will be capable of imaging as well as performing grism and integral-field spectroscopy. As part of its primary goals, WFIRST will study the early cosmos, validate the ΛCDM cosmology, and identify hundreds of new exoplanets. Intriguingly, the planned High Latitude Imaging and Spectroscopy Surveys, in particular, will perform deep observations over the 2000 deg^2 of the sky, down to 26.7 magnitudes at 5σ in the Y-band.

15.2 Pushing the Redshift Frontier of the Quasar Survey

In this decade, we have seen at least three advances in the high-z quasar surveys: (i) discovery of luminous $z \gtrsim 7.5$ quasars from near-infrared observations (Bañados et al. 2018; Yang et al. 2020a; Wang et al. 2021a), (ii) systematic searches of $z \gtrsim 6$ faint quasars from deep-sky optical imaging (Matsuoka et al. 2018a, 2021), and (iii) attempted searches to find hidden populations of lensed quasars (Fan et al. 2019a; Yue et al. 2021a, 2022, Andika et al., in preparation).

It is now well-known that the quasar luminosity function shape evolves mildly up to $z \sim 6$ (Matsuoka et al. 2018a). However, its normalization term, which determines the total spatial density of bright quasars, declines rapidly as the redshift increases (Jiang et al. 2016; Wang et al. 2019). Assuming an exponential decline model, the number density of bright quasars falls by the factor of 3 per redshift unit at $z = 3$–5. Furthermore, at $z = 5$–7, this drop accelerates to the factor of 6. To put it another way, for typical luminous quasars with $M_{1450} = -26$, or corresponds to quasars hosting 10^9 $M_\odot$ black holes presuming Eddington limited accretion, their number density declines to < 1 Gpc^{-3} at $z \gtrsim 6$. Therefore, they are among the scarcest sources detected in the young universe (Bañados et al. 2016).

We anticipate that only one $z \sim 9$ quasar with $M_{1450} < -26$ will be found in the entire observable universe if we extrapolate the number density evolution displayed on the left side

of Figure 15.1. This prediction will test whether $z = 9$–10 is the central era where most bright quasars are established. Within the next decade, new-generation surveys will be able to push the frontier to this redshift range. Reaching this epoch and assembling a large statistical sample of $z = 7$–9 quasars should be top priorities for the high-z quasar community.

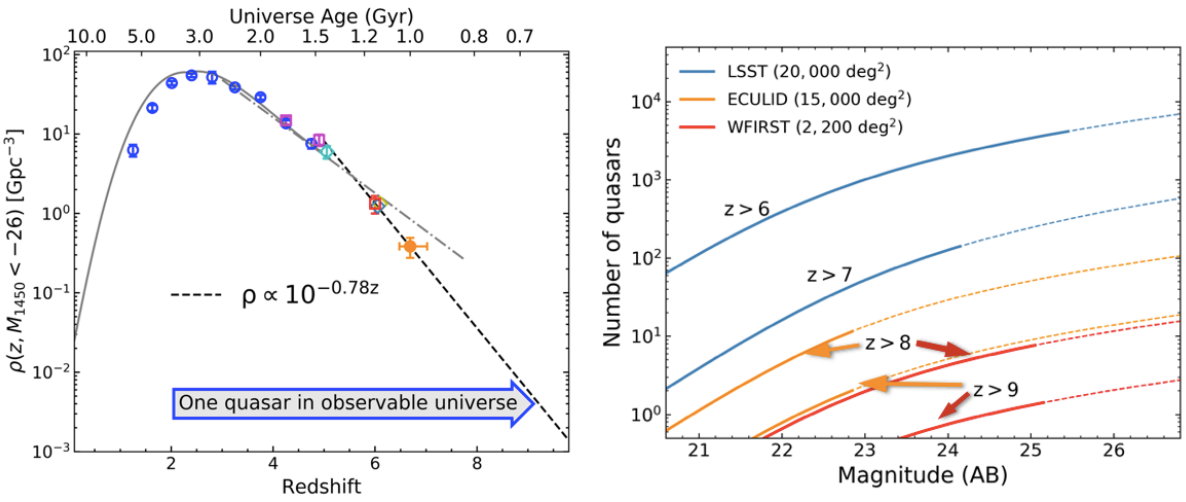

Figure 15.1. *Left panel*: In the early cosmos, the number density of bright quasars declines rapidly. By extrapolating the $z = 5$–7 quasar luminosity functions, we expect to detect only one quasar hosting a 10^9 $M_\odot$ black hole at $z \gtrsim 9$ (Wang et al. 2019). *Right panel*: predicted number of discovered quasars in the upcoming wide-sky surveys – e.g., LSST, Euclid, and WFIRST. Dropout selection would find quasars up to magnitudes of 23–25 (see solid lines), assembling a substantial sample of reionization-epoch quasars at $z \gtrsim 7$, with a few tens $z \gtrsim 8$ sources, eventually reaching $z \sim 9$. Image credit: Fan et al. (2019b).

Up to now, all $z \gtrsim 6$ quasars have been located via wide-field multi-band imaging data, which are then spectroscopically followed up later (e.g., Bañados et al. 2016; Yang et al. 2019b; Wang et al. 2019). Novel search strategies based on machine learning (e.g., Wenzl et al. 2021; Nanni et al. 2021), spectral energy distribution fitting (e.g., Reed et al. 2019; Andika et al. 2020), and Bayesian modeling (e.g., Mortlock et al. 2012; Barnett et al. 2021) approaches have increased the effectivity of quasar candidate search compared to the conventional color-based selection. These methods rely on the continuum dropout induced by the intergalactic medium absorption blueward of the Lyα line as the primary differentiating characteristic to isolate quasars from galactic or low-z contaminants. At $z \gtrsim 7$, the Lyman-break shifts to the near-infrared regime. Therefore, the next generation of sky surveys, particularly those based on Euclid, LSST, and WFIRST, will be critical for discovering and analyzing distant quasars.

The predicted number of discoverable quasars within these surveys is shown in Figure 15.1. This estimation is made by utilizing the luminosity function of $z \sim 6$ quasars from Matsuoka et al. (2018a) and a normalization extrapolated from $z = 5$–6 data (Wang et al. 2019). Considering the depth and area covered by LSST, this survey will provide hundreds of new $z = 6$–7 quasars, allowing us to perform comprehensive statistical studies on them. On the other hand, Euclid and WFIRST will be the principal probe for surveying the universe at $z \gtrsim 8$, where we expect to find tens of quasar samples. Note that survey volumes will limit quasar discoveries at $z \gtrsim 9$, where we predict only a few bright quasars live in this very early epoch.

In addition to that, spectroscopic confirmations of $z \gtrsim 8$ quasar candidates are challenging. These quasars are faint, having AB magnitudes of 22–25, necessitating spectroscopy with large-aperture telescopes. Previous understanding implies that the rate of success of spectroscopic identification at the higher-redshift regime is low. For example, Bañados et al. (2016) and Wang et al. (2019) claimed a quasar identification success rate of $\sim 30\%$ at $z = 6$–7, while the results at $z \gtrsim 7$ are significantly lower ($< 10\%$). We anticipate this efficiency to increase as we discover additional quasars so that our training datasets grow in size. However, identifications at the highest-redshift frontier will remain formidable and time-consuming, especially when using today's generation of 8–10 m telescopes. High-sensitivity spectroscopy with JWST will be very suited for characterizing the already-confirmed quasars. In addition, high-throughput spectrographs with expansive coverage of wavelengths on future telescopes like the European Extremely Large Telescope, Giant Magellan Telescope, and Thirty Meter Telescope (hereafter called ELTs) will be the most effective means for confirming the nature of the quasar candidates. Finally, slitless spectroscopy with Euclid and WFIRST supplies additional tools for directly identifying $z \gtrsim 7$ quasars, producing samples with less color-selection bias.

15.3 Exploring the Co-Evolution of Galaxy and Black Hole

High-z quasars exhibit metal-enriched broad-line emissions in their spectra (Onoue et al. 2020; Schindler et al. 2020). Their host galaxies are one of the most luminous sources seen at (sub)millimeter regimes (Andika et al. 2020), showing a lot of warm dust ($\sim 10^7$–$10^8\ M_\odot$) and cool molecular gas ($\sim 10^9$–$10^{10}\ M_\odot$; Carilli & Walter 2013). Assuming a dust heating process driven by the star formation, this implies star formation rates of a few thousand $M_\odot\ \mathrm{yr}^{-1}$, meaning that the rapid black hole growth should occur concurrently with the build-up of the host galaxy. Sensitive and high-resolution ALMA data show a broad spectrum of host galaxy features among the brightest high-z quasars, such as major mergers with numerous components, isolated rotationally supported systems, and dispersion-dominated compact systems (Novak et al. 2019; Neeleman et al. 2021; Meyer et al. 2022).

Interestingly, the quasar host's dynamical masses, traced with the interstellar [C II] kinematics, seem to be a magnitude lower than the number expected from the black hole–galaxy mass relation found in the local universe (e.g., Decarli et al. 2018). This result implies that the assembly of the supermassive black holes takes place faster than the growth of the associated quasar hosts, at least at $z \gtrsim 6$ (see Figure 15.2). However, this might be induced by possible selection biases as well as unaccounted systematics (Huang et al. 2018; Izumi et al. 2021; Habouzit et al. 2022). On a broader scale, theoretical models imply that bright quasars might reside in the large halos and most crowded locations in the high-z universe (Lapi et al. 2006; Porciani & Norberg 2006). However, observational evidence is currently unclear and paints a complicated picture (Decarli et al. 2017; Mazzucchelli et al. 2017; Ota et al. 2018; Calvi et al. 2019; Mignoli et al. 2020). Luminous high-z quasars are promising tracers for analyzing the growth of the first massive galaxies, but the interaction between galaxy growth and black hole assembly remains puzzling (Fan et al. 2019b).

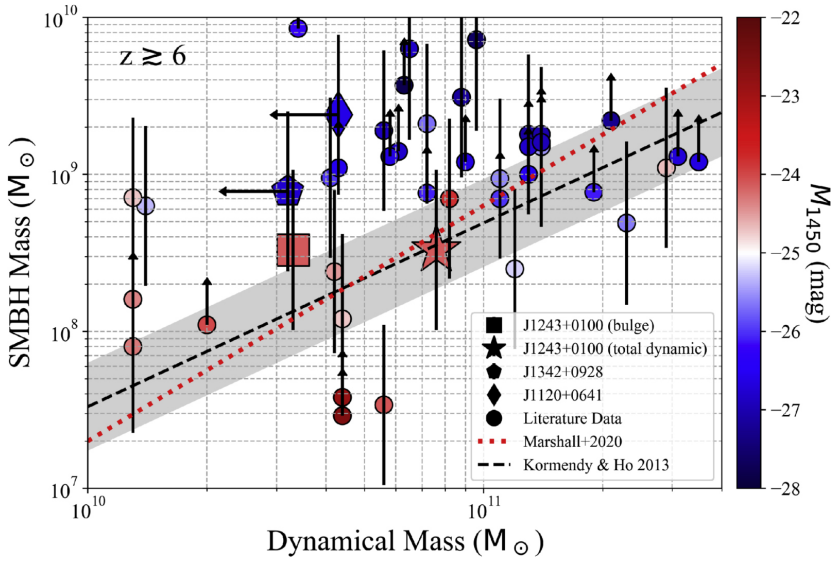

Figure 15.2. Correlation between the host galaxy dynamical mass and the black hole mass for the quasars at $z \gtrsim 6$, differentiated by their M_{1450} (Izumi et al. 2019). The black dashed line represents the black hole–bulge mass co-evolution found at the local universe (Kormendy & Ho 2013), while the dotted red line depicts the predicted correlation for $z \sim 7$ quasars (Marshall et al. 2020a). Most of the luminous quasars ($M_{1450} \lesssim -26$) are observed above the local relation. Image credit: Izumi et al. (2021).

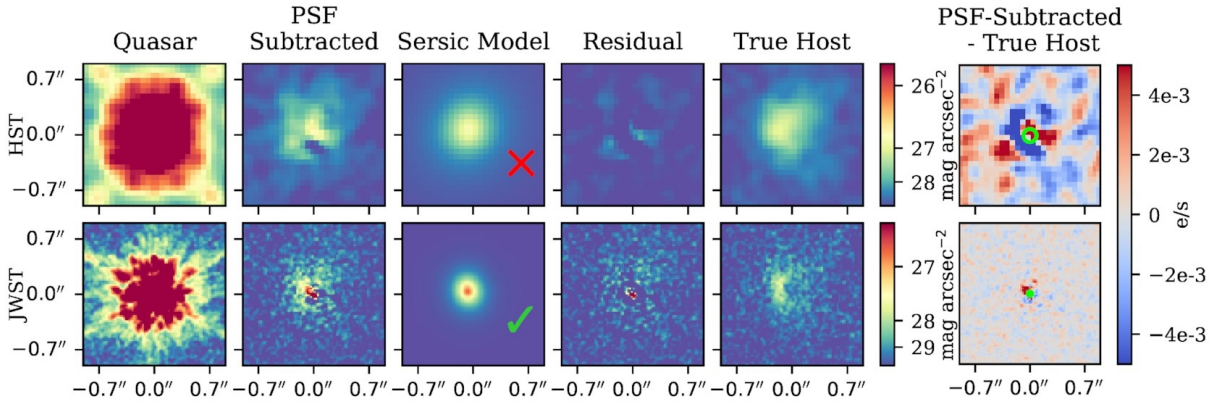

Figure 15.3. Mock images of the quasar host galaxy based on the BlueTides simulation (Feng et al. 2016; Marshall et al. 2020a). The *upper panel* displays HST/WFC3 F160W images, while the *lower panel* depicts JWST/NIRCam F150W images. From left to right, we show the original quasar plus host galaxy image, the residual after PSF subtraction, the best Sérsic model for the galaxy, the residual image after complete model subtraction, the true simulated host image without quasar emission, and the difference between the PSF-subtracted image and the true host image. The green circles represent the PSF size, the green tick indicates a statistically significant detection, and the red cross depicts no quasar host detected. Image credit: Marshall et al. (2021b).

While extremely crucial, direct observation of the nebular emission and stellar light from the $z \gtrsim 6$ host galaxies at rest-frame ultraviolet to near-infrared wavelengths is currently missing. This data will open an alternative window to measure the star formation history and stellar mass as well as to investigate the feedback mechanisms in the quasar hosts (Marshall et al. 2020b,a). The mixture of intense quasar central emission and low surface brightness of the hosts makes

this beyond the capability of the existing observatories, including HST (see Figure 15.3). Such observations will only be possible in the future thanks to effective integral-field spectrographs mounted on the ELTs and JWST (Marshall et al. 2021b). High-fidelity space-based imaging, effective ELTs adaptive optics systems, and high-contrast imaging methods established for exoplanet discovery will allow successful subtraction of central point sources to characterize the star-forming regions and stellar lights in the quasar host galaxies. Deep infrared imaging with JWST and WFIRST, in addition, will enable us to explore low-luminosity galaxies and large-scale structures surrounding the first quasars (Onoue et al. 2021; Wang et al. 2021b, 2020b; Marshall et al. 2021a). ALMA upgrades by incorporating the very-long-baseline interferometry technique to enhance resolution would ultimately allow us to probe the interstellar medium characteristics of the host galaxies down to the scales of individual star-forming regions, i.e., a few parsecs. This kind of investigation might reveal the processes that initiate the formation of the stellar components and explore the galaxy kinematics inside the black hole's sphere of influence. Therefore, these instruments will give a multiwavelength perspective of the quasar hosts, linking the black hole assembly with the emergence of the first massive galaxies.

The most distant bright quasars trace the evolution of black holes at cosmic dawn and their connection to galaxy formation. They are also excellent targets for investigating the intergalactic medium condition during the reionization period. Quasars are multiwavelength and multiscale phenomena by nature. Accordingly, a broad range of new tools is essential to advance the quasar research into the earliest epochs and fainter populations, primarily to establish a comprehensive physical understanding of their characteristics and address fundamental questions related to the origin and evolution of the black holes at cosmic dawn.

***Facilities*:** ALMA, Blanco (DECam), ESO:VISTA (VIRCAM), Gemini:Gillett (GNIRS), HST (WFC3, ACS), Magellan:Baade (FIRE), NTT (SOFI), PS1 (GPC1), UKIRT (WFCAM), WISE.

***Software*:** APLpy (Robitaille & Bressert 2012; Robitaille 2019), Astropy (Astropy Collaboration et al. 2013, 2018), Astroquery (Ginsburg et al. 2019), CosmoCalc (Wright 2006), Dask (Rocklin 2015), Linetools (Prochaska et al. 2016), Lmfit (Newville et al. 2019), Large Survey Database (Juric 2012), Matplotlib (Caswell et al. 2019), NumPy (Harris et al. 2020), Pandas (Reback et al. 2021), Scikit-learn (Pedregosa et al. 2012), SciPy (Virtanen et al. 2020), Spectral-cube (Robitaille et al. 2016), SpectRes (Carnall 2017), TOPCAT (Taylor 2017)

***Notes*:** The image on the cover page reveals how the high-redshift quasar P172+18 and its associated radio jets could have appeared. Today, this is one of the farthest quasars with radio jets ever discovered, and it has been characterized with the aid of ESO's Very Large Telescope. This source is so far away that the light from it has traveled for nearly 13 billion years to reach our Earth. Credit: ESO/M. Kornmesser.

Appendix A

Test on the Confirmed Lensed Quasars

The content of this chapter is adapted from the manuscript ***Andika, I. T.****, Jahnke, K., van der Wel, A., et al. (2022; in preparation).*

In this chapter, we utilize a sample of low-z lensed quasars from the Gravitationally Lensed Quasar Database (Inada et al. 2012; Agnello et al. 2015, 2018; Spiniello et al. 2018; Lemon et al. 2018, 2019, 2020; Jaelani et al. 2021) for performing a supplementary test to our CNN classifier. The training data is constructed like the one described in the main text (see Sections 5.2–6.1). This time, however, we expand the redshift of the background quasars to $1.5 \leq z \leq 7.2$ and the luminosities to $-28 \leq M_{1450} \leq -22$, and we distribute the new 300 sources uniformly throughout the M_{1450}–z parameter space. As a result, our CNN classifier accurately classifies 28 of the 34 sources accessible in the DES data. Figure A.1 test shows the computed lens probabilities with image separations and redshifts. Finally, In Figure A.2, we provide examples of 16 images and their lens probability scores ($P_{\rm lens}$).

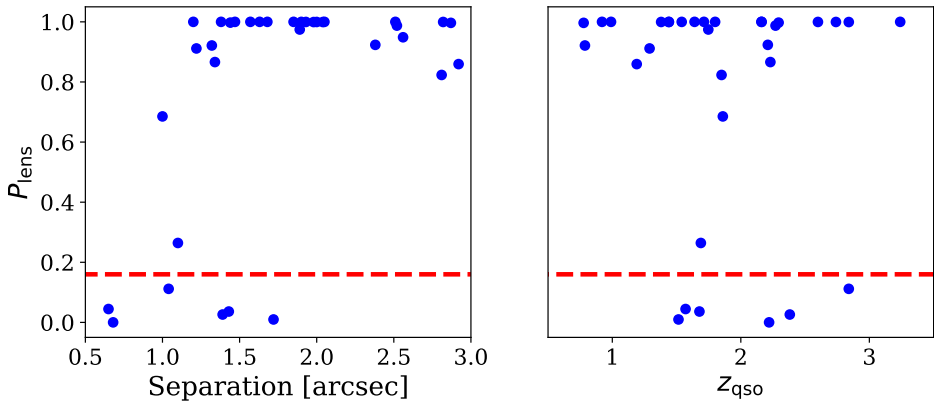

Figure A.1. Lens probabilities for a sample of known lensed quasars, compared to their image separations and background source redshifts. The data are displayed as blue dots, while the red dashed line indicates the probability threshold for classifying a source as a lens.

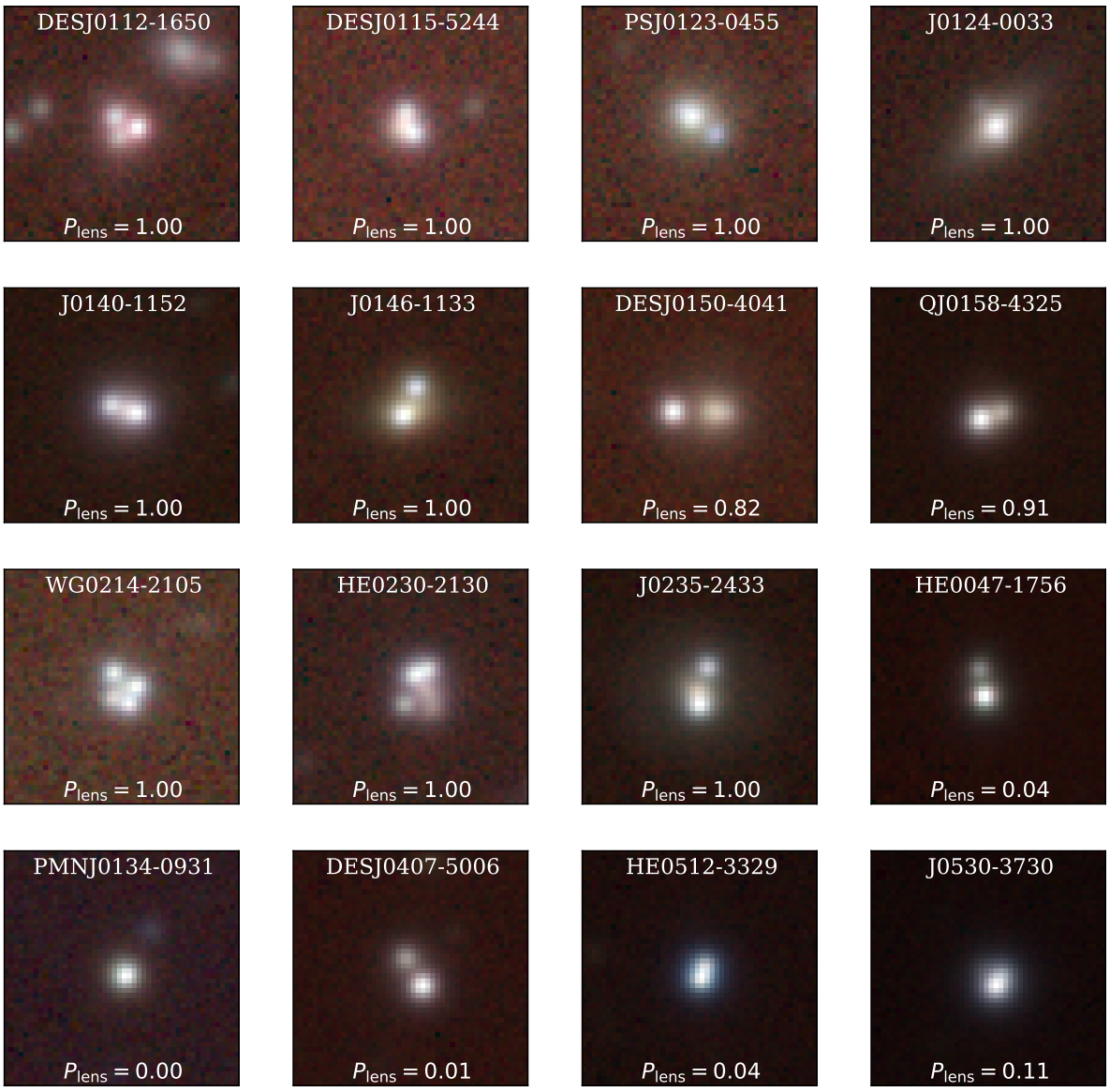

Figure A.2. Sample of confirmed lensed quasars (see text) from literature. The images are based on $12\farcs6 \times 12\farcs6$ DES *izY* cutouts stretched by square root. The lens probabilities of the systems are denoted in the figure.

Appendix B

Investigating the Effects of Different IGM and Sub-DLA Contributions

The content of this chapter is based on the work originally published as ***Andika, I. T.****, Jahnke, K., Bañados, E., et al. (2022; AJ 163: 251).*

We addressed in the main text (Section 11.3) how a combination of a sub-DLA and a neutral IGM caused the damping wing signal in the spectrum of PSO J083+11. Here, we will investigate how multiple combinations of these two factors impact the observed Lyα absorption. In Figure B.1 (see left panels), we show how the neutral hydrogen fraction of the IGM, from $\overline{x}_{\rm HI} = 0.0$ to 0.7, consequently modifies the inferred neutral hydrogen column density of the sub-DLA from $\log N_{\rm HI} = 20.11$ to 19.49 cm^{-2}. We also look into the influence of the quasar's proximity zone when it extends beyond particular redshifts (see right panels) on the deduced $\overline{x}_{\rm HI}$ and $N_{\rm HI}$. Subsequently, we attempt to describe the IGM damping wing using the formula from Miralda-Escudé (1998), assuming a constant neutral fraction from the quasar's proximity zone at redshift $z = z_{\rm s}$ to $z = 5.5$, while being fully ionized at $z \lesssim 5.5$. We discover that the IGM neutral fractions of $\overline{x}_{\rm HI} > 0.5$ appear unlikely since the best-fit models do not suit the measured fluxes near $\lambda = 1216$–1225 Å. Cases with $\overline{x}_{\rm HI} \lesssim 0.5$, on the other hand, appear to provide comparable excellent fits to the data. Finally, as mentioned in Section 11.3, we select our fiducial model, i.e., a 10% neutral IGM plus a best-fit sub-DLA profile of $\log N_{\rm HI} = 20.0 \pm 0.30$ cm^{-2}. This value encompasses the best-fit $N_{\rm HI}$ ranges for all situations with $\overline{x}_{\rm HI} \leq 50\%$.

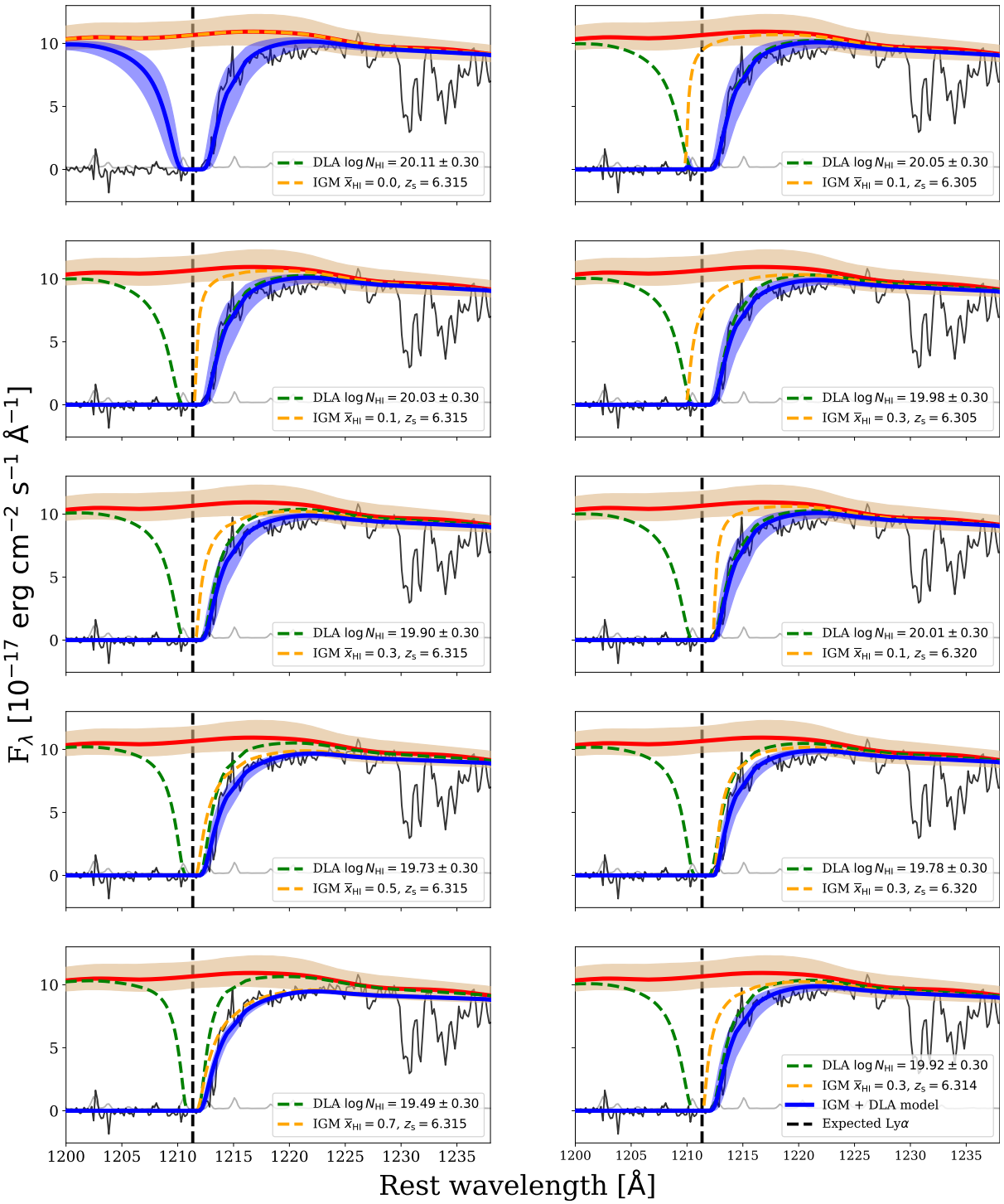

Figure B.1. Effect of different IGM and sub-DLA contributions to the observed damping wing signal. *All panels* illustrate the spectrum of PSO J083+11 (solid black line), its 1σ noise (grey line), the corresponding PCA model (red line), and the best-fit damping wing fit (blue line). The damping wing profile is shown in the *top left panel* assuming no IGM contribution (i.e., $\overline{x}_{\rm HI} = 0.0$). The remaining *left panels* show the IGM affecting the sub-DLA Voigt absorptions (green dashed lines, see legends) using the already attenuated quasar emission (orange dashed lines) as input. The joint model (blue line) provides the best fit to the measured data (solid black lines). The *right panels* display examples of how the quasar's proximity zones stretch outside or inside the sub-DLA redshifts while still providing quite good matches.

Appendix C

Damping Wing Modeling using the MUSE and FIRE Spectra

The content of this chapter is based on the work originally published as ***Andika, I. T.****, Jahnke, K., Bañados, E., et al. (2022; AJ 163: 251).*

As stated in Section 11.3, we favor utilizing the MUSE + GNIRS data for reconstructing the intrinsic quasar emission since it has a superior overall signal in the spectra. As a comparison, we try to employ the MUSE plus lower quality FIRE spectra for the Lyα damping wing profiling. This combined dataset is proved to be quite challenging to be used for predicting the PSO J083+11's intrinsic emission.

As shown in Figure C.1, there are spurious peaks in the data, most likely due to the imperfect telluric correction and spectrophotometric calibration in the low-signal regimes, making it virtually impossible for the PCA to align with the relevant emission profiles. To obtain a reasonable solution that does not contain unphysical elements, we have to disturb the PCA fit heavily. However, in the end, the PCA fit does not converge to a reasonable minimum within the range of physical parameters.

Despite the difficulties in modeling the PSO J083+11's intrinsic emission, we again attempt to fit the Lyα damping wing as described in Section 11.3. The best-fit value for the pure sub-DLA model is $\log N_{\rm HI} = 20.23 \pm 0.30$, while the best-fit value for the combined IGM + DLA model is $\log N_{\rm HI} = 19.66 \pm 0.30$ cm^{-2}. The pure sub-DLA model, on the other hand, persistently overestimates the fluxes at $\lambda = 1216$–1225 Å (see Figure C.2). Furthermore, the joint IGM + DLA model necessitates an IGM with a hydrogen neutral fraction of $\overline{x}_{\rm HI} = 0.8$, which appears to be significantly too high at $z \sim 6$ and disagrees the result from previous studies (e.g., Davies et al. 2018a; Bañados et al. 2019; Wang et al. 2020a; Yang et al. 2020b). As a result, we reject this model when making quantitative assertions.

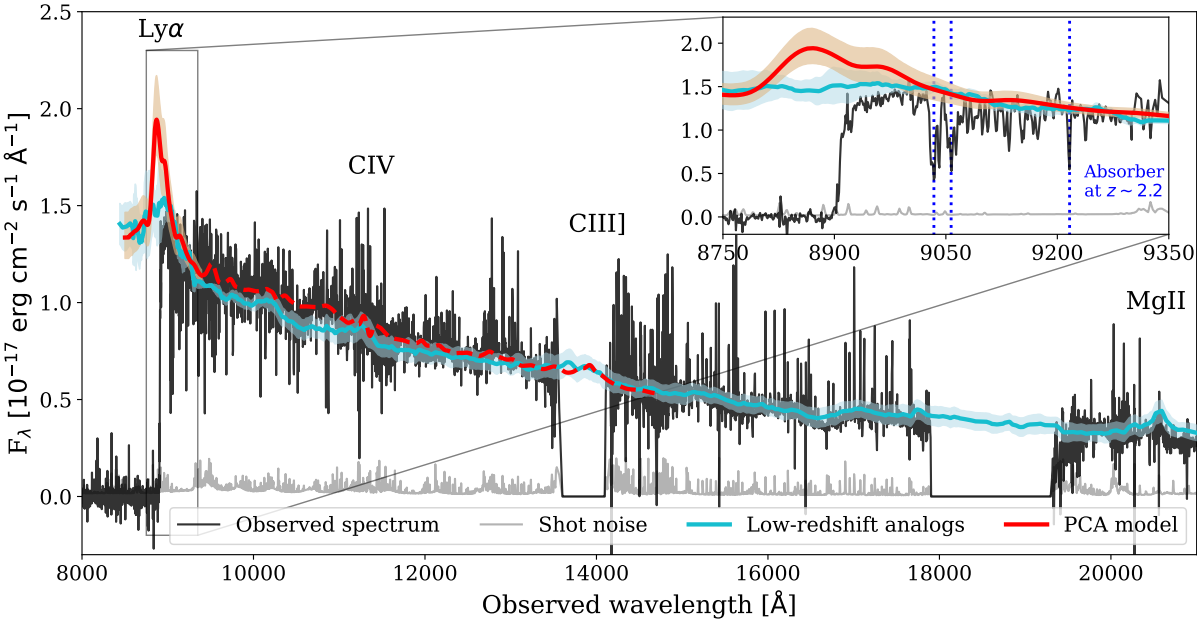

Figure C.1. PSO J083+11's MUSE + FIRE spectrum (black line) and shot noise (grey line) are presented. The cyan line represents the median composite spectrum of the low-z analogs, whereas the light blue region represents the 1σ dispersion around the median. The red line and shaded region display the PCA model used to forecast the blue side of the quasar spectrum, as well as its 1σ dispersion. The red dashed line indicates the wavelengths and spectra utilized in the PCA fit to forecast the Lyα emission. The inset image offers a zoomed-in view of the area surrounding Lyα.

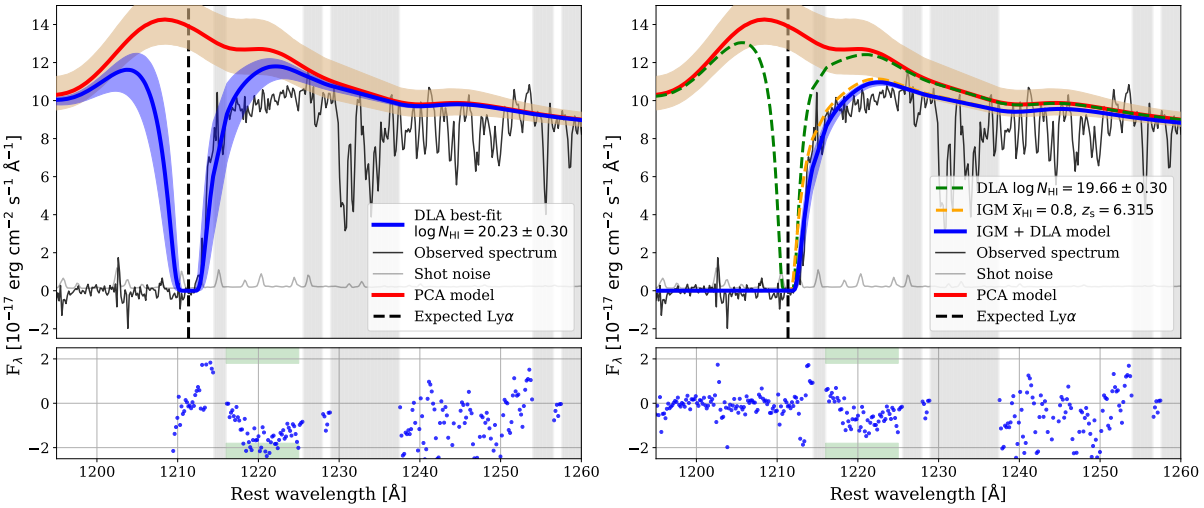

Figure C.2. The MUSE + FIRE spectrum of PSO J083+11 (black line), shot noise (grey line), and the corresponding PCA model (red line and shaded area) in the wavelengths where the quasar's Lyα emission is predicted. The absorption from a $z = 6.314$ sub-DLA with a hydrogen column density of $\log N_{\rm HI} = 20.23 \pm 0.30$ cm^{-2} is shown in the *left panel* (blue line and shaded region). The *right panel* shows a joint model in which we include attenuation owing to an IGM with $\overline{x}_{\rm HI} = 0.8$ (orange dashed line) and a sub-DLA with $\log N_{\rm HI} = 19.66 \pm 0.30$ cm^{-2} (green dashed line). This combined IGM + DLA model (blue line and shaded region) fits the data better at λ =1216–1225 Å (see wavelengths indicated with green), but it appears to be unphysical (see text). The plot also shows the residual of the fits (blue circles) and masked wavelength regions to prevent strong absorption lines or highly contaminated areas due to imperfect skylines subtraction (grey shaded area).

Publications

Parts of the material reported in this dissertation have already been presented in the academic papers listed as follows.

- **Andika, I. T.**, Jahnke, K., van der Wel, A., et al. 2022. *A Search for Gravitationally Lensed Quasars in the Early Universe through Spectral Energy Distribution Modeling and Deep Learning*. Manuscript to be submitted to The Astrophysical Journal and is presented in Part II of this work.
- **Andika, I. T.**, Jahnke, K., Bañados, E., et al. 2022. *Staring at the Shadows of Archaic Galaxies: Damped Lyα and Metal Absorbers Toward a Young $z \sim 6$ Weak-line Quasar*. Manuscript accepted by The Astronomical Journal 163: 251, doi:10.3847/1538-3881/ac6422 and utilized in Part IV of this work.
- **Andika, I. T.**, Jahnke, K., Onoue, M., et al. 2020. *Probing the Nature of High-redshift Weak Emission Line Quasars: A Young Quasar with a Starburst Host Galaxy*. Manuscript accepted by The Astrophysical Journal 903: 34, doi:10.3847/1538-4357/abb9a6 and used in Part II and III of this work.

This work was made possible by the following proposals, which provided scientific resources and observational datasets.

- **Andika, I. T.**, Jahnke, K., Onoue, M., et al. 2022. *The Hunt for Gravitationally Lensed Quasars in the Early Universe*. ESO VLT/FORS2 Proposal: 110.243U. This proposal is utilized in Chapter 5.
- Decarli, R., **Andika, I. T.**, Jahnke, K., et al. 2021. *A Molecular Line Scan on the Infrared-luminous Quasar PSO J083+11 at $z = 6.34$*. IRAM/NOEMA Proposal: S21DI. This proposal is used in Chapter 9.
- **Andika, I. T.**, Jahnke, K., Bañados, E., et al. 2019. *What is the Environment of the Highest Accreting Black Hole at $z > 6$?* ALMA Proposal: 2019.1.01436.S. This proposal is modified for producing the content presented in Chapter 9.

- **Andika, I. T.**, Jahnke, K., Onoue, M., et al. 2019. *Probing the Environment of the Highest Accreting Supermassive Black Hole at $z > 6$.* ESO VLT/MUSE Proposal: 0104.B-0665(A). This proposal inspired the materials written in Chapter 11 and 12.
- Jahnke, K., **Andika, I. T.**, Bañados, E., et al. 2019. *Is the $z = 6.3$ Quasar PSO J083+11 an accretion monster or gravitationally lensed?* HST/WFC3–ACS Proposal: 15707. This proposal is put to use to establish Chapter 8.
- Onoue, M., **Andika, I. T.**, Jahnke, K., et al. 2019. *Confirmation of an Extremely Active Supermassive Black Hole at $z = 6.34$.* Gemini/GNIRS Proposal: GN-2019A-FT-204. This proposal is adapted for creating Chapter 7.

Additional articles that present complementary discoveries but are not included in this dissertation are as follows:

- Wenzl, L., Schindler, J.-T., Fan, X., **Andika, I. T.**, et al. 2021. *Random Forests as a Viable Method to Select and Discover High-redshift Quasars.* The Astronomical Journal 162: 72, doi:10.3847/1538-3881/ac0254.
- Bañados, E., Mazzucchelli, C., Momjian, E., Eilers, A.-C., Wang, F., Schindler, J.-T., Connor, T., **Andika, I. T.**, et al. 2021. *The Discovery of a Highly Accreting, Radio-loud Quasar at $z = 6.82$.* The Astrophysical Journal 909: 80, doi:10.3847/1538-4357/abe239.
- Onoue, M., Bañados, E., Mazzucchelli, C., Venemans, B. P., Schindler, J.-T., Walter, F., Hennawi, J. F., **Andika, I. T.**, et al. 2020. *No Redshift Evolution in the Broad-line-region Metallicity up to $z = 7.54$: Deep Near-infrared Spectroscopy of ULAS J1342+0928.* The Astrophysical Journal 898: 105, doi:10.3847/1538-4357/aba193.
- Marian, V., Jahnke, K., **Andika, I. T.**, et al. 2020. *A Significant Excess in Major Merger Rate for AGNs with the Highest Eddington Ratios at $z < 0.2$.* The Astrophysical Journal 904: 79, doi:10.3847/1538-4357/abbd3e.
- **Andika, I. T.**, Arifyanto, M. I., & Kollatschny, W. 2020. *A Study of [O III]/[O II] Lines Ratio in Type 1 Active Galactic Nucleus: Influence of Radio Jets and Eddington Ratio to Narrow Line Region Emission.* Astronomische Nachrichten 341: 300, doi:10.1002/asna.202013697.
- **Andika, I. T.**, Arifyanto, M. I., & Kollatschny, W. 2019. *Star Formation Rates in Type 1 Active Galactic Nucleus Host Galaxies.* Journal of Physics Conference Series 1127: 012037, doi:10.1088/1742-6596/1127/1/012037.
- **Andika, I. T.**, Arifyanto, M. I., Istiqomah, A. N., et al. 2019. *Cosmic Evolution of Nearby Radio Active Galactic Nuclei.* Journal of Physics Conference Series 1231: 012005, doi:10.1088/1742-6596/1231/1/012005.

Glossary

ΛCDM	Lambda Cold Dark Matter
ACS	Advanced Camera for Survey
ALMA	Atacama Large Millimeter/Submillimeter Array
AUC	Area Under the Curve
BLR	Broad-line region
CCD	Charge-coupled device
CMB	Cosmic Microwave Background
CNN	Convolutional Neural Network
DELS	Dark Energy Spectroscopic Instrument Legacy Imaging Surveys
DES	Dark Energy Survey
DLA	Damped Lyman-α
ELT	Extremely Large Telescope
ESA	European Space Agency
ESO	European Southern Observatory
FIR	Far-infrared
FIRE	Folded-port InfraRed Echellette
FORS2	FOcal Reducer/low dispersion Spectrograph 2
FWHM	Full Width at Half Maximum
GNIRS	Gemini Near-infrared Spectrograph
HST	Hubble Space Telescope
HyLIRG	Hyper-luminous Infrared Galaxy
IGM	Intergalactic Medium
IRAM	Institute de Radioastronomie Millimétrique
JWST	James Webb Space Telescope
LAE	Lyman-α Emitter
LBG	Lyman-break Galaxies
LSST	Large Synoptic Survey Telescope / Rubin Observatory Legacy Survey of Space and Time

MCMC	Markov Chain Monte Carlo
MUSE	Multi Unit Spectrograph Explorer
NASA	National Aeronautics and Space Administration
NLR	Narrow-line Region
NOEMA	NOrthern Extended Millimeter Array
NTT	New Technology Telescope
QSO	Quasi-stellar Object
Quasar	Quasi-stellar Radio Source
Pan-STARRS	Panoramic Survey Telescope and Rapid Response System
PCA	Principal Component Analysis
PI	Principal Investigator
PSF	Point-spread Function
PSO	Pan-STARRS Object
REW	Rest-frame Equivalent Width
ROC	Receiver Operating Characteristic
S/N	Signal-to-noise Ratio
SDSS	Sloan Digital Sky Survey
SED	Spectral Energy Distribution
SFH	Star Formation History
SFR	Star Formation Rate
SMBH	Supermassive Black Hole
SIE	Singular Isothermal Ellipsoid
SIS	Singular Isothermal Sphere
SoFI	Son OF ISAAC – Infrared Spectrometer And Array Camera
TIR	Total Infrared
UHS	UKIRT Hemisphere Survey
UKIDSS	UKIRT Infrared Deep Sky Survey
UKIRT	United Kingdom Infrared Telescope
ULIRG	Ultra-luminous Infrared Galaxy
VHS	VISTA Hemisphere Survey
VISTA	Visible and Infrared Survey Telescope for Astronomy
VLT	Very Large Telescope
WFC3	Wide Field Camera 3
WFIRST	Wide-Field Infrared Survey Telescope / Nancy Grace Roman Space Telescope
WISE	Wide-field Infrared Survey Explorer
WLQ	Weak Emission Line Quasar / Weak-line Quasar

Bibliography

Abadi, M., Barham, P., Chen, J., et al. 2016, "TensorFlow: A system for large-scale machine learning", arXiv e-prints, arXiv:1605.08695. https://arxiv.org/abs/1605.08695

Abbott, T. M. C., Abdalla, F. B., Alarcon, A., et al. 2018, "Dark Energy Survey year 1 results: Cosmological constraints from galaxy clustering and weak lensing", Phys. Rev. D, 98, 043526, doi: 10.1103/PhysRevD.98.043526

Abbott, T. M. C., Adamów, M., Aguena, M., et al. 2021, "The Dark Energy Survey Data Release 2", ApJS, 255, 20, doi: 10.3847/1538-4365/ac00b3

Abdurro'uf, Accetta, K., Aerts, C., et al. 2021, "The Seventeenth Data Release of the Sloan Digital Sky Surveys: Complete Release of MaNGA, MaStar and APOGEE-2 Data", arXiv e-prints, arXiv:2112.02026. https://arxiv.org/abs/2112.02026

Abolfathi, B., Aguado, D. S., Aguilar, G., et al. 2018, "The Fourteenth Data Release of the Sloan Digital Sky Survey: First Spectroscopic Data from the Extended Baryon Oscillation Spectroscopic Survey and from the Second Phase of the Apache Point Observatory Galactic Evolution Experiment", ApJS, 235, 42, doi: 10.3847/1538-4365/aa9e8a

Agnello, A., Kelly, B. C., Treu, T., & Marshall, P. J. 2015, "Data mining for gravitationally lensed quasars", MNRAS, 448, 1446, doi: 10.1093/mnras/stv037

Agnello, A., Schechter, P. L., Morgan, N. D., et al. 2018, "Quasar lenses and pairs in the VST-ATLAS and Gaia", MNRAS, 475, 2086, doi: 10.1093/mnras/stx3226

Akerman, C. J., Carigi, L., Nissen, P. E., Pettini, M., & Asplund, M. 2004, "The evolution of the C/O ratio in metal-poor halo stars", A&A, 414, 931, doi: 10.1051/0004-6361:20034188

Andika, I. T., Jahnke, K., Onoue, M., et al. 2020, "Probing the Nature of High-redshift Weak Emission Line Quasars: A Young Quasar with a Starburst Host Galaxy", ApJ, 903, 34, doi: 10.3847/1538-4357/abb9a6

Andika, I. T., Jahnke, K., Bañados, E., et al. 2022, "Staring at the Shadows of Archaic Galaxies: Damped Lyα and Metal Absorbers Toward a Young $z \sim 6$ Weak-line Quasar", AJ, 163, 251, doi: 10.3847/1538-3881/ac6422

Antonucci, R. 1993, "Unified models for active galactic nuclei and quasars.", ARA&A, 31, 473, doi: 10.1146/annurev.aa.31.090193.002353

Arrigoni Battaia, F., Hennawi, J. F., Prochaska, J. X., et al. 2019, "QSO MUSEUM I: a sample of 61 extended Lyα-emission nebulae surrounding $z \sim 3$ quasars", MNRAS, 482, 3162, doi: 10.1093/mnras/sty2827

Asplund, M., Grevesse, N., Sauval, A. J., & Scott, P. 2009, "The Chemical Composition of the Sun", ARA&A, 47, 481, doi: 10.1146/annurev.astro.46.060407.145222

Astropy Collaboration, Robitaille, T. P., Tollerud, E. J., et al. 2013, "Astropy: A community Python package for astronomy", A&A, 558, A33, doi: 10.1051/0004-6361/201322068

Astropy Collaboration, Price-Whelan, A. M., Sipőcz, B. M., et al. 2018, "The Astropy Project: Building an Open-science Project and Status of the v2.0 Core Package", AJ, 156, 123, doi: 10.3847/1538-3881/aabc4f

Auger, M. W., Treu, T., Bolton, A. S., et al. 2010, "The Sloan Lens ACS Survey. X. Stellar, Dynamical, and Total Mass Correlations of Massive Early-type Galaxies", ApJ, 724, 511, doi: 10.1088/0004-637X/724/1/511

Bañados, E., Decarli, R., Walter, F., et al. 2015a, "Bright [C II] 158 μm Emission in a Quasar Host Galaxy at $z = 6.54$", ApJ, 805, L8, doi: 10.1088/2041-8205/805/1/L8

Bañados, E., Venemans, B., Walter, F., et al. 2013, "The Galaxy Environment of a QSO at $z \sim 5.7$", ApJ, 773, 178, doi: 10.1088/0004-637X/773/2/178

Bañados, E., Venemans, B. P., Morganson, E., et al. 2014, "Discovery of Eight $z \sim 6$ Quasars from Pan-STARRS1", AJ, 148, 14, doi: 10.1088/0004-6256/148/1/14

—. 2015b, "Constraining the Radio-loud Fraction of Quasars at $z > 5.5$", ApJ, 804, 118, doi: 10.1088/0004-637X/804/2/118

Bañados, E., Venemans, B. P., Decarli, R., et al. 2016, "The Pan-STARRS1 Distant $z > 5.6$ Quasar Survey: More than 100 Quasars within the First Gyr of the Universe", ApJS, 227, 11, doi: 10.3847/0067-0049/227/1/11

Bañados, E., Venemans, B. P., Mazzucchelli, C., et al. 2018, "An 800-million-solar-mass black hole in a significantly neutral Universe at a redshift of 7.5", Nature, 553, 473, doi: 10.1038/nature25180

Bañados, E., Rauch, M., Decarli, R., et al. 2019, "A Metal-poor Damped Lyα System at Redshift 6.4", ApJ, 885, 59, doi: 10.3847/1538-4357/ab4129

Bacon, R., Accardo, M., Adjali, L., et al. 2010, "The MUSE second-generation VLT instrument", in Society of Photo-Optical Instrumentation Engineers (SPIE) Conference Series, Vol. 7735, Ground-based and Airborne Instrumentation for Astronomy III, ed. I. S. McLean, S. K. Ramsay, & H. Takami, 773508, doi: 10.1117/12.856027

Barkana, R. 1998, "Fast Calculation of a Family of Elliptical Mass Gravitational Lens Models", ApJ, 502, 531, doi: 10.1086/305950

Barkana, R., & Loeb, A. 2001, "In the beginning: the first sources of light and the reionization of the universe", Phys. Rep., 349, 125, doi: 10.1016/S0370-1573(01)00019-9

Barnett, R., Warren, S. J., Cross, N. J. G., et al. 2021, "A complete search for redshift $z \gtrsim 6.5$ quasars in the VIKING survey", MNRAS, 501, 1663, doi: 10.1093/mnras/staa3808

Bartelmann, M., & Schneider, P. 2001, "Weak gravitational lensing", Phys. Rep., 340, 291, doi: 10.1016/S0370-1573(00)00082-X

Becker, G. D., Bolton, J. S., & Lidz, A. 2015, "Reionisation and High-Redshift Galaxies: The View from Quasar Absorption Lines", PASA, 32, e045, doi: 10.1017/pasa.2015.45

Beelen, A., Cox, P., Benford, D. J., et al. 2006, "350 μm Dust Emission from High-Redshift Quasars", ApJ, 642, 694, doi: 10.1086/500636

Begelman, M. C., & Volonteri, M. 2017, "Hyperaccreting black holes in galactic nuclei", MNRAS, 464, 1102, doi: 10.1093/mnras/stw2446

Begelman, M. C., Volonteri, M., & Rees, M. J. 2006, "Formation of supermassive black holes by direct collapse in pre-galactic haloes", MNRAS, 370, 289, doi: 10.1111/j.1365-2966.2006.10467.x

Bentz, M. C. 2016, "AGN Reverberation Mapping", in Astrophysics and Space Science Library, Vol. 439, Astronomy at High Angular Resolution, ed. H. M. J. Boffin, G. Hussain, J.-P. Berger, & L. Schmidtobreick, 249, doi: 10.1007/978-3-319-39739-9_13

Berg, T. A. M., Fumagalli, M., D'Odorico, V., et al. 2021, "Sub-damped Lyman-α systems in the XQ-100 survey - II. Chemical evolution at $2.4 \leq z \leq 4.3$", MNRAS, 502, 4009, doi: 10.1093/mnras/stab184

Best, W. M. J., Magnier, E. A., Liu, M. C., et al. 2018, "Photometry and Proper Motions of M, L, and T Dwarfs from the Pan-STARRS1 3π Survey", ApJS, 234, 1, doi: 10.3847/1538-4365/aa9982

Birrer, S., Treu, T., Rusu, C. E., et al. 2019, "H0LiCOW - IX. Cosmographic analysis of the doubly imaged quasar SDSS 1206+4332 and a new measurement of the Hubble constant", MNRAS, 484, 4726, doi: 10.1093/mnras/stz200

Bondi, H. 1952, "On spherically symmetrical accretion", MNRAS, 112, 195, doi: 10.1093/mnras/112.2.195

Bonvin, V., Chan, J. H. H., Millon, M., et al. 2018, "COSMOGRAIL. XVII. Time delays for the quadruply imaged quasar PG 1115+080", A&A, 616, A183, doi: 10.1051/0004-6361/201833287

Boroson, T. A., & Green, R. F. 1992, "The Emission-Line Properties of Low-Redshift Quasi-stellar Objects", ApJS, 80, 109, doi: 10.1086/191661

Bosman, S. E. I., Fan, X., Jiang, L., et al. 2018, "New constraints on Lyman-α opacity with a sample of 62 quasarsat $z > 5.7$", MNRAS, 479, 1055, doi: 10.1093/mnras/sty1344

Bosman, S. E. I., Kakiichi, K., Meyer, R. A., et al. 2020, "Three Lyα Emitting Galaxies within a Quasar Proximity Zone at $z \sim 5.8$", ApJ, 896, 49, doi: 10.3847/1538-4357/ab85cd

Bosman, S. E. I., Ďurovčíková, D., Davies, F. B., & Eilers, A.-C. 2021a, "A comparison of quasar emission reconstruction techniques for $z \geq 5.0$ Lyman-α and Lyman-β transmission", MNRAS, 503, 2077, doi: 10.1093/mnras/stab572

Bosman, S. E. I., Davies, F. B., Becker, G. D., et al. 2021b, "Hydrogen reionisation ends by $z = 5.3$: Lyman-α optical depth measured by the XQR-30 sample", arXiv e-prints, arXiv:2108.03699. https://arxiv.org/abs/2108.03699

Bouwens, R. J., Illingworth, G. D., Oesch, P. A., et al. 2015, "UV Luminosity Functions at Redshifts $z \sim 4$ to $z \sim 10$: 10,000 Galaxies from HST Legacy Fields", ApJ, 803, 34, doi: 10.1088/0004-637X/803/1/34

Bradley, L., Sipocz, B., Robitaille, T., et al. 2019, "astropy/photutils: v0.6", v0.6, Zenodo, doi: 10.5281/zenodo.2533376

Brammer, G. B., van Dokkum, P. G., & Coppi, P. 2008, "EAZY: A Fast, Public Photometric Redshift Code", ApJ, 686, 1503, doi: 10.1086/591786

Brown, M. J. I., Moustakas, J., Smith, J. D. T., et al. 2014, "An Atlas of Galaxy Spectral Energy Distributions from the Ultraviolet to the Mid-infrared", ApJS, 212, 18, doi: 10.1088/0067-0049/212/2/18

Burgasser, A. J. 2014, "The SpeX Prism Library: 1000+ low-resolution, near-infrared spectra of ultracool M, L, T and Y dwarfs", in Astronomical Society of India Conference Series, Vol. 11, Astronomical Society of India Conference Series, 7–16. https://arxiv.org/abs/1406.4887

Cañameras, R., Schuldt, S., Shu, Y., et al. 2021, "HOLISMOKES. VI. New galaxy-scale strong lens candidates from the HSC-SSP imaging survey", A&A, 653, L6, doi: 10.1051/0004-6361/202141758

Calvi, R., Rodríguez Espinosa, J. M., Mas-Hesse, J. M., et al. 2019, "MOS spectroscopy of protocluster candidate galaxies at $z = 6.5$", MNRAS, 489, 3294, doi: 10.1093/mnras/stz2177

Calzetti, D., Armus, L., Bohlin, R. C., et al. 2000, "The Dust Content and Opacity of Actively Star-forming Galaxies", ApJ, 533, 682, doi: 10.1086/308692

Carilli, C. L., & Walter, F. 2013, "Cool Gas in High-Redshift Galaxies", ARA&A, 51, 105, doi: 10.1146/annurev-astro-082812-140953

Carnall, A. C. 2017, "SpectRes: A Fast Spectral Resampling Tool in Python", arXiv e-prints, arXiv:1705.05165. https://arxiv.org/abs/1705.05165

Carnall, A. C., McLure, R. J., Dunlop, J. S., & Davé, R. 2018, "Inferring the star formation histories of massive quiescent galaxies with BAGPIPES: evidence for multiple quenching mechanisms", MNRAS, 480, 4379, doi: 10.1093/mnras/sty2169

Carnall, A. C., McLure, R. J., Dunlop, J. S., et al. 2019, "The VANDELS survey: the star-formation histories of massive quiescent galaxies at $1.0 < z < 1.3$", MNRAS, 490, 417, doi: 10.1093/mnras/stz2544

Carnero Rosell, A., Santiago, B., dal Ponte, M., et al. 2019, "Brown dwarf census with the Dark Energy Survey year 3 data and the thin disc scale height of early L types", MNRAS, 489, 5301, doi: 10.1093/mnras/stz2398

Caswell, T. A., Droettboom, M., Hunter, J., et al. 2019, "matplotlib/matplotlib v3.1.0", v3.1.0, Zenodo, doi: 10.5281/zenodo.2893252

Chambers, K. C., Magnier, E. A., Metcalfe, N., et al. 2016, "The Pan-STARRS1 Surveys", arXiv e-prints, arXiv:1612.05560. https://arxiv.org/abs/1612.05560

Chan, J. H. H., Rojas, K., Millon, M., et al. 2021, "Measuring accretion disk sizes of lensed quasars with microlensing time delay in multi-band light curves", A&A, 647, A115, doi: 10.1051/0004-6361/202038971

Charlot, S., & Fall, S. M. 2000, "A Simple Model for the Absorption of Starlight by Dust in Galaxies", ApJ, 539, 718, doi: 10.1086/309250

Chen, H., & Gnedin, N. Y. 2021, "The Distribution and Evolution of Quasar Proximity Zone Sizes", ApJ, 911, 60, doi: 10.3847/1538-4357/abe7e7

Chwolson, O. 1924, "Über eine mögliche Form fiktiver Doppelsterne", Astronomische Nachrichten, 221, 329, doi: 10.1002/asna.19242212003

Comerford, J. M., Haiman, Z., & Schaye, J. 2002, "Constraining the Redshift $z \sim 6$ Quasar Luminosity Function Using Gravitational Lensing", ApJ, 580, 63, doi: 10.1086/343116

Cooke, R., Pettini, M., Steidel, C. C., Rudie, G. C., & Nissen, P. E. 2011, "The most metal-poor damped Lyα systems: insights into chemical evolution in the very metal-poor regime", MNRAS, 417, 1534, doi: 10.1111/j.1365-2966.2011.19365.x

Cooke, R. J., Pettini, M., & Jorgenson, R. A. 2015, "The Most Metal-poor Damped Lyα Systems: An Insight into Dwarf Galaxies at High-redshift", ApJ, 800, 12, doi: 10.1088/0004-637X/800/1/12

Cooke, R. J., Pettini, M., & Steidel, C. C. 2017, "Discovery of the most metal-poor damped Lyman-α system", MNRAS, 467, 802, doi: 10.1093/mnras/stx037

Cooper, T. J., Simcoe, R. A., Cooksey, K. L., et al. 2019, "Heavy Element Absorption Systems at $5.0 < z < 6.8$: Metal-poor Neutral Gas and a Diminishing Signature of Highly Ionized Circumgalactic Matter", ApJ, 882, 77, doi: 10.3847/1538-4357/ab3402

Cornachione, M. A., Morgan, C. W., Burger, H. R., et al. 2020, "Near-infrared and Optical Continuum Emission Region Size Measurements in the Gravitationally lensed Quasars Q0957+561 and SBS0909+532", ApJ, 905, 7, doi: 10.3847/1538-4357/abc25d

da Cunha, E., Groves, B., Walter, F., et al. 2013, "On the Effect of the Cosmic Microwave Background in High-redshift (Sub-)millimeter Observations", ApJ, 766, 13, doi: 10.1088/0004-637X/766/1/13

Davies, F. B. 2020, "Ionization bias and the ghost proximity effect near $z \gtrsim 6$ quasars in the shadow of proximate absorption systems", MNRAS, 494, 2937, doi: 10.1093/mnras/staa528

Davies, F. B., Furlanetto, S. R., & McQuinn, M. 2016, "Quasar ionization front Lyα emission in an inhomogeneous intergalactic medium", MNRAS, 457, 3006, doi: 10.1093/mnras/stw055

Davies, F. B., Hennawi, J. F., & Eilers, A.-C. 2019, "Evidence for Low Radiative Efficiency or Highly Obscured Growth of $z > 7$ Quasars", ApJ, 884, L19, doi: 10.3847/2041-8213/ab42e3

—. 2020a, "Time-dependent behaviour of quasar proximity zones at $z \sim 6$", MNRAS, 493, 1330, doi: 10.1093/mnras/stz3303

Davies, F. B., Wang, F., Eilers, A.-C., & Hennawi, J. F. 2020b, "Constraining the Gravitational Lensing of $z \gtrsim 6$ Quasars from Their Proximity Zones", ApJ, 904, L32, doi: 10.3847/2041-8213/abc61f

Davies, F. B., Hennawi, J. F., Bañados, E., et al. 2018a, "Quantitative Constraints on the Reionization History from the IGM Damping Wing Signature in Two Quasars at $z > 7$", ApJ, 864, 142, doi: 10.3847/1538-4357/aad6dc

—. 2018b, "Predicting Quasar Continua near Lyα with Principal Component Analysis", ApJ, 864, 143, doi: 10.3847/1538-4357/aad7f8

Dawson, K. S., Schlegel, D. J., Ahn, C. P., et al. 2013, "The Baryon Oscillation Spectroscopic Survey of SDSS-III", AJ, 145, 10, doi: 10.1088/0004-6256/145/1/10

Dayal, P., Rossi, E. M., Shiralilou, B., et al. 2019, "The hierarchical assembly of galaxies and black holes in the first billion years: predictions for the era of gravitational wave astronomy", MNRAS, 486, 2336, doi: 10.1093/mnras/stz897

De Looze, I., Cormier, D., Lebouteiller, V., et al. 2014, "The applicability of far-infrared fine-structure lines as star formation rate tracers over wide ranges of metallicities and galaxy types", A&A, 568, A62, doi: 10.1051/0004-6361/201322489

De Rosa, G., Decarli, R., Walter, F., et al. 2011, "Evidence for Non-evolving Fe II/Mg II Ratios in Rapidly Accreting $z \sim 6$ QSOs", ApJ, 739, 56, doi: 10.1088/0004-637X/739/2/56

De Rosa, G., Venemans, B. P., Decarli, R., et al. 2014, "Black Hole Mass Estimates and Emission-line Properties of a Sample of Redshift $z > 6.5$ Quasars", ApJ, 790, 145, doi: 10.1088/0004-637X/790/2/145

Decarli, R., Walter, F., Venemans, B. P., et al. 2017, "Rapidly star-forming galaxies adjacent to quasars at redshifts exceeding 6", Nature, 545, 457, doi: 10.1038/nature22358

—. 2018, "An ALMA [C II] Survey of 27 Quasars at $z > 5.94$", ApJ, 854, 97, doi: 10.3847/1538-4357/aaa5aa

Dey, A., Schlegel, D. J., Lang, D., et al. 2019, "Overview of the DESI Legacy Imaging Surveys", AJ, 157, 168, doi: 10.3847/1538-3881/ab089d

Diamond-Stanic, A. M., Fan, X., Brandt, W. N., et al. 2009, "High-redshift SDSS Quasars with Weak Emission Lines", ApJ, 699, 782, doi: 10.1088/0004-637X/699/1/782

DiPompeo, M. A., Hickox, R. C., Myers, A. D., & Geach, J. E. 2017, "A unifying evolutionary framework for infrared-selected obscured and unobscured quasar host haloes", MNRAS, 464, 3526, doi: 10.1093/mnras/stw2589

Dodelson, S., & Schmidt, F. 2020, *Modern Cosmology, Second Edition* (Academic Press)

D'Odorico, V., Feruglio, C., Ferrara, A., et al. 2018, "Witnessing Galaxy Assembly at the Edge of the Reionization Epoch", ApJ, 863, L29, doi: 10.3847/2041-8213/aad7b7

Drake, A. B., Farina, E. P., Neeleman, M., et al. 2019, "Lyα Halos around $z \sim 6$ Quasars", ApJ, 881, 131, doi: 10.3847/1538-4357/ab2984

Dunne, L., Eales, S. A., & Edmunds, M. G. 2003, "A census of metals at high and low redshift and the connection between submillimetre sources and spheroid formation", MNRAS, 341, 589, doi: 10.1046/j.1365-8711.2003.06440.x

Dye, S., Lawrence, A., Read, M. A., et al. 2018, "The UKIRT Hemisphere Survey: definition and J-band data release", MNRAS, 473, 5113, doi: 10.1093/mnras/stx2622

Eddington, A. S. 1919, "The total eclipse of 1919 May 29 and the influence of gravitation on light", The Observatory, 42, 119

Eilers, A.-C., Davies, F. B., & Hennawi, J. F. 2018a, "The Opacity of the Intergalactic Medium Measured along Quasar Sightlines at $z \sim 6$", ApJ, 864, 53, doi: 10.3847/1538-4357/aad4fd

Eilers, A.-C., Davies, F. B., Hennawi, J. F., et al. 2017, "Implications of $z \sim 6$ Quasar Proximity Zones for the Epoch of Reionization and Quasar Lifetimes", ApJ, 840, 24, doi: 10.3847/1538-4357/aa6c60

Eilers, A.-C., Hennawi, J. F., & Davies, F. B. 2018b, "First Spectroscopic Study of a Young Quasar", ApJ, 867, 30, doi: 10.3847/1538-4357/aae081

Eilers, A.-C., Hennawi, J. F., Davies, F. B., & Simcoe, R. A. 2021, "Detecting and Characterizing Young Quasars. II. Four Quasars at $z \sim 6$ with Lifetimes $< 10^4$ Yr", ApJ, 917, 38, doi: 10.3847/1538-4357/ac0a76

Eilers, A.-C., Hennawi, J. F., Decarli, R., et al. 2020, "Detecting and Characterizing Young Quasars. I. Systemic Redshifts and Proximity Zone Measurements", ApJ, 900, 37, doi: 10.3847/1538-4357/aba52e

Einstein, A. 1911, "Über den Einfluß der Schwerkraft auf die Ausbreitung des Lichtes", Annalen der Physik, 340, 898, doi: 10.1002/andp.19113401005

—. 1936, "Lens-Like Action of a Star by the Deviation of Light in the Gravitational Field", Science, 84, 506, doi: 10.1126/science.84.2188.506

Euclid Collaboration, Schirmer, M., Jahnke, K., et al. 2022, "Euclid preparation. XVIII. The NISP photometric system", arXiv e-prints, arXiv:2203.01650. https://arxiv.org/abs/2203.01650

Fabbian, D., Nissen, P. E., Asplund, M., Pettini, M., & Akerman, C. 2009, "The C/O ratio at low metallicity: constraints on early chemical evolution from observations of Galactic halo stars", A&A, 500, 1143, doi: 10.1051/0004-6361/200810095

Fan, X., Strauss, M. A., Becker, R. H., et al. 2006, "Constraining the Evolution of the Ionizing Background and the Epoch of Reionization with $z \sim 6$ Quasars. II. A Sample of 19 Quasars", AJ, 132, 117, doi: 10.1086/504836

Fan, X., Wang, F., Yang, J., et al. 2019a, "The Discovery of a Gravitationally Lensed Quasar at $z = 6.51$", ApJ, 870, L11, doi: 10.3847/2041-8213/aaeffe

Fan, X., Barth, A., Banados, E., et al. 2019b, "The First Luminous Quasars and Their Host Galaxies", BAAS, 51, 121. https://arxiv.org/abs/1903.04078

Farina, E. P., Venemans, B. P., Decarli, R., et al. 2017, "Mapping the Lyα Emission around a $z \sim 6.6$ QSO with MUSE: Extended Emission and a Companion at a Close Separation", ApJ, 848, 78, doi: 10.3847/1538-4357/aa8df4

Farina, E. P., Arrigoni-Battaia, F., Costa, T., et al. 2019, "The REQUIEM Survey. I. A Search for Extended Lyα Nebular Emission Around 31 $z > 5.7$ Quasars", ApJ, 887, 196, doi: 10.3847/1538-4357/ab5847

Feng, H.-C., Hu, C., Li, S.-S., et al. 2021, "Reverberation Mapping of Changing-look Active Galactic Nucleus NGC 3516", ApJ, 909, 18, doi: 10.3847/1538-4357/abd851

Feng, Y., Di-Matteo, T., Croft, R. A., et al. 2016, "The BlueTides simulation: first galaxies and reionization", MNRAS, 455, 2778, doi: 10.1093/mnras/stv2484

Ferrara, A., Salvadori, S., Yue, B., & Schleicher, D. 2014, "Initial mass function of intermediate-mass black hole seeds", MNRAS, 443, 2410, doi: 10.1093/mnras/stu1280

Finkelstein, S. L., Bagley, M., Song, M., et al. 2021, "A Census of the Bright $z = 8.5$–11 Universe with the Hubble and Spitzer Space Telescopes in the CANDELS Fields", arXiv e-prints, arXiv:2106.13813. https://arxiv.org/abs/2106.13813

Fischler, M. A., & Bolles, R. C. 1981, "Random sample consensus: A paradigm for model fitting with applications to image analysis and automated cartography", Commun. ACM, 24, 381–395, doi: 10.1145/358669.358692

Fitzpatrick, E. L. 1999, "Correcting for the Effects of Interstellar Extinction", PASP, 111, 63, doi: 10.1086/316293

Flaugher, B., Diehl, H. T., Honscheid, K., et al. 2015, "The Dark Energy Camera", AJ, 150, 150, doi: 10.1088/0004-6256/150/5/150

Flesch, E. W. 2021, "The Million Quasars (Milliquas) v7.2 Catalogue, now with VLASS associations. The inclusion of SDSS-DR16Q quasars is detailed", arXiv e-prints, arXiv:2105.12985. https://arxiv.org/abs/2105.12985

Foreman-Mackey, D., Hogg, D. W., Lang, D., & Goodman, J. 2013, "emcee: The MCMC Hammer", PASP, 125, 306, doi: 10.1086/670067

Francis, P. J., Hewett, P. C., Foltz, C. B., & Chaffee, F. H. 1992, "An Objective Classification Scheme for QSO Spectra", ApJ, 398, 476, doi: 10.1086/171870

Fujimoto, S., Oguri, M., Nagao, T., Izumi, T., & Ouchi, M. 2020, "Truth or Delusion? A Possible Gravitational Lensing Interpretation of the Ultraluminous Quasar SDSS J010013.02+280225.8 at $z = 6.30$", ApJ, 891, 64, doi: 10.3847/1538-4357/ab718c

Fumagalli, M., O'Meara, J. M., Prochaska, J. X., Rafelski, M., & Kanekar, N. 2015, "Directly imaging damped Lyα galaxies at $z > 2$ - III. The star formation rates of neutral gas reservoirs at $z \sim 2.7$", MNRAS, 446, 3178, doi: 10.1093/mnras/stu2325

Fynbo, J. P. U., Heintz, K. E., Neeleman, M., et al. 2018, "ALMA observations of a metal-rich damped Lyα absorber at $z = 2.5832$: evidence for strong galactic winds in a galaxy group", MNRAS, 479, 2126, doi: 10.1093/mnras/sty1520

Garel, T., Blaizot, J., Guiderdoni, B., et al. 2015, "The UV, Lyman-α, and dark matter halo properties of high-redshift galaxies", MNRAS, 450, 1279, doi: 10.1093/mnras/stv374

Genzel, R., Eisenhauer, F., & Gillessen, S. 2010, "The Galactic Center massive black hole and nuclear star cluster", Reviews of Modern Physics, 82, 3121, doi: 10.1103/RevModPhys.82.3121

Ghez, A. M., Salim, S., Weinberg, N. N., et al. 2008, "Measuring Distance and Properties of the Milky Way's Central Supermassive Black Hole with Stellar Orbits", ApJ, 689, 1044, doi: 10.1086/592738

Ghisellini, G. 2013, *Radiative Processes in High Energy Astrophysics* (Springer, Heidelberg), doi: 10.1007/978-3-319-00612-3

Giallongo, E., Grazian, A., Fiore, F., et al. 2015, "Faint AGNs at $z > 4$ in the CANDELS GOODS-S field: looking for contributors to the reionization of the Universe", A&A, 578, A83, doi: 10.1051/0004-6361/201425334

Gilman, D., Birrer, S., Nierenberg, A., et al. 2020, "Warm dark matter chills out: constraints on the halo mass function and the free-streaming length of dark matter with eight quadruple-image strong gravitational lenses", MNRAS, 491, 6077, doi: 10.1093/mnras/stz3480

Gilman, D., Birrer, S., Treu, T., Nierenberg, A., & Benson, A. 2019, "Probing dark matter structure down to 10^7 solar masses: flux ratio statistics in gravitational lenses with line-of-sight haloes", MNRAS, 487, 5721, doi: 10.1093/mnras/stz1593

Ginsburg, A., Sipőcz, B. M., Brasseur, C. E., et al. 2019, "astroquery: An Astronomical Web-querying Package in Python", AJ, 157, 98, doi: 10.3847/1538-3881/aafc33

Gordon, K. D., Fouesneau, M., Arab, H., et al. 2016, "The Panchromatic Hubble Andromeda Treasury. XV. The BEAST: Bayesian Extinction and Stellar Tool", ApJ, 826, 104, doi: 10.3847/0004-637X/826/2/104

Gould, A. 1995, "Microlensing Search of 10^6 Quasars", ApJ, 455, 37, doi: 10.1086/176553

Green, G. M., Schlafly, E., Zucker, C., Speagle, J. S., & Finkbeiner, D. 2019, "A 3D Dust Map Based on Gaia, Pan-STARRS 1, and 2MASS", ApJ, 887, 93, doi: 10.3847/1538-4357/ab5362

Greig, B., Mesinger, A., Davies, F. B., et al. 2021, "IGM damping wing constraints on reionisation

from covariance reconstruction of two $z \gtrsim 7$ QSOs", arXiv e-prints, arXiv:2112.04091. https://arxiv.org/abs/2112.04091

Gunn, J. E., & Peterson, B. A. 1965, "On the Density of Neutral Hydrogen in Intergalactic Space.", ApJ, 142, 1633, doi: 10.1086/148444

Guo, H., Shen, Y., & Wang, S. 2018, "PyQSOFit: Python code to fit the spectrum of quasars". http://ascl.net/1809.008

Guth, A. H. 1981, "Inflationary universe: A possible solution to the horizon and flatness problems", Phys. Rev. D, 23, 347, doi: 10.1103/PhysRevD.23.347

Habouzit, M., Volonteri, M., Latif, M., Dubois, Y., & Peirani, S. 2016, "On the number density of 'direct collapse' black hole seeds", MNRAS, 463, 529, doi: 10.1093/mnras/stw1924

Habouzit, M., Onoue, M., Bañados, E., et al. 2022, "Co-evolution of massive black holes and their host galaxies at high redshift: discrepancies from six cosmological simulations and the key role of JWST", MNRAS, 511, 3751, doi: 10.1093/mnras/stac225

Harikane, Y., Inoue, A. K., Mawatari, K., et al. 2021, "A Search for H-Dropout Lyman Break Galaxies at z∼12-16", arXiv e-prints, arXiv:2112.09141. https://arxiv.org/abs/2112.09141

Harris, C. R., Millman, K. J., van der Walt, S. J., et al. 2020, "Array programming with NumPy", Nature, 585, 357, doi: 10.1038/s41586-020-2649-2

Harris, D. W., Jensen, T. W., Suzuki, N., et al. 2016, "The Composite Spectrum of BOSS Quasars Selected for Studies of the Lyα Forest", AJ, 151, 155, doi: 10.3847/0004-6256/151/6/155

Hartley, P., Jackson, N., Sluse, D., Stacey, H. R., & Vives-Arias, H. 2019, "Strong lensing reveals jets in a sub-microJy radio-quiet quasar", MNRAS, 485, 3009, doi: 10.1093/mnras/stz510

Hazard, C., Jauncey, D., Goss, W. M., & Herald, D. 2018, "The Sequence of Events that led to the 1963 Publications in Nature of 3C 273, the First Quasar and the First Extragalactic Radio Jet", PASA, 35, e006, doi: 10.1017/pasa.2017.62

Hazard, C., Mackey, M. B., & Shimmins, A. J. 1963, "Investigation of the Radio Source 3C 273 By The Method of Lunar Occultations", Nature, 197, 1037, doi: 10.1038/1971037a0

Heckman, T. M., & Best, P. N. 2014, "The Coevolution of Galaxies and Supermassive Black Holes: Insights from Surveys of the Contemporary Universe", ARA&A, 52, 589, doi: 10.1146/annurev-astro-081913-035722

Helou, G., Khan, I. R., Malek, L., & Boehmer, L. 1988, "IRAS Observations of Galaxies in the Virgo Cluster Area", ApJS, 68, 151, doi: 10.1086/191285

Herenz, E. C., Wisotzki, L., Saust, R., et al. 2019, "The MUSE-Wide Survey: A determination of the Lyman-α emitter luminosity function at $3 < z < 6$", A&A, 621, A107, doi: 10.1051/0004-6361/201834164

Hickox, R. C., & Alexander, D. M. 2018, "Obscured Active Galactic Nuclei", ARA&A, 56, 625, doi: 10.1146/annurev-astro-081817-051803

Honscheid, K., & DePoy, D. L. 2008, "The Dark Energy Camera (DECam)", arXiv e-prints, arXiv:0810.3600. https://arxiv.org/abs/0810.3600

Hopkins, P. F., Hernquist, L., Cox, T. J., et al. 2005, "Black Holes in Galaxy Mergers: Evolution of Quasars", ApJ, 630, 705, doi: 10.1086/432438

Hopkins, P. F., Hernquist, L., Cox, T. J., & Kereš, D. 2008, "A Cosmological Framework for the Co-Evolution of Quasars, Supermassive Black Holes, and Elliptical Galaxies. I. Galaxy Mergers and Quasar Activity", ApJS, 175, 356, doi: 10.1086/524362

Hosokawa, T., Yorke, H. W., Inayoshi, K., Omukai, K., & Yoshida, N. 2013, "Formation of Primordial Supermassive Stars by Rapid Mass Accretion", ApJ, 778, 178, doi: 10.1088/0004-637X/778/2/178

Hryniewicz, K., Czerny, B., Nikołajuk, M., & Kuraszkiewicz, J. 2010, "SDSS J094533.99+100950.1 - the remarkable weak emission line quasar", MNRAS, 404, 2028, doi: 10.1111/j.1365-2966.2010.16418.x

Hsueh, J. W., Enzi, W., Vegetti, S., et al. 2020, "SHARP - VII. New constraints on the dark matter free-streaming properties and substructure abundance from gravitationally lensed quasars", MNRAS, 492, 3047, doi: 10.1093/mnras/stz3177

Huang, K.-W., Di Matteo, T., Bhowmick, A. K., Feng, Y., & Ma, C.-P. 2018, "BLUETIDES simulation: establishing black hole-galaxy relations at high redshift", MNRAS, 478, 5063, doi: 10.1093/mnras/sty1329

Hutsemékers, D., Sluse, D., & Kumar, P. 2020, "Spatially separated continuum sources revealed by microlensing in the gravitationally lensed broad absorption line quasar SDSS J081830.46+060138.0", A&A, 633, A101, doi: 10.1051/0004-6361/201936973

Inada, N., Oguri, M., Shin, M.-S., et al. 2012, "The Sloan Digital Sky Survey Quasar Lens Search. V. Final Catalog from the Seventh Data Release", AJ, 143, 119, doi: 10.1088/0004-6256/143/5/119

Inayoshi, K., Haiman, Z., & Ostriker, J. P. 2016, "Hyper-Eddington accretion flows on to massive black holes", MNRAS, 459, 3738, doi: 10.1093/mnras/stw836

Inayoshi, K., Visbal, E., & Haiman, Z. 2020, "The Assembly of the First Massive Black Holes", ARA&A, 58, 27, doi: 10.1146/annurev-astro-120419-014455

Inoue, A. K., Shimizu, I., Iwata, I., & Tanaka, M. 2014, "An updated analytic model for attenuation by the intergalactic medium", MNRAS, 442, 1805, doi: 10.1093/mnras/stu936

Ishigaki, M., Kawamata, R., Ouchi, M., et al. 2018, "Full-data Results of Hubble Frontier Fields: UV Luminosity Functions at $z \sim 6$–10 and a Consistent Picture of Cosmic Reionization", ApJ, 854, 73, doi: 10.3847/1538-4357/aaa544

Ivezić, Ž., Kahn, S. M., Tyson, J. A., et al. 2019, "LSST: From Science Drivers to Reference Design and Anticipated Data Products", ApJ, 873, 111, doi: 10.3847/1538-4357/ab042c

Izumi, T., Onoue, M., Matsuoka, Y., et al. 2019, "Subaru High-z Exploration of Low-Luminosity Quasars (SHELLQs). VIII. A less biased view of the early co-evolution of black holes and host galaxies", PASJ, 71, 111, doi: 10.1093/pasj/psz096

Izumi, T., Matsuoka, Y., Fujimoto, S., et al. 2021, "Subaru High-z Exploration of Low-luminosity Quasars (SHELLQs). XIII. Large-scale Feedback and Star Formation in a Low-luminosity Quasar at $z = 7.07$ on the Local Black Hole to Host Mass Relation", ApJ, 914, 36, doi: 10.3847/1538-4357/abf6dc

Jackson, N. 2013, "Quasar lensing", Bulletin of the Astronomical Society of India, 41, 19. https://arxiv.org/abs/1304.4172

Jaelani, A. T., Rusu, C. E., Kayo, I., et al. 2021, "Survey of Gravitationally Lensed Objects in HSC Imaging (SuGOHI) - VII. Discovery and confirmation of three strongly lensed quasars", MNRAS, 502, 1487, doi: 10.1093/mnras/stab145

Jaki, S. L. 1978, "Johann Georg von Soldner and the gravitational bending of light, with an English translation of his essay on it published in 1801", Foundations of Physics, 8, 927, doi: 10.1007/BF00715064

Jensen, T. W., Vivek, M., Dawson, K. S., et al. 2016, "Spectral Evolution in High Redshift Quasars from the Final BOSS Sample", ApJ, 833, 199, doi: 10.3847/1538-4357/833/2/199

Jiang, L., Fan, X., Vestergaard, M., et al. 2007, "Gemini Near-Infrared Spectroscopy of Luminous $z \sim 6$ Quasars: Chemical Abundances, Black Hole Masses, and Mg II Absorption", AJ, 134, 1150, doi: 10.1086/520811

Jiang, L., McGreer, I. D., Fan, X., et al. 2016, "The Final SDSS High-redshift Quasar Sample of 52 Quasars at $z > 5.7$", ApJ, 833, 222, doi: 10.3847/1538-4357/833/2/222

Jiang, L., Kashikawa, N., Wang, S., et al. 2021, "Evidence for GN-z11 as a luminous galaxy at redshift 10.957", Nature Astronomy, 5, 256, doi: 10.1038/s41550-020-01275-y

Juric, M. 2012, "LSD: Large Survey Database framework", Astrophysics Source Code Library, record ascl:1209.003. http://ascl.net/1209.003

Kakuma, R., Ouchi, M., Harikane, Y., et al. 2021, "SILVERRUSH. IX. Lyα Intensity Mapping with Star-forming Galaxies at $z = 5.7$ and 6.6: A Possible Detection of Extended Lyα Emission at $\gtrsim$100 Comoving Kiloparsecs around and beyond the Virial-radius Scale of Galaxy Dark Matter Halos", ApJ, 916, 22, doi: 10.3847/1538-4357/ac0725

Kanekar, N., Prochaska, J. X., Christensen, L., et al. 2018, "Massive, Absorption-selected Galaxies at Intermediate Redshifts", ApJ, 856, L23, doi: 10.3847/2041-8213/aab6ab

Kaspi, S. 2007, "Advances in Reverberation Mapping", in Astronomical Society of the Pacific Conference Series, Vol. 373, The Central Engine of Active Galactic Nuclei, ed. L. C. Ho & J. W. Wang, 13. https://arxiv.org/abs/0705.1722

Katz, H., Sijacki, D., & Haehnelt, M. G. 2015, "Seeding high-redshift QSOs by collisional runaway in primordial star clusters", MNRAS, 451, 2352, doi: 10.1093/mnras/stv1048

Kausch, W., Noll, S., Smette, A., et al. 2015, "Molecfit: A general tool for telluric absorption correction. II. Quantitative evaluation on ESO-VLT/X-Shooterspectra", A&A, 576, A78, doi: 10.1051/0004-6361/201423909

Kelson, D. D. 2003, "Optimal Techniques in Two-dimensional Spectroscopy: Background Subtraction for the 21st Century", PASP, 115, 688, doi: 10.1086/375502

Kennicutt, R. C., & Evans, N. J. 2012, "Star Formation in the Milky Way and Nearby Galaxies", ARA&A, 50, 531, doi: 10.1146/annurev-astro-081811-125610

Khrykin, I. S., Hennawi, J. F., Worseck, G., & Davies, F. B. 2021, "The first measurement of the quasar lifetime distribution", MNRAS, 505, 649, doi: 10.1093/mnras/stab1288

Kingma, D. P., & Ba, J. 2014, "Adam: A Method for Stochastic Optimization", arXiv e-prints, arXiv:1412.6980. https://arxiv.org/abs/1412.6980

Klitsch, A., Zwaan, M. A., Péroux, C., et al. 2019, "ALMACAL V: absorption-selected galaxies with evidence for excited ISMs", MNRAS, 482, L65, doi: 10.1093/mnrasl/sly187

Kormendy, J., & Ho, L. C. 2013, "Coevolution (Or Not) of Supermassive Black Holes and Host Galaxies", ARA&A, 51, 511, doi: 10.1146/annurev-astro-082708-101811

Kormendy, J., & Richstone, D. 1995, "Inward Bound—The Search For Supermassive Black Holes In Galactic Nuclei", ARA&A, 33, 581, doi: 10.1146/annurev.aa.33.090195.003053

Krogager, J. K., Møller, P., Fynbo, J. P. U., & Noterdaeme, P. 2017, "Consensus report on 25 yr of searches for damped Lyα galaxies in emission: confirming their metallicity-luminosity relation at $z \gtrsim 2$", MNRAS, 469, 2959, doi: 10.1093/mnras/stx1011

Kubota, A., & Done, C. 2019, "Modelling the spectral energy distribution of super-Eddington quasars", MNRAS, 489, 524, doi: 10.1093/mnras/stz2140

Kulkarni, G., Hennawi, J. F., Rollinde, E., & Vangioni, E. 2014, "Chemical Constraints on the Contribution of Population III Stars to Cosmic Reionization", ApJ, 787, 64, doi: 10.1088/0004-637X/787/1/64

Kulkarni, V. P., Woodgate, B. E., York, D. G., et al. 2006, "A Fabry-Pérot Imaging Search for Lyα Emission in Quasar Absorbers at $z \sim 2.4$", ApJ, 636, 30, doi: 10.1086/497885

Kumar, P., Chand, H., Srianand, R., et al. 2018, "Polarimetric and spectroscopic study of radio-quiet weak emission line quasars", MNRAS, 479, 5075, doi: 10.1093/mnras/sty1802

Kusakabe, H., Blaizot, J., Garel, T., et al. 2020, "The MUSE Hubble Ultra Deep Field Survey. XIV. Evolution of the Lyα emitter fraction from $z = 3$ to $z = 6$", A&A, 638, A12, doi: 10.1051/0004-6361/201937340

Laor, A., & Davis, S. W. 2011, "Cold accretion discs and lineless quasars", MNRAS, 417, 681, doi: 10.1111/j.1365-2966.2011.19310.x

Lapi, A., Shankar, F., Mao, J., et al. 2006, "Quasar Luminosity Functions from Joint Evolution of Black Holes and Host Galaxies", ApJ, 650, 42, doi: 10.1086/507122

Laureijs, R., Amiaux, J., Arduini, S., et al. 2011, "Euclid Definition Study Report", arXiv e-prints, arXiv:1110.3193. https://arxiv.org/abs/1110.3193

Lawrence, A., Warren, S. J., Almaini, O., et al. 2007, "The UKIRT Infrared Deep Sky Survey (UKIDSS)", MNRAS, 379, 1599, doi: 10.1111/j.1365-2966.2007.12040.x

LeCun, Y., Boser, B., Denker, J. S., et al. 1989, "Backpropagation Applied to Handwritten Zip Code Recognition", Neural Computation, 1, 541, doi: 10.1162/neco.1989.1.4.541

Leighly, K. M., Halpern, J. P., Jenkins, E. B., & Casebeer, D. 2007a, "The Intrinsically X-Ray-weak Quasar PHL 1811. II. Optical and UV Spectra and Analysis", ApJS, 173, 1, doi: 10.1086/519768

Leighly, K. M., Halpern, J. P., Jenkins, E. B., et al. 2007b, "The Intrinsically X-Ray Weak Quasar PHL 1811. I. X-Ray Observations and Spectral Energy Distribution", ApJ, 663, 103, doi: 10.1086/518017

Lemon, C., Auger, M. W., McMahon, R., et al. 2020, "The STRong lensing Insights into the Dark Energy Survey (STRIDES) 2017/2018 follow-up campaign: discovery of 10 lensed quasars and 10 quasar pairs", MNRAS, 494, 3491, doi: 10.1093/mnras/staa652

Lemon, C. A., Auger, M. W., & McMahon, R. G. 2019, "Gravitationally lensed quasars in Gaia - III. 22 new lensed quasars from Gaia data release 2", MNRAS, 483, 4242, doi: 10.1093/mnras/sty3366

Lemon, C. A., Auger, M. W., McMahon, R. G., & Ostrovski, F. 2018, "Gravitationally lensed quasars in Gaia - II. Discovery of 24 lensed quasars", MNRAS, 479, 5060, doi: 10.1093/mnras/sty911

Li, S.-S., Yang, S., Yang, Z.-X., et al. 2021, "Reverberation Mapping of Two Luminous Quasars: The Broad-line Region Structure and Black Hole Mass", ApJ, 920, 9, doi: 10.3847/1538-4357/ac116e

Liddle, A. 2015, *An Introduction to Modern Cosmology, Third Edition* (John Wiley & Sons)

Liu, Y., & Zhang, S. N. 2011, "Dusty Torus Formation by Anisotropic Radiative Pressure Feedback of Active Galactic Nuclei", ApJ, 728, L44, doi: 10.1088/2041-8205/728/2/L44

Loeb, A., & Furlanetto, S. R. 2013, *The First Galaxies in the Universe* (Princeton University Press)

Luo, B., Brandt, W. N., Hall, P. B., et al. 2015, "X-ray Insights into the Nature of PHL 1811 Analogs and Weak Emission-line Quasars: Unification with a Geometrically Thick Accretion Disk?", ApJ, 805, 122, doi: 10.1088/0004-637X/805/2/122

Lupi, A., Haiman, Z., & Volonteri, M. 2021, "Forming massive seed black holes in high-redshift quasar host progenitors", MNRAS, 503, 5046, doi: 10.1093/mnras/stab692

Ma, Q., Maio, U., Ciardi, B., & Salvaterra, R. 2017, "Metal enrichment signatures of the first stars on high-z DLAs", MNRAS, 472, 3532, doi: 10.1093/mnras/stx1839

Mackenzie, R., Pezzulli, G., Cantalupo, S., et al. 2021, "Revealing the impact of quasar luminosity on giant Lyα nebulae", MNRAS, 502, 494, doi: 10.1093/mnras/staa3277

Madau, P., & Dickinson, M. 2014, "Cosmic Star-Formation History", ARA&A, 52, 415, doi: 10.1146/annurev-astro-081811-125615

Mandelbaum, R. 2018, "Weak Lensing for Precision Cosmology", ARA&A, 56, 393, doi: 10.1146/annurev-astro-081817-051928

Marculewicz, M., & Nikolajuk, M. 2020, "Black Hole Masses of Weak Emission Line Quasars Based on the Continuum Fit Method", ApJ, 897, 117, doi: 10.3847/1538-4357/ab9597

Marshall, M., Cohen, S. H., Croft, R., et al. 2021a, "Unveiling Stellar Light from Host Galaxies of $z \sim 6$ Quasars", JWST Proposal. Cycle 1, ID. #1813

Marshall, M. A., Ni, Y., Di Matteo, T., et al. 2020a, "The host galaxies of $z = 7$ quasars: predictions from the BLUETIDES simulation", MNRAS, 499, 3819, doi: 10.1093/mnras/staa2982

Marshall, M. A., Wyithe, J. S. B., Windhorst, R. A., et al. 2021b, "Observing the host galaxies of high-redshift quasars with JWST: predictions from the BLUETIDES simulation", MNRAS, 506, 1209, doi: 10.1093/mnras/stab1763

Marshall, M. A., Mechtley, M., Windhorst, R. A., et al. 2020b, "Limits to Rest-frame Ultraviolet Emission from Far-infrared-luminous $z = 6$ Quasar Hosts", ApJ, 900, 21, doi: 10.3847/1538-4357/abaa4c

Mason, C. A., Treu, T., Schmidt, K. B., et al. 2015, "Correcting the $z \sim 8$ Galaxy Luminosity Function for Gravitational Lensing Magnification Bias", ApJ, 805, 79, doi: 10.1088/0004-637X/805/1/79

Matsuoka, Y., Iwasawa, K., Onoue, M., et al. 2018a, "Subaru High-z Exploration of Low-luminosity Quasars (SHELLQs). IV. Discovery of 41 Quasars and Luminous Galaxies at $5.7 \leq z \leq 6.9$", ApJS, 237, 5, doi: 10.3847/1538-4365/aac724

Matsuoka, Y., Strauss, M. A., Kashikawa, N., et al. 2018b, "Subaru High-z Exploration of Low-luminosity Quasars (SHELLQs). V. Quasar Luminosity Function and Contribution to Cosmic Reionization at $z = 6$", ApJ, 869, 150, doi: 10.3847/1538-4357/aaee7a

Matsuoka, Y., Iwasawa, K., Onoue, M., et al. 2021, "Subaru High-z Exploration of Low-Luminosity Quasars (SHELLQs). XVI. 69 New Quasars at $5.8 < z < 7.0$", arXiv e-prints, arXiv:2111.12766. https://arxiv.org/abs/2111.12766

Mazzucchelli, C., Bañados, E., Venemans, B. P., et al. 2017, "Physical Properties of 15 Quasars at $z \gtrsim 6.5$", ApJ, 849, 91, doi: 10.3847/1538-4357/aa9185

McGreer, I. D., Jiang, L., Fan, X., et al. 2013, "The $z = 5$ Quasar Luminosity Function from SDSS Stripe 82", ApJ, 768, 105, doi: 10.1088/0004-637X/768/2/105

McMahon, R. G., Banerji, M., Gonzalez, E., et al. 2013, "First Scientific Results from the VISTA Hemisphere Survey (VHS)", The Messenger, 154, 35

—. 2021, "VizieR Online Data Catalog: The VISTA Hemisphere Survey (VHS) catalog DR5 (McMahon+, 2020)", VizieR Online Data Catalog, II/367

McMullin, J. P., Waters, B., Schiebel, D., Young, W., & Golap, K. 2007, "CASA Architecture and Applications", in Astronomical Society of the Pacific Conference Series, Vol. 376, Astronomical Data Analysis Software and Systems XVI, ed. R. A. Shaw, F. Hill, & D. J. Bell, 127

Mesinger, A. 2018, "Reionization and Cosmic Dawn: theory and simulations", in Proceedings of the International Astronomical Union, Vol. 333, Peering towards Cosmic Dawn, ed. V. Jelić & T. van der Hulst, 3–11, doi: 10.1017/S1743921317011139

Metcalf, R. B., Meneghetti, M., Avestruz, C., et al. 2019, "The strong gravitational lens finding challenge", A&A, 625, A119, doi: 10.1051/0004-6361/201832797

Meusinger, H., & Balafkan, N. 2014, "A large sample of Kohonen-selected SDSS quasars with weak emission lines: selection effects and statistical properties", A&A, 568, A114, doi: 10.1051/0004-6361/201423810

Meyer, R. A., Bosman, S. E. I., & Ellis, R. S. 2019, "New constraints on quasar evolution: broad-line velocity shifts over $1.5 \lesssim z \lesssim 7.5$", MNRAS, 487, 3305, doi: 10.1093/mnras/stz1504

Meyer, R. A., Decarli, R., Walter, F., et al. 2022, "Constraining Galaxy Overdensities around Three $z \sim 6.5$ Quasars with ALMA and MUSE", ApJ, 927, 141, doi: 10.3847/1538-4357/ac4f67

Mignoli, M., Gilli, R., Decarli, R., et al. 2020, "Web of the giant: Spectroscopic confirmation of a large-scale structure around the $z = 6.31$ quasar SDSS J1030+0524", A&A, 642, L1, doi: 10.1051/0004-6361/202039045

Millon, M., Courbin, F., Bonvin, V., et al. 2020, "TDCOSMO. II. Six new time delays in lensed quasars from high-cadence monitoring at the MPIA 2.2 m telescope", A&A, 642, A193, doi: 10.1051/0004-6361/202038698

Milutinovic, N., Ellison, S. L., Prochaska, J. X., & Tumlinson, J. 2010, "Ionization corrections in a multiphase interstellar medium: lessons from a $z_{\rm abs} \sim 2$ sub-DLA", MNRAS, 408, 2071, doi: 10.1111/j.1365-2966.2010.17280.x

Miralda-Escudé, J. 1998, "Reionization of the Intergalactic Medium and the Damping Wing of the Gunn-Peterson Trough", ApJ, 501, 15, doi: 10.1086/305799

Mitra, K., Chatterjee, S., DiPompeo, M. A., Myers, A. D., & Zheng, Z. 2018, "The Halo Occupation Distribution of obscured quasars: revisiting the unification model", MNRAS, 477, 45, doi: 10.1093/mnras/sty556

Møller, P., Christensen, L., Zwaan, M. A., et al. 2018, "ALMA + VLT observations of a damped Lyman-α absorbing galaxy: massive, wide CO emission, gas-rich but with very low SFR", MNRAS, 474, 4039, doi: 10.1093/mnras/stx2845

Morgan, C. W., Hyer, G. E., Bonvin, V., et al. 2018, "Accretion Disk Size Measurement and Time Delays in the Lensed Quasar WFI 2033-4723", ApJ, 869, 106, doi: 10.3847/1538-4357/aaed3e

Mortlock, D. J., Patel, M., Warren, S. J., et al. 2012, "Probabilistic selection of high-redshift quasars", MNRAS, 419, 390, doi: 10.1111/j.1365-2966.2011.19710.x

Mortlock, D. J., Warren, S. J., Venemans, B. P., et al. 2011, "A luminous quasar at a redshift of $z = 7.085$", Nature, 474, 616, doi: 10.1038/nature10159

Morton, D. C. 2003, "Atomic Data for Resonance Absorption Lines. III. Wavelengths Longward of the Lyman Limit for the Elements Hydrogen to Gallium", ApJS, 149, 205, doi: 10.1086/377639

Murphy, E. J., Condon, J. J., Schinnerer, E., et al. 2011, "Calibrating Extinction-free Star Formation Rate Diagnostics with 33 GHz Free-free Emission in NGC 6946", ApJ, 737, 67, doi: 10.1088/0004-637X/737/2/67

Nanni, R., Hennawi, J. F., Wang, F., et al. 2021, "Paving the Way for Euclid and JWST via Optimal Selection of High-z Quasars", arXiv e-prints, arXiv:2111.03073. https://arxiv.org/abs/2111.03073

Neeleman, M., Kanekar, N., Prochaska, J. X., Rafelski, M. A., & Carilli, C. L. 2019, "[C II] 158 μm Emission from $z \sim 4$ H I Absorption-selected Galaxies", ApJ, 870, L19, doi: 10.3847/2041-8213/aaf871

Neeleman, M., Prochaska, J. X., Kanekar, N., & Rafelski, M. 2020, "A cold, massive, rotating disk galaxy 1.5 billion years after the Big Bang", Nature, 581, 269, doi: 10.1038/s41586-020-2276-y

Neeleman, M., Novak, M., Venemans, B. P., et al. 2021, "The Kinematics of $z \gtrsim 6$ Quasar Host Galaxies", ApJ, 911, 141, doi: 10.3847/1538-4357/abe70f

Netzer, H. 2013, *The Physics and Evolution of Active Galactic Nuclei* (Cambridge University Press), doi: https://doi.org/10.1017/CBO9781139109291

—. 2015, "Revisiting the Unified Model of Active Galactic Nuclei", ARA&A, 53, 365, doi: 10.1146/annurev-astro-082214-122302

Newville, M., Otten, R., Nelson, A., et al. 2019, "lmfit/lmfit-py 0.9.14", 0.9.14, Zenodo, doi: 10.5281/zenodo.3381550

Ni, Q., Brandt, W. N., Luo, B., et al. 2018, "Connecting the X-ray properties of weak-line and typical quasars: testing for a geometrically thick accretion disk", MNRAS, 480, 5184, doi: 10.1093/mnras/sty1989

—. 2022, "Sensitive Chandra coverage of a representative sample of weak-line quasars: revealing the full range of X-ray properties", MNRAS, 511, 5251, doi: 10.1093/mnras/stac394

Nightingale, J., Hayes, R., Kelly, A., et al. 2021, "PyAutoLens: Open-Source Strong Gravitational Lensing", The Journal of Open Source Software, 6, 2825, doi: 10.21105/joss.02825

Nikołajuk, M., & Walter, R. 2012, "The environment of weak emission-line quasars", MNRAS, 420, 2518, doi: 10.1111/j.1365-2966.2011.20216.x

Nissen, P. E., Chen, Y. Q., Carigi, L., Schuster, W. J., & Zhao, G. 2014, "Carbon and oxygen abundances in stellar populations", A&A, 568, A25, doi: 10.1051/0004-6361/201424184

Novak, M., Bañados, E., Decarli, R., et al. 2019, "An ALMA Multiline Survey of the Interstellar Medium of the Redshift 7.5 Quasar Host Galaxy J1342+0928", ApJ, 881, 63, doi: 10.3847/1538-4357/ab2beb

Oesch, P. A., Brammer, G., van Dokkum, P. G., et al. 2016, "A Remarkably Luminous Galaxy at $z = 11.1$ Measured with Hubble Space Telescope Grism Spectroscopy", ApJ, 819, 129, doi: 10.3847/0004-637X/819/2/129

Ohsuga, K., Mori, M., Nakamoto, T., & Mineshige, S. 2005, "Supercritical Accretion Flows around Black Holes: Two-dimensional, Radiation Pressure-dominated Disks with Photon Trapping", ApJ, 628, 368, doi: 10.1086/430728

Onoue, M., Kashikawa, N., Matsuoka, Y., et al. 2019, "Subaru High-z Exploration of Low-luminosity Quasars (SHELLQs). VI. Black Hole Mass Measurements of Six Quasars at $6.1 \leq z \leq 6.7$", ApJ, 880, 77, doi: 10.3847/1538-4357/ab29e9

Onoue, M., Bañados, E., Mazzucchelli, C., et al. 2020, "No Redshift Evolution in the Broad-line-region Metallicity up to $z = 7.54$: Deep Near-infrared Spectroscopy of ULAS J1342+0928", ApJ, 898, 105, doi: 10.3847/1538-4357/aba193

Onoue, M., Ding, X., Izumi, T., et al. 2021, "A Complete Census of Supermassive Black Holes and Host Galaxies at $z = 6$", JWST Proposal. Cycle 1, ID. #1967

Ota, K., Venemans, B. P., Taniguchi, Y., et al. 2018, "Large-scale Environment of a $z = 6.61$ Luminous Quasar Probed by Lyα Emitters and Lyman-Break Galaxies", ApJ, 856, 109, doi: 10.3847/1538-4357/aab35b

Ouchi, M., Ono, Y., & Shibuya, T. 2020, "Observations of the Lyman-α Universe", ARA&A, 58, 617, doi: 10.1146/annurev-astro-032620-021859

Overzier, R. A. 2022, "Conditions for Direct Black Hole Seed Collapse near a Radio-loud Quasar 1 Gyr after the Big Bang", ApJ, 926, 114, doi: 10.3847/1538-4357/ac448c

Pacucci, F., Dayal, P., Harikane, Y., Inoue, A. K., & Loeb, A. 2022, "Are the Newly-Discovered $z \sim 13$ Drop-out Sources Starburst Galaxies or Quasars?", arXiv e-prints, arXiv:2201.00823. https://arxiv.org/abs/2201.00823

Pacucci, F., & Loeb, A. 2019, "Most Lensed Quasars at $z > 6$ are Missed by Current Surveys", ApJ, 870, L12, doi: 10.3847/2041-8213/aaf86a

—. 2022, "The search for the farthest quasar: consequences for black hole growth and seed models", MNRAS, 509, 1885, doi: 10.1093/mnras/stab3071

Pâris, I., Petitjean, P., Rollinde, E., et al. 2011, "A principal component analysis of quasar UV spectra at $z \sim 3$", A&A, 530, A50, doi: 10.1051/0004-6361/201016233

Pâris, I., Petitjean, P., Aubourg, É., et al. 2018, "The Sloan Digital Sky Survey Quasar Catalog: Fourteenth data release", A&A, 613, A51, doi: 10.1051/0004-6361/201732445

Paul, J. D., Plotkin, R. M., Shemmer, O., et al. 2022, "Connecting Low- and High-Redshift

Weak Emission-Line Quasars via HST Spectroscopy of Lyα Emission", arXiv e-prints, arXiv:2203.03817. https://arxiv.org/abs/2203.03817

Pedregosa, F., Varoquaux, G., Gramfort, A., et al. 2012, "Scikit-learn: Machine Learning in Python", arXiv e-prints, arXiv:1201.0490. https://arxiv.org/abs/1201.0490

Perlmutter, S., Aldering, G., della Valle, M., et al. 1998, "Discovery of a supernova explosion at half the age of the Universe", Nature, 391, 51, doi: 10.1038/34124

Peterson, B. M., & Bentz, M. C. 2006, "Black hole masses from reverberation mapping", New A Rev., 50, 796, doi: 10.1016/j.newar.2006.06.062

Piana, O., Dayal, P., Volonteri, M., & Choudhury, T. R. 2021, "The mass assembly of high-redshift black holes", MNRAS, 500, 2146, doi: 10.1093/mnras/staa3363

Planck Collaboration, Aghanim, N., Akrami, Y., et al. 2020, "Planck 2018 results. VI. Cosmological parameters", A&A, 641, A6, doi: 10.1051/0004-6361/201833910

Plotkin, R. M., Shemmer, O., Trakhtenbrot, B., et al. 2015, "Detection of Rest-frame Optical Lines from X-shooter Spectroscopy of Weak Emission Line Quasars", ApJ, 805, 123, doi: 10.1088/0004-637X/805/2/123

Pons, E., McMahon, R. G., Simcoe, R. A., et al. 2019, "A new bright $z = 6.82$ quasar discovered with VISTA: VHS J0411-0907", MNRAS, 484, 5142, doi: 10.1093/mnras/stz292

Porciani, C., & Norberg, P. 2006, "Luminosity- and redshift-dependent quasar clustering", MNRAS, 371, 1824, doi: 10.1111/j.1365-2966.2006.10813.x

Prakash, A., Licquia, T. C., Newman, J. A., et al. 2016, "The SDSS-IV Extended Baryon Oscillation Spectroscopic Survey: Luminous Red Galaxy Target Selection", ApJS, 224, 34, doi: 10.3847/0067-0049/224/2/34

Prochaska, J., Hennawi, J., Westfall, K., et al. 2020, "PypeIt: The Python Spectroscopic Data Reduction Pipeline", The Journal of Open Source Software, 5, 2308, doi: 10.21105/joss.02308

Prochaska, J. X., Tejos, N., Crighton, N., et al. 2016, "Linetools/Linetools: Second Major Release", v0.2, Zenodo, doi: 10.5281/zenodo.168270

Quiret, S., Péroux, C., Zafar, T., et al. 2016, "The ESO UVES advanced data products quasar sample - VI. Sub-damped Lyman-α metallicity measurements and the circumgalactic medium", MNRAS, 458, 4074, doi: 10.1093/mnras/stw524

Ramos Almeida, C., & Ricci, C. 2017, "Nuclear obscuration in active galactic nuclei", Nature Astronomy, 1, 679, doi: 10.1038/s41550-017-0232-z

Reback, J., Jbrockmendel, McKinney, W., et al. 2021, "pandas-dev/pandas: Pandas 1.3.0", v1.3.0, Zenodo, doi: 10.5281/zenodo.3509134

Reed, S. L., Banerji, M., Becker, G. D., et al. 2019, "Three new VHS-DES quasars at $6.7 < z < 6.9$ and emission line properties at $z > 6.5$", MNRAS, 487, 1874, doi: 10.1093/mnras/stz1341

Refsdal, S. 1964, "On the possibility of determining Hubble's parameter and the masses of galaxies from the gravitational lens effect", MNRAS, 128, 307, doi: 10.1093/mnras/128.4.307

Reinoso, B., Schleicher, D. R. G., Fellhauer, M., Klessen, R. S., & Boekholt, T. C. N. 2018, "Collisions in primordial star clusters. Formation pathway for intermediate mass black holes", A&A, 614, A14, doi: 10.1051/0004-6361/201732224

Reis, R. C., Reynolds, M. T., Miller, J. M., & Walton, D. J. 2014, "Reflection from the strong gravity regime in a lensed quasar at redshift $z = 0.658$", Nature, 507, 207, doi: 10.1038/nature13031

Richards, G. T., Lacy, M., Storrie-Lombardi, L. J., et al. 2006, "Spectral Energy Distributions and Multiwavelength Selection of Type 1 Quasars", ApJS, 166, 470, doi: 10.1086/506525

Riess, A. G., Filippenko, A. V., Challis, P., et al. 1998, "Observational Evidence from Supernovae for an Accelerating Universe and a Cosmological Constant", AJ, 116, 1009, doi: 10.1086/300499

Robitaille, T. 2019, "APLpy v2.0: The Astronomical Plotting Library in Python", doi: 10.5281/zenodo.2567476

Robitaille, T., & Bressert, E. 2012, "APLpy: Astronomical Plotting Library in Python", Astrophysics Source Code Library. http://ascl.net/1208.017

Robitaille, T., Ginsburg, A., Beaumont, C., Leroy, A., & Rosolowsky, E. 2016, "spectral-cube: Read and analyze astrophysical spectral data cubes". http://ascl.net/1609.017

Rocklin, M. 2015, "Dask: Parallel computation with blocked algorithms and task scheduling", in Proceedings of the 14th Python in Science Conference, ed. K. Huff & J. Bergstra, 130 – 136

Rojas, K., Savary, E., Clément, B., et al. 2021, "Strong lens systems search in the Dark Energy Survey using Convolutional Neural Networks", arXiv e-prints, arXiv:2109.00014. https://arxiv.org/abs/2109.00014

Rousselot, P., Lidman, C., Cuby, J. G., Moreels, G., & Monnet, G. 2000, "Night-sky spectral atlas of OH emission lines in the near-infrared", A&A, 354, 1134

Ryden, B. 2016, *Introduction to Cosmology, Second Edition* (Cambridge University Press), doi: https://doi.org/10.1017/9781316651087

Salviander, S., Shields, G. A., Gebhardt, K., & Bonning, E. W. 2007, "The Black Hole Mass-Galaxy Bulge Relationship for QSOs in the Sloan Digital Sky Survey Data Release 3", ApJ, 662, 131, doi: 10.1086/513086

Sandage, A. 1965, "The Existence of a Major New Constituent of the Universe: the Quasistellar Galaxies.", ApJ, 141, 1560, doi: 10.1086/148245

Sanders, D. B., & Mirabel, I. F. 1996, "Luminous Infrared Galaxies", ARA&A, 34, 749, doi: 10.1146/annurev.astro.34.1.749

Sanders, D. B., Soifer, B. T., Elias, J. H., et al. 1988a, "Ultraluminous Infrared Galaxies and the Origin of Quasars", ApJ, 325, 74, doi: 10.1086/165983

Sanders, D. B., Soifer, B. T., Elias, J. H., Neugebauer, G., & Matthews, K. 1988b, "Warm Ultraluminous Galaxies in the IRAS Survey: The Transition from Galaxy to Quasar?", ApJ, 328, L35, doi: 10.1086/185155

Scaramella, R., Amiaux, J., Mellier, Y., et al. 2021, "Euclid preparation: I. The Euclid Wide Survey", arXiv e-prints, arXiv:2108.01201. https://arxiv.org/abs/2108.01201

Schauer, A. T. P., Regan, J., Glover, S. C. O., & Klessen, R. S. 2017, "The formation of direct collapse black holes under the influence of streaming velocities", MNRAS, 471, 4878, doi: 10.1093/mnras/stx1915

Schindler, J.-T., Farina, E. P., Bañados, E., et al. 2020, "The X-SHOOTER/ALMA Sample of Quasars in the Epoch of Reionization. I. NIR Spectral Modeling, Iron Enrichment, and Broad Emission Line Properties", ApJ, 905, 51, doi: 10.3847/1538-4357/abc2d7

Schlafly, E. F., Meisner, A. M., & Green, G. M. 2019, "The unWISE Catalog: Two Billion Infrared Sources from Five Years of WISE Imaging", ApJS, 240, 30, doi: 10.3847/1538-4365/aafbea

Schlegel, D. J., Finkbeiner, D. P., & Davis, M. 1998, "Maps of Dust Infrared Emission for Use in Estimation of Reddening and Cosmic Microwave Background Radiation Foregrounds", ApJ, 500, 525, doi: 10.1086/305772

Schmidt, B. P., Suntzeff, N. B., Phillips, M. M., et al. 1998, "The High-Z Supernova Search: Measuring Cosmic Deceleration and Global Curvature of the Universe Using Type IA Supernovae", ApJ, 507, 46, doi: 10.1086/306308

Schmidt, M. 1963, "3C 273 : A Star-Like Object with Large Red-Shift", Nature, 197, 1040, doi: 10.1038/1971040a0

—. 1966, "Redshifts of Fourteen Quasi-Stellar Radio Sources", ApJ, 144, 443, doi: 10.1086/148627

Schmidt, R. W., & Wambsganss, J. 2010, "Quasar microlensing", General Relativity and Gravitation, 42, 2127, doi: 10.1007/s10714-010-0956-x

Schneider, P. 2015, *Extragalactic Astronomy and Cosmology: An Introduction* (Springer, Berlin, Heidelberg), doi: 10.1007/978-3-642-54083-7

Schneider, P., & Sluse, D. 2013, "Mass-sheet degeneracy, power-law models and external convergence: Impact on the determination of the Hubble constant from gravitational lensing", A&A, 559, A37, doi: 10.1051/0004-6361/201321882

Selsing, J., Fynbo, J. P. U., Christensen, L., & Krogager, J. K. 2016, "An X-Shooter composite of bright $1 < z < 2$ quasars from UV to infrared", A&A, 585, A87, doi: 10.1051/0004-6361/201527096

Shalyapin, V. N., Goicoechea, L. J., Morgan, C. W., Cornachione, M. A., & Sergeyev, A. V. 2021, "Resolving the inner accretion flow towards the central supermassive black hole in SDSS J1339+1310", A&A, 646, A165, doi: 10.1051/0004-6361/202038770

Shang, Z., Brotherton, M. S., Wills, B. J., et al. 2011, "The Next Generation Atlas of Quasar Spectral Energy Distributions from Radio to X-Rays", ApJS, 196, 2, doi: 10.1088/0067-0049/196/1/2

Shemmer, O., Brandt, W. N., Schneider, D. P., et al. 2006, "Chandra Observations of the Highest Redshift Quasars from the Sloan Digital Sky Survey", ApJ, 644, 86, doi: 10.1086/503543

Shemmer, O., Trakhtenbrot, B., Anderson, S. F., et al. 2010, "Weak Line Quasars at High Redshift: Extremely High Accretion Rates or Anemic Broad-line Regions?", ApJ, 722, L152, doi: 10.1088/2041-8205/722/2/L152

Shen, Y. 2013, "The mass of quasars", Bulletin of the Astronomical Society of India, 41, 61. https://arxiv.org/abs/1302.2643

Shen, Y., Richards, G. T., Strauss, M. A., et al. 2011, "A Catalog of Quasar Properties from Sloan Digital Sky Survey Data Release 7", ApJS, 194, 45, doi: 10.1088/0067-0049/194/2/45

Shen, Y., Wu, J., Jiang, L., et al. 2019, "Gemini GNIRS Near-infrared Spectroscopy of 50 Quasars at $z \gtrsim 5.7$", ApJ, 873, 35, doi: 10.3847/1538-4357/ab03d9

Simcoe, R. A., Onoue, M., Eilers, A.-C., et al. 2020, "Interstellar and Circumgalactic Properties of an Unseen $z = 6.84$ Galaxy: Abundances, Ionization, and Heating in the Earliest Known Quasar Absorber", arXiv e-prints, arXiv:2011.10582. https://arxiv.org/abs/2011.10582

Simcoe, R. A., Burgasser, A. J., Schechter, P. L., et al. 2013, "FIRE: A Facility Class Near-Infrared Echelle Spectrometer for the Magellan Telescopes", PASP, 125, 270, doi: 10.1086/670241

Skrzypek, N., Warren, S. J., Faherty, J. K., et al. 2015, "Photometric brown-dwarf classification. I. A method to identify and accurately classify large samples of brown dwarfs without spectroscopy", A&A, 574, A78, doi: 10.1051/0004-6361/201424570

Sluse, D., Sonnenfeld, A., Rumbaugh, N., et al. 2017, "H0LiCOW - II. Spectroscopic survey and galaxy-group identification of the strong gravitational lens system HE 0435-1223", MNRAS, 470, 4838, doi: 10.1093/mnras/stx1484

Smette, A., Sana, H., Noll, S., et al. 2015, "Molecfit: A general tool for telluric absorption correction. I. Method and application to ESO instruments", A&A, 576, A77, doi: 10.1051/0004-6361/201423932

Soltan, A. 1982, "Masses of quasars.", MNRAS, 200, 115, doi: 10.1093/mnras/200.1.115

Songaila, A., & Cowie, L. L. 2010, "The Evolution of Lyman Limit Absorption Systems to Redshift Six", ApJ, 721, 1448, doi: 10.1088/0004-637X/721/2/1448

Soto, K. T., Lilly, S. J., Bacon, R., Richard, J., & Conseil, S. 2016, "ZAP - enhanced PCA sky subtraction for integral field spectroscopy", MNRAS, 458, 3210, doi: 10.1093/mnras/stw474

Spergel, D., Gehrels, N., Breckinridge, J., et al. 2013, "Wide-Field InfraRed Survey Telescope-Astrophysics Focused Telescope Assets WFIRST-AFTA Final Report", arXiv e-prints, arXiv:1305.5422. https://arxiv.org/abs/1305.5422

Spergel, D., Gehrels, N., Baltay, C., et al. 2015, "Wide-Field InfrarRed Survey Telescope-Astrophysics Focused Telescope Assets WFIRST-AFTA 2015 Report", arXiv e-prints, arXiv:1503.03757. https://arxiv.org/abs/1503.03757

Spiniello, C., Agnello, A., Napolitano, N. R., et al. 2018, "KiDS-SQuaD: The KiDS Strongly lensed Quasar Detection project", MNRAS, 480, 1163, doi: 10.1093/mnras/sty1923

Spinoglio, L., & Fernández-Ontiveros, J. A. 2021, "AGN types and unification model", in Proceedings of the International Astronomical Union, Vol. 356, Nuclear Activity in Galaxies Across Cosmic Time, ed. M. Pović, P. Marziani, J. Masegosa, H. Netzer, S. H. Negu, & S. B. Tessema, 29–43, doi: 10.1017/S1743921320002549

Stacey, H. R., McKean, J. P., Robertson, N. C., et al. 2018, "Gravitational lensing reveals extreme dust-obscured star formation in quasar host galaxies", MNRAS, 476, 5075, doi: 10.1093/mnras/sty458

Stacey, H. R., McKean, J. P., Powell, D. M., et al. 2021, "The rocky road to quiescence: compaction and quenching of quasar host galaxies at $z \sim 2$", MNRAS, 500, 3667, doi: 10.1093/mnras/staa3433

Stockton, A. 1980, "The lens galaxy of the twin QSO 0957+561", ApJ, 242, L141, doi: 10.1086/183419

Sultana, F., Sufian, A., & Dutta, P. 2019, "Advancements in Image Classification using Convolutional Neural Network", arXiv e-prints, arXiv:1905.03288. https://arxiv.org/abs/1905.03288

Suyu, S. H., Marshall, P. J., Blandford, R. D., et al. 2009, "Dissecting the Gravitational Lens B1608+656. I. Lens Potential Reconstruction", ApJ, 691, 277, doi: 10.1088/0004-637X/691/1/277

Suyu, S. H., Bonvin, V., Courbin, F., et al. 2017, "H0LiCOW - I. H_0 Lenses in COSMOGRAIL's Wellspring: program overview", MNRAS, 468, 2590, doi: 10.1093/mnras/stx483

Suzuki, N. 2006, "Quasar Spectrum Classification with Principal Component Analysis (PCA): Emission Lines in the Lyα Forest", ApJS, 163, 110, doi: 10.1086/499272

Tanaka, T., & Haiman, Z. 2009, "The Assembly of Supermassive Black Holes at High Redshifts", ApJ, 696, 1798, doi: 10.1088/0004-637X/696/2/1798

Tang, J.-J., Goto, T., Ohyama, Y., et al. 2019, "Rapid black hole growth at the dawn of the Universe: a super-Eddington quasar at $z = 6.6$", MNRAS, 484, 2575, doi: 10.1093/mnras/stz134

Taylor, M. 2017, "TOPCAT: Desktop Exploration of Tabular Data for Astronomy and Beyond", arXiv e-prints, arXiv:1707.02160. https://arxiv.org/abs/1707.02160

Toshikawa, J., Kashikawa, N., Overzier, R., et al. 2016, "A Systematic Survey of Protoclusters at $z \sim 3$–6 in the CFHTLS Deep Fields", ApJ, 826, 114, doi: 10.3847/0004-637X/826/2/114

Trakhtenbrot, B., Volonteri, M., & Natarajan, P. 2017, "On the Accretion Rates and Radiative Efficiencies of the Highest-redshift Quasars", ApJ, 836, L1, doi: 10.3847/2041-8213/836/1/L1

Treu, T. 2010, "Strong Lensing by Galaxies", ARA&A, 48, 87, doi: 10.1146/annurev-astro-081309-130924

Treu, T., & Ellis, R. S. 2015, "Gravitational Lensing: Einstein's unfinished symphony", Contemporary Physics, 56, 17, doi: 10.1080/00107514.2015.1006001

Treu, T., & Marshall, P. J. 2016, "Time delay cosmography", A&A Rev., 24, 11, doi: 10.1007/s00159-016-0096-8

Tsuzuki, Y., Kawara, K., Yoshii, Y., et al. 2006, "Fe II Emission in 14 Low-Redshift Quasars. I. Observations", ApJ, 650, 57, doi: 10.1086/506376

Urry, C. 2004, "AGN Unification: An Update", in Astronomical Society of the Pacific Conference Series, Vol. 311, AGN Physics with the Sloan Digital Sky Survey, ed. G. T. Richards & P. B. Hall, 49. https://arxiv.org/abs/astro-ph/0312545

Urry, C. M., & Padovani, P. 1995, "Unified Schemes for Radio-Loud Active Galactic Nuclei", PASP, 107, 803, doi: 10.1086/133630

Utsumi, Y., Goto, T., Kashikawa, N., et al. 2010, "A Large Number of $z > 6$ Galaxies Around a QSO at $z = 6.43$: Evidence for a Protocluster?", ApJ, 721, 1680, doi: 10.1088/0004-637X/721/2/1680

Vanden Berk, D. E., Richards, G. T., Bauer, A., et al. 2001, "Composite Quasar Spectra from the Sloan Digital Sky Survey", AJ, 122, 549, doi: 10.1086/321167

Ďurovčíková, D., Katz, H., Bosman, S. E. I., et al. 2020, "Reionization history constraints from neural network based predictions of high-redshift quasar continua", MNRAS, 493, 4256, doi: 10.1093/mnras/staa505

Venemans, B. P., Walter, F., Zschaechner, L., et al. 2016, "Bright [C II] and Dust Emission in Three $z > 6.6$ Quasar Host Galaxies Observed by ALMA", ApJ, 816, 37, doi: 10.3847/0004-637X/816/1/37

Venemans, B. P., McMahon, R. G., Walter, F., et al. 2012, "Detection of Atomic Carbon [C II] 158 μm and Dust Emission from a $z = 7.1$ Quasar Host Galaxy", ApJ, 751, L25, doi: 10.1088/2041-8205/751/2/L25

Venemans, B. P., Bañados, E., Decarli, R., et al. 2015, "The Identification of Z-dropouts in Pan-STARRS1: Three Quasars at 6.5< z< 6.7", ApJ, 801, L11, doi: 10.1088/2041-8205/801/1/L11

Venemans, B. P., Decarli, R., Walter, F., et al. 2018, "Dust Emission in an Accretion-rate-limited Sample of $z \gtrsim 6$ Quasars", ApJ, 866, 159, doi: 10.3847/1538-4357/aadf35

Vestergaard, M., & Osmer, P. S. 2009, "Mass Functions of the Active Black Holes in Distant Quasars from the Large Bright Quasar Survey, the Bright Quasar Survey, and the Color-selected Sample of the SDSS Fall Equatorial Stripe", ApJ, 699, 800, doi: 10.1088/0004-637X/699/1/800

Vestergaard, M., & Wilkes, B. J. 2001, "An Empirical Ultraviolet Template for Iron Emission in Quasars as Derived from I Zwicky 1", ApJS, 134, 1, doi: 10.1086/320357

Virtanen, P., Gommers, R., Oliphant, T. E., et al. 2020, "SciPy 1.0: Fundamental Algorithms for Scientific Computing in Python", Nature Methods, 17, 261, doi: https://doi.org/10.1038/s41592-019-0686-2

Volonteri, M. 2010, "Formation of supermassive black holes", A&A Rev., 18, 279, doi: 10.1007/s00159-010-0029-x

Volonteri, M., Sikora, M., Lasota, J. P., & Merloni, A. 2013, "The Evolution of Active Galactic Nuclei and their Spins", ApJ, 775, 94, doi: 10.1088/0004-637X/775/2/94

Walsh, D., Carswell, R. F., & Weymann, R. J. 1979, "0957+561 A, B: twin quasistellar objects or gravitational lens?", Nature, 279, 381, doi: 10.1038/279381a0

Walter, F., Riechers, D., Cox, P., et al. 2009, "A kiloparsec-scale hyper-starburst in a quasar host less than 1gigayear after the Big Bang", Nature, 457, 699, doi: 10.1038/nature07681

Wang, F., Yang, J., Fan, X., et al. 2019, "Exploring Reionization-era Quasars. III. Discovery of 16 Quasars at $6.4 \lesssim z \lesssim 6.9$ with DESI Legacy Imaging Surveys and the UKIRT Hemisphere Survey and Quasar Luminosity Function at $z \sim 6.7$", ApJ, 884, 30, doi: 10.3847/1538-4357/ab2be5

Wang, F., Davies, F. B., Yang, J., et al. 2020a, "A Significantly Neutral Intergalactic Medium Around the Luminous $z = 7$ Quasar J0252-0503", ApJ, 896, 23, doi: 10.3847/1538-4357/ab8c45

Wang, F., Banados, E., Bian, F., et al. 2020b, "Mapping A Distant Protocluster Anchored by A Luminous Quasar in the Epoch of Reionization", HST Proposal. Cycle 28, ID. #16187

Wang, F., Yang, J., Fan, X., et al. 2021a, "A Luminous Quasar at Redshift 7.642", ApJ, 907, L1, doi: 10.3847/2041-8213/abd8c6

Wang, F., Fan, X., Hennawi, J., et al. 2021b, "A SPectroscopic survey of biased halos In the Reionization Era (ASPIRE): A JWST Quasar Legacy Survey", JWST Proposal. Cycle 1, ID. #2078

Wang, R., Wagg, J., Carilli, C. L., et al. 2013, "Star Formation and Gas Kinematics of Quasar Host Galaxies at $z \sim 6$: New Insights from ALMA", ApJ, 773, 44, doi: 10.1088/0004-637X/773/1/44

Wang, R., Wu, X.-B., Neri, R., et al. 2016, "Probing the Interstellar Medium and Star Formation of the Most Luminous Quasar at $z = 6.3$", ApJ, 830, 53, doi: 10.3847/0004-637X/830/1/53

Weilbacher, P. M., Streicher, O., Urrutia, T., et al. 2012, "Design and capabilities of the MUSE data reduction software and pipeline", in Society of Photo-Optical Instrumentation Engineers

(SPIE) Conference Series, Vol. 8451, Software and Cyberinfrastructure for Astronomy II, ed. N. M. Radziwill & G. Chiozzi, 84510B, doi: 10.1117/12.925114

Weilbacher, P. M., Streicher, O., Urrutia, T., et al. 2014, "The MUSE Data Reduction Pipeline: Status after Preliminary Acceptance Europe", in Astronomical Society of the Pacific Conference Series, Vol. 485, Astronomical Data Analysis Software and Systems XXIII, ed. N. Manset & P. Forshay, 451. https://arxiv.org/abs/1507.00034

Weilbacher, P. M., Palsa, R., Streicher, O., et al. 2020, "The data processing pipeline for the MUSE instrument", A&A, 641, A28, doi: 10.1051/0004-6361/202037855

Wenzl, L., Schindler, J.-T., Fan, X., et al. 2021, "Random Forests as a Viable Method to Select and Discover High-redshift Quasars", AJ, 162, 72, doi: 10.3847/1538-3881/ac0254

Weymann, R. J., Latham, D., Angel, J. R. P., et al. 1980, "The triple QSO PG1115 + 08: another probable gravitational lens", Nature, 285, 641, doi: 10.1038/285641a0

Willott, C. J., Bergeron, J., & Omont, A. 2015, "Star Formation Rate and Dynamical Mass of 10^8 Solar Mass Black Hole Host Galaxies At Redshift 6", ApJ, 801, 123, doi: 10.1088/0004-637X/801/2/123

—. 2017, "A Wide Dispersion in Star Formation Rate and Dynamical Mass of 10^8 Solar Mass Black Hole Host Galaxies at Redshift 6", ApJ, 850, 108, doi: 10.3847/1538-4357/aa921b

Willott, C. J., Omont, A., & Bergeron, J. 2013, "Redshift 6.4 Host Galaxies of 10^8 Solar Mass Black Holes: Low Star Formation Rate and Dynamical Mass", ApJ, 770, 13, doi: 10.1088/0004-637X/770/1/13

Willott, C. J., Delorme, P., Reylé, C., et al. 2010, "The Canada-France High-z Quasar Survey: Nine New Quasars and the Luminosity Function at Redshift 6", AJ, 139, 906, doi: 10.1088/0004-6256/139/3/906

Wolfe, A. M., Gawiser, E., & Prochaska, J. X. 2005, "Damped Lyα Systems", ARA&A, 43, 861, doi: 10.1146/annurev.astro.42.053102.133950

Wong, K. C., Suyu, S. H., Chen, G. C. F., et al. 2020, "H0LiCOW - XIII. A 2.4 per cent measurement of H_0 from lensed quasars: 5.3σ tension between early- and late-Universe probes", MNRAS, 498, 1420, doi: 10.1093/mnras/stz3094

Woods, T. E., Agarwal, B., Bromm, V., et al. 2019, "Titans of the early Universe: The Prato statement on the origin of the first supermassive black holes", PASA, 36, e027, doi: 10.1017/pasa.2019.14

Worseck, G., Khrykin, I. S., Hennawi, J. F., Prochaska, J. X., & Farina, E. P. 2021, "Dating individual quasars with the He II proximity effect", MNRAS, 505, 5084, doi: 10.1093/mnras/stab1685

Worseck, G., & Prochaska, J. X. 2011, "GALEX Far-ultraviolet Color Selection of UV-bright High-redshift Quasars", ApJ, 728, 23, doi: 10.1088/0004-637X/728/1/23

Wright, E. L. 2006, "A Cosmology Calculator for the World Wide Web", PASP, 118, 1711, doi: 10.1086/510102

Wright, E. L., Eisenhardt, P. R. M., Mainzer, A. K., et al. 2010, "The Wide-field Infrared Survey Explorer (WISE): Mission Description and Initial On-orbit Performance", AJ, 140, 1868, doi: 10.1088/0004-6256/140/6/1868

Wu, J., Brandt, W. N., Anderson, S. F., et al. 2012, "X-Ray and Multiwavelength Insights into the Nature of Weak Emission-line Quasars at Low Redshift", ApJ, 747, 10, doi: 10.1088/0004-637X/747/1/10

Wu, J., Brandt, W. N., Hall, P. B., et al. 2011, "A Population of X-Ray Weak Quasars: PHL 1811 Analogs at High Redshift", ApJ, 736, 28, doi: 10.1088/0004-637X/736/1/28

Wu, X.-B., Wang, F., Fan, X., et al. 2015, "An ultraluminous quasar with a twelve-billion-solar-mass black hole at redshift 6.30", Nature, 518, 512, doi: 10.1038/nature14241

Wyithe, J. S. B., & Loeb, A. 2002a, "Magnification of light from many distant quasars by gravitational lenses", Nature, 417, 923, doi: 10.1038/nature00794

Wyithe, J. S. B., & Loeb, A. 2002b, "A Physical Model for the Luminosity Function of High-Redshift Quasars", ApJ, 581, 886, doi: 10.1086/344249

Wyithe, J. S. B., Yan, H., Windhorst, R. A., & Mao, S. 2011, "A distortion of very-high-redshift galaxy number counts by gravitational lensing", Nature, 469, 181, doi: 10.1038/nature09619

Yang, J., Wang, F., Wu, X.-B., et al. 2016, "A Survey of Luminous High-redshift Quasars with SDSS and WISE. II. the Bright End of the Quasar Luminosity Function at $z \approx 5$", ApJ, 829, 33, doi: 10.3847/0004-637X/829/1/33

Yang, J., Venemans, B., Wang, F., et al. 2019a, "Far-infrared Properties of the Bright, Gravitationally Lensed Quasar J0439+1634 at $z = 6.5$", ApJ, 880, 153, doi: 10.3847/1538-4357/ab2a02

Yang, J., Wang, F., Fan, X., et al. 2019b, "Exploring Reionization-era Quasars. IV. Discovery of Six New $z \gtrsim 6.5$ Quasars with DES, VHS, and unWISE Photometry", AJ, 157, 236, doi: 10.3847/1538-3881/ab1be1

—. 2020a, "Pōniuā'ena: A Luminous $z = 7.5$ Quasar Hosting a 1.5 Billion Solar Mass Black Hole", ApJ, 897, L14, doi: 10.3847/2041-8213/ab9c26

—. 2020b, "Measurements of the $z \sim 6$ Intergalactic Medium Optical Depth and Transmission Spikes Using a New $z > 6.3$ Quasar Sample", ApJ, 904, 26, doi: 10.3847/1538-4357/abbc1b

Yip, C. W., Connolly, A. J., Vanden Berk, D. E., et al. 2004, "Spectral Classification of Quasars in the Sloan Digital Sky Survey: Eigenspectra, Redshift, and Luminosity Effects", AJ, 128, 2603, doi: 10.1086/425626

Young, P., Gunn, J. E., Kristian, J., Oke, J. B., & Westphal, J. A. 1980, "The double quasar Q0957+561 A, B: a gravitational lens image formed by a galaxy at $z = 0.39$.", ApJ, 241, 507, doi: 10.1086/158365

Yue, M., Fan, X., Yang, J., & Wang, F. 2021a, "Revisiting the Lensed Fraction of High-Redshift Quasars", arXiv e-prints, arXiv:2112.02821. https://arxiv.org/abs/2112.02821

—. 2022, "A Mock Catalog of Gravitationally Lensed Quasars for the LSST Survey", arXiv e-prints, arXiv:2201.06761. https://arxiv.org/abs/2201.06761

Yue, M., Yang, J., Fan, X., et al. 2021b, "ALMA Observations of the Sub-kpc Structure of the Host Galaxy of a $z = 6.5$ Lensed Quasar: A Rotationally Supported Hyper-Starburst System at the Epoch of Reionization", ApJ, 917, 99, doi: 10.3847/1538-4357/ac0af4

Zwicky, F. 1937, "On the Masses of Nebulae and of Clusters of Nebulae", ApJ, 86, 217, doi: 10.1086/143864